AN EXPERIMENTAL STUDY OF LOWER HYBRID CURRENT DRIVE ON THE VERSATOR II TOKAMAK

by

Matthew James Mayberry

B.A., University of California, San Diego
(1980)

Submitted to the Department of Physics
in Partial Fulfillment of the
Requirements for the
Degree of

DOCTOR OF PHILOSOPHY
at the
MASSACHUSETTS INSTITUTE OF TECHNOLOGY
March 11, 1986

Signature of Author
Department of Physics
March 11, 1986

Certified by
Prof. Miklos Porkolab
Thesis Supervisor

Accepted by
Prof. George F. Koster
Chairman, Departmental Graduate Committee

AN EXPERIMENTAL STUDY OF LOWER HYBRID CURRENT DRIVE ON THE VERSATOR II TOKAMAK

by

Matthew James Mayberry

Submitted to the Department of Physics
on March 11, 1986, in Partial Fulfillment of the
Requirements for the
Degree of
Doctor of Philosophy in Physics

Abstract

It is shown experimentally that the lower hybrid current drive density limit is a function of the rf source frequency. In previous 800 MHz experiments on Versator II, current drive effects disappeared abruptly at densities above $\overline{n}_e \simeq 6 \times 10^{12}\,\mathrm{cm}^{-3}$. With a newly constructed 2.45 GHz rf system, up to 95 kW of rf power has been coupled to Versator II plasmas using a phased four-waveguide grill. With the higher rf frequency, fully rf-driven discharges have been achieved at densities up to $\overline{n}_e = 1.0 \times 10^{13}\,\mathrm{cm}^{-3}$, without raising the level of the toroidal magnetic field ($B_T < 13\,\mathrm{kG}$). Consequently, in the present experiment, quasi-steady-state current drive has been demonstrated with values of the parameter $\omega_{pe}^2/\omega_{ce}^2$ exceeding unity. The flat-top current drive efficiency scaling for the density range $\overline{n}_e = 0.2 - 1.0 \times 10^{13}\,\mathrm{cm}^{-3}$ is given by $\tilde{\eta} = \overline{n}IR/P = 0.0072$ (MKS units, $10^{20}\,\mathrm{m}^{-3}$).

In ohmically-heated discharges, 2.45 GHz current drive effects are observed at densities exceeding $\overline{n}_e = 2 \times 10^{13}\,\mathrm{cm}^{-3}$. In addition, factor-of-two increases in the global partical confinement time have been recorded for densities $\overline{n}_e < 2 \times 10^{13}\,\mathrm{cm}^{-3}$. However, in electron heating experiments with $\Delta\phi = \pi$ and $P_{rf} \sim P_{OH}$ in the density range $\overline{n}_e = 1.0 - 1.5 \times 10^{13}\,\mathrm{cm}^{-3}$, no bulk heating was observed.

Measurements of the plasma hard x-ray emission during 2.45 GHz quasi-steady-state current drive indicate that an energetic electron tail is generated in the center of the plasma with energies exceeding 160 keV. From simulations of the bremsstrahlung emission, it is estimated that less than 10% of the injected rf power is dissipated due to tail-bulk Coulomb collisions. This indicates that weak electron Landau damping and poor radial confinement of the fast electron tail may contribute to the low 2.45 GHz current drive efficiency as well as the lack of bulk heating.

Thesis Supervisor: Dr. Miklos Porkolab

Title: Professor of Physics

Acknowledgments

First of all, I would like to thank Prof. Miklos Porkolab, my thesis advisor and mentor, for his numerous suggestions and contributions during the course of this experiment, and for his continuous support and encouragement over the past five and a half years. Among other things, I have grown to respect and admire Miklos' forthright approach with people, and I hope to emulate this quality as I set forth on my own career. I would also like to thank Prof. George Bekefi for his constant encouragement, beginning with my first tour of Versator II (which convinced me to attend graduate school at MIT).

I am deeply indebted to Drs. Kuo-In Chen and Stanley Luckhardt for their patient guidance and selfless contributions throughout this project, as well as to the Versator II technical staff, Tom Evans, Ed Fitzgerald, Jerry Lorden, and Jack Nickerson, for their sedulous craftsmanship and tireless support. To my fellow graduate students, Bob Kaplan, Dr. Rajeev Rohatgi, and Joel Villaseñor, my sincerest thanks for your assistance and friendship during the course of these experiments.

I would be remiss if I failed to recognize the many individuals outside the Versator group whose contributions were instrumental to the success of this experiment. My appreciation goes to: Prof. Ronald Parker and the Alcator C Staff for their generous contributions of equipment and supplies, including the loan of the 2.45 GHz klystrons and S-band waveguide components; the incomparable Dave Griffin, for his design of the S-band high power rf system; Dr. Alan Fisher, for designing of the rf detection circuitry and electronics; Dr. Schweikhard von Goeler of PPPL, for his assistance with the design of the x-ray pulse height analysis diagnostics; Dr. Scott Texter, for providing me with a copy of his bremsstrahlung x-ray modelling code; and Dr. Paul Bonoli, for his current drive modelling calculations and for many enlightening discussions.

Finally, I would like to thank my family and my friends for their never-ending support throughout this episode of my life.

To my parents,
Leonard and Elsie Mayberry,
To my grandmother,
Jean Harbison,
And to my fiancée,
Karen Elizabeth Tice.

Table of Contents

List Of Figures

List Of Tables

Chapter 1

Introduction

The prospect of using externally-excited radiofrequency (rf) waves to drive a steady state plasma current in a tokamak reactor has generated a great deal of interest in the plasma fusion community in recent years. Previously, the tokamak had been considered to be inherently a pulsed device, since the toroidal plasma current, needed both for Joule heating and plasma confinement, was generated inductively with the ohmic heating (OH) transformer. A number of non-inductive current drive schemes[1,2] have been proposed over the years, including the injection of neutralized ion beams, relativistic electron beams, and rf waves ranging in frequency from $f \sim 10\,\mathrm{MHz}$ (Alfven Waves) to $f \sim 100\,\mathrm{GHz}$ (ECRH). A scheme for producing a steady state toroidal current using intermediate frequency lower hybrid waves ($f \sim 1\,\mathrm{GHz}$) was first proposed by Fisch[3] in 1978. The idea was to launch waves with high phase velocities which travelled preferentially in one direction around the torus. Upon Landau damping on a population of superthermal electrons, these waves would then transfer momentum and energy to the particles. generating a net current [see Fig. 1.1]. The fact that lower hybrid waves can be launched from all-metal phased arrays of waveguides is highly attractive from the reactor engineering standpoint. The feasibility of using such a technique for steady state current drive in a reactor hinges on the rf power requirements, i.e. the efficiency of current generation in amps per watt.

1.1 Elementary Derivation of Current Drive Efficiency

In the absence of inductive electric fields (i.e. in the steady state), the efficiency of lower hybrid current drive can be estimated easily based on simple, physical arguments.[2] Consider the resonant interaction of high phase velocity waves, $v_\phi \gg v_e$, where $v_e = (2T_e/m_e)^{1/2}$ is the electron thermal velocity, with electrons having a velocity parallel to the magnetic field given by $v_{\|} \simeq v_\phi$. The current generated by

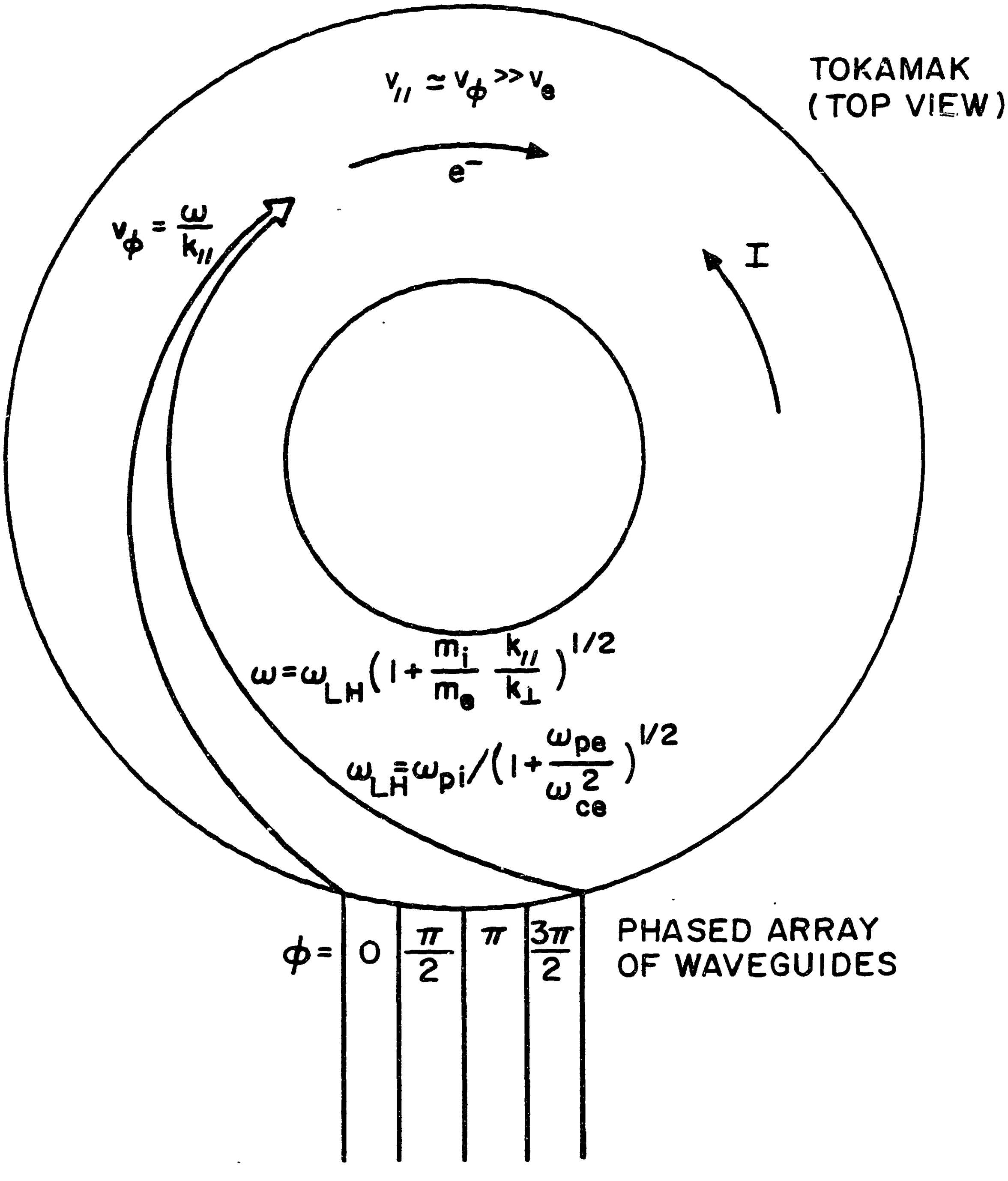

Fig. 1.1: A scheme for generating a steady-state toroidal plasma current in a tokamak reactor using lower hybrid waves.

the quasi-linear diffusion of particles in velocity space is approximately given by:

$$J \simeq n_r e v_\phi, \tag{1.1}$$

where n_r is the density of the resonant electrons. The rf diffusion of the resonant particles is opposed by a frictional force due to Coulomb collisions, given by:

$$F \simeq n_r m_e v_\phi \nu_r, \tag{1.2}$$

where $\nu_r = \nu_0 (v_e/v_\phi)^3$ is the collision frequency of the resonant electrons with the bulk population, and $\nu_0 = \omega_{pe}^4 \log\Lambda / 4\pi n v_e^3$. In the latter expression, $\omega_{pe} = (ne^2/m_e\epsilon_0)^{1/2}$ is the electron plasma frequency, n is the bulk density, and $\log\Lambda$ is the Coulomb logarithm. In the steady state, the rf power required to maintain the current will be equal to the collisional power dissipation:

$$P = F \cdot v \simeq n_r m_e v_\phi^2 \nu_r. \tag{1.3}$$

Dividing the driven current by the dissipated power leads to an expression for the current drive efficiency:

$$J/P \simeq \frac{4\pi\epsilon_0}{e\log\Lambda} \frac{v_\phi^2}{\omega_{pe}^2}. \tag{1.4}$$

Volume averaging, the figure of merit for lower hybrid current drive may be written in the following form:

$$\tilde{\eta} = \frac{\bar{n}(10^{20}\,\mathrm{m}^{-3}) I(\mathrm{kA}) R(\mathrm{m})}{P(\mathrm{kW})} \propto \left(\frac{v_\phi}{c}\right)^2 = \frac{1}{N_{\|}^2}, \tag{1.5}$$

where $\bar{n}$ is the line-averaged density, I is the rf current, R is the major radius, and P is the rf power. The wave parallel index of refraction, $N_{\|} = ck_{\|}/\omega$, is determined by the geometry and relative waveguide phasing of the launching antenna. The higher the resonant wave phase velocity, the more favorable the efficiency, due to the lower collisionality of the resonant electrons ($\nu_r \sim v^{-3}$). However, for the lower hybrid slow waves used in present-day experiments, the minimum $N_{\|}$ value is limited by the following condition for accessibility to the plasma core:[4]

$$N_{\|} > N_{\|acc} = \frac{\omega_{pe}}{\omega_{ce}} + \sqrt{1 + \frac{\omega_{pe}^2}{\omega_{ce}^2}\left(1 - \frac{\omega_{ce}\omega_{ci}}{\omega^2}\right)}, \tag{1.6}$$

where $\omega_{ce} = eB/m_e$ is the electron cyclotron frequency, and $\omega_{ci} = Z_i eB/m_i$ is the ion cyclotron frequency, with Z_i the ion charge state. For typical reactor conditions, $\omega_{pe}^2/\omega_{ce}^2 \sim 0.5 - 1.0$, and $\omega_{ce}\omega_{ci}/\omega^2 \sim 1$, so that $N_{\|acc} \geq 2$, resulting in a figure of merit of $\tilde{\eta} \sim 0.25 - 0.50$. This implies that on the order of one hundred megawatts of power may be required to drive 10 MA of current in a reactor sized device with a major radius of $3 - 5$ meters and a density exceeding $\bar{n} = 10^{20}\,\mathrm{m}^{-3}$.[2,4] It is not clear yet from the present-day experimental results whether the efficiency of steady state current drive with lower hybrid slow waves can be made sufficiently high to be practical for a steady state reactor. Future experiments are being planned to test the possibility of using fast waves[5] with higher phase velocities to drive currents with higher efficiencies.

1.2 The Experimental Development of Lower Hybrid Current Drive

Before the discovery of current drive, lower hybrid experiments concentrated on heating ions. The rf frequencies were chosen to correspond to the lower hybrid resonance frequency, $\omega_{LH} = \omega_{pi}/(1 + \omega_{pe}^2/\omega_{ce}^2)^{1/2}$, in the normal operating regime of tokamaks ($\bar{n} \leq 5 \times 10^{13}\,\mathrm{cm}^{-3}$, $B \leq 20\,\mathrm{kG}$). Hence, $f \sim f_{LH} = \omega_{LH}/2\pi \leq 1\,\mathrm{GHz}$. Lower hybrid current drive was only observed when the density was lowered to the point where $\omega/\omega_{LH} \geq 2$. The first experimental verification of significant wave-driven currents ($\sim 15\,\mathrm{kA}$) were reported on the JFT-2 tokamak[6] in Japan, and the Versator II tokamak[7] in the US. In these experiments, where the plasma current was sustained largely by the OH transformer, the rf current was inferred from loop voltage drops, current increases, and the production of superthermal electrons.

The main achievements of the pioneering experiments on Versator were to demonstrate:[7] 1) that bulk heating was not responsible for the loop voltage drops, since Thomson scattering measurements clearly showed that the temperature actually dropped substantially ($\sim 30\%$) during current drive, 2) that the current drive effects were strongly dependent on the phasing of the six-waveguide antenna, with the largest rf current (and temperature decrease) produced when waves were launched in the direction of the electron ohmic drift, and 3) that a sharp upper density limit existed for current drive, above which the current drive efficiency dropped sharply to zero. On Versator, this "density limit" for the 800 MHz rf frequency occurred at $\overline{n}_e \simeq 6 \times 10^{12}\,\mathrm{cm}^{-3}$. This result was entirely unexpected since the Fisch theory[3] predicted that the current drive efficiency, I/P should scale with density as $1/\bar{n}$ [see Eqn. (1.5)]. It was conjectured that operation in the low density "slideaway" regime,[8] where the target plasmas were characterized by highly non-thermal electron distribution functions, was a necessary prerequisite for efficient current drive.[7]

The high conductivity of the "slideaway" plasmas made it quite difficult to prove that the plasma current could be fully sustained by rf waves alone, since even a small inductive loop voltage contribution could drive a substantial plasma current. For example, in superthermal ohmic discharges on the ASDEX tokamak,[9] plasma currents exceeding 200 kA were sustained for over 10 sec with a loop voltage of only 0.12 V at densities $\overline{n}_e = 1 - 2 \times 10^{12}\,\mathrm{cm}^{-3}$. In order to demonstrate the feasibility of steady state lower hybrid current drive, it remained to be shown that the plasma current could be sustained fully by rf waves, with no assist from the OH transformer or other sources of inductive voltage. This would require rf pulse lengths which were longer than the L/R response time of the plasma, where L is the total plasma inductance (internal plus external), and R is the plasma resistance. It also needed to be demonstrated that current drive could be achieved at high densities ($\bar{n} > 1 \times 10^{13}\,\mathrm{cm}^{-3}$).

The first of these objectives was met successfully on the PLT tokamak[10] when rf current "flat-topping" was demonstrated for the first time. In these experiments the OH transformer primary current was clamped following the plasma start-up. The subsequent L/R decay of the plasma current was then fully arrested by the injection of sufficient rf power. In this way, a fully rf-driven current of 165 kA was maintained with the loop voltage nearly equal to zero for a period of 3.5 sec. For shorter periods (0.3 sec), up to 420 kA of plasma current could be maintained with up to 500 kW of rf power. Careful measurements of the equilibrium vertical field current eliminated the possibility that the current was driven by current profile modifications (changes in the internal inductance). These experiments also provided the first measurements of lower hybrid current drive efficiency in the absence of a dc electric field. The current drive figure of merit obtained was $\tilde{\eta} = \bar{n}IR/P \simeq 0.1$, in reasonable agreement with the Fisch theory.[3] However, once again with an operating frequency of 800 MHz, efficient current drive was limited to low densities, in this case below $\overline{n}_e = 8 \times 10^{12}\,\mathrm{cm}^{-3}$.

Fully rf-driven discharges at reactor-relevant densities $10^{13} \leq \bar{n}(\mathrm{cm}^{-3}) \leq 10^{14}$ were demonstrated for the first time on the Alcator C tokamak[11] where a high frequency lower hybrid system at $f = 4.6\,\mathrm{GHz}$ was used to sustain 150 – 200 kA of current with up to 1.1 MW of rf power. Wave accessibility in these experiments was achieved with a high toroidal magnetic field (6 – 10 T), so that the corresponding value of $\omega_{pe}^2(0)/\omega_{ce}^2(0)$ remained fairly low, on the order of ~ 0.15. With the OH primary open-circuited, the current drive efficiency scaling of Fisch,[3] $\tilde{\eta} = \bar{n}IR/P$, was established experimentally for the first time over a wide density range, with $\tilde{\eta} = 0.12$ at 10 T and $\tilde{\eta} = 0.08$ at $8\,T$. The higher current drive efficiency at the higher magnetic field strength is believed to be due to improved accessibility of low-$N_{\|}$ waves. Note that in both the Alcator[11] and PLT[10] experiments, the steady state current drive efficiency also depended strongly on waveguide phasing with flat-topping only possible for $\Delta\phi = 60 - 135°$. At present, the maximum flat-top current drive density on Alcator, $\bar{n} = 10^{14}\,\mathrm{cm}^{-3}$, appears to be limited by the rf power available without significant impurity injection. The density limit for wave-electron interaction appears at higher densities, $\overline{n}_e \simeq 1.5 - 2 \times 10^{14}\,\mathrm{cm}^{-3}$ in H plasmas.[12] The Alcator 4.6 GHz results represent more than an order-of-magnitude improvement in density over the previous 800 MHz experiments.

More recent experiments have focussed on other possible applications of LHCD in addition to steady state current drive which may help to reduce the volt-second requirements of the OH transformer during reactor start-up. On the PLT[13], WT-2[14] and JIPP T-II[15] tokamaks it has been shown that rf waves can be used to initiate a tokamak discharge with no inductive assist from the OH transformer. In the PLT experiment,[13] 200 kW of rf power was used to break down the plasma and raise the discharge current to a level in excess of 100 kA, at a density of $\overline{n}_e \sim 1 \times 10^{12}\,\mathrm{cm}^{-3}$. In the WT-2[14] and JIPP T-II[15] experiments, ECRH power (35 GHz) was also injected to aid with the preionization of the fill gas. The successful demonstration of rf start-up has opened up the possibility of completely eliminating the OH transformer in a tokamak reactor.

In case fully rf-driven operation of tokamaks proves too inefficient at reactor densities, lower hybrid waves may still be used to assist the OH transformer in ramping up the plasma current at low densities where current drive is the most efficient. In current ramp-up, the rf power level is increased beyond the level needed to Maintain the current at a constant level. Since the plasma current increases with time, a negative loop voltage is induced which tends to oppose the current change. The efficiency of the ramp-up process may be characterized by the rate at which rf energy is converted into poloidal field energy due to the slowing down of the fast electrons by the negative electric field. Subtracting out the inductive contribution, P_{ext}, which arises mainly from the vertical field (which must be ramped up to maintain equilibrium), the ramp-up efficiency may be written:[16]

$$\epsilon = \frac{\frac{d}{dt}\left(\frac{1}{2}LI^2\right) - P_{ext}}{P_{rf}}, \tag{1.6}$$

where $\frac{1}{2}LI^2$ is the poloidal field energy, L is the total plasma inductance, and P_{rf} is the injected rf power. On PLT,[16] at densities of $\overline{n}_e \simeq 2 \times 10^{12}\,\mathrm{cm}^{-3}$, ramp-up efficiencies of up to $\epsilon = 0.20$ have been obtained. At higher densities, the efficiency is reduced because the fast electrons are slowed down increasingly by collisions rather than the electric field. On Alcator C,[17] efficiencies of $5 - 10\%$ have been achieved at densities $\bar{n} \geq 1 \times 10^{13}\,\mathrm{cm}^{-3}$.

In the current ramping experiments, the OH current is maintained constant while the plasma current is increased during the rf pulse. An alternative approach, demonstrated on the ASDEX[18] and Alcator C[4] tokamaks, is to prevent the increase in the plasma current by inducing an additional negative loop voltage by ramping up the current in the OH transformer primary. Such a current increase leads to a recharging of the OH transformer. On ASDEX,[18] flux swings of $\int \dot{I}_{OH} M dt = 0.24\,\mathrm{V\,sec}$ (M is the mutual inductance between the plasma and the OH coil) have been generated with a 1 sec, 690 kW rf pulse, while maintaining a plasma with

$\bar{n}_e = 4 \times 10^{12}\,\mathrm{cm}^{-3}$, and $I_p = 290\,\mathrm{kA}$. In Alcator C,[4] 10% of the volt-second requirement of the transformer was reduced during a 200 ms pulse (typical ramp-rates on the order of 300 kA/s have been achieved). These achievements offer a new scenario for cyclic operation of a tokamak reactor in which high density OH-burn phases are alternated with low-density LH-driven transformer recharging.

1.3 The Density Limit

Nearly every lower hybrid current drive experiment to date has encountered an upper "density limit," above which current drive effects sharply disappear. Although a number of theoretical models have been proposed to explain this effect,[19] the physical mechanism responsible for the density limit is still not completely understood today.[20] However, parametric interactions near the plasma surface (or inside) are prime candidates.[12,21] In order to motivate the 2.45 GHz current drive experiment on Versator, we will briefly review what is presently known experimentally about the lower hybrid density limit.

Following the first demonstrations of current drive in the 800 MHz experiments on JFT-2[6] and Versator II,[7] it was not clear whether operation in the low density "slideaway" regime ($\bar{n} \leq 6 \times 10^{12}\,\mathrm{cm}^{-3}$) was necessary because preformed tails were generated, or because wave-ion interactions were avoided when $\omega/\omega_{LH} \geq 2$. More recent experiments on the PLT[20] and ASDEX[22] tokamaks have demontrated that generating a preformed superthermal electron tail by lowering the density prior to rf injection does not change the critical density observed later when the density is raised by gas puffing during the rf pulse. Under certain conditions, hard x-ray measurements on PLT[10] and Alcator C[11] have also shown negligible superthermal x-ray emission just prior to efficient quasi-steady state current drive. These results indicate that, at least in the case of steady state current drive, the density limit is insensitive to the target plasma superthermals.

In many current drive experiments, including Alcator C,[12,17] PLT,[20] JFT-2,[6,23] WEGA III,[19,24] and ASDEX,[22] it has been observed that the sudden disappearance of wave-electron interactions at high densities is accompanied by an increase in parametric decay activity, ion tail formation, and in the case of deuterium plasmas, neutron production. Similar effects have also been observed on the FT[25] tokamak where 2.45 GHz electron heating experiments are carried out using a 2×2 waveguide array phased at $\Delta\phi = \pi$. In the Alcator,[12,17] PLT,[20] JFT-2,[6,23] and ASDEX[22] experiments, it appears that parametric decay occurring at the plasma surface may prevent the penetration of the pump wave power to the center of the plasma. Such instabilities and the associated ion heating were already noted in the old ATC experiments.[21] The threshhold density for the parametric decay also usually coincides with the onset of energetic ion tail formation near the plasma surface, indicating that the low frequency decay waves are damping on ions rather than electrons. However, in other cases, such as on FT[25] and on Alcator C[12,17] at high currents ($I > 450$ kA), ion tails have been observed at densities below the parametric decay threshhold, indicating that a direct switchover of wave interaction from electrons to ions may take place near the center of the plasma due to strong quasi-linear ion Landau damping.[4,19] While both of these mechanisms are expected to become important for $\omega/\omega_{LH} \leq 2$, the one which dominates in a given experiment (and hence determines the density limit) appears to depend on the plasma parameters such as the current, magnetic field, density and temperature profiles and impurities. Better insight into the wave-ion interaction physics is essential not only for an understanding of the lower hybrid current drive density limit, but also for the process of lower hybrid ion heating.

While the critical density is rather insensitive to variations in plasma parameters for a given experiment, the density limit does appear to depend strongly on the frequency of the rf source.[4,20,21] This can be seen in Table 1.1, where we have listed the operating parameters for a number of lower hybrid experiments ranging in frequency from 800 MHz ($\bar{n}_c \simeq 6-8 \times 10^{12}\,\mathrm{cm}^{-3}$) to 4.6 GHz ($\bar{n}_c \simeq 1 \times 10^{14}\,\mathrm{cm}^{-3}$). The critical density where the current drive effects disappear (or electron heating effects in the case of FT) scales approximately with frequency as $\bar{n}_c \sim f^{1.7}$.[4] However, in these experiments, the toroidal magnetic field also increases with frequency and density, so that the value of $\omega_{pe}^2/\omega_{ce}^2$ always remains low ≤ 0.3, insuring the

TABLE 1.1

LOWER HYBRID CURRENT DRIVE DENSITY LIMIT

DEVICE	a (cm)	R (cm)	B_{max} (T)	f (GHz)	$N_{\parallel}$	$\bar{n}_c$ (10^{13} cm^{-3})	$\overline{\omega_{pe}^2/\omega_{ce}^2}$	$\tilde{\eta}_{max}$
ALCATOR C	17	64	10	4.6	2	>10 15^a	$\gtrsim$0.1	0.12
FT	20	83	8	2.45	2	5^a	.08–0.3	NA
ASDEX	40	165	2.2	1.3	1.8	2.0	0.3	0.1
PETULA-B	17	72	2.8	1.3	2.4	2.0	0.3	0.11
T-7	35	122	1.9	0.9	2.5	1.0	0.3	NA
VERSATOR II	13	40.5	1.4	0.8	2.5,7.5	0.6	0.4	0.01
					8^b	0.6	0.4	NA
				2.45	2	$\gtrsim$2	>1	0.0072
PLT	45	132	3.2	0.8	2	0.8	0.08	0.1
WEGA III	15	72	2.3	0.8	3	1.2	0.2	NA
JFT-2	25	90	1.5	0.75	2.5,5.5	0.7	0.3	NA

[a] Density limit for electron heating effects.

[b] Top launch antenna.

accessibility of low-$N_{\|}$ waves to the plasma core. Consequently, the variation of the current drive density limit with frequency has not yet been isolated in a single device. In particular, it has not been shown up until now that the density limit on a given device can be raised by increasing the frequency of the rf source, while leaving the toroidal magnetic field and other plasma parameters (i.e., T_e) unchanged. This requires a demonstration of quasi-steady-state current drive in a regime which has remained unexplored, namely where the parameter $\omega_{pe}^2/\omega_{ce}^2$ approaches unity. However, it is exactly this regime which must be explored before the feasibility of steady state lower hybrid current drive in a reactor can be determined. The primary goals for the work described within this thesis are as follows: 1) to demonstrate the frequency scaling of the lower hybrid current drive density limit on the Versator II tokamak, 2) to gain some understanding of the physics behind the density limit, and 3) to study current drive in the regime $\omega_{pe}^2/\omega_{ce}^2 \sim 1$.

1.4 Scope of This Work

In order to study the frequency scaling of the density limit on the Versator II tokamak, a new 100 kW, 40 ms rf system at 2.45 GHz has been constructed. Power is coupled to plasmas through a 4-waveguide array, side-launching antenna. The travelling wave spectrum which is launched when the antenna is phased at $\Delta\phi = +90°$ is very similar to that of the 800 MHz 4-waveguide side-launcher used in previous experiments,[7,26] where the plasma current was maintained by a combination of ohmic and rf drive. Recently, the OH system on Versator has been modified to permit open-circuiting of the OH transformer primary following the start-up phase of the discharge.[27] Under these conditions, 800 MHz current drive effects still disappear at densities above $\bar{n}_e \simeq 6\times10^{12}\,\mathrm{cm}^{-3}$, as shown in Table 1.1.[28] With the new 2.45 GHz rf system, fully rf-driven discharges have been achieved at densities up to $\bar{n}_e = 1.0 \times 10^{13}\,\mathrm{cm}^{-3}$, with 80 kW of net injected rf power.[29] The toroidal magnetic field has remained at $B \leq 13\,\mathrm{kG}$, the same level used in the earlier 800 MHz experiments.[7,26] Therefore, in the present 2.45 GHz experiments the parameter $\omega_{pe}^2/\omega_{ce}^2$ has exceeded unity during quasi-steady-state current drive.[29]

In addition to the investigation of 2.45 GHz "flat-top" current drive efficiency, current ramping has been studied and compared to the recent theory developed by Fisch and Karney.[30] At high densities, $\overline{n}_e > 1 \times 10^{13}\,\mathrm{cm}^{-3}$, where the available rf power level is insufficient for maintaining the plasma current, we have also injected rf power into ohmically-sustained plasmas in an attempt to determine the upper density limit for 2.45 GHz current drive on Versator. While current drive effects become small at densities above $\overline{n}_e \sim 2 \times 10^{13}\,\mathrm{cm}^{-3}$, it is not known whether this is due to a "density limit" or to the limited rf power available. In particular, accessibility at these densities $(\omega_{pe}^2/\omega_{ce}^2 \geq 2)$ becomes poor. Nevertheless, these results represent more than a factor of three increase in the density limit on Versator as the frequency was raised from 0.8 GHz to 2.45 GHz. The global particle confinement of current-driven plasmas has been studied following the previous 800 MHz experiments at low densities, $\overline{n}_e \leq 6 \times 10^{12}\,\mathrm{cm}^{-3}$, where factor-of-two increases in the bulk particle confinement were observed during current drive.[31,32] In the present 2.45 GHz experiment, similar improvements are observed, at densities up to $\overline{n}_e \sim 2 \times 10^{13}\,\mathrm{cm}^{-3}$.[33] Electron heating has also been attempted with $\Delta\phi = \pi$ and $P_{rf} \sim P_{OH}$ in the density range $\overline{n} = 1 - 1.5 \times 10^{13}\,\mathrm{cm}^{-3}$, but without much success. One possible reason is poor electron tail confinement. Finally, two diagnostics have been developed as a part of this work to study the x-ray emission from the fast electron tails generated during LHCD. In an attempt to determine the electron velocity distribution function and its properties during quasi-steady-state current, the x-ray measurements made during 2.45 GHz flat-top experiments have been modelled with a relativistic bremsstrahlung code. Similar work has been carried out on PLT[34,35] and Alcator C[36].

The Versator II tokamak, upon which these experiments were performed, has been adequately described in previous graduate student theses,[37-41] and therefore will not be described in detail here. The set-up used for the present experiment including the location of the rf antennas and the various diagnostics is shown in Fig. 1.2. Typical tokamak and rf system parameters are shown in Table 1.2.

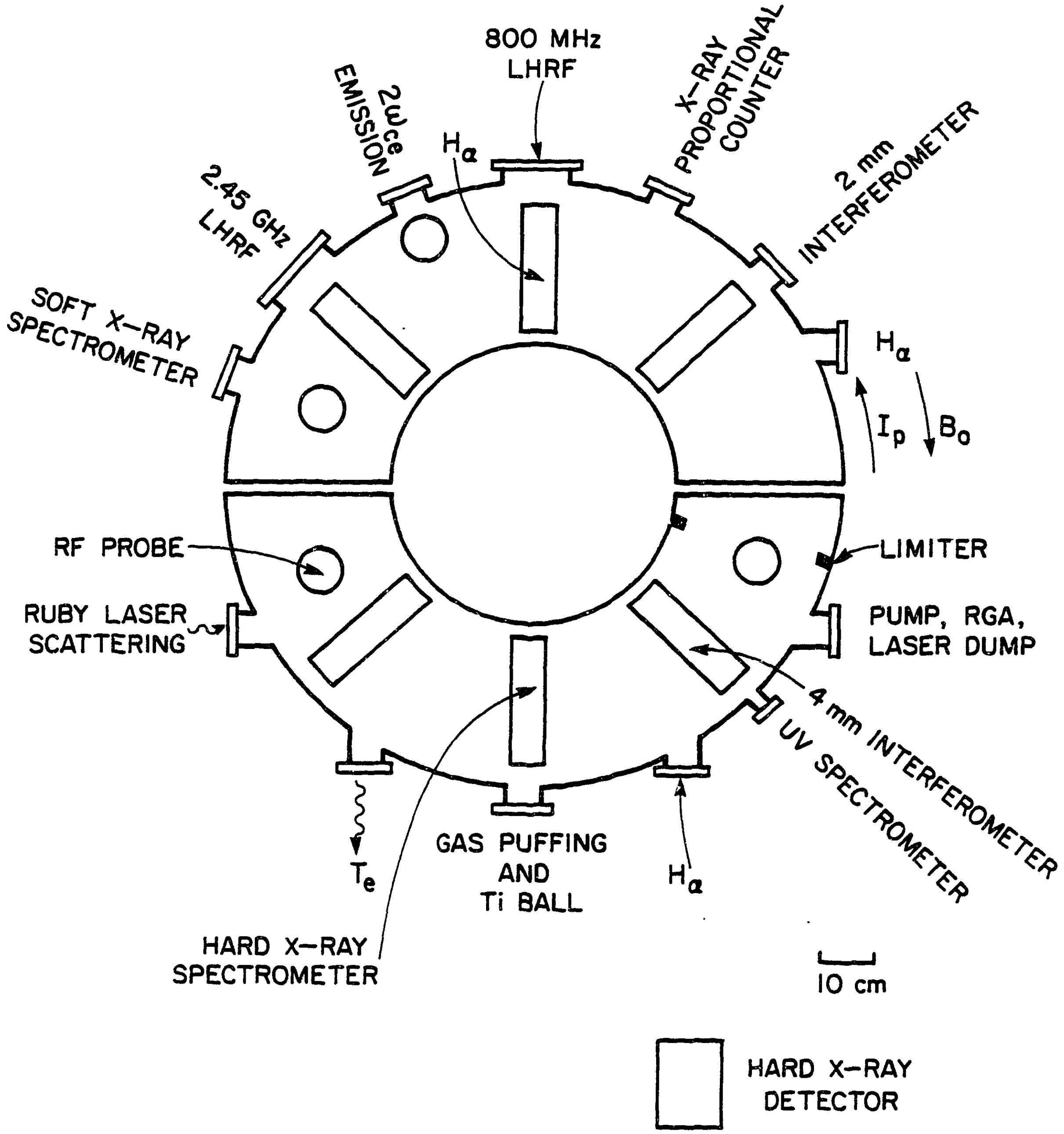

Fig. 1.2: Top view of the Versator II tokamak showing the locations of the 2.45 GHz and 800 MHz lower hybrid grills as well as the port allocations for the diagnostics used during the 2.45 GHz current drive experiments.

TABLE 1.2

Versator II Tokamak and Lower-Hybrid Rf System Parameters

Tokamak	
Major radius R_o	40.5 cm
Limiter radius a	13 cm
Toroidal magnetic field B_o	$\leq$ 14 kG
Plasma current I_p	15 - 70 kA
Line-averaged electron density $\bar{n}_e$	0.2 - 2.5 x 10^{13} cm^{-3}
Central electron temperature T_{eo}	100 - 450 eV
Central ion temperature T_{io}	$\sim T_{eo}/3$
Effective ionic charge Z_{eff}	~ 2
Safety factor q_L	4 - 20
Rf System	
Frequency $\omega/2\pi$	2.45 GHz
Maximum power P_{rf}	100 kW
Maximum pulse length τ_{rf}	40 ms
Antenna	4-waveguide phased array
Waveguide dimensions	1.00 cm x 8.64 cm
Launched spectrum ($\Delta\phi = +90°$)	$1 < N_{\parallel} < 4$
Microwave windows	External, ceramic

1.5 Outline

The theory of lower hybrid current drive is outlined in Chapter 2, as well as the linear theory of lower hybrid wave propagation, accessibility, and absorption. In Chapter 3, the 2.45 GHz rf system is described, including a brief discussion of the high power coupling performance of the antenna. The experimental results are presented in Chapters 4 through 6. In Chapter 4, the flat-top current drive and ramp-up experiments, carried out with the OH primary open-circuited, are described. In Chapter 5, the combined OH/rf experiments are discussed, including the search for a 2.45 GHz density limit, the study of particle confinement, and the attempts at electron bulk heating. The x-ray measurements are presented in Chapter 6. Finally, in Chapter 7, the results are summarized and tied together with the aid of the Bonoli-Englade simulation model for steady state current drive which incorporates a relativistic 1-d Fokker-Planck calculation (with 2-d effects) and a toroidal ray tracing code.

Chapter 2

Theory of Lower Hybrid Current Drive

In lower hybrid current drive, energy and parallel momentum are transferred from externally-excited waves in the plasma to resonant electrons via quasi-linear Landau damping. The current is carried by the small fraction of electrons which comprises the non-thermal tail of the velocity distribution function. Efficient lower hybrid current drive requires the following: 1) the efficient coupling of rf power from an antenna to the normal wave modes of the plasma, 2) accessibility of the waves to the center of the plasma, 3) strong electron Landau absorption near the center of the plasma, 4) good radial confinement of the tail particles, and 5) weak thermalization of the tail particles with the bulk plasma. In the first half of this chapter, we will address the basic issues of lower hybrid wave propagation, accessibility, and absorption in the context of linear theory. A discussion of waveguide coupling theory is postponed until Chapter 3. In the second half of the chapter, we present a simple model of lower hybrid current drive first given by Fisch.[3] He assumes that the radial confinement time of the tail particles greatly exceeds the slowing down time due to bulk collisions, in which case the steady state current drive efficiency is determined entirely by the collisional power dissipation. The validity of this model will be examined later when our experimental results are discussed in Chapter 8.

2.1 Linear Theory of Lower Hybrid Wave Propagation and Damping

In this section, we consider the linear propagation and absorption of lower hybrid waves[43-46] in a magnetized plasma. In addition to electron Landau damping, two other linear mechanisms for the absorption of wave power are examined, namely perpendicular ion Landau damping and collisional damping. These latter two damping mechanisms are relevant to the study of current drive because they may deprive the resonant electrons of wave power. The dominance of resonant ion absorption over resonant electron absorption at high densities ($\omega/\omega_{LH} \simeq 1 - 1.5$)

may be be responsible for the current drive density limit observed in experiments. Collisional absorption of wave power in the colder edge region of the plasma also becomes more prominent at high densities. The inclusion of thermal effects modifies the wave propagation characteristics in the vicinity of the lower hybrid resonance layer. However, wave propagation in the current drive regime ($\omega/\omega_{LH} \geq 2$) is well described by cold plasma theory. Hence, we begin this section with a basic description of lower hybrid wave propagation and accessibility in a cold magnetized plasma.

2.1.1 Lower Hybrid Wave Propagation in a Cold Plasma

For wave fields which vary as $\exp[i(\mathbf{k}\cdot\mathbf{x} - \omega t)]$, with $|\mathbf{k}| \gg |\partial/\partial\mathbf{x}|$ (WKB approximation), the wave equation in a magnetized plasma may be written as:

$$\mathbf{k}\times\mathbf{k}\times\mathbf{E} + \frac{\omega^2}{c^2}\mathbf{K}\cdot\mathbf{E} = 0, \tag{2.1}$$

where $\mathbf{E}$ is perturbed electric field, and $\mathbf{K}$ is the dielectric tensor. We will assume that the magnetic field $\mathbf{B_0}$ is oriented in the z-direction. Then for the lower hybrid range of frequencies, $\omega_{ci}^2 \ll \omega^2 \ll \omega_{ce}^2$, the dielectric tensor $\mathbf{K}$ is given by:[5]

$$\mathbf{K} = \begin{pmatrix} K_\perp & -iK_{xy} & 0 \\ iK_{xy} & K_\perp & 0 \\ 0 & 0 & K_\parallel \end{pmatrix}, \tag{2.2}$$

where

$$K_\perp \simeq 1 + \frac{\omega_{pe}^2}{\omega_{ce}^2} - \frac{\omega_{pi}^2}{\omega^2}$$

$$K_{xy} \simeq \frac{\omega_{pe}^2}{\omega\omega_{ce}}$$

$$K_\parallel \simeq 1 - \frac{\omega_{pe}^2}{\omega^2},$$

with $\omega_{p\alpha} = n_\alpha Z_\alpha^2 e^2/\epsilon_0 m_\alpha$. Setting the determinant of the system of equations (2.1) to zero yields the cold plasma electromagnetic dispersion relation for lower hybrid waves:

$$D(\mathbf{x},\mathbf{k},\omega) = aN_\perp^4 - bN_\perp^2 + c = 0, \tag{2.3}$$

where

$$a = K_\perp$$
$$b = (K_\perp + K_\parallel)(K_\perp - N_\parallel^2) - K_{xy}^2$$
$$c = K_\parallel\left[(N_\parallel^2 - K_\perp)^2 - K_{xy}^2\right],$$

with $\mathbf{N} = c\mathbf{k}/\omega$. We will assume for now that $N_\parallel$ is a constant which is fixed by the antenna. This assumption will be relaxed later when we consider the effects of toroidal geometry on lower hybrid wave propagation.

Two modes of wave propagation are indicated by the two solutions to Eqn. (2.3):

$$N_\perp^2 = \frac{b \pm (b^2 - 4ac)^{1/2}}{2a}, \tag{2.4}$$

with the plus sign corresponding to the "slow" wave, and the minus sign corresponding to the "fast" wave. For the slow wave branch, a resonance ($N_\perp^2 \to \infty$) occurs when $a = K_\perp = 0$. This condition defines the lower hybrid frequency:

$$\omega_{LH} = \frac{\omega_{pi}}{\left(1 + \omega_{pe}^2/\omega_{ce}^2\right)^{1/2}}. \tag{2.5}$$

To date, it is this slow wave branch which has been used in lower hybrid heating and current drive experiments.

At the edge of the plasma, the slow wave dispersion relation becomes:

$$N_\perp^2 = \left(1 - \frac{\omega_{pe}^2}{\omega^2}\right)\left(1 - N_\parallel^2\right). \tag{2.6}$$

Hence, slow wave propagation for $N_\parallel > 1$ can only occur inside a critical cut-off layer ($k_\perp \to 0$) given by $\omega = \omega_{pe}(n_{cr})$. This is generally not a limitation, since good waveguide coupling is achieved by inserting the antenna mouth beyond this cut-off layer. Slow wave penetration beyond the cut-off layer will continue unimpeded unless coupling to the fast wave mode occurs. In this case, the waves will be inaccessible to the center of the plasma since the inward propagating slow wave is mode-converted to an outward propagating fast wave. The density at which this occurs is found by setting $b^2 - 4ac = 0$ in Eqn. (2.4). The solutions are given by:

$$\frac{\omega_{pi}}{\omega} = N_\parallel Y \pm \sqrt{1 + N_\parallel^2\left(Y^2 - 1\right)}, \tag{2.7}$$

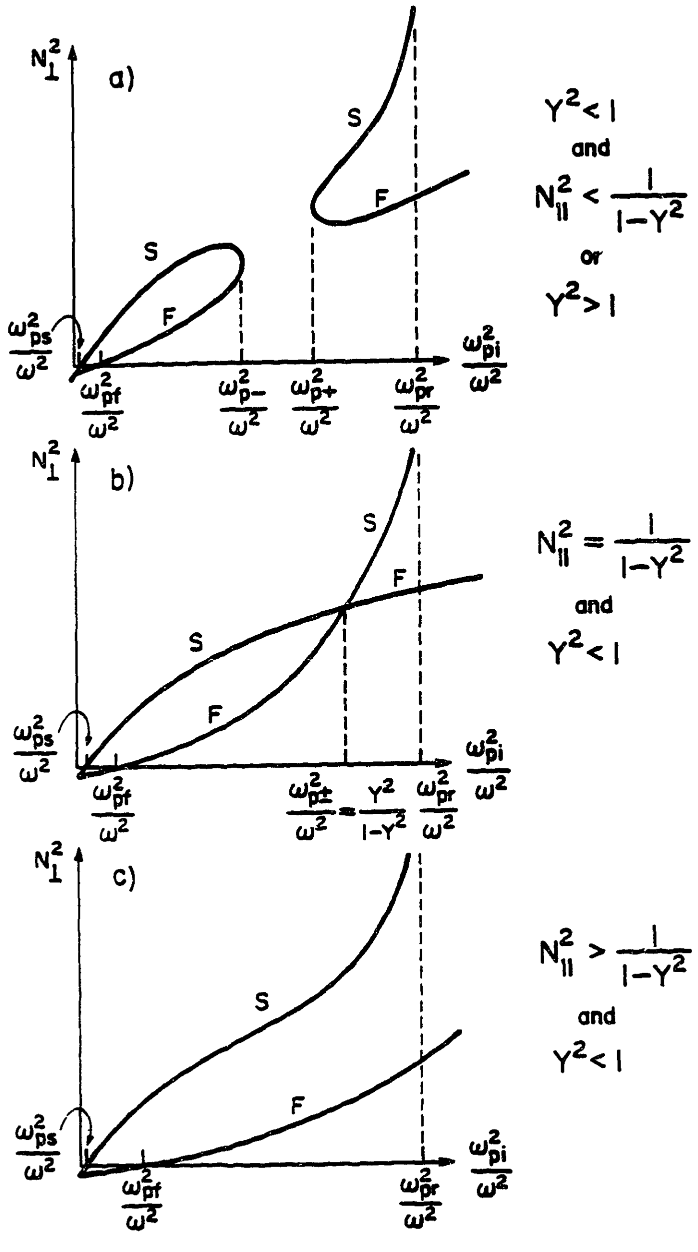

Fig. 2.1: $N_\perp^2$ is plotted versus density (ω_{pi}^2/ω^2) for the slow (S) and fast (F) wave branches of the cold lower-hybrid dispersion relation [Eqn. (2.3)]. The slow and fast wave cut-offs are given by ω_{ps}^2/ω^2 and ω_{pf}^2/ω^2 respectively. The lower hybrid resonance is located at ω_{pr}^2/ω^2. The confluence points where the slow and fast wave modes converge are denoted by ω_{p-}^2/ω^2 and ω_{p+}^2/ω^2.

where $Y^2 = \omega^2/\omega_{ce}\omega_{ci}$. The qualitative behavior of these roots is shown in Fig. 2.1, where $N_\perp^2$ is plotted as a function of density (ω_{pi}^2/ω^2) for the slow (S) and fast (F) wave branches. The slow and fast wave cut-offs are labeled by ω_{ps}^2/ω^2 and ω_{pf}^2/ω^2 respectively. The lower hybrid resonance layer is located at $\omega_{pi}^2/\omega^2 = \omega_{pr}^2/\omega^2 = (1 - Y^2)^{-1}$. When the determinant in Eqn. (2.7) is greater than zero, there are two confluence points, corresponding to ω_{p-} and ω_{p+}, which are separated by a region of evanescence $(N_\perp^2 < 0)$ [see Fig. 2.1a)]. In this case, propagation to the lower hybrid resonance layer cannot occur unless the waves tunnel through the evanescent layer. On the other hand, if the determinant of Eqn. (2.7) is less than zero, then the confluence points are eliminated and the wave is accessible all the way to the lower hybrid resonance layer [see Fig. 2.1c)]. In the marginal case, shown in Fig. 2.1b), $N_\parallel^2 = (1 - Y^2)^{-1}$, and the mode coupling density is single valued, given by $\omega_{p-}^2/\omega^2 = \omega_{p+}^2/\omega^2 = Y^2/(1 - Y^2)$. Note that the elimination of the evanescent region requires a sufficiently high magnetic field $(Y^2 < 1)$ as well as a sufficiently large value for the parallel index of refraction. From a further analysis of Eqn. (2.7), the following accessibility conditions may be obtained:[45,47,48]

1) If $Y^2 < 1$ and $\omega_{pi0}^2/\omega^2 > Y^2/(1 - Y^2)$, then

$$N_\parallel \geq N_{\parallel acc} = \frac{1}{(1 - Y^2)^{1/2}}, \tag{2.8a}$$

2) If $Y^2 > 1$ or $Y^2 < 1$ and $\omega_{pi0}^2/\omega^2 < Y^2/(1 - Y^2)$, then

$$N_\parallel \geq N_{\parallel acc} = \frac{\omega_{pi0}}{\omega} Y + \left[1 + \frac{\omega_{pi0}^2}{\omega^2}(Y^2 - 1)\right]^{1/2} . \tag{2.8b}$$

Case 1) corresponds to the situation shown in Fig. 2.1c), while case 2) corresponds to the situation in Fig. 2.1a). In the latter case, the accessibility condition results from the requirement that $\omega_{pi0}^2/\omega^2 < \omega_{p-}^2/\omega^2$. If $Y^2 < 1$ and the maximum density is given by $\omega_{pi0}^2/\omega^2 = Y^2/(1 - Y^2)$, then it is easily seen that accessibility conditions 1) and 2) become equivalent, namely $N_{\parallel acc}^2 = 1/(1 - Y^2)$. Note that propagation to higher densities $Y^2/(1 - Y^2) < \omega_{pi0}^2/\omega^2 < 1/(1 - Y^2)$ requires no further increase in $N_\parallel$. The condition for wave accessibility all the way to the lower hybrid resonance layer is obtained by substituting $Y^2 = \omega_{LH}^2/\omega_{ce}\omega_{ci}$ into

Eqn. (2.8a), which gives:[47]

$$N_{\parallel}^2 \geq 1 + \left.\frac{\omega_{pe}^2}{\omega_{ce}^2}\right|_{\omega=\omega_{LH}} . \tag{2.9}$$

During lower hybrid current drive and electron heating experiments, where $\omega/\omega_{LH}(0) \geq 1.5$, the relevant accessibility condition is usually given by Eqn. (2.8b).

Lower hybrid wave penetration is improved by raising the magnetic field or by lowering the wave frequency. This is illustrated in Fig. 2.2, where we have plotted $N_{\perp}^2$ from the cold plasma dispersion relation (2.4) as a function of major radius along the midplane of the tokamak. The dispersion curves are plotted for various $N_{\parallel}$ values ranging between 1.5 and 3.5, in increments of $\Delta N_{\parallel} = 0.1$. We have included the toroidal magnetic field gradient, given by $B(R) = B_0 R_0/R$. In addition, we have assumed a Gaussian density profile $n_e(r) = n_{e0}\exp(-r^2/\lambda_n^2)$, where $r = R - R_0$, and $\lambda_n = 10\,\mathrm{cm}$. The parameters for Fig. 2.2a) are: $B_0 = 13\,\mathrm{kG}$, $\bar{n} = 1.0 \times 10^{13}\,\mathrm{cm}^{-3}$, $f = 2.45\,\mathrm{GHz}$. Under these conditions, $Y^2 \simeq 8.3$, and the relevant accessibility condition at the center of the plasma, given by Eqn. (2.8b), is $N_{\parallel} > N_{\parallel acc} = 2.35$. This is in agreement with the dispersion diagram. Note that because the toroidal field is stronger on the inside of a tokamak, the wave penetration is more favorable from the inside. In Fig. 2.2b) the toroidal field was reduced to $B_0 = 10\,\mathrm{kG}$, and in this case, only waves with $N_{\parallel} > 2.88$ are accessible all the way to the center. A comparison of Figs. 2.2a) and b) shows that raising the toroidal field improves accessibility. In Fig. 2.2c), the effect of lowering the wave frequency is shown. In this case, the parameters are: $f = 800\,\mathrm{MHz}$, $\bar{n}_e = 1.0 \times 10^{13}\,\mathrm{cm}^{-3}$, $B_0 = 13\,\mathrm{kG}$. Under these conditions, $Y^2 = 0.89$ and $\omega_{pi0}^2/\omega^2 = 0.12 < Y^2/(1 - Y^2)$. Therefore, using Eqn. (2.8b) for the accessibility condition, we find $N_{\parallel acc} \simeq 1.93$. A comparison between Fig. 2.1a) and c) shows that accessibility is worse for the higher wave frequency.

It is evident from Figs. 2.1a) – c) that $N_{\perp}^2$ can become quite large away from the plasma edge and the mode coupling layers. Under these conditions ($N = ck/\omega \gg 1$) the lower hybrid wave polarization becomes electrostatic ($\omega B_1 \ll kE_1$). The dispersion relation (2.3) then reduces to the form:

$$D(\mathbf{x}, \mathbf{k}, \omega) = K_{\perp} k_{\perp}^2 + K_{\parallel} k_{\parallel}^2 = 0, \tag{2.10}$$

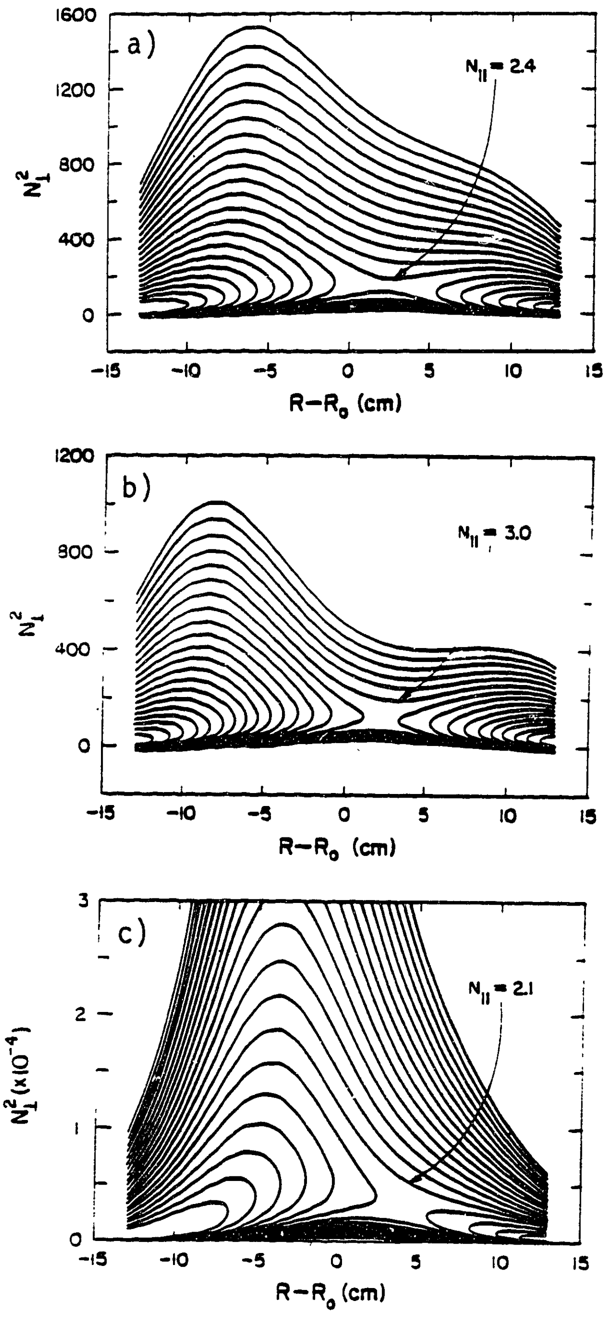

Fig. 2.2: $N_\perp^2$ versus major radius $R - R_0$ along the midplane of the tokamak calculated from the cold plasma dispersion relation [Eqn. (2.4)]. $N_\parallel$ ranges from 1.5 to 3.5 in increments of $\Delta N_\parallel = 0.1$. A toroidal magnetic field gradient and a gaussian ($\lambda_n = 10\,\mathrm{cm}$) plasma density profile with $\bar{n}_e = 1.0 \times 10^{13}\,\mathrm{cm}^{-3}$ are assumed. The remaining parameters are: a) $f = 2.45\,\mathrm{GHz}$, $B_0 = 13\,\mathrm{kG}$; b) $f = 2.45\,\mathrm{GHz}$, $B_0 = 10\,\mathrm{kG}$: c) $f = 800\,\mathrm{MHz}$, $B_0 = 13\,\mathrm{kG}$. The accessible $N_\parallel$ value is indicated for each case.

which may be rewritten as:

$$\omega = \omega_{LH} \left(1 + \frac{m_i}{m_e} \frac{k_{\|}^2}{k^2} \right)^{1/2} . \tag{2.11}$$

This is the familiar electrostatic dispersion relation for cold lower hybrid waves. It can be shown that if a spectrum of waves is excited by an oscillating point source in the plasma, the electrostatic wave energy propagates away along singular "resonance cone" trajectories.[49] The angle of propagation relative to the magnetic field is given by the direction of the group velocity $\mathbf{v_g}$:

$$\begin{aligned} \tan\theta_g &= \frac{v_{g\perp}}{v_{g\|}} = \frac{\partial\omega/\partial k_\perp}{\partial\omega/\partial k_\|} \\ &= \pm\left[\frac{m_e}{m_i}\left(\frac{\omega^2}{\omega_{LH}^2} - 1\right)\right]^{1/2} = -\frac{k_\|}{k_\perp}. \end{aligned} \tag{2.12}$$

Equation (2.12) also indicates that the wavevector $\mathbf{k}$ is perpendicular to the group velocity $\mathbf{v_g}$. In more realistic experimental situations, waves are excited by a periodic source with finite spatial extent. In this case the spatial extent of the wave fields in the plasma is determined by the resonance cone trajectories from the boundaries of the source. It is evident from Eqn. (2.12) that near the lower hybrid resonance, as $\omega \to \omega_{LH}$, the angle of propagation, θ_g, becomes nearly parallel with the magnetic field, since $v_{g\perp} \to 0$. On the other hand, $\mathbf{k}$ points nearly perpendicular to $\mathbf{B_0}$ since $k_\perp \simeq k \gg k_\|$. As $k_\perp \to \infty$, our initial "cold" plasma assumptions break down, since $\omega/k_\perp \to v_{ti}$, and we must consider thermal corrections to the dispersion relation (2.11).

2.1.2 Thermal Effects: Mode Conversion

Finite electron and ion temperature effects introduce a third branch into the electromagnetic dispersion relation (2.3), namely the ion plasma wave. Coupling to this new electrostatic branch from the cold plasma slow wave branch occurs when $k_\perp$ becomes sufficiently high in the vicinity of the lower hybrid resonance layer. In the electrostatic limit, the dispersion relation may be written in the form:[46,50,51]

$$D(\mathbf{x},\mathbf{k},\omega) = \delta k_\perp^4 + K_\perp k_\perp^2 + k_\|^2 K_\| = 0, \tag{2.13}$$

where

$$\delta = -3\frac{\omega_{pi}^2}{\omega^4}\frac{T_i}{m_i}\left(1 + \frac{1}{4}\frac{T_e}{T_i}Y^4\right).$$

In the derivation of Eqn. (2.13) it is assumed that the electrons are strongly magnetized $[(k_\perp \rho_{ce})^2 \ll 1]$, while the ions are essentially unmagnetized $[(k_\perp \rho_{ci})^2 \gg 1]$, following straight line orbits. There are only two roots to Eqn. (2.13) since the fast wave branch has been eliminated by the electrostatic approximation. The dispersion relation (2.13) can be rewritten in a more familiar form:[43]

$$\omega^2 = \omega_{LH}^2 \left[1 + \frac{k_\parallel^2}{k^2}\frac{m_i}{m_e} + \frac{3k_\perp^2 T_i}{\omega^2 m_i}\left(1 + \frac{1}{4}\frac{T_e}{T_i}Y^4\right)\right], \tag{2.14}$$

where the third term represents the new contribution due to the ion plasma wave. When $k_\perp$ becomes sufficiently large, the second and third terms become equal and mode conversion from the inward propagating cold slow wave to an outward propagating ion plasma wave occurs.

The mode conversion density is obtained from the condition that the two roots of the quadratic equation (2.13) are equal $(K_\perp^2 = 4\delta k_\parallel^2 K_\parallel)$:

$$\left.\frac{\omega_{pi}}{\omega}\right|_{MC} = \left\{1 - Y^2 + \frac{2N_\parallel}{c}\left(\frac{3T_i}{m_e}\right)^{1/2}\left[1 + \frac{1}{4}\frac{T_e}{T_i}Y^4\right]^{1/2}\right\}^{-1/2}. \tag{2.15}$$

For parameters typical of the Versator 800 MHz ion heating experiment,[40] namely $N_\parallel = 5.5$, $T_{e0} = 400\,\mathrm{eV}$, $T_{i0} = 150\,\mathrm{eV}$, and $B_0 = 14\,\mathrm{kG}$, we find $n_e|_{MC} = 2.2 \times 10^{13}\,\mathrm{cm}^{-3}$, which corresponds to $\omega/\omega_{LH} = 1.2$. When $k_\perp$ becomes large, so that $\omega/k_\perp v_{ti} \to 1$, the possibility of perpendicular ion Landau damping must be considered. The value of $\omega/k_\perp v_{ti}$ can be estimated by evaluating Eqn. (2.13) at the mode conversion layer $(k_\perp^2 = -K_\perp/2\delta)$ using Eqn. (2.15):

$$\left(\frac{\omega}{k_\perp v_{ti}}\right)_{MC} \simeq \frac{4.4}{N_\parallel^{1/2}}\frac{1}{[T_i(\mathrm{keV})]^{1/4}}, \tag{2.16}$$

where we assumed that $(1/4)(T_e/T_i)Y^4 \ll 1$. For the typical Versator 800 MHz ion heating parameters listed previously, $(\omega/k_\perp v_{ti})_{MC} \simeq 2.9$, and strong ion Landau damping is expected to occur. Note that for the 2.45 GHz frequency, a mode conversion layer cannot be present in the plasma due to the low magnetic field strength $(B_0 < 15\,\mathrm{kG},\ Y^2 > 6.3)$.

2.1.3 Thermal Effects: Absorption

In this subsection, we consider three mechanisms for the absorption of lower hybrid wave power: 1) parallel electron Landau damping, 2) perpendicular ion Landau damping, and 3) collisional damping. In the current drive and electron bulk heating regime,[4] $\omega/\omega_{LH}(0) \geq 2$, electron Landau damping is the dominant absorption mechanism. Strong electron Landau damping requires a sufficiently large $N_{\parallel}$ value so that $\omega/k_{\parallel}v_{te} < 3$. At higher densities, $\omega/\omega_{LH}(0) \simeq 1-2$, perpendicular ion tails may be generated due to perpendicular ion Landau damping near the mode conversion layer if $N_{\parallel}$ is sufficiently high (see Eqn. 2.16). Bulk ion heating is expected if the ion tail confinement time exceeds the tail-bulk thermalization time. At high densities and low temperatures, collisional absorption of wave power in the edge region of the plasma may become important.

The theoretical damping rates are obtained from the imaginary part of the dispersion relation:

$$k_I \simeq -\frac{D_I(\mathbf{x},\mathbf{k}_R,\omega)}{(\partial D_R/\partial k_\perp)_{\mathbf{k}=\mathbf{k}_R}}, \tag{2.17}$$

where $D = D_R + iD_I$ and $k_\perp = k_{\perp R} + ik_I$, and we have taken the limit of weak damping, $k_I \ll k_{\perp R}$. The spatial damping leads to a net decrease in the wave power P as the wave propagates in the x direction which is given by:

$$P(x) = P_0 \exp\left[2\int_0^x k_I(x')dx'\right]. \tag{2.18}$$

The resonant contributions to the wave damping are given by:[44]

$$k_I = k_\perp \frac{\sqrt{\pi}}{\partial D_R/\partial k_\perp^2}\frac{\omega_{pi}^2}{\omega^2}\left[\frac{m_i}{m_e}\frac{k_\parallel^2}{k_\perp^2}\xi_{0e}^3 \exp \xi_{0e}^2 + \varsigma_i^3 \exp \varsigma_i^2\right], \tag{2.19}$$

where $\xi_{0e} = \omega/k_\parallel v_e$, and $\varsigma_i = \omega/k_\perp v_i$. The first term corresponds to the electron Landau damping in the parallel direction, while the second corresponds to ion Landau damping in the perpendicular direction. Collisionless wave absorption due to Landau damping results from the phase mixing of particle orbits with respect to the wave fields. Particles with velocities slightly less than the resonant wave phase velocity, $v < v_\phi$, gain energy from the wave, while particles with velocities slightly greater than the wave phase velocity, $v > v_\phi$, lose energy to the wave. For a Maxwellian distribution of particles, more particles gain energy than lose energy, and wave damping results. The ion term in Eqn. (2.19) can be obtained by treating the ions as unmagnetized (straight line orbits). This is justified as long as a mechanism exists to destroy the phase correlation between the wave and the ions in their cyclotron orbits on a time scale $\tau \sim \omega_{ci}^{-1}$.[51] One such mechanism is stochastic ion motion.[52] For electric field strengths above a threshold value, ion Landau damping is predicted because the ion cyclotron orbits do not close on themselves, destroying the harmonic resonance.

For linear damping, given by Eqn. (2.19), it can be shown[44] that strong wave absorption occurs when $\omega/k_\parallel v_{te} \leq 3$ for electrons and when $\omega/k_\perp v_{ti} \leq 3$ for ions. For the electrons, this condition may be written in practical units as:

$$N_\parallel^L \geq \frac{5.3}{[T_e(\mathrm{keV})]^{1/2}}. \qquad (2.20)$$

A more self consistent treatment given by quasi-linear theory takes into account the flattening of the distribution in the resonant region which tends to reduce the damping rate. Hence, higher $N_\parallel$ values are required for strong damping:[53]

$$N_\parallel^{QL} \geq \frac{7.0}{[T_e(\mathrm{keV})]^{1/2}}. \qquad (2.21)$$

Quasi-linear flattening of the electron distribution due to parallel Landau damping is the physical mechanism responsible for current drive.

Waves with $N_\parallel$ values too low to satisfy condition (2.21) for strong bulk electron Landau damping may still be absorbed if a high energy tail is present in the plasma. If the tail density is relatively small, $n_t \ll n_e$, then the real part of the dispersion relation is unaffected. The damping rate due to the tail component is then given by:[49]

$$k_I^t = \frac{n_t}{n_e} k_\perp \frac{\sqrt{\pi}}{\partial D/\partial k_\perp^2} \frac{\omega_{pi}^2}{\omega^2} \frac{m_i}{m_e} \frac{k_\parallel^2}{k^2} \left(\frac{\omega}{k_\parallel v_{te}'}\right)^3 \exp\left(-\frac{\omega^2}{k_\parallel^2 {v_{te}'}^2}\right), \qquad (2.22)$$

where ${v_{te}'}^2 = 2T_t/m_e$, and T_t is the tail temperature.

If ion Landau damping dominates over electron Landau damping at high densities, then an upper density limit for current drive and electron heating will result. The electron to ion "switchover" density occurs where the wave power absorbed by the ions equals the wave power absorbed by the electrons. Due to the exponential dependence of the damping rates on the wave phase velocities, an approximate condition for equal absorption is given by $\omega/k_{\parallel}v_{te} \simeq \omega/k_{\perp}v_{ti}$. We define a quantity Z_0, which is the ratio of these quantities at the switchover density:[4,19]

$$Z_0 = \frac{v_{\phi\parallel}/v_{te}}{v_{\phi\perp}/v_{ti}} = \frac{N_\perp}{N_\parallel}\left(\frac{m_e}{m_i}\frac{T_i}{T_e}\right)^{1/2} \sim 1. \tag{2.23}$$

The ratio $N_\perp/N_\parallel$ is determined by the electrostatic dispersion relation given by Eqn. (2.13):

$$N_\perp \simeq N_\parallel \phi \left(\frac{m_i}{m_e}\right)^{1/2}\left(\frac{\omega^2}{\omega_{LH}^2} - 1\right)^{-1/2}. \tag{2.24}$$

where $1 \leq \phi \leq \sqrt{2}$. The value of $\phi = 1$ is exactly what was obtained for the cold lower hybrid waves [see Eqn. (2.12)]. Similarly, it can be shown from Eqn. (2.13) that at the mode conversion layer ($k_\perp^2 = -K_\perp/2\delta$), a value of $\phi = \sqrt{2}$ is obtained. Note that $N_\perp/N_\parallel$ is nearly independent of the $N_\parallel$ value of the wave. This leads to the resonance cone propagation discussed earlier. By combining Eqns. (2.23) and (2.24), we find the switchover density,

$$\left.\frac{\omega^2}{\omega_{LH}^2}\right|_{cr} = 1 + \frac{\phi^2}{Z_0^2}\frac{T_i}{T_e}. \tag{2.25}$$

A more accurate estimate for Z_0 may be obtained by equating the power absorbed by the electrons and ions calculated from quasi-linear theories. The results, however, are very close to our initial guess, that $Z_0 \simeq 1$. Hence, near the mode conversion layer, $\phi^2/Z_0 \simeq 2$. For typical 800 MHz current drive conditions, $T_i/T_e \simeq 1/2$, and we obtain the value $n_{cr} = 1.2 \times 10^{13}\,\text{cm}^{-3}$, or $\bar{n}_{cr} \simeq 8 \times 10^{12}\,\text{cm}^{-3}$, which is somewhat higher than the experimental value[7] for the current drive density limit, $\bar{n}_e \simeq 6 \times 10^{12}\,\text{cm}^{-3}$. While Eqn. (2.25) predicts the observed density limit scaling with frequency, $\bar{n}_c \propto f^2$, in most experiments the critical density lies below the predicted value from Eqn (2.25) by up to a factor of two. It these cases, the disappearance of current drive is well correlated with the appearance of parametric instabilities, indicating that a direct switchover from electron to ion interaction due to linear mode conversion is not the actual mechanism responsible for the density limit. It should also be pointed out that Eqn. (2.25) is only valid if a mode conversion layer exists in the plasma. Furthermore, the magnetic field must be sufficiently high ($Y^2 < 1$) for waves to be accessible to the mode conversion layer. Therefore, this theory is not applicable to 800 MHz current drive when $B_0 \leq 12.2\,\mathrm{kG}$, or to 2.45 GHz current drive when $B_0 \leq 37.5\,\mathrm{kG}$. For the 2.45 GHz experiment, we expect electron Landau damping to be the dominant resonant absorption mechanism.

An important nonresonant absorption mechanism in the colder outer regions of the plasma is collisional absorption.[49] Collisional absorption becomes important when the electron-ion collision frequency ν_{ei} becomes non-negligible compared to the wave frequency. The contribution may be evaluated from the cold electrostatic dispersion relation Eqn. (2.10) by replacing m_e with $m_e(1 + i\nu/\omega)$. The damping rate is then given by:

$$k^c_{\perp I} \simeq -\frac{\nu_{ei}}{2\omega} k_{\|} \sqrt{\frac{m_i}{m_e}} \left(\frac{\omega^2}{\omega^2_{LH}} - 1\right)^{-1/2} \left[1 + Y^2 \left(\frac{\omega^2}{\omega^2_{LH}} - 1\right)^{-1}\right], \tag{2.26}$$

where $\nu_{ei} = \omega^4_{pe} \ln \Lambda / 4\pi n v^3_e$ is the electron-ion collision frequency. Far away from resonance, when $\omega^2 \gg \omega^2_{LH}$, this equation becomes:

$$\begin{aligned} k^c_{\perp I} &\simeq N_{\|} \sqrt{\frac{m_i}{m_e}} \frac{\omega_{LH} \nu_{ei}}{2c\omega} \qquad (2.27) \\ &\simeq \frac{0.79 N_{\|}}{f(\mathrm{GHz})} \left[\frac{n(10^{13}\,\mathrm{cm}^{-3})}{T_e(\mathrm{eV})}\right]^{3/2} \qquad \mathrm{cm}^{-1} \end{aligned}$$

For typical 2.45 GHz current drive parameters, $n = 1.5 \times 10^{13}\,\mathrm{cm}^{-3}$, $T_e = 50\,\mathrm{eV}$, and $N_{\|} = 3$, we estimate $k_{\perp I} = 5.0 \times 10^{-3}\,\mathrm{cm}^{-1}$, which corresponds to a damping length of approximately 100 cm. For purely radial propagation, this would predict a small effect since the plasma radius is 13 cm. However, if k_θ is significant, then collisional damping will be important, since the damping length is comparable to the circumference of the plasma. An accurate determination of the relative wave power absorbed by electrons due to Landau damping and collisional damping must include the effects of toroidal geometry on wave propagation.

2.1.4 Toroidal Wave Propagation Effects

In slab (x, z) geometry or in cylindrical (r, θ, z) geometry, the parallel index of refraction of a wave, $N_{\|}$ $(= N_z)$, is a constant which is determined by the launching structure, e.g. a waveguide grill. The constancy of $N_{\|}$ is due to the symmetry along the direction of the magnetic field. In toroidal geometry (r, θ, ϕ), this symmetry is broken. For instance, in a tokamak, both the toroidal magnetic field strength, B_ϕ, and the poloidal field strength, B_θ vary along the helical field lines.

Due to the axial symmetry of the tokamak, the perturbed wave fields will vary as $\exp[-i(n\phi - \omega t)]$, where n, the toroidal mode number, is a constant. The wave vector may be written as $\mathbf{k} = \mathbf{e}_r k_r + \mathbf{e}_\theta(m/r) + \mathbf{e}_\phi(n/R)$, where m is the poloidal mode number, and $R = R_0 + r\cos\theta$. In cylindrical geometry, m is a constant due to poloidal symmetry, and $m \simeq 0$, as fixed by the antenna. In toroidal geometry, m may vary. For $\mathbf{B} = \mathbf{e}_r B_r(r,\theta) + \mathbf{e}_\theta B_\theta(r,\theta) + \mathbf{e}_\phi B_\phi(r,\theta)$, with $|B_r| \ll B_\theta \ll B_\phi$, $N_{\|}$ is given by:[44]

$$\begin{aligned} N_{\|} = \frac{c}{\omega}\frac{\mathbf{k}\cdot\mathbf{B}}{|\mathbf{B}|} &\simeq \frac{c}{\omega}\left(\frac{m}{r}B_\theta + \frac{n}{R}B_\phi\right) \Big/ |\mathbf{B}| \\ &\simeq \frac{c}{\omega}\frac{n}{R}\left(1 + \frac{m}{nq}\right), \end{aligned} \tag{2.28}$$

where $q(r,\theta) = B_\phi(r,\theta)r/B_\theta(r,\theta)R$ is the local safety factor. The largest changes in $N_{\|}$ result from variations in the poloidal mode number m, which are amplified when q is small (near the center of the plasma).

As indicated in the previous sections, variations in $N_{\|}$ may have a profound effect upon wave accessibility and wave absorption, both resonant and non-resonant. In general, detailed numerical calculations are necessary to determine the evolution of $N_{\|}$ in complex geometries. In ray tracing theory,[44] the equations of geometrical optics,

$$\begin{aligned} \frac{d\mathbf{x}}{dt} &= -\frac{\partial D/\partial \mathbf{k}}{\partial D/\partial \omega}, \\ \frac{d\mathbf{k}}{dt} &= +\frac{\partial D/\partial \mathbf{x}}{\partial D/\partial \omega} \end{aligned} \tag{2.29}$$

are used to calculate the evolution of the wavevector $\mathbf{k}$ and the group velocity $d\mathbf{x}/dt$ of lower hybrid waves as they propagate in toroidal geometry. This approach is valid only when the waves can be treated as infinite plane waves, i.e. when $|\mathbf{k}| \gg |\partial/\partial\mathbf{x}|$ (WKB approximation). This condition is satisfied except near cut-off layers or reflection layers, where $k_r \to 0$. In these regions, the quantitative interpretation of the results is still a subject of debate.

A sample case from the ray tracing code developed by Dr. Paul Bonoli at MIT is shown in Fig. 2.3 for typical Versator 2.45 GHz experimental conditions: $\bar{n}_e = 8 \times 10^{12}\,\mathrm{cm}^{-3}$, $B = 11\,\mathrm{kG}$, $T_{e0} = 300\,\mathrm{eV}$ and $T_{i0} = 120\,\mathrm{eV}$. The propagation of a single ray with $N_\parallel = 4.0$ is shown projected in the poloidal plane. as well as the evolution of m and $N_\parallel$ as a function of the toroidal angle ϕ. The calculated absorption of the wave power along the ray trajectory due to electron and ion Landau damping and collisional damping is also plotted. For this case, the electron distribution was taken from a self-consistent ray tracing/Fokker Planck code calculation. Hence, electron tail Landau damping is included.

A typical ray with mode numbers $m = 0$ and $n = 83$ ($N_\parallel = 4.0$) is launched from the low field side of the tokamak ($\theta = 0$, $\phi = 0$). As the wave propagates radially inward towards the center of the plasma, $N_\parallel$ increases slightly from 4.0 to 4.7, mainly due to the decrease in major radius [see Eqn. (2.27)]. In this case, the change in the poloidal mode number was relatively small ($m \simeq -12$). Approximately 15% of the wave power was absorbed on this "first pass" due to Landau damping on tail electrons. After a radial reflection ($k_r \to 0$) near the center of the plasma, the ray propagates back out to the plasma edge, where it undergoes a reflection from the cut-off layer near the bottom of the plasma. This time when the ray propagates inward, the poloidal mode number increases substantially ($m \simeq 200$), and $N_\parallel$ increases to a value $N_\parallel \simeq 10$. This is a substantial upshift from the launched value, and it results in Landau damping on the bulk electrons since $\omega/k_\parallel v_e \simeq 2.9$. The propagation of the ray is followed in a similar manner for several more passes until the wave power is completely absorbed. For these parameters, 96% of the power was absorbed due to electron Landau damping, while

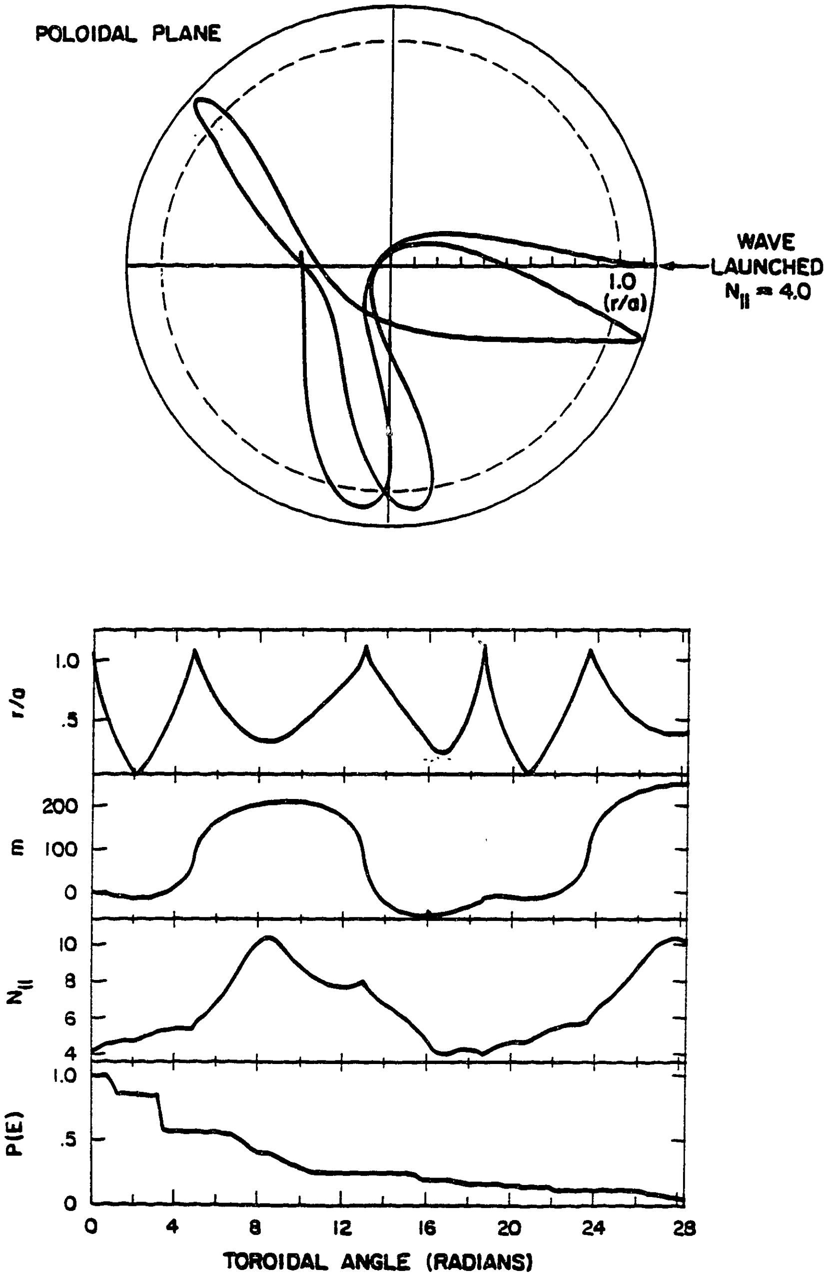

Fig. 2.3: Lower hybrid ray trajectory for typical Versator 2.45 GHz experimental conditions: $\bar{n}_e = 8 \times 10^{12}\,\mathrm{cm}^{-3}$, $B_0 = 11\,\mathrm{kG}$, $T_{e0} = 300\,\mathrm{eV}$, and $T_{i0} = 120\,\mathrm{eV}$. Upper: the propagation of a single ray with $N_{\parallel} = 4.0$ projected in the poloidal plane. Lower: variations in the radius, r/a, the poloidal mode number, m, the parallel refractive index, $N_{\parallel}$, and the normalized wave amplitude, $P(E)$, as a function of toroidal angle.

the remaining 4% was absorbed due to collisional damping.

A simple model which describes the behavior of m as a function of the poloidal angle has been given by Bonoli.[44] By using the cold plasma electrostatic dispersion relation in the ray equations (2.29), and assuming $\mathbf{B} = \mathbf{e}_\phi B_\phi(r,\theta) + \mathbf{e}_\theta B_\theta(r)$, where $B_\phi = B_0/[1 + (r/R_0)\cos\theta]$ and $B_\theta \ll B_\phi$, it can be shown that the evolution of m is given by:

$$\frac{dm}{d\theta} = -k_\parallel R_0 q(r) \left[1 + \frac{\omega_{pe}^2/\omega_{ce}^2}{K_\perp}\right] \frac{r}{R} \sin\theta. \tag{2.30}$$

For $k_\parallel > 0$, and $q(r) > 0$, Eqn. (2.30) indicates that $dm/d\theta \propto -\sin\theta$. Hence, the largest increases in m occur at the bottom of the plasma, while the largest decreases occur at the top. This is shown clearly in Fig. 2.3 at the toroidal angles of $\phi = 5$, 13, and 24 radians where the reflections of the waves from the outer surface of the plasma occur. The enhancement of $dm/d\theta$ in the outer region of the plasma is due to the dependence on $q(r)$ and r/R [see Eqn. (2.30)]. Conversely, the effect of m on the $N_\parallel$ value in Eqn. (2.28), is expected to be the greatest near the center of the plasma since m is divided by q. Indeed, this is seen in Fig. 2.3 where large $N_\parallel$ values are found at the toroidal angles of $\phi = 8.5$ and 28 radians, where m is large, but r/a (and hence q) is small.

Theoretical modelling results for 2.45 GHz steady state current drive using a combined ray tracing/Fokker-Planck code will be presented in Chapter 8.

2.2 The Fisch Model of Lower Hybrid Current Drive

In the lower hybrid current drive theory first put forth by Fisch,[3] parallel momentum is transferred via Landau damping from waves with parallel phase velocity $v_{\phi\parallel} = \omega/k_\parallel$ to electrons satisfying the resonance condition $\omega - k_\parallel v_\parallel = 0$. When the spectrum of waves is asymmetric with respect to the parallel electron distribution function, then the damping leads to a net change in the toroidal current. The accelerating force on the resonant electrons due to the rf waves is balanced in the steady state against the retarding force due to coulomb collisions with the background distribution of electrons and ions. Efficient current drive is therefore achieved when the rf waves are resonant with high velocity, relatively collisionless electrons. In order to accurately determine the rf current drive efficiency, perpendicular collisional dynamics and relativistic effects must be taken into account. When the plasma current varies with time (e.g. current ramp-up), then the additional force on the resonant electrons due to the induced toroidal electric field must also be accounted for.

2.2.1 1-d Steady-State Theory

The evolution of the distribution function in the presence of parallel rf diffusion is governed by the Fokker-Planck equation:[3]

$$\frac{\partial f}{\partial t} = \left[\left(\frac{\partial}{\partial v_{||}}\right) D_{QL}(v_{||})\right] \frac{\partial f}{\partial v_{||}} + \left(\frac{\partial f}{\partial t}\right)_c, \tag{2.31}$$

where D_{QL} is the quasi-linear diffusion coefficient and $(\partial f/\partial t)_c$ is the Fokker-Planck collision operator. Here the dc electric field is assumed to be zero. In general, when evaluating $(\partial f/\partial t)_c$, collisional scattering in both the parallel and perpendicular directions must be considered. In the one-dimensional theory perpendicular collisions are ignored, and the distribution function in the perpendicular direction is taken to be a Maxwellian with $T_\perp = T_e$, where T_e is the bulk temperature.

For a wave spectrum of sufficient amplitude, localized to the region $v_1 < v_{\phi ||} < v_2$, the steady state solution to Eqn. (2.31) is approximately a Maxwellian distribution outside the interval $v_1 < v_{||} < v_2$, with a flat "raised plateau" inside the interval [see Fig. 2.4]. In this case, it is straightforward to calculate the current carried by the resonant electrons. The height of the plateau is found by evaluating the bulk Maxwellian distribution function at the point of intersection with the plateau, namely at $v_{||} = v_1$:

$$f(v_{||}) \simeq f(v_1) = \frac{e^{-v_1^2/v_e^2}}{\pi^{1/2} v_e} \qquad \text{for} \qquad v_1 \leq v_{||} \leq v_2, \tag{2.32}$$

where $v_e = (2T_e/m_e)^{1/2}$. The current carried by the resonant electrons is given by:

$$J = \int_{v_1}^{v_2} n e v_{||} f(v_1)\, dv_{||}. \tag{2.33}$$

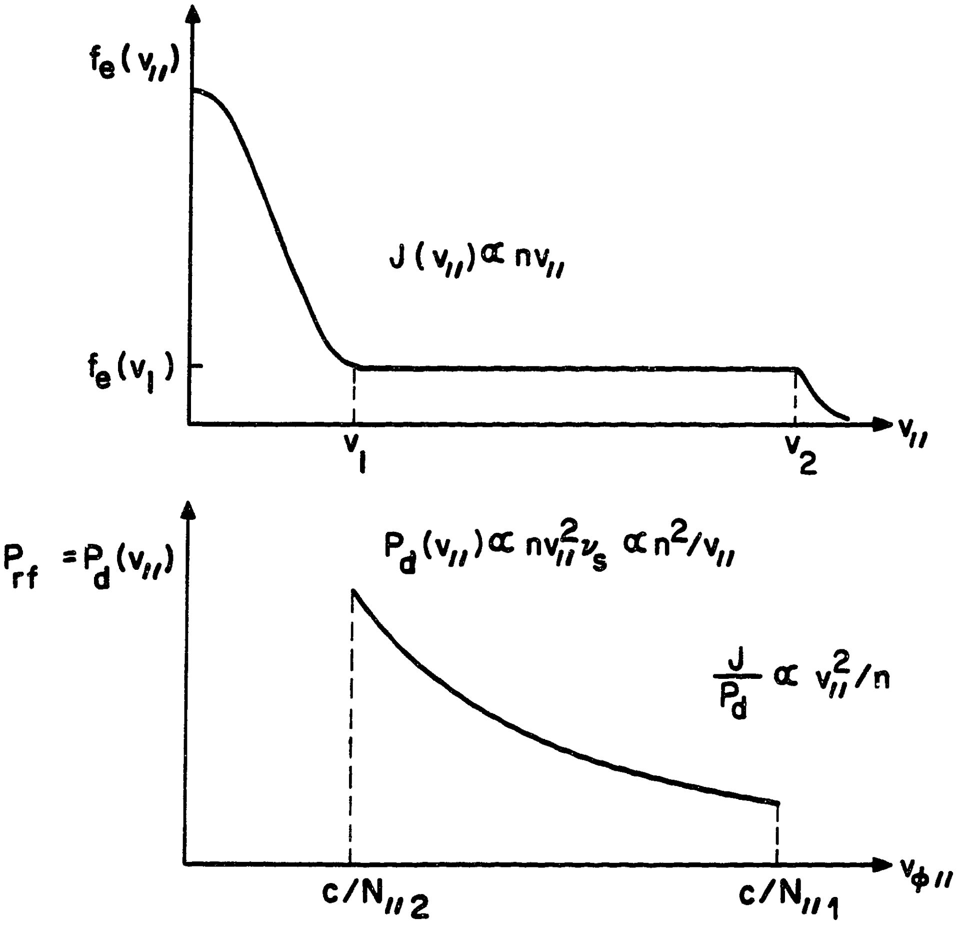

Fig. 2.4: Upper: the quasi-linear electron distribution function used in the Fisch 1-d calculation of LHCD efficiency. Lower: the resonant rf power spectrum required to balance the power dissipated due to tail-bulk collisions.

Normalizing to thermal values,

$$\tilde{J} = \frac{J}{nev_e} = \frac{e^{-w_1^2}}{\pi^{1/2}} \frac{w_2^2 - w_1^2}{2}, \tag{2.34}$$

where $w_i = v_i/v_e$, with $i = 1, 2$.

In the steady state, the dissipated power due to collisions between the plateau electrons and the bulk electrons and ions must be exactly equal to the rf power absorbed. This power is given by

$$P_d = \int_{v_1}^{v_2} nmv_{\|}^2 \nu_s f(v_1)\, dv_{\|}, \tag{2.35}$$

where $\nu_s = \nu_s^{e/e} + \nu_s^{e/i}$ is the momentum loss collision frequency given by $\nu_s = \nu_0(v_e^3/v_{\|}^3)(2+Z_i)$ in the high velocity limit ($v_{\|}/v_e \gg 1$), where $\nu_0 \equiv \omega_{pe}^4 \log \Lambda / 4\pi n v_e^3$. Hence, the normalized dissipated power is:

$$\tilde{P}_d = \frac{P_d}{nmv_e^2 \nu_0} = \frac{e^{-w_1^2}}{\pi^{1/2}}(2 + Z_i) \log(w_2/w_1). \tag{2.36}$$

The quantity of interest in current drive experiments is the efficiency, given by I/P (kA/kW). Since J/P_d is a local quantity, an accurate calculation of I/P requires a knowledge of the density and temperature profiles. Averaging over the plasma cross section, we have:

$$\frac{I}{P} = \frac{\langle J \rangle}{2\pi R \langle P_d \rangle}. \tag{2.37}$$

Using Eqns. (2.34), (2.36), and (2.37) we obtain the current drive figure of merit, $\bar{n}IR/P$, which in practical units can be written approximately as[4]:

$$\tilde{\eta} = \frac{\bar{n}(10^{20}\mathrm{m}^{-3}) I(\mathrm{kA}) R(\mathrm{m})}{P(\mathrm{kW})} \simeq .0054\, T(1\,\mathrm{keV}) \frac{\tilde{J}}{\tilde{P}}, \tag{2.38}$$

where

$$\frac{\tilde{J}}{\tilde{P}} = \langle w^2 \rangle \frac{1}{2 + Z_i}$$

and

$$\langle w^2 \rangle \equiv \left(\frac{w_2^2 - w_1^2}{2} \right) \frac{1}{\log(w_2/w_1)}.$$

The exact numerical coefficient in Eqn. (2.38) depends on profiles. The figure of merit can also be written in terms of the $N_{\|}$ values defining the wave spectrum, $N_{\|1} < N_{\|} < N_{\|2}$:

$$\tilde{\eta} = \frac{\bar{n}(10^{20}\,\mathrm{m}^{-3}) I(\mathrm{kA}) R(\mathrm{m})}{P(\mathrm{kW})} \simeq \frac{1.4}{2+Z_i} \frac{1}{\langle N_{\|}^2 \rangle}, \tag{2.39}$$

where

$$\frac{1}{\langle N_{\|}^2 \rangle} = \left(\frac{1}{N_{\|1}^2} - \frac{1}{N_{\|2}^2} \right) \frac{1}{2 \log(N_{\|2}/N_{\|1})}.$$

From equation (2.39) it appears that $\bar{n}IR/P$ is a constant which depends only on Z_i and on the wave spectrum. This is only true if the entire launched wave spectrum is accessible to the plasma center. Otherwise, the quantity $N_{\|1}$ must be replaced by $N_{\|acc}$ given by Eqn. (2.8). In this case, $\bar{n}IR/P$ depends weakly on the density, magnetic field, and rf frequency. We also note that in general the power absorbed by electron Landau damping, P_{abs}, will be less than the injected power P_{rf}. For instance, the rf power which is inaccessible to the plasma center may get collisionally damped at the plasma edge. Therefore, in Eqns. (2.36) - (2.38), P should be replaced by $P_{abs} = \alpha P_{rf}$, where α is the fraction of the injected rf power absorbed by the resonant electrons. This theory also assumes that the spectrum is not too broad and that the wave phase velocity is optimized, including spatial damping.

2.2.2 2-d and Relativistic Effects

A more accurate calculation of the steady-state rf-driven current and current drive efficiency must include perpendicular dynamics. For broad wave spectra this requires a numerical solution of the 2-d Fokker-Planck equation (2.31). In the 1-d theory, only the collisional loss of momentum in the parallel direction was considered. The proper slowing down equations in two dimensions, however, describe the loss of energy in addition to the loss of momentum.[54] The loss of parallel momentum due to collisions is accompanied, on the average, with a gain in perpendicular velocity due to the pitch angle scattering collisions with the background ions and electrons. Because of this, electrons in the resonant region of velocity space $v_1 < v_{||} < v_2$ have, on the average, higher perpendicular energies, and hence lower collisionality. Lower collisionality results in less dissipated power. Furthermore, when these electrons are pitch-angle scattered out of the resonant region, they may still carry a net current as long as they are slowed down before isotropizing completely. The net result of these 2-d effects is an enhanced current J and an improved current drive efficiency J/P when compared to the 1-d theory.

Fisch and Boozer[54] have calculated the 2-d current drive efficiency analytically in the high velocity limit ($v_{||} \gg v_e$), assuming a narrow wave spectrum resonant at the parallel velocity $w = v_{||}/v_e$. They neglect any distortion of the background Maxwellian distribution of electrons and ions due to the presence of the rf tail. In their model, resonant electrons are given a "kick" in velocity space by the rf waves before they slow down due to collisions. The "kick" increases the energy of the particle and reduces its collisionality with the background particles since $\nu \sim u^{-3}$, where $u = v/v_e$. Hence, the total current contribution, integrated over the slowing down time, increases. The current drive efficiency is given by:[54]

$$\frac{\tilde{J}}{\tilde{P}_d} = \frac{1}{2}\frac{\hat{s}\cdot\nabla(wu^3)}{\hat{s}\cdot\nabla u^2}\frac{4}{5+Z_i}, \tag{2.40}$$

where $\tilde{J}$ and $\tilde{P}_d$ are normalized to thermal quantities, $\hat{s}$ is the direction of the rf "kick" in velocity space, and ∇ is the gradient operator in velocity space. For lower hybrid current drive, $\hat{s}$ is in the parallel direction, so that Eqn. (2.40) becomes:[54]

$$\frac{\tilde{J}}{\tilde{P}_d} = w^2\frac{4}{5+Z_i}, \tag{2.41}$$

where we used the high velocity limit ($w \simeq u \gg 1$). This expression is to be compared with the result [Eqns. (2.34) and (2.35)] from the 1-d theory in the limit of a narrow spectrum ($w_2 - w_1 = \Delta w \ll w_1$). In this case, for $Z_i = 1$, the efficiency from the 2-d theory is exactly a factor of two higher than that from the 1-d theory. In addition, the scaling with Z_i is more favorable for the 2-d theory. This is due to the increased pitch angle scattering with higher Z_i which tends to enhance the broadening of the plateau in the perpendicular direction.

This result compares reasonably well with the 2-d numerical calculations of Karney and Fisch,[55] where a relatively narrow wave spectrum is assumed ($v_2/v_1 \leq 2$). In this case, the 2-d numerical value for $\tilde{J}/\tilde{P}_d$ exceeds the 1-d value by a factor of 2.5. The Z_i scaling is in close agreement with Eqn. (2.40). Similar numerical calculations have been carried out by Fuchs et al.,[56] for broader wave spectra ($v_2/v_1 \leq 5$) which are more representative of present day experiments. They find the same enhancement in $\tilde{J}/\tilde{P}_d$ ($\times 2.5$) over the 1-d theory. In both of these 2-d calculations, it is found that the perpendicular temperature of the plateau region is significantly enhanced over the bulk temperature ($T_\perp \simeq 30 - 50T_e$). Furthermore, the height of the plateau is raised due to the distortion of the distribution function at low velocities, $v_{\|} < v_1$, resulting in a significant enhancement of the current $\tilde{J}$ compared with the 1-d value [Eqn. (2.34)]. Recently, a 1-d analytical model has been developed which correctly predicts the results of the 2-d numerical calculations.[56] It should be pointed out, however, that these 2-d effects do not significantly change the scaling of the current drive efficiency with density given by the original Fisch 1-d theory, namely $I/P \propto 1/n$.

In the theories presented so far, the resonant electron energies were assumed to be non-relativistic ($\varepsilon = \gamma - 1 \ll 1$ where ε is the kinetic energy normalized to mc^2). In this limit, the current drive efficiency scales as $J/P \propto \varepsilon$. This scaling breaks down at relativistic energies. As the resonant electrons become relativistic, and therefore heavier, their slowing down frequency increases.[57] In addition, the momentum transferred from waves to relativistic electrons results in less current since the current is proportional to velocity and $v = p/\gamma m$. While theories differ on the efficiency scaling at mildly relativistic energies, there is agreement on the maximum attainable current drive efficiency.[5,58] As $\varepsilon \rightarrow \infty$,

$$\left(\frac{J}{P}\right)_c = \frac{J/enc}{P_d/mc^2\nu_c} \rightarrow 1, \tag{2.42}$$

where $\nu_c = \nu_0 v_e^3/c^3$. For comparison with equation (2.38), the above limit is equivalent to $(\tilde{J}/\tilde{P}) = 256/T(1\,\mathrm{keV})$. Karney and Fisch include finite temperature effects in their calculations and find that the limit given by Eqn. (2.42) improves slightly with increasing temperature.[5] For the present experiment, these relativistic corrections are expected to be small ($\varepsilon < 0.2$). In future fast wave current drive experiments, however, relativistic effects will not be negligible since $N_{\|} \simeq 1 - 2$.

2.2.3 Current Drive in the Presence of Electric Fields (Ramp-up)

Recently there has been interest in using LHCD to start up or ramp up the plasma current in tokamaks. Under these conditions, the effects of the induced electric field on the response of the plasma current cannot be ignored. The plasma resists any attempt to change the current on a time scale less than the L/R time where L is the plasma inductance and R is the plasma resistance. When the plasma current is ramped up ($I_{rf} - I > 0$, where I_{rf} is the current driven by P_{rf} in the steady state) then a negative voltage is induced which tends to drive current in the opposing direction. When the plasma current is underdriven ($I_{rf} - I < 0$), then the induced voltage tends to add to the rf-driven current. In the absence of externally applied voltages, the plasma current response is given by:

$$\frac{dI}{dt} = \frac{I_{rf} - I}{L/R}, \tag{2.43}$$

where we assumed that I_{rf} was constant and independent of the induced voltage $V = -L\, dI/dt$, and that the resistance R was constant and independent of the rf power. Such a circuit model is unrealistic because it neglects the nonlinear current produced by the simultaneous application of both the voltage and the rf.[59]

If the electric field is small enough, so that the collisional slowing down of the resonant electrons dominates over the influence of the electric field, then I_{rf} will be nearly independent of the electric field. In this limit of small electric field, Fisch has calculated a modified conductivity appropriate for lower-hybrid current driven plasmas. It is given by:[59]

$$\sigma = \sigma_{sp}[1 + \alpha(Z_i) J_N w^2], \tag{2.44}$$

where $\alpha(Z_i) = [1+2/(3+Z_i)](Z_i+0.72)/32(2/\pi)^{1/2}$, $J_N = J_{rf}/env_e$ [with J_{rf} given by (2.40)], $w = v_{\|}/v_e$, and $\sigma_{sp} \simeq 32(2/\pi)^{1/2} ne^2/m\nu_0(Z_i + 0.72)$. The evolution of the plasma current may be determined by using Eqn. (2.43) with $R = R_{sp}/[1 +$

$\alpha(Z_i)J_N w^2]$. The enhanced conductivity during rf current drive limits the rate of current ramp-up.

In recent ramp-up experiments on PLT,[16] rf energy was converted into poloidal field energy with a relatively high efficiency $\{\epsilon = [\frac{d}{dt}(\frac{1}{2}LI^2) - P_{ext}]/P_{rf} \sim 0.20\}$. These results cannot be explained with the theory of enhanced conductivity. In order to interpret the PLT results, Fisch and Karney have developed a more general theory[30] which is valid in the regime where the dc electric field dominates over collisions in influencing the energetic current carrying electrons.

In this theory, the fraction of absorbed rf power converted into poloidal field energy, P_{el}/P_{abs}, is calculated as a function of $u = v/v_R$, where v_R is the runaway threshold velocity defined by $v_R^2 = \omega_{pe}^4 m \log\Lambda/4\pi n|qE|$. This threshold velocity is related to v_b, the runaway velocity of Dreicer, by $v_R = v_b(2 + Z_i)^{-1/2}$. The magnitude of u indicates the relative influence of the electric field and collisions on the slowing down of the resonant electrons. When $u \ll 1$, collisions dominate, and the energy of the resonant electron is channeled primarily into bulk heating so that $P_{el}/P_{abs} \to 0$. When $u \gg 1$, the electric field dominates the slowing down of the resonant electrons and we expect $P_{el}/P_{abs} \to 1$. In this latter regime, however, backward runaways are easily generated, and when well confined, they act as a poloidal field energy sink. Thus, we expect that the most efficient conversion of rf energy to poloidal field energy occurs when $u \sim 1$.

Neglecting runaways, the quantity P_{el}/P_{abs}, for high velocity lower hybrid waves, is given by:

$$\frac{P_{el}}{P_{abs}} = \frac{\partial G/\partial u}{u}, \tag{2.45}$$

where

$$G(u > 0) = \frac{u^4}{5 + Z_i + [2u^2 + 2(5 + Z_i)^2/3(3 + Z)]u^2/(u^2 + 1)},$$
$$G(u < 0) = \frac{u^4}{5 + Z_i} - \frac{2u^6}{3(3 + Z_i)}.$$

This function is plotted in Fig. 2.5 in terms of P_{el}/P_{rf}, where we have assumed that $\alpha = P_{abs}/P_{rf} = 0.75$ and $Z_i = 2$. Note that $u > 0$ corresponds to ramp-up, and that $|u| \sim (|E|/n)^{1/2}$. Three regions are distinguishable on the plot: 1) the regime of steady state current drive at the origin, where $E = 0$ and $P_{el}/P_{rf} = 0$, 2) the regime of high conductivity near the origin where $u \ll 1$, and $P_{el}/P_{rf} \ll 1$, and 3) the region beyond, where efficient conversion of rf energy to field energy takes place.

Both P_{el}/P_{abs} and u can be related to measurable quantities.[60] The quantity P_{el} is defined as:

$$P_{el} = -VI_t, \tag{2.46}$$

where I_t is the total tail current driven by the rf and the electric field. This current is given by:

$$I_t = I - \frac{V}{R_{sp}}, \tag{2.47}$$

where V/R_{sp} is the back current carried by the bulk plasma and I is the net plasma current. The voltage V is determined from the poloidal field power flow relation:

$$VI + \frac{d}{dt}\left(\frac{1}{2}LI^2\right) = I(M_{OH}\dot{I}_{OH} + M_v\dot{I}_v) \equiv P_{ext}, \tag{2.48}$$

where I is the total current, $L = L_{int} + L_{ext}$ is the total plasma inductance with $L_{int} = \mu_0 R\ell_i/2$ and $L_{ext} = \mu_0 R(\ln\frac{8R}{a} - 2)$, and P_{ext} is the power flow from the external OH and vertical field coils. Combining equations (2.46), (2.47), and (2.48) we obtain:

$$P_{el} = \frac{d}{dt}\left(\frac{1}{2}LI^2\right) - P_{ext} + \frac{V^2}{R_{sp}}. \tag{2.49}$$

All of the quantities on the right hand side of Eqn. (2.49) are measurable. Similarly, $v_R \propto \sqrt{n/V}$ can be determined experimentally. Two assumptions must still be made, however, before a comparison between theory and experiment can be carried out.[60] First, we must assume a value for the absorption efficiency $\alpha = P_{abs}/P_{rf}$. Second, it is assumed that the resonant phase velocity of the waves is related to the launched phase velocity by $v_\phi = c/N_{\parallel}\beta$, where β is the factor by which $N_{\parallel}$ is upshifted as the waves propagate into the plasma. Furthermore, a narrow wave packet is assumed which characterizes the launched wave spectrum. With β and α as free parameters, then, the experimental data can be compared to the theory.

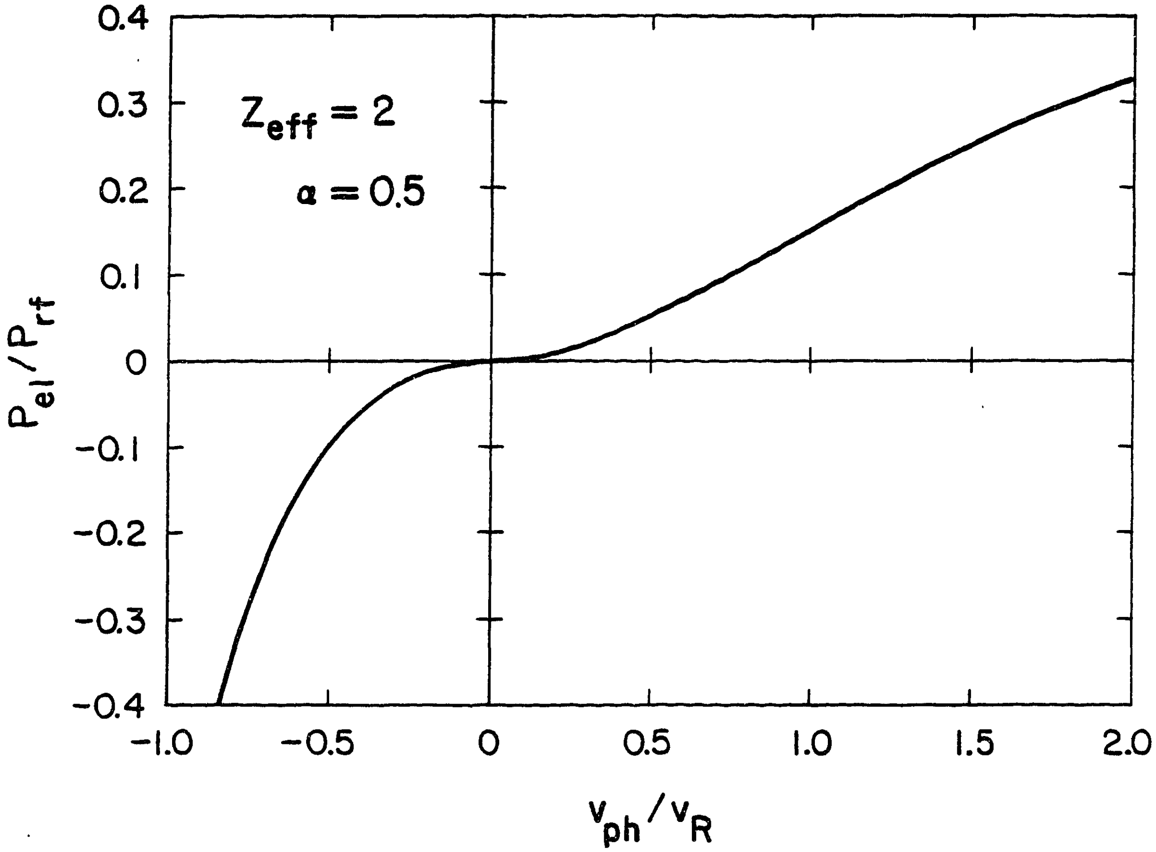

Fig. 2.5: P_{el}/P_{rf} versus $u = v_{ph}/v_R$ from the Fisch-Karney ramp-up theory for the parameters $Z_{eff} = 2$ and $\alpha = P_{abs}/P_{rf}$.

In the theoretical analysis of the PLT data,[30,60] the runaways were neglected because they were not expected to be confined for a long time. In general, though, a theory of current drive in the presence of a dc electric field must include the runaway contribution to the current. While some work has been done in this area,[61] a consistent theory has yet to be developed which includes the effects of radial tail confinement losses on the ramp-up efficiency.

Chapter 3

The S-Band High Power Rf System

A new 100 kW, 40 ms rf system was constructed for the 2.45 GHz current drive studies on Versator. With this system, up to 95 kW of net rf power has been coupled to tokamak plasmas using a four-waveguide phased array antenna with external microwave windows. The rf system, shown schematically in Fig. 3.1, consists of three main subsystems: 1) the high power microwave components, including the two klystron amplifiers, the power splitting and phase shifting network, and the antenna, 2) the high voltage klystron power supply, and 3) the low power rf drive and rf power and phase monitoring circuitry. The main design features of each of these subsystems are described in the first three sections of this chapter. In the final section, the high power performance of the antenna during current drive and heating experiments is discussed.

3.1 High Power Microwave Components

Two Varian Model 5K070SH-2 klystron amplifiers, on loan from the Alcator-C project[62], have been used for the high power source of microwave radiation at 2450 MHz. Each klystron is capable of amplifying up to 50 kW of rf power, with a maximum rated duty cycle of 0.3% and an overall efficiency (beam power to rf power) of approximately 40%. We have obtained a combined output from these klystrons of 100 kW for pulse durations up to our power supply limit of 40 ms. The absolute maximum ratings for the beam voltage and beam current are 31 kV and 4 A, respectively. Normally, with an optimized rf drive level, a beam voltage of 29 kV is sufficient for full power operation. The rf gain of the 5K070SH-2 klystron is nearly 60 dB.

Each klystron is seated in an electromagnet which focuses the electron beam, and minimizes the body current drawn by the tube. Defocusing of the klystron

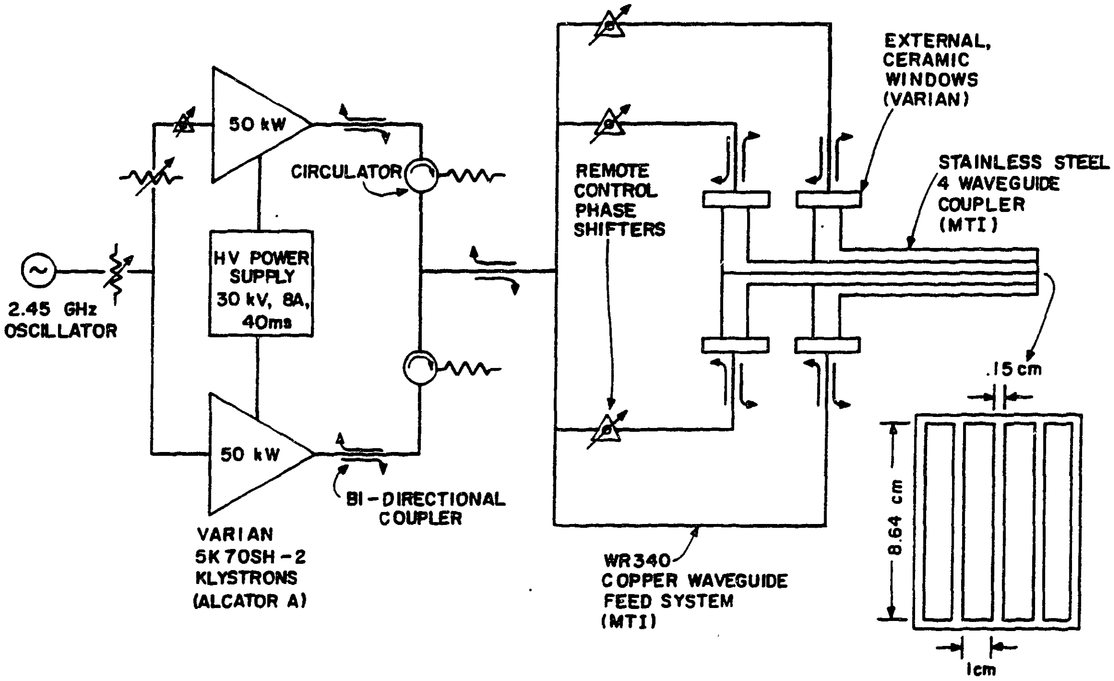

Fig. 3.1: Schematic diagram of the Versator II 2.45 GHz rf system.

beam during high voltage pulsing can result in permanent damage to the delicate resonant cavities. Therefore, we have implemented protective circuitry which triggers a power supply crowbar in the event that the body current level in either klystron exceeds the maximum rated value of 100 mA. For added protection during line voltage "brownouts," when the focus coil current may droop slightly, we have also installed a battery-operated fault circuit which monitors the output voltage of the focus coil power supplies. During normal operation of the klystrons, with the focus coils properly aligned, the body current should not exceed about 70 mA.

The klystrons can be operated without damage into a maximum VSWR of 2.0, which corresponds to a reflected power of approximately 11%. High power water-cooled ferrite circulators are used to isolate the klystrons from impedance mismatches occurring in the antenna or in the waveguide transmission system. The klystrons are also equipped with Varian arc detectors which can sense visible arcs near the klystron output windows, as well as excessive reflected power levels. In either case, the circuits issue a power supply crowbar command.

The heat generated in the klystrons, magnets, and circulators is dissipated mainly by water cooling. A closed-loop water cooling system capable of delivering 50 gpm at 60 psi was constructed for this purpose. The circulated water is cooled in a heat exchanger with MIT chilled water flowing through the primary coil. All the water cooling lines are interlocked with Shur-flo switches, and in case of interrupted water flow, the focus coil power supply interlocks are disabled, triggering a high voltage crowbar.

The high power rf components in the transmission system, including the power splitting network, and the phase shifters, were fabricated by Microwave Techniques, Inc. of Raymond, ME. In order to minimize the transmission losses between the klystrons and the antenna, the klystrons were located in the Versator room only fifteen feet from the tokamak. In addition, the entire WR340 rectangular waveguide transmission system is fabricated from copper, with the exception of the phase shifters, which are made from aluminum. The transmission loss from klystron to antenna is less than 5%. Because of the relatively low power density in this system

($2.7\,\mathrm{kW/cm^2}$ maximum), no problems were encountered with waveguide arcing and pressurization of the waveguides was not necessary.

The power splitting network consists of four magic tees (180° hybrids). The outputs from the two klystrons are first combined before being split equally four ways. This ensures an equal distribution of power to the four waveguides of the antenna. Following the 4-way power split, three of the lines are fed through mechanical phase shifters consisting of 90° hybrid couplers and dual motor-driven sliding "bucket" shorts. Power entering the phase shifter through one port of the hybrid coupler is split equally two ways and reflected off the short circuits. After the reflected power recombines in the hybrid it leaves through the opposite port. The position of the shorts determines the overall path length, and hence the phasing of the waveguide. With these phase shifters, the relative phasing of adjacent waveguides in the antenna can be varied continuously from 0° to 360° on a shot-to-shot basis. The phase shifters are remotely operated from the control room.

The forward and reflected power is monitored at seven different locations in the transmission system with bi-directional couplers, or reflectometers (see Fig. 3.1). Two of these are located at the outputs of the klystron. Their reflected power ports are incorporated permanently into the klystron arc-detection circuitry. A third reflectometer, used to measure the total forward and reflected power, is located just after the magic tee where the klystron outputs are combined. The remaining four reflectometers are located adjacent to the microwave windows on the antenna, and are used to measure the reflectivity $R = P_{ref}/P_{fwd}$ and the phase of each waveguide in the array. The rf power and phase measurements will be discussed in Section 3.3.

We have used externally-mounted "pillbox"-type ceramic microwave windows for the vacuum seals on the waveguide antenna. Altogether, five window assemblies were fabricated by Varian Associates of Palo Alto, CA. Three of these units were rebuilt versions of old windows which were salvaged from surplus Alcator A antennae. Two of the windows were purchased new (Varian Model W340AA2).

The microwave properties of the windows are quite good (VSWR $\sim$ 1.05 – 1.10) and no problems were encountered with arcing on the vacuum side of the window surfaces. Difficulties were encountered, however, in obtaining a reliable vacuum seal with these windows, especially with the rebuilt units, due to the two piece construction of the vacuum flange. Future removal of the rebuilt windows from the waveguide array is highly discouraged!

Our antenna consists of a horizontal array of four rectangular waveguides placed side by side. The vertical and horizontal dimensions of each waveguide are 8.64 cm and 1.0 cm respectively, and the septum thickness is 0.15 cm. The waves are propagated through the antenna waveguides in the fundamental TE_{10} mode, with the electric field oriented in the horizontal direction, parallel to the toroidal magnetic field of the tokamak for coupling to the lower hybrid slow wave.

The waveguide grill was designed and fabricated by Microwave Techniques, Inc. A photograph of the antenna is shown in Fig. 3.2. The antenna is constructed entirely from type 304 stainless steel. All of the machined parts were electropolished prior to electron beam welding. In order to minimize the evacuated volume in the antenna, the lengths of the waveguides were kept relatively short; the overall length of the antenna is 77 cm. In order to avoid obstructing adjacent tokamak ports, the waveguide feeds into the antenna were oriented in the vertical direction. Each of the four identical transitions from the narrow antenna guide to the full-sized WR340 waveguide incorporates two consecutive mitre bends, with the first bend outward and the second bend upward. For convenience, the front and rear transitions are spaced apart exactly one wavelength ($\lambda_g = 17.4$ cm) so that all four waveguides have the same effective path length.

To allow for variable positioning of the waveguide mouth relative to the plasma edge, the antenna is mounted on a bellows. The entire antenna structure slides in and out along stainless steel guide rods, riding on oilite bronze bushings and ball bearing pillow blocks. The radial position is controlled with a mechanical worm gear jack, which allows accurate positioning to within 1 mm. The flex guide, located at the top of the vertical waveguide run above the antenna, takes up any

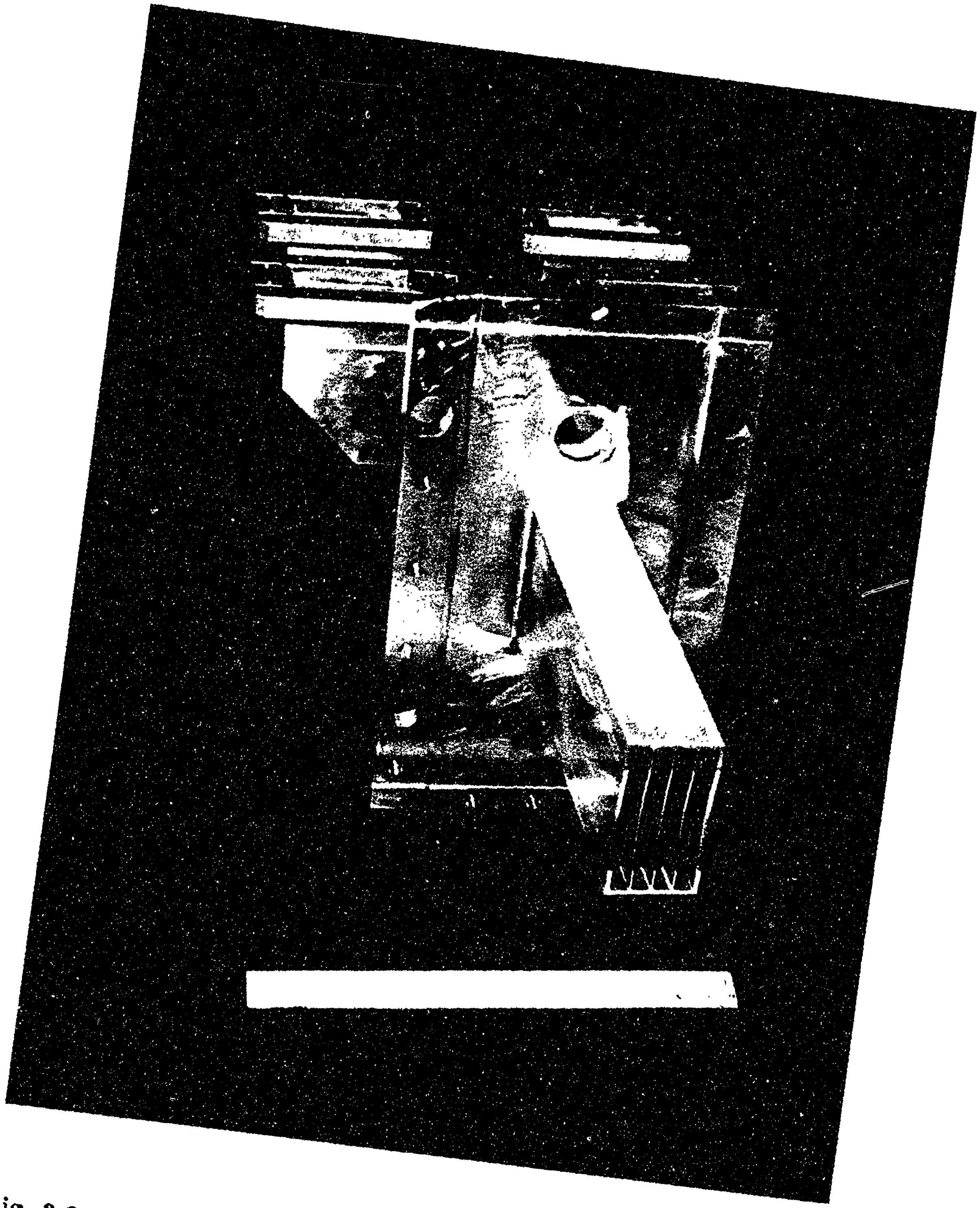

Fig. 3.2: Photograph of the four-waveguide coupler.

misalignment in the rigid waveguide feed system when the antenna is moved.

3.2 High Voltage Power Supply

To power the S-band klystrons, a new 30 kV, 8 A regulated power supply was constructed. A schematic diagram of the power supply is shown in Fig. 3.3.

Two capacitor bank/crowbar units obtained from the Alcator C project were rebuilt and incorporated into the S-band power supply. These units contained a total of twelve 8.8 μF, 33 kV Maxwell capacitors. Eight more 60 μF, 10 kV capacitors (two sets of four in series) have been added for a total capacitance of 136 μF, and a maximum stored energy of 74 kJ. This is sufficient for full power rf pulse lengths up to 40 ms, without the loss of voltage regulation in the modulator. A 40 kV, 25 mA Hipotronix power supply is used as the high voltage charging supply.

To insure personnel safety and provide equipment protection, the capacitor banks are equipped with two mechanical high voltage drop relays which discharge the bank through a 25 kΩ resistor ($\tau_{RC} \sim 3$ sec). The solenoids of the drop relays are connected to the ac line voltage via a series-wired safety interlock chain. Fault conditions which open the safety interlock chain include: 1) open doors to the power supply room, the HV safety enclosure, or the capacitor bank cabinets, 2) intrusion into the klystron area when the Versator room interlocks are armed, 3) activation of the panic buttons located in the HV enclosure, and in the control room, 4) crowbar HV not ready, 5) insufficient air flow to the cathode of the crowbar ignitron, 6) insufficient air flow for modulator tube cooling, 7) crowbar triggered, or not reset.

In order to prevent permanent klystron damage in the event of an arc or a high voltage fault, it is necessary to divert the stored energy of the capacitor bank away from the klystrons as quickly as possible. Therefore, the capacitor bank is also equipped with a high power ignitron crowbar circuit. When the ignitron (type GL37248) is fired, the capacitor bank is discharged into a high power load

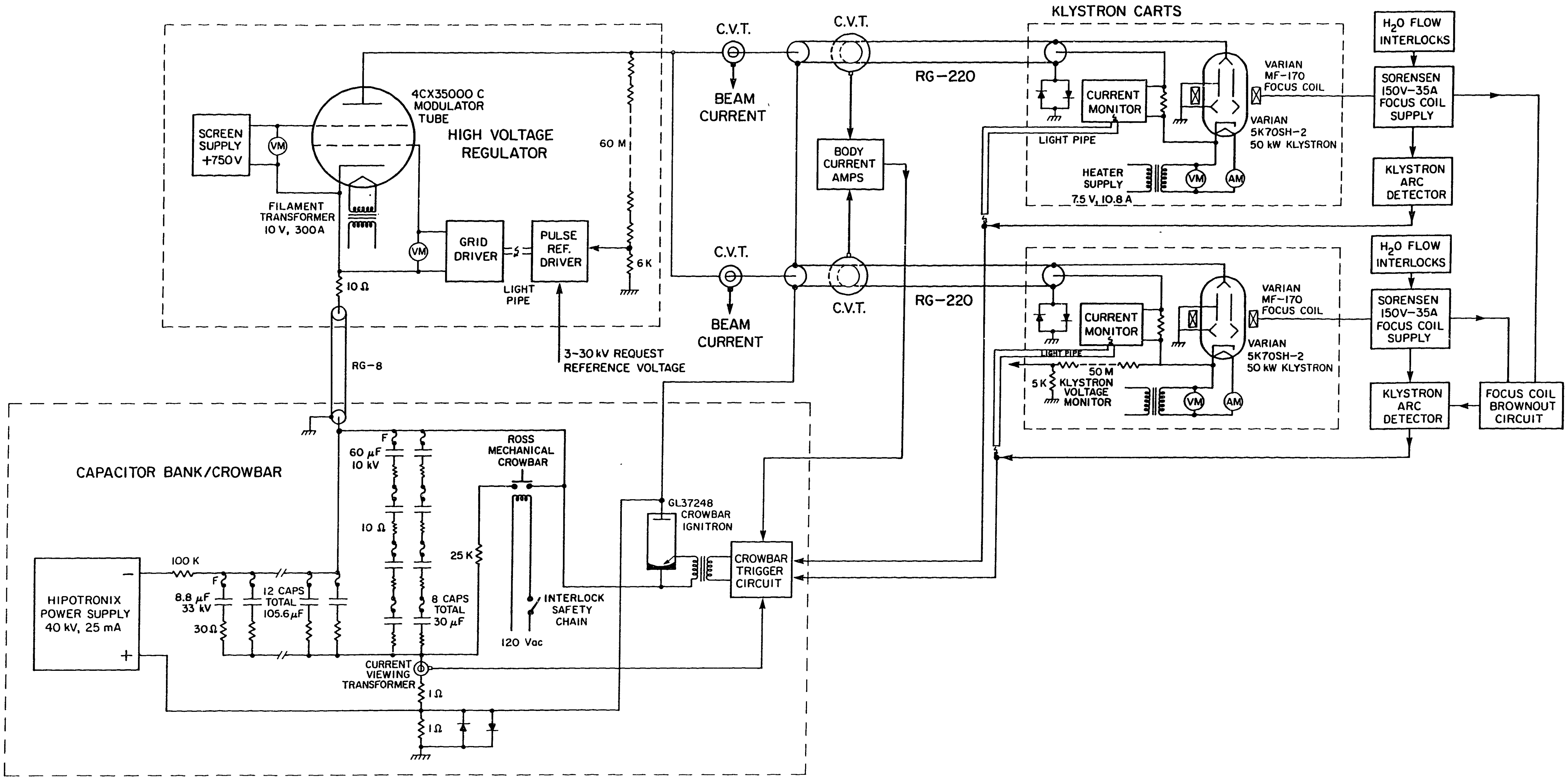

Fig. 3.3: Schematic diagram of the S-band high voltage klystron power supply, showing the capacitor banks, the modulator tube regulation circuitry, and the klystron cart connections.

resistor ($R < 1\,\Omega$) with an RC time constant of $25\,\mu$s. The ignitron is fired with a standard krytron triggering circuit. The following fault conditions result in a power supply crowbar: 1) klystron window arcs, 2) excessive power reflected to either klystron, 3) insufficient focus coil voltage, 4) insufficient klystron water cooling flow, 5) excessive current drawn by either klystron, 6) excessive capacitor bank return current, 7) excessive klystron body current. Each of these fault systems was thoroughly tested before high power operation of the S-band rf system was commenced.

An Eimac 4CX35000C radial beam power tetrode is used as the switching tube between the capacitor bank and the klystrons. A 10 V, 300 A filament transformer supplies the heater current. We operate the tube with the screen grid biased at +750 V relative to the cathode. The plate voltage of the tube (and hence the klystron voltage) is then determined by the voltage level on the control grid. In order to regulate the klystron voltage, a feedback circuit has been incorporated into the grid drive circuitry. In the feedback loop, the plate voltage is measured with a 10,000:1 compensated voltage divider and compared with a user-controllable reference gate pulse which is generated in the pulse reference driver board. The amplified difference signal is then coupled via a light pipe to the grid driver circuit, closing the feedback loop. There are two principle advantages to voltage feedback regulation as opposed to simple modulator tube switching. First, the klystron voltage pulse does not decay with the capacitor bank voltage (as long as the bank voltage is high enough to allow for a sufficient voltage drop across the modulator tube). Second, the klystron voltage is easily controlled by adjusting the grid drive reference gate pulse level, rather than raising or lowering the capacitor bank voltage. This allows the klystron rf output level to be easily varied without changing the rf drive level from its optimized value.

The modulator tube output is fed to the klystron cathodes via high voltage RG-220 coaxial transmission lines. The klystron beam current flows through the center conductor, while the klystron collector current returns through the outer shield. The klystron body current is the net current flowing through the transmission-line (klystron beam current minus klystron collector current). Hence, the klystron beam current and body current can each be measured easily with current viewing transformers (CVTs). Body current amplifier circuits improve the low frequency response of the CVTs and provide amplified signals for display as well as crowbar trigger signals in case of a fault. Inside the klystron carts, the total klystron current flowing to the heater/cathode is monitored with a series resistor. The overcurrent fault protection circuit is connected via a light pipe to the capacitor bank crowbar trigger circuit. Also located inside the klystron carts are the klystron heater supplies (7.5 Vac, 10.5 Aac), and a 10000:1 resistive voltage divider used to monitor the klystron beam voltage.

3.3 Low Power Rf Circuitry

We begin this section with a description of the low power microwave circuitry used to drive the high power klystron amplifiers. Next, the detectors and amplifiers used to measure the rf power, reflectivity and phase in each of the antenna waveguides is described, along with the calibration procedures. Finally, the arc detection fault circuitry used to protect the antenna and the microwave windows is described. For reference throughout this section, a schematic diagram of the low power microwave circuitry is shown in Fig. 3.4.

For full power operation, the klystron amplifiers each require an input rf drive level of approximately 50 – 100 mW. The 2.450 GHz rf drive signal is generated by a 40 mW phase-locked oscillator (Miteq Model PLM-2450C-0-20P). Before being fed to the klystrons, the oscillator signal is split equally two ways and then amplified by 1 W solid state GaAs FET amplifiers (Mini-circuits Model No. ZHL-42). The rf drive signals are gated on using a TTL-modulated PIN diode switch (Triangle Microwave QL1046). To avoid sudden application of rf power to the plasma, the PIN diode switch can be turned on gradually with a ramping circuit, with exponential rise times continuously variable from 10 μs to 20 ms.

The amplitudes of the two rf drive signals and their relative phase are con-

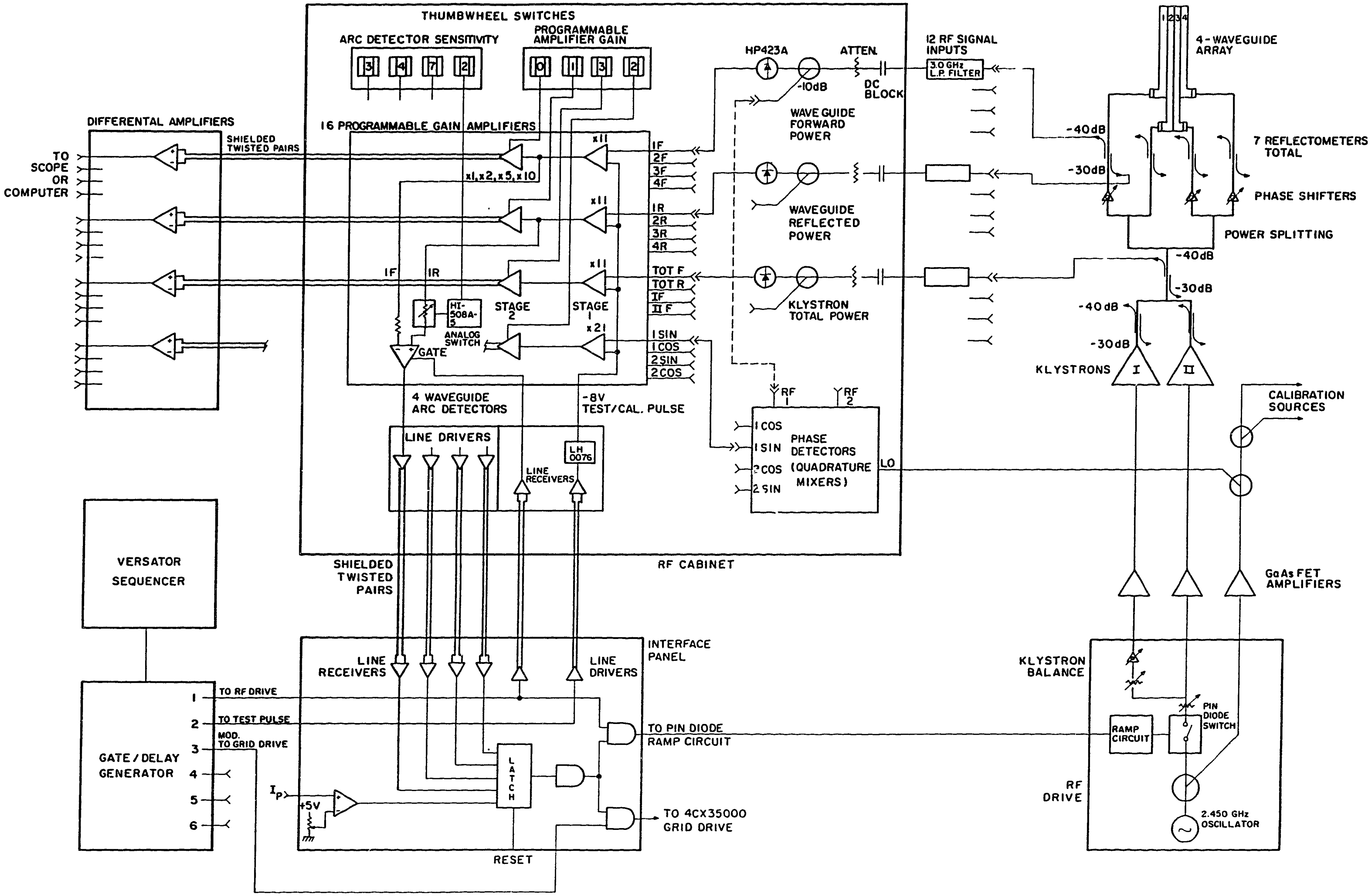

Fig. 3.4: Schematic diagram of the low power microwave circuitry, including the rf drive, the waveguide power and phase detection circuitry, and the waveguide arc detectors.

trolled with the variable attenuators and the phase shifter located on the input side of the GaAs FET amplifiers. Normally, the attenuators are set to maximize the output power of each klystron, without exceeding the level which just saturates the tube. The phase shifter is then adjusted to maximize the total klystron output power, which is measured at the output of the magic tee where the individual klystron outputs are summed together. Once the rf drive settings are optimized, the rf output level may be controlled by varying the klystron beam voltage as discussed earlier.

Altogether, twelve detector channels have been designed and fabricated to allow measurements of the forward and reflected power in each of the antenna waveguides, as well as the total forward and reflected power, and the output power from each klystron. The coupled signals from the seven reflectometers in the S-band transmission system are directed to an rf-shielded cabinet located in the control room which houses the rf detection circuitry. Before entering the rf cabinet, the rf signals are fed through 3 GHz low-pass filters to eliminate spurious harmonics, and inner/outer dc blocks for electrical isolation. Inside the cabinet, the rf power level in each of the twelve channels is measured with an HP423A coaxial crystal detector. Interchangeable fixed attenuators on the roof of the rf cabinet are used to keep the input power level within the calibrated range of each detector.

The phase in any two of the detector channels may be measured relative to a local oscillator (LO) signal obtained from the rf drive circuitry. Commercially produced quadrature mixers (Triangle Microwave Model FR-1228) have been used as phase detectors. Since the LO and rf signals are at the same frequency, the mixers provide two IF outputs corresponding to $\sin\phi$ and $\cos\phi$, where ϕ is the phase between the rf and LO input signals. For convenience, the phase of the LO signal may be changed with a mechanical phase shifter.

The twelve outputs from the crystal detectors, along with the four outputs from the phase detectors, are amplified by a set of sixteen two-stage programmable-gain amplifiers. The outputs from these amplifiers are sent via shielded twisted-pair cabling to a set of differential amplifiers located outside the rf cabinet where the outputs are made available for oscilloscope display and computer storage. The overall gain of the amplifiers may be calibrated with a reference voltage test pulse which is fed into the first stage of the amplifier chain. In order to calibrate the rf detectors, as well as the rf signal path between the reflectometers and the amplifiers, known signal levels of varying amplitudes were fed into each of the rf signal cables at the point where they connect to the reflectometers. The calibration curves for each detector channel are stored in the computer memory for rapid rf coupling data analysis.

Before the waveguide grill can be phased properly, the forward phase in each of the four waveguides must be measured as a function of the phase shifter setting. The relative phasing of the waveguides is first established by setting all four waveguides in phase at the reflectometers. This corresponds to an antenna phasing of $(0, 0, \pi. \pi)$. Once all three phase shifters are calibrated over their range of motion, they can be used to set the relative phasing between adjacent waveguides to any desired value. Normally, during experimental runs or during rf conditioning, the reflected phase of the waveguides is monitored in order to detect the onset of rf breakdown in the antenna waveguides.

To protect the antenna and the microwave windows from damage due to arcing, four arc detector circuits have been incorporated into the amplifier chain. A simple comparator circuit is used to monitor the ratio of the forward and reflected power signals at the outputs of the first stage amplifiers. If the reflectivity becomes too high, possibly indicating an arc in the antenna or the windows, the rf drive and modulator gate pulses are switched off within a few microseconds. The operator controls the sensitivity of the circuit by varying the attenuation of the forward power signal before it enters the comparator. The output fault signal is sent outside the rf cabinet to an interface panel which contains the logic circuitry used to gate off the rf drive and modulator timing pulses. Pulsing the rf system into vacuum with the grill set for plasma coupling usually results in excessively high reflection coefficients which trip the arc detectors. A plasma current monitoring circuit located in the arc detector interface panel can be used to inhibit pulsing into vacuum during tokamak discharges. This can occur when the plasma is not broken down, or when the discharge terminates prior to the rf firing time.

3.4 Antenna Coupling and High Power Performance

The efficient coupling of rf power from an antenna to the waves in a plasma requires that the antenna impedance be matched to the plasma impedance. With the lower hybrid waveguide "grill" this is accomplished by adjusting the position of the antenna relative to the plasma edge, since the coupling depends mainly on the density at the waveguide mouth. The linear theory of waveguide coupling to lower hybrid slow waves, first developed by Brambilla, predicts the antenna reflectivity as well as the $N_{||}$-spectrum of the launched waves. In the original theory,[63] the waveguides are modelled with infinitely high parallel conducting plates, while the plasma is modelled with a linear density ramp extending in the perpendicular direction from the antenna mouth. A more recent version of the theory by Stevens et al.[64] includes a finite density step at the waveguide mouth, given by n_0. Optimum coupling in this case is predicted when the plasma is "overdense" at the waveguide mouth:

$$n_0 \simeq |N_{||}^2 - 1| n_c, \tag{3.1}$$

where n_c is the slow wave cut-off density given by $\omega = \omega_{pe}(n_c)$.

We have used a version of the Brambilla coupling code which includes the effects of finite waveguide height as well as the density step to calculate the launched spectrum for our S-band four-waveguide grill.[40] The results are shown in Fig. 3.5 for 90° and 180° phasings of adjacent waveguides. We have assumed that $n_0/n_c = 10$, and $L = n(dn/dx)^{-1} = 1.2\,\mathrm{cm}$, based on previous probe measurements of the edge density on Versator.[40] For 180° phasing $(0, \pi, 0, \pi)$, a symmetric power spectrum characteristic of a standing wave is produced with the peak values of $N_{||} = \pm 5$ corresponding to two wavelengths across the face of the grill. In this case, equal amounts of power are launched in each toroidal direction. In contrast, when the antenna is phased at +90° $(0, \pi/2, \pi, 3\pi/2)$, an asymmetric travelling wave spectrum is produced, with 73% of the power launched in the direction of the electron ohmic

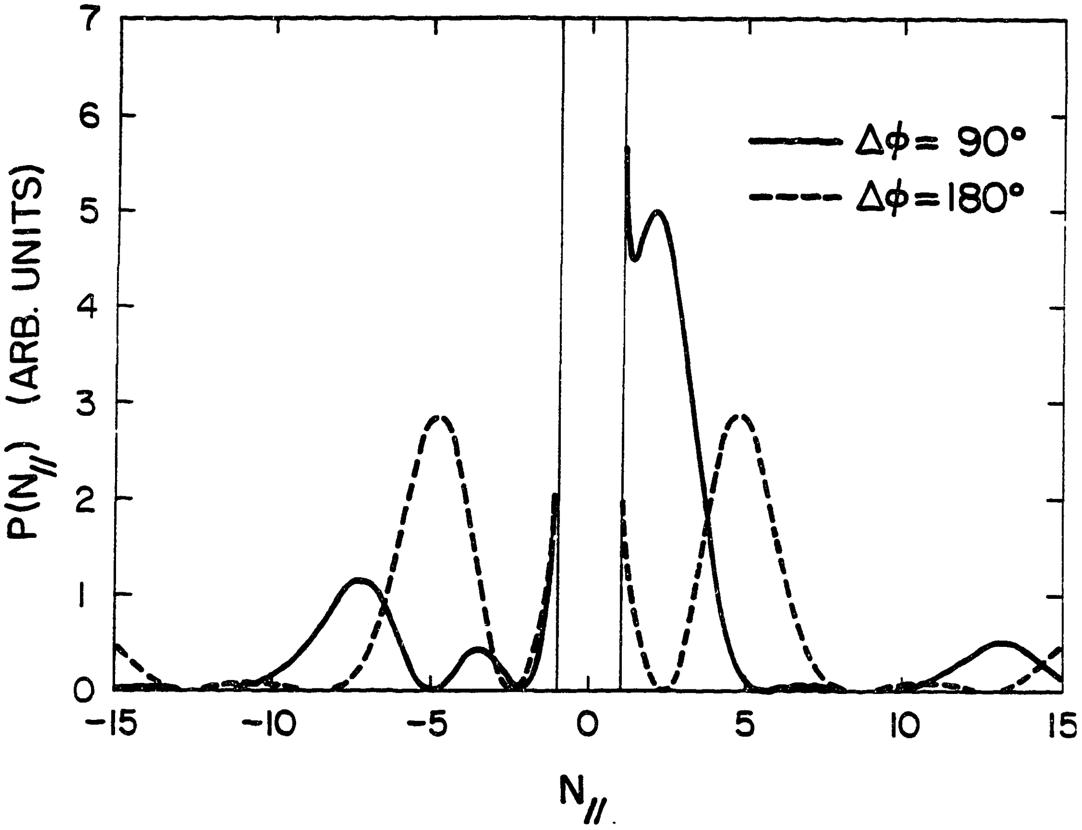

Fig. 3.5: Calculated $N_\parallel$ power spectra of the S-band four-waveguide grill with $\Delta\phi = 90°, 180°$ phasings, and plasma edge parameters $n_0/n_c = 10$ and $L = n(dn/dx)^{-1} = 1.2\,\mathrm{cm}$.

drift (positive $N_{\|}$ direction). The bulk of this power is concentrated at low $N_{\|}$ values between 1 and 4. The spectrum of the 2.45 GHz antenna is nearly identical to that of the 800 MHz four-waveguide side-launch antenna used in previous Versator current drive studies.[7,65]

Although detailed low power coupling studies have not been undertaken in the present S-band experiment, we have routinely monitored the coupling during high power current drive and heating experiments. Generally, the coupling has been quite good, with antenna reflectivities in the range of $5-10\%$ for waveguide phasings $\Delta\phi = 90 - 180^\circ$ and plasma densities $\bar{n}_e \geq 5 \times 10^{12}\,\mathrm{cm}^{-3}$. At lower densities, the reflectivities are somewhat higher, typically in the range $10 - 25\%$. The antenna coupling is relatively insensitive to the grill position, at least within its movable range, which is $0.2 - 1.2\,\mathrm{cm}$ behind the limiter radius. Instead, we have found the coupling to be more sensitive to the radial equilibrium position of the plasma, with the most favorable coupling occurring when the plasma is well-centered, or located towards the outside of the vacuum chamber.

In Fig. 3.6, the global reflectivity of the S-band antenna is plotted as a function of waveguide phasing. The solid circles correspond to data taken at a density of $\bar{n}_e = 1.8 \times 10^{13}\,\mathrm{cm}^{-3}$ when 85 kW of rf power was injected into ohmically heated plasmas. The coupling is quite good for $\Delta\phi = 90 - 180^\circ$, with the minimum reflectivity (4%) occurring at $\Delta\phi \simeq \pm 120^\circ$. The solid curve in Fig. 3.6 is calculated from the Brambilla code. The value for the density step $(n_0/n_c = 7)$ was chosen to best fit the data. Note that the condition for optimum coupling given by Eqn. (3.1) is fairly well satisfied since $N_{\|} \simeq 3$ for $\Delta\phi = 120^\circ$. However, while the agreement with the data is fairly good for the higher phase angles, the measured reflectivities at the low phase angles ($\Delta\phi = 0^\circ$, $\pm 30^\circ$) are much lower than predicted by the theory ($R = .65$ for $\Delta\phi = 0^\circ$). One possible explanation for the discrepancy is the formation of plasma in the evacuated waveguides due to rf breakdown. This would tend to reduce the antenna reflectivity since rf power could be absorbed by the plasma. However, at this phasing, $\Delta\phi \leq 45^\circ$, our code is really not applicable since it neglects coupling to the fast wave surface mode,[66] which cannot be justified

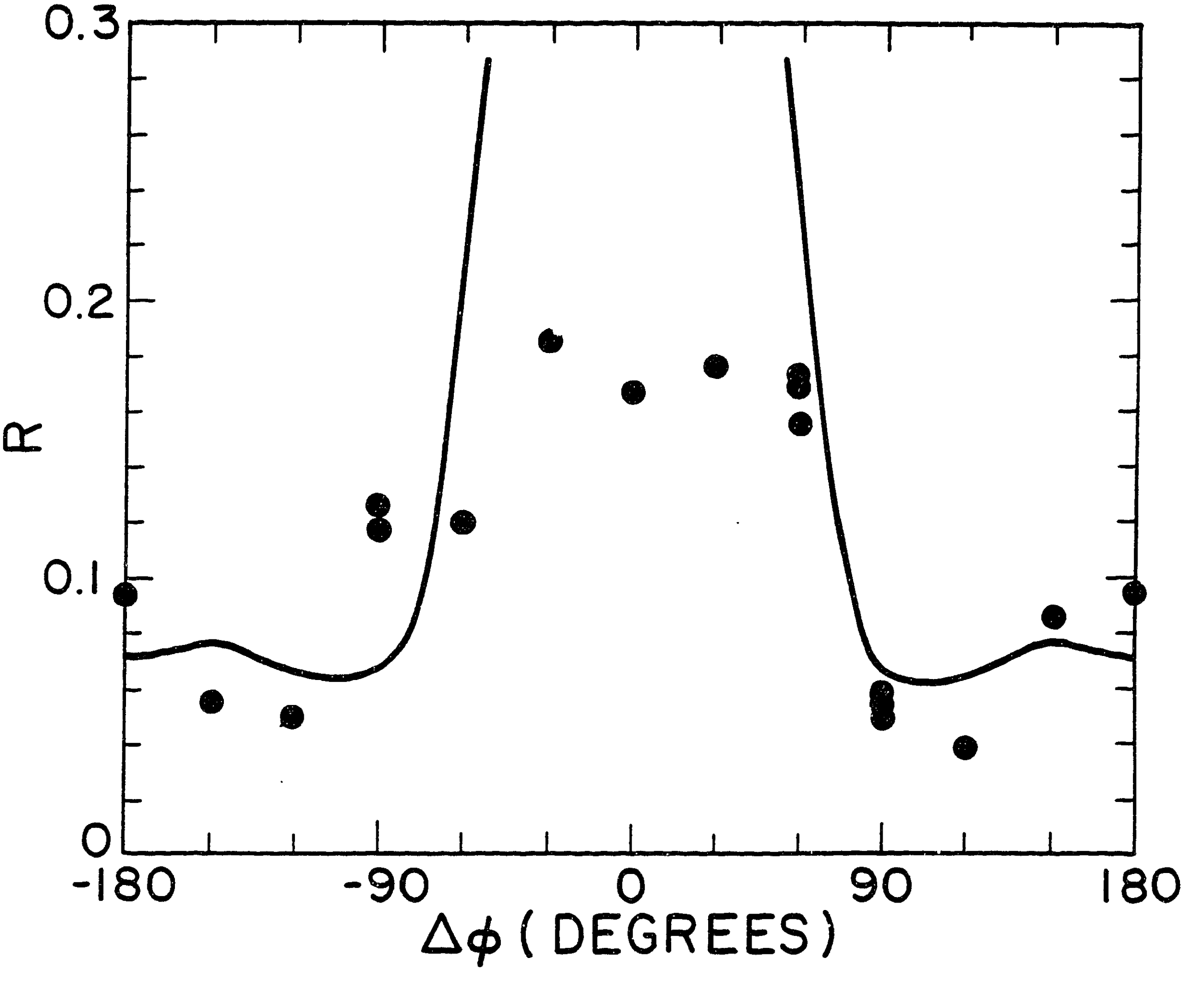

Fig. 3.6: Global reflectivity of the S-band antenna as a function of waveguide phasing measured during high power current drive experiments with $P_{rf} = 85\,\mathrm{kW}$, and $\overline{n}_e = 1.8 \times 10^{13}\,\mathrm{cm}^{-3}$. The solid curve is calculated from the Brambilla theory assuming $n_0/n_c = 7$ and $L = 0.7\,\mathrm{cm}$.

at small values of $\Delta\phi$. Hence, in the range of interest, $\Delta\phi > 60°$, we consider the agreement between experiment and theory to be satisfactory.

In general, the limiting factor in high power grill performance may be the formation of plasma in the evacuated waveguides due to multipactor-initiated rf breakdown.[4] The plasma formation, which is inferred from changes in the reflected power and phase, can lead to a reduction in the transmitted power through the antenna as well as a loss of phase control. The plasma formation is believed to arise from electron-stimulated desorption and subsequent ionization of gas from the waveguide walls. Rf breakdown is also enhanced by electron multiplication due to secondary electron emission.[40] The problem is aggrevated when external vacuum windows are used, since a cyclotron resonance layer then passes through the evacuated region of the waveguides.

Prior to installation on the tokamak, the S-band grill was baked out in a vacuum furnace at 350°C for nine hours in order to desorb gas from the waveguide walls. Following its emplacement on the tokamak, the grill was conditioned in vacuum with the waveguide phasing set at $\Delta\phi = 0°$ to minimize the reflected power. Typically, $3 - 5$ ms pulse lengths were used, with the rf system fired every $3 - 5$ sec. The first evidence of rf conditioning appeared at a power level of approximately 25 kW. The conditioning effects included a gradual decrease in the waveguide reflectivities during the rf pulse, reflected phase shifts, and the evolution of H_2 gas. With continued pulsing, however, these effects disappeared, allowing the rf power to be raised. This procedure was repeated until the maximum available rf power level of 100 kW was reached, requiring a total of about 15 hours of conditioning.

Despite regular rf conditioning to the 100 kW level prior to experimental runs, rf breakdown often limited the incident power level to 80 kW ($2.4\,\mathrm{kW/cm^2}$) when power was coupled to plasmas. Similar difficulties, encountered previously with 800 MHz couplers on Versator, were attributed to the presence of the cyclotron resonance layer ($\omega = \omega_{ce}$) in the evacuated waveguides. Studies with the 800 MHz four-waveguide side-launcher[67] have shown that the elimination of the cyclotron resonance layer with an auxiliary magnetic field coil could lead to substantial improvements in power-handling (from .13 kW/cm^2 to at least .94 kW/cm^2 in those experiments). In light of these results, we constructed a similar magnetic field coil for the S-band antenna.

The configuration of the coil is shown in Fig. 3.7. The field is applied in the vertical direction in order to add to the stray tokamak fields and to provide magnetic insulation between the vertical waveguide walls. In order to produce the cyclotron resonance field of 875 G, the coils are connected in series with the toroidal field magnets. A simple Helmholtz-type arrangement, as used in the 800 MHz studies, would have produced a vertical field error in the tokamak as large as 65%, prohibiting plasma breakdown and start-up. Therefore, additional coils, wound in the opposite direction, were added to the outside of the main waveguide coils to cancel the stray dipole fields in the plasma. The local vertical field error produced with this arrangement is less than 20 G, which is quite acceptable for normal tokamak operation. The magnetic field profile, calculated for a waveguide coil current of 35 kA, is shown in Fig. 3.8. With the waveguide field raised sufficiently high to completely eliminate the cyclotron resonance layer from the evacuated waveguides, incident power levels up to 100 kW (2.9 kW/cm^2) during plasma injection have been achieved with no evidence of reflected phase shifts or other signs of plasma formation in the waveguides. The maximum power level coupled to plasmas to date is 95 kW. Although the waveguide coil has clearly improved the performance of the S-band grill, further work is needed to determine conclusively whether this improvement is due to the elimination of the cyclotron resonance layer or to magnetic insulation effects.

3.5 Summary

A new 100 kW, 40 ms rf system, constructed for the Versator 2.45 GHz current drive studies, has been described. Two 50 kW klystrons, used as the source of rf power, are powered by a 30 kV, 8 A regulated power supply, which is voltage feedback regulated to provide flat output pulses, as well as easy control of the output level. The klystron output power is fed through a power splitting and

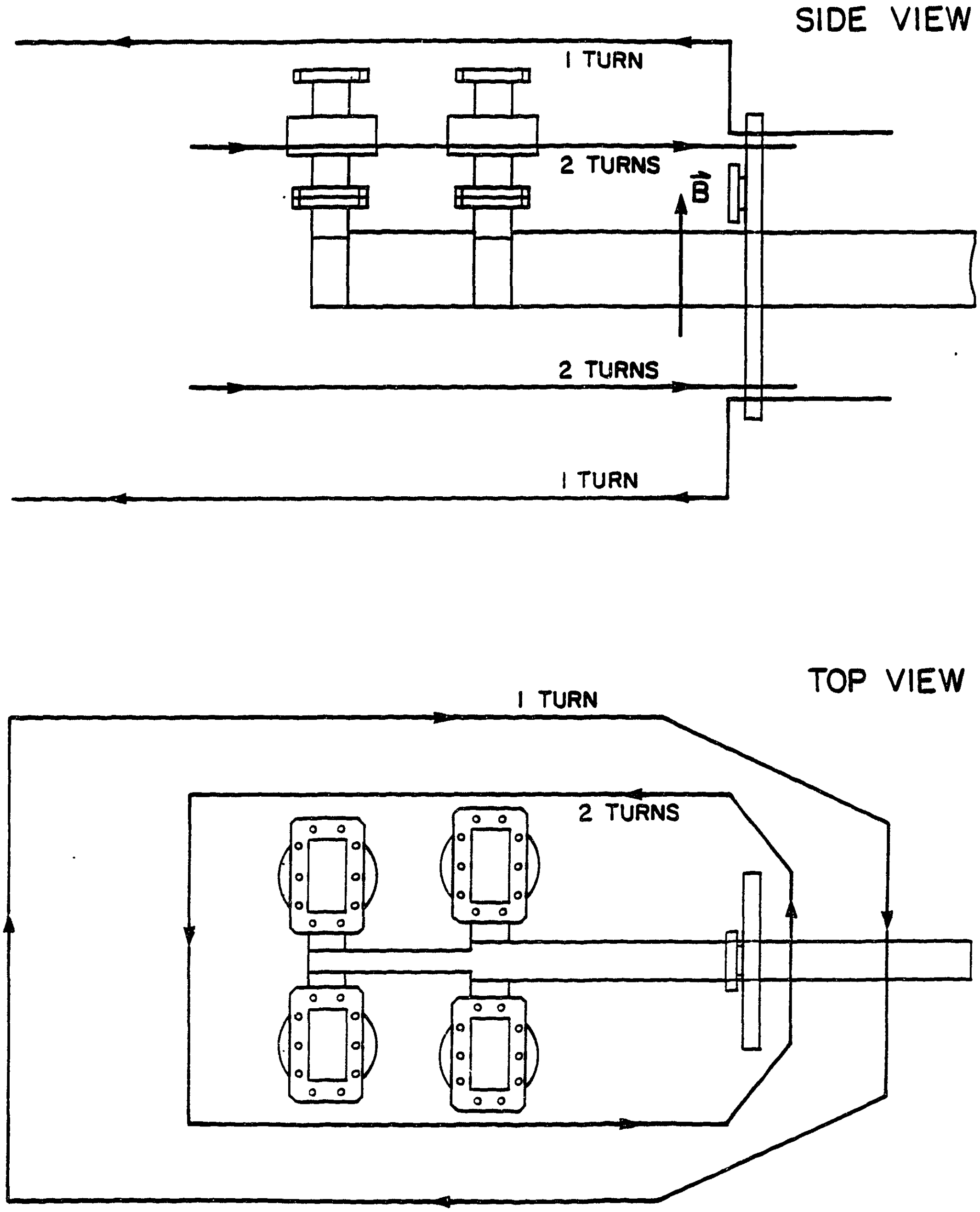

Fig. 3.7: Configuration of the magnetic field coils used to eliminate the cyclotron resonance layer from the evacuated region of the S-band antenna. The inner coils generate an upward vertical field in the waveguides, while the outer coils serve to reduce the field error introduced in the tokamak.

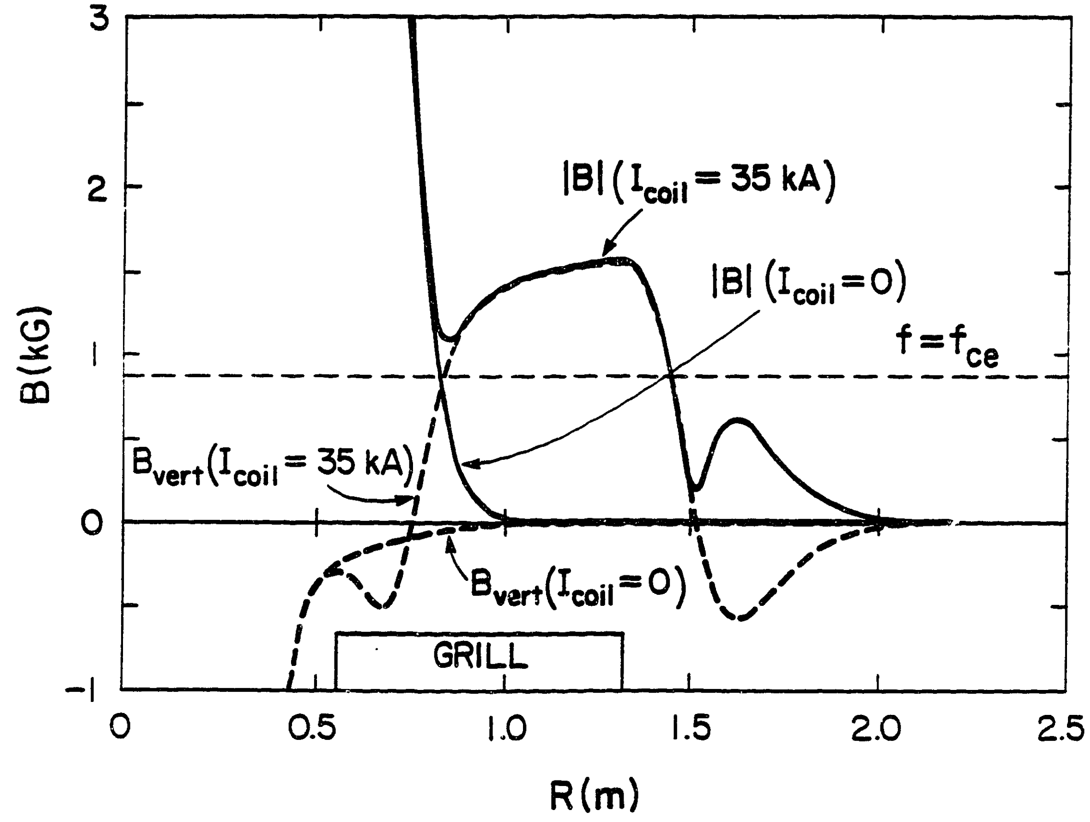

Fig. 3.8: Calculated magnetic field versus major radius in the region of the waveguide grill with and without the rf-breakdown suppression coil.

phase shifting network to a four-waveguide array stainless steel antenna. With a relative waveguide phasing of $\Delta\phi = 90^\circ$, this antenna launches an asymmetric power spectrum with $N_{\|} \simeq 1 - 4$ in the positive $N_{\|}$ direction. The power and phase detection circuitry used to monitor the antenna reflectivities and phase have also been described along with the low power klystron drive circuitry. The antenna coupling during plasma injection has been quite good, with $P_{ref}/P_{fwd} \sim 0.05 - 0.10$ for $\bar{n}_e > 5 \times 10^{12}\,\mathrm{cm}^{-3}$ and $\Delta\phi = 90^\circ - 180^\circ$. However, despite regular rf conditioning in vacuum to the 100 kW power level, early current drive experiments were limited to the 80 kW level because of rf breakdown in the evacuated waveguides. Since external ceramic windows have been used for the antenna, the problem has been attributed to the presence of a cyclotron resonance layer in the evacuated waveguides. Since the cyclotron resonance has been eliminated with an auxiliary magnetic field coil, up to 95 kW ($2.9\,\mathrm{kW/cm^2}$) has been successfully coupled to plasmas, with no evidence of rf breakdown.

Chapter 4

Quasi-Steady-State Current Drive and Ramp-up Results

In this chapter it is shown that the density limit can be raised by increasing the rf frequency, without raising the toroidal magnetic field to improve wave accessibility. Fully rf-driven plasmas, with the OH transformer primary open-circuited, have been achieved at densities up to $\overline{n}_e = 1.0 \times 10^{13}\,\mathrm{cm}^{-3}$, with record values of the dielectric constant, $1 + \omega_{pe}^2/\omega_{ce}^2$. The steady state current drive efficiency scaling for the density range $\overline{n}_e = 0.2 - 1.0 \times 10^{13}\,\mathrm{cm}^{-3}$ is given by $\overline{n}(10^{20}\,\mathrm{m}^{-3})I(\mathrm{kA})R(\mathrm{m})/P(\mathrm{kW}) \simeq 0.0072$. Current ramp-up, with negative loop voltage, has also been achieved at densities up to $\overline{n}_e = 7 \times 10^{12}\,\mathrm{cm}^{-3}$, with ramp-up rates as high as $\dot{I} = 400\,\mathrm{kA/s}$, and ramp-up efficiencies up to $\epsilon = [\frac{d}{dt}(\frac{1}{2}LI^2) - P_{ext}]/P_{rf} \simeq 0.14$.

For all of the data presented in this chapter, the OH transformer primary was open-circuited immediately after the plasma current start-up. The flat-top discharges, where the current is maintained at a constant level by rf waves, are described in Sections 4.1 - 4.4. In Section 4.5, the ramp-up discharges ($\dot{I} > 0$, $V_L < 0$) are described, in which power flows from the electron tail into the poloidal field. At higher densities, $\overline{n}_e > 1 \times 10^{13}\,\mathrm{cm}^{-3}$, flat-topping has not been possible because of the limited rf power available. In Section 4.6, measurements of the plasma current decay rate during rf injection at densities $\overline{n}_e = 1.0 - 1.7 \times 10^{13}\,\mathrm{cm}^{-3}$ are described. In Section 4.7, the experimental data for all three types of discharges (flat-top, ramp-up, and decay) is compared to the Fisch/Karney theory of current drive in the presence of an electric field.

4.1 Demonstration of Quasi-Steady-State Current Drive

In order to demonstrate quasi-steady-state current drive by lower hybrid waves, the plasma current must be maintained at a constant level, with the loop voltage equal to zero, for a time comparable to the L/R response time of the plasma. The largest source of inductive voltage, the OH transformer, can be eliminated by open-circuiting the primary coil. However, other contributions to the inductive voltage may arise from changing currents in the equilibrium field coils, or from changes in the plasma current, in/out position (external inductance), or the current profile (internal inductance). In this section, we describe a typical 2.45 GHz rf-driven discharge and evaluate possible inductive contributions to the plasma current.

A typical discharge where the plasma current is "flat-topped" with 2.45 GHz rf power is shown in Fig. 4.1. With the OH primary open-circuited, 16 kA of plasma current is maintained for 23 ms with 60 kW of rf power. The inductive voltage, measured with loops outside the vacuum vessel, is nearly zero for the entire duration of the rf pulse. The line-averaged density is $\bar{n}_e \simeq 7 \times 10^{12}\,\mathrm{cm}^{-3}$, the toroidal magnetic field is $B_T \simeq 10\,\mathrm{kG}$, and the relative waveguide phasing is $\Delta\phi = +90^\circ$. In this discharge, the plasma current is started up and raised to its maximum level of 26 kA by rapidly decreasing the OH transformer flux. When the OH primary current reaches zero, open-circuiting prevents any further changes in the transformer flux.[27] Subsequent inductive loop voltage contributions from the OH system are therefore eliminated. With no ohmic drive, the plasma current decays with a characteristic L/R time of 15 ms, where L and R are the plasma inductance and resistance. This current decay induces a positive loop voltage of approximately 0.5 V. At $t = 14\,\mathrm{ms}$, when 60 kW of rf power is injected into the plasma, the current decay is arrested and the loop voltage drops to zero.

From the traces shown in Fig. 4.1, we can evaluate possible sources of inductive current drive contributions. For instance, a voltage may be induced by changes in the plasma current I or the plasma inductance L according to $V = -L\dot{I} - \dot{L}I/2$, where $L = L_{int} + L_{ext}$. The external inductance, given by $L_{ext} = \mu_0 R(\ln\frac{8R}{a} - 2)$, is a function of the major radius R, which can be determined from in/out plasma position measurements. The internal inductance, given by $L_{int} = \mu_0 R\ell_i/2$, requires the additional measurement of $\ell_i = \overline{B_\theta^2}/B_\theta^2(a)$, where B_θ is the poloidal

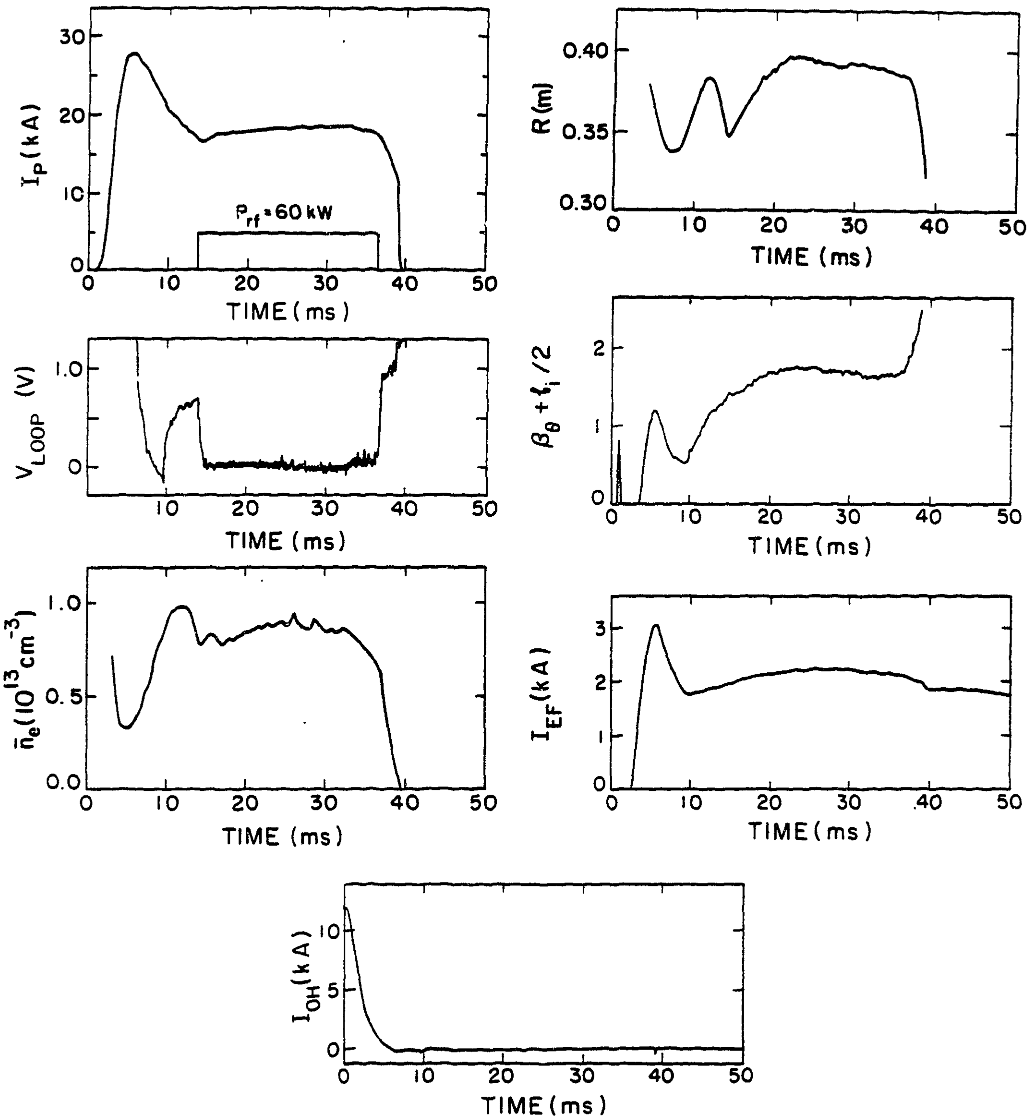

Fig. 4.1: Traces from a typical “flat-top”discharge where 16 kA of plasma current is maintained with 60 kW of 2.45 GHz rf power for a period of 23 ms. The OH primary was open-circuited at $t = 6$ ms. The relative waveguide phasing was $\Delta\phi = +90°$ and the average toroidal field value during the rf pulse was 10 kG.

field and the bar indicates an average over the plasma cross section. Under certain conditions, $\ell_i/2$ can be determined from a measurement of the equilibrium vertical field, using the Shafranov equation:[67]

$$B_V = \frac{\mu_0 I_p}{4\pi R}(\ln\frac{8R}{a} - \frac{3}{2} + \beta_\theta + \frac{\ell_i}{2}), \tag{4.1}$$

where $\beta_\theta = 2\mu_0\bar{p}/B_\theta^2(a)$ is the ratio of the average plasma pressure $\bar{p}$ to the poloidal field pressure at the plasma edge. Unfortunately, for the discharge of Fig. 4.1, β_θ is not negligible compared to $\ell_i/2$, and therefore the behavior of the internal inductance remains uncertain. It appears, however, that at least the external inductance remains nearly constant during the rf pulse, after an initial motion of the plasma towards the outside. This shift in plasma equilibrium which routinely occured upon rf injection will be interpreted in Section 4.4.3.

Finally, we must consider the induced voltage resulting from changes in the vertical field current, given by $V = M_v\dot{I}_v$ where $M_v \simeq 3.5\,\mu$H is the mutual inductance between the plasma and the vertical field coils and I_v is the vertical field current. Slight variations in the vertical field during the rf pulse are unavoidable because the current is supplied by capacitor banks, and there is no regulation of the current through feedback circuitry. The plasma equilibrium is controlled by adjusting the charging voltages and firing times of up to four vertical field capacitor banks. Because of the large in/out motion due to the rf, it was quite difficult to obtain flat-top discharges which were well centered for the duration of the rf pulse.

The various inductive current drive sources can be compared using the poloidal field power flow relation given in Chapter 2 by Equation (2.48). We can also include the power flow of the fast electron tail, given by

$$\frac{dE_t}{dt} = \alpha P_{rf} - P_d - P_{el} - P_\tau, \tag{4.2}$$

where E_t is the total tail energy, and αP_{rf} is the fraction of the injected rf power absorbed by electron Landau damping, of which P_{el} is converted to poloidal field energy, and P_d is dissipated due to collisions with the bulk, and $P_\tau = E_t/\tau_t$, where τ_t is the tail confinement time. Combining Eqns. (2.48) and (2.49) with Eqn. (4.2), and assuming that $dE_t/dt = 0$, we obtain:

$$P_d + P_r + \frac{V^2}{R_{sp}} + \frac{d}{dt}\left(\frac{1}{2}LI^2\right) = I(M_{OH}\dot{I}_{OH} + M_v\dot{I}_v) + \alpha P_{rf}, \tag{4.3}$$

where V is given by Eqn. (2.48). Note that in the steady state, in the absence of radial tail confinement losses, $\alpha P_{rf} = P_d \propto \bar{n} I_{rf} R \langle n_{\parallel}^2 \rangle$.[3] The power flow between the fast electron tail, the poloidal field, and the bulk plasma is illustrated in Fig. 4.2.

The temporal behavior of the inductive terms in Eqn. (4.3) is plotted in Fig. 4.3 for the discharge of Fig. 4.1. The rate of change of the poloidal field energy, $\dot{W} = \frac{d}{dt}(\frac{1}{2}LI^2)$, was obtained by assuming a constant internal inductance $\ell_i/2 = 0.85$. The $\dot{W}$ trace shows an initial positive transient at the beginning of the rf pulse due to the initial increase in the plasma current and the outward motion of the plasma column (increasing L). After $t = 21\,\mathrm{ms}$, $\dot{W}$ remains small. The average over the entire rf pulse is $\dot{W} \simeq +1.2\,\mathrm{kW}$. The external power flow from the vertical field, given by $P_{ext} = M_v\dot{I}_v$ is slightly positive at the beginning of the rf pulse ($P_{ext} \simeq +3\,\mathrm{kW}$) and slightly negative at the end of the rf pulse ($P_{ext} \simeq -3\,\mathrm{kW}$). The average over the entire rf pulse is $P_{ext} = +0.54\,\mathrm{kW}$. The net inductive power flow averaged over the rf pulse is $\dot{W} - P_{ext} = +0.63\,\mathrm{kW}$ indicating slight ramp-up. Finally, the calculated loop voltage in the plasma, while slightly negative during the first few milleseconds of rf injection, averages to $V = -0.040\,\mathrm{V}$ over the rf pulse. From these estimates we determine that the contributions from the inductive terms in Eqn. (4.3) are small compared to the injected rf power level of 60 kW. Assuming that a significant fraction of the rf power is absorbed, and that tail losses are relatively small, we conclude that after an initial transient period of approximately 5 ms, the plasma current is fully driven by rf waves under steady state conditions.

The "flat-top" pulse length in Fig. 4.1 is limited by the toroidal field and vertical field capacitor bank circuits. The toroidal field bank is fired and crowbarred prior to the plasma discharge start-up. Because of this, the toroidal field decays by more than 20% for rf pulse lengths exceeding 20 ms in duration ($\tau_{L/R} \sim 90\,\mathrm{ms}$). Eventually, this adversely affects the current drive efficiency by worsening the wave

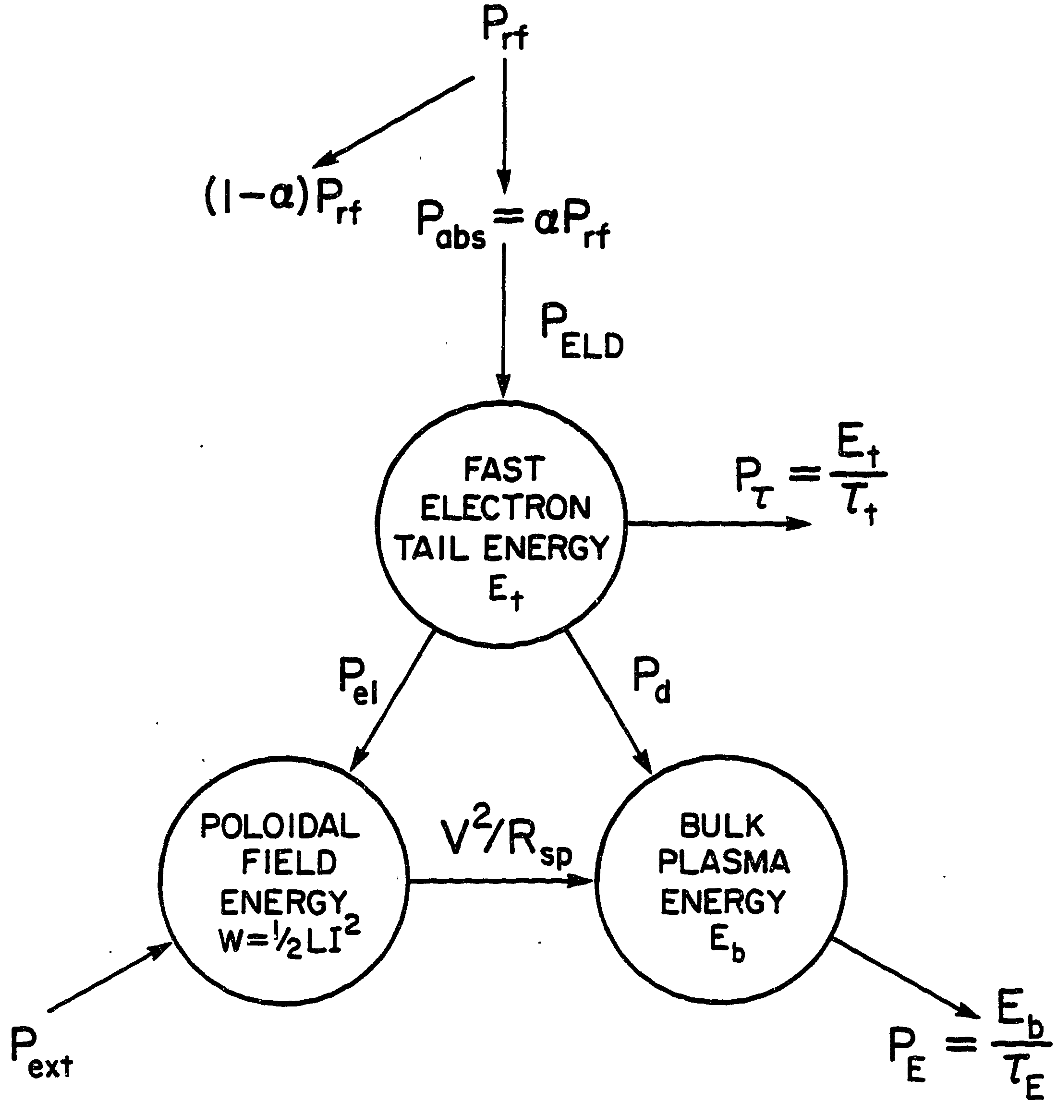

Fig. 4.2: Diagram showing the power flow during lower hybrid current drive between the fast electron tail, the poloidal magnetic field, and the bulk plasma.

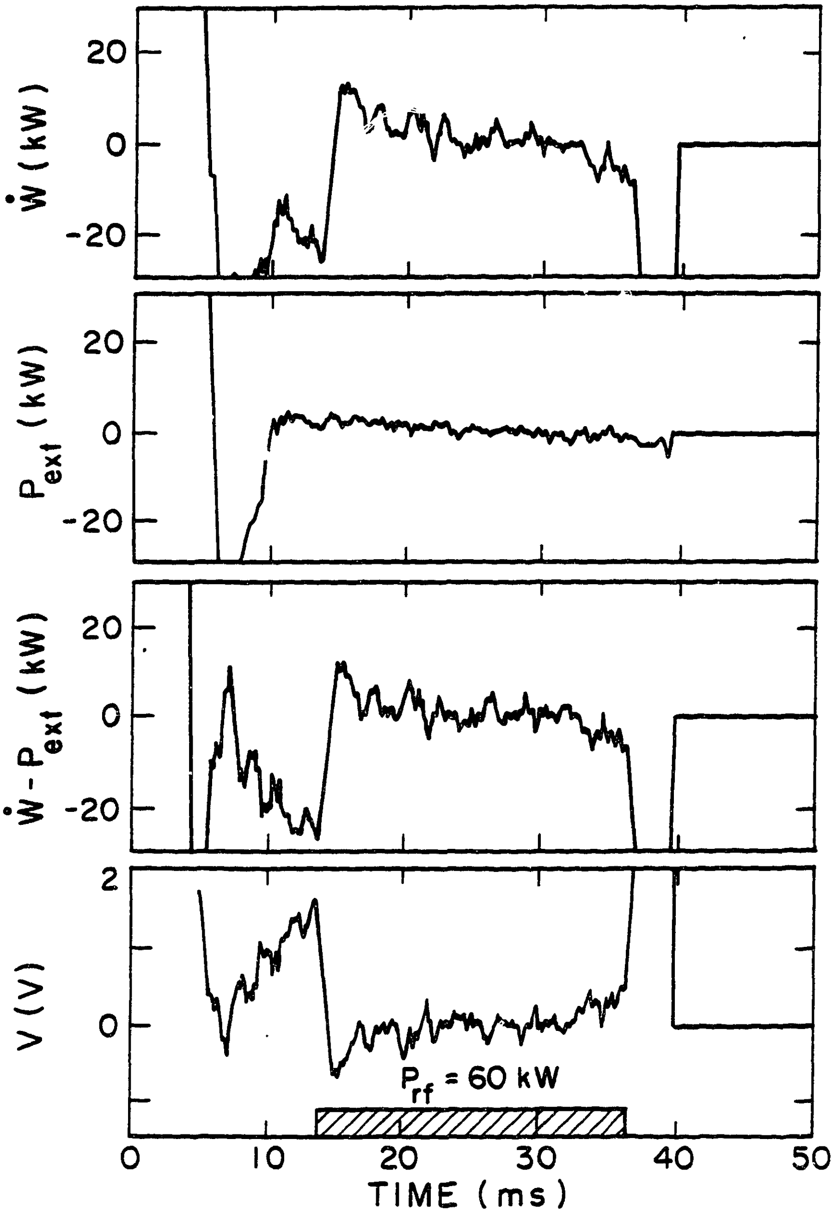

Fig. 4.3: Temporal evolution of the inductive contributions during the flat-top discharge of Fig. 4.1

accessibility. (The dependence of the current drive efficiency on B_T is discussed in Section 4.3). The decay of the vertical field also prevents longer flat-top pulse lengths because of the negative loop voltage induced and because of the eventual loss of plasma equilibrium control. Despite these limitations, the 23 ms rf pulse length in Fig. 4.1 exceeds the ohmic L/R time by 50%, and is estimated to be about one-half of the L/R time of the rf-heated plasma according to the Fisch conductivity[59] given by Eqn. (2.44).

4.2 Current Drive Above the 800 MHz Density Limit

The highest density 2.45 GHz flat-top discharge is shown in Fig. 4.4.[29] In this discharge, 17 kA of plasma current was maintained for 15 ms with 78 kW of rf power. The line-averaged density, $\bar{n}_e = 1.0 \times 10^{13}\,\mathrm{cm}^{-3}$, is 70% above the 800 MHz density limit.

A 4 mm interferometer density profile measurement made on a shot to shot basis during similar discharges indicates that the density profile is peaked on axis with $n_e(0) \geq 1.5\bar{n}_e$. Hence, for the discharge in Fig. 4.4, $n_e(0) \geq 1.5 \times 10^{13}\,\mathrm{cm}^{-3}$. Since the toroidal field decays during the rf pulse from an initial value of 11.0 kG to a final value of 9.2 kG, this implies that the central value of $\omega_{pe}^2(0)/\omega_{ce}^2(0)$ increases from 1.2 to 1.8 during the rf pulse. These are record values for a fully rf-driven discharge.

With $\omega_{pe}^2/\omega_{ce}^2 > 1$, the penetration of low-$N_\parallel$ waves to the plasma core is expected to be quite poor. The accessibility condition from Chapter 2 is:

$$N_\parallel > N_{\parallel,acc} = \frac{\omega_{pe}}{\omega_{ce}} + \sqrt{1 + \frac{\omega_{pe}^2}{\omega_{ce}^2}\left(1 - \frac{\omega_{ce}\omega_{ci}}{\omega^2}\right)}. \tag{4.4}$$

If we require the waves to penetrate half way in to the plasma center ($r/a = 0.5, n_e(r) \sim \bar{n}_e$), then on the high toroidal field side of the plasma, $N_{\parallel,acc}$ increases from 1.9 to 2.2, while on the low field side, $N_{\parallel,acc}$ increases from 2.4 to 2.9. For the Brambilla spectrum shown in Fig. 3.5, this implies that only about 30 – 50% of the

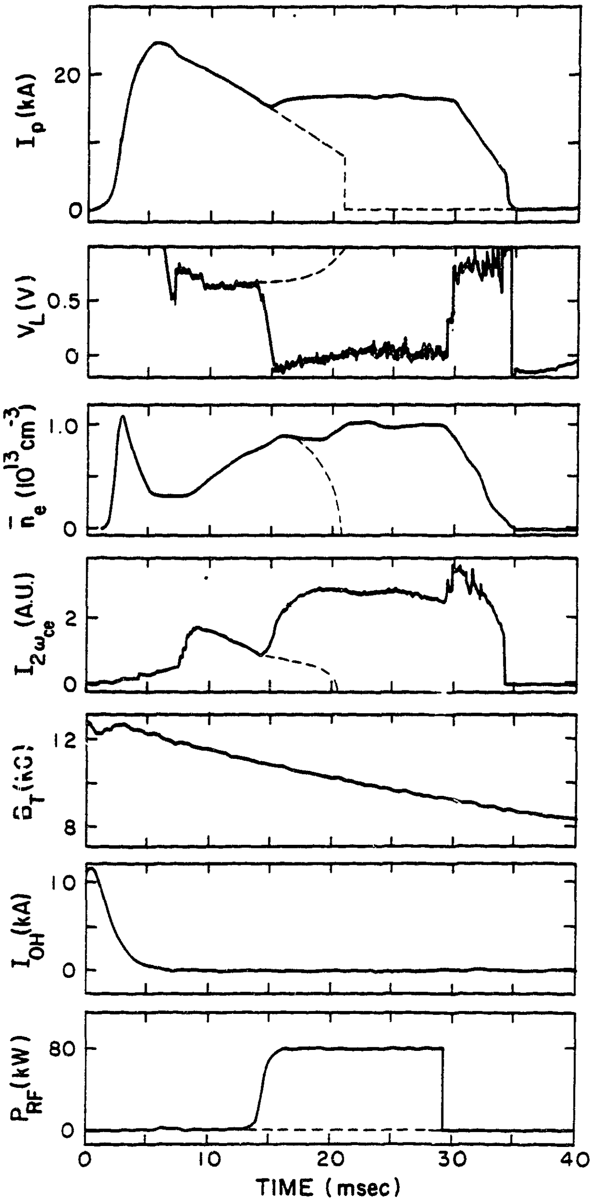

Fig. 4.4: The highest density 2.45 GHz flat-top discharge achieved to date, with $\overline{n}_e = 1.0 \times 10^{13}\,\mathrm{cm}^{-3}$.

wave power launched in the positive direction is expected to reach the central region of the plasma near the end of the rf pulse. The fraction of accessible wave power may be improved somewhat when toroidal wave propagation effects are included because the $N_{\|}$ values may be upshifted from the launched values.

From the 2.45 GHz discharge of Fig. 4.4, we can conclude that the 800 MHz density limit is not due to the inaccessibility of low-$N_{\|}$ waves to the plasma center. It is evident from Eq. (4.3) that accessibility should be worse for higher frequency waves, at higher densities, and at lower toroidal fields (higher values of $\omega_{pe}^2/\omega_{ce}^2$). The launched $N_{\|}$ spectra of the 4-waveguide 2.45 GHz coupler and the 800 MHz 4-waveguide side-launch coupler are nearly identical. The toroidal field strength was approximately the same in both experiments. Therefore, accessibility is expected to be worse for 2.45 GHz discharges than for the lower density 800 MHz discharges ($\bar{n}_e \leq 6\times10^{12}\,\mathrm{cm}^{-3}$). In spite of this, the current drive density limit has been raised substantially by increasing the frequency of the rf source from 800 MHz to 2.45 GHz. Flat-topping the plasma current at even higher densities ($\bar{n}_e > 1\times10^{13}\,\mathrm{cm}^{-3}$) should be possible if more rf power were available. Evidence of 2.45 GHz current drive at densities up to and above $\bar{n}_e = 2\times10^{13}\,\mathrm{cm}^{-3}$ will be presented in Section 4.6 and in the next chapter.

4.3 Current Drive Efficiency

The 2.45 GHz current drive efficiency, given by $\tilde{\eta} = \bar{n}IR/P$, has been evaluated for flat-top discharges with the following parameters: $I_p = 14 - 24\,\mathrm{kA}$, $\bar{n}_e = (0.2 - 1.0)\times10^{13}\,\mathrm{cm}^{-3}$, $B_T = 9 - 14\,\mathrm{kG}$, $P_{rf} = 31 - 95\,\mathrm{kW}$, $\Delta\phi = +90^\circ$. In Fig. 4.5(a), the ratio of the current to the net injected rf power, I/P_{rf}, is plotted versus the line-averaged density $\bar{n}$, while in Fig. 4.5(b), $\bar{n}I$ versus P_{rf} is shown.[29] Both plots are consistent with an efficiency scaling of $\tilde{\eta} = \bar{n}(10^{20}\,\mathrm{m}^{-3})I(\mathrm{kA})R(\mathrm{m})/P_{rf}(\mathrm{kW}) = 0.0072$. For comparison, the 800 MHz flat-top current drive efficiency measured at $\bar{n} = 3\times10^{12}\,\mathrm{cm}^{-3}$ is $\tilde{\eta} = 0.01$. The slightly higher current drive efficiency for the lower rf frequency may be due to more favorable wave accessibility.

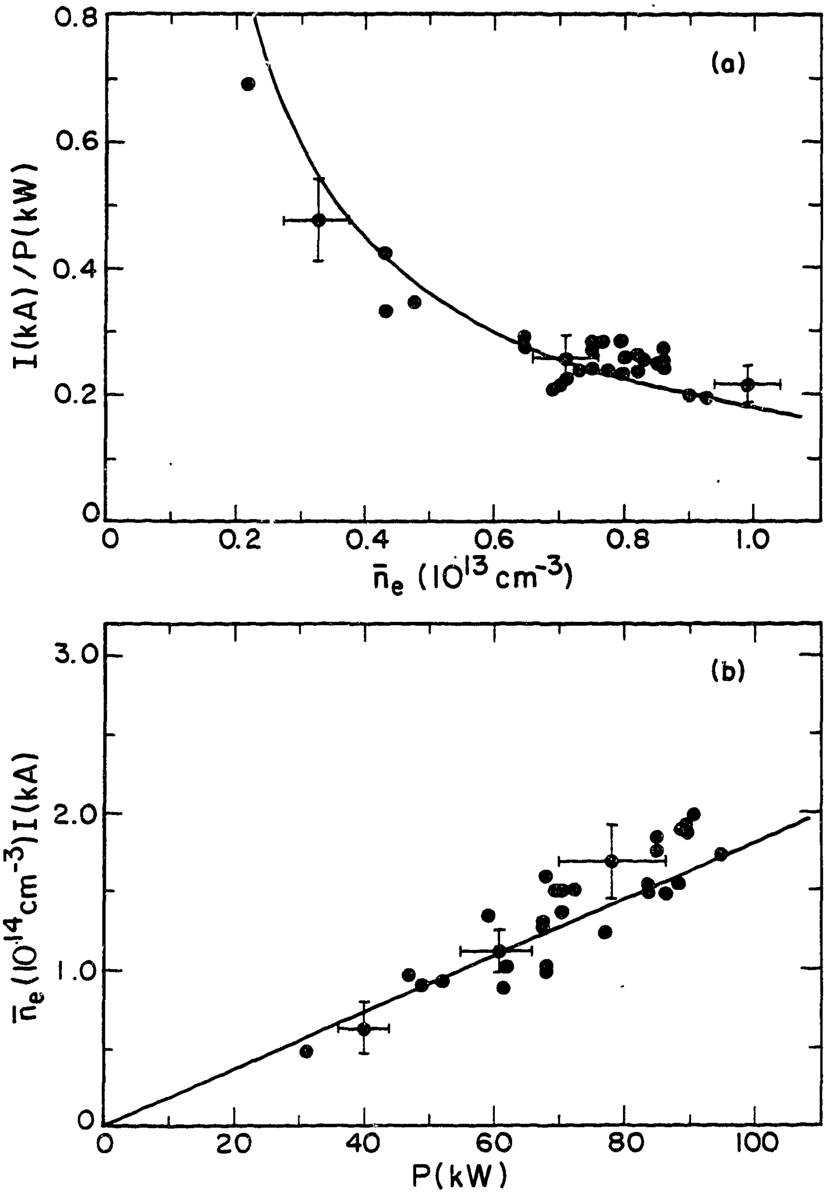

Fig. 4.5: Flat-top current drive plots for $\Delta\phi = +90°$, $B_t = 1.0 - 1.2\,\mathrm{T}$: (a) I/P_{rf} vs. $\bar{n}_e$, (b) $\bar{n}_e I$ vs. P_{rf}. Solid curves, $\tilde{\eta} = 0.0072(10^{20}\,\mathrm{m}^{-3}) \cdot \mathrm{kA} \cdot \mathrm{m/kW}$.

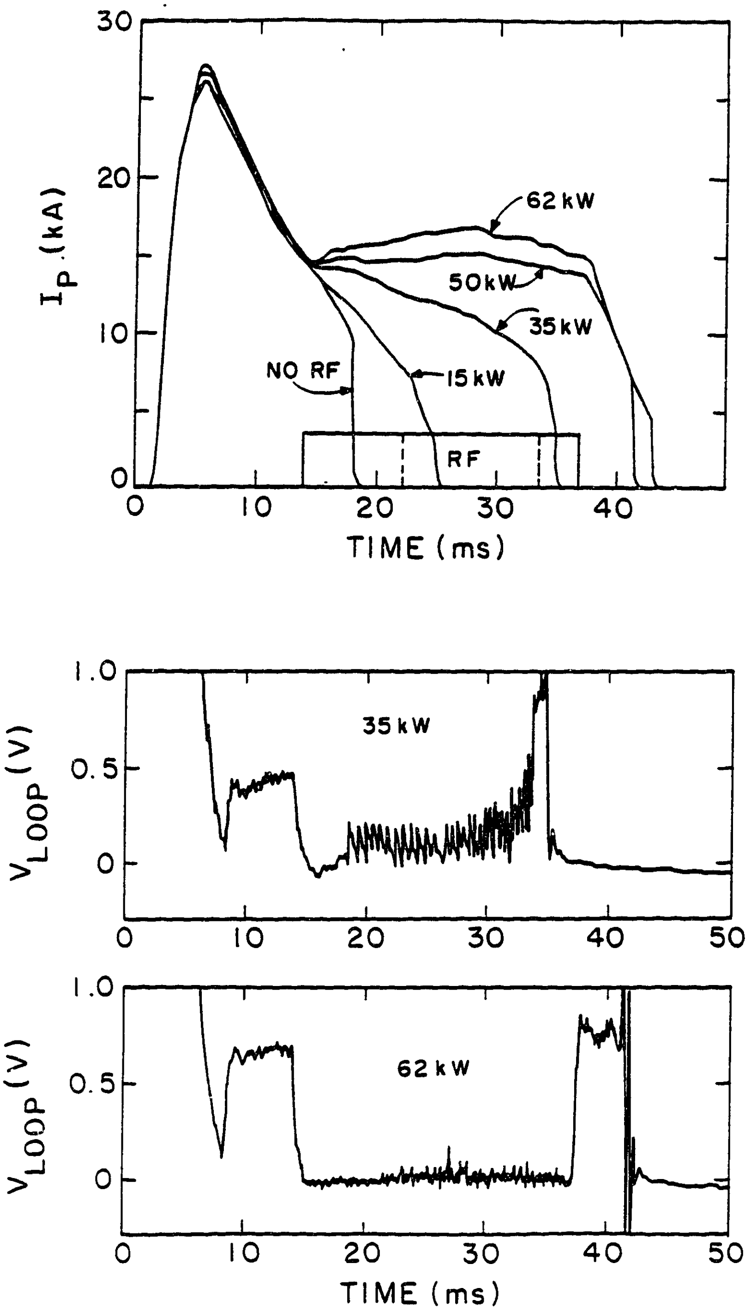

Fig. 4.6: Upper: plasma current traces for different levels of injected rf power. Lower: loop voltage traces for $P_{rf} = 35\,\mathrm{kW},\ 62\,\mathrm{kW}$.

The sensitivity of the 2.45 GHz flat-top efficiency measurements to variations in the rf power level is shown in Fig. 4.6. All of these discharges were obtained at a density of $\bar{n}_e \simeq 7 \times 10^{12}\,\mathrm{cm}^{-3}$, with $\Delta\phi = +90^\circ$. At the lowest rf power levels, the plasma current decays and the loop voltage remains positive. The repetitive spikes appearing on the loop voltage are a characteristic signature of the runaway-driven Parail-Pogutse instability[68] observed previously in low density ohmic plasmas and during lower hybrid current drive in the presence of an electric field.[41,65] In this case, the electric field is induced by the plasma current decay. Note that when the instability turns on, the rate of plasma current decay increases. This observation will be discussed further in Subsection 4.4.2. By raising the rf power to a sufficiently high level, the plasma current can be flat-topped, and the instability eliminated. Raising the rf power level further results in an initial period of current ramp-up. For the efficiency data of Fig. 4.5, the rf power level was adjusted so that the plasma current was maintained nearly constant for the entire duration of the rf pulse ($\tau_{rf} > 15\,\mathrm{ms}$), with the loop voltage equal to zero and free of instability spikes.

The dependence of current drive on waveguide phasing is depicted in Fig. 4.7. In these discharges the density was $\bar{n}_e \simeq 7 \times 10^{12}\,\mathrm{cm}^{-3}$ and the rf power level was in the range $P_{rf} = 60 - 70\,\mathrm{kW}$. The most efficient flat-top current drive phasing is $\Delta\phi = +90^\circ$. Flat-topping is also possible, though 5 - 10% less efficient, with $+60^\circ$ and $+120^\circ$ phasings. With other phases (including -90°) substantially less rf current is driven, as expected, and to date flat-topping of the toroidal plasma current has not been possible.

An accurate determination of the current drive efficiency scaling with toroidal magnetic field B_T has not been possible in these experiments because of the sizeable decay ($\sim 20\%$) of the toroidal field during long rf pulses. It appears that the current drive efficiency is a relatively weak function of B_T within the range where long-pulse flat-topped discharges have been produced. A toroidal field scan was performed at $\bar{n}_e \simeq 1.1 \times 10^{13}\,\mathrm{cm}^{-3}$, with $I_p = 26\,\mathrm{kA}$ at the time of rf injection. The plasma current traces for some of these discharges are shown in Fig. 4.8. The traces are

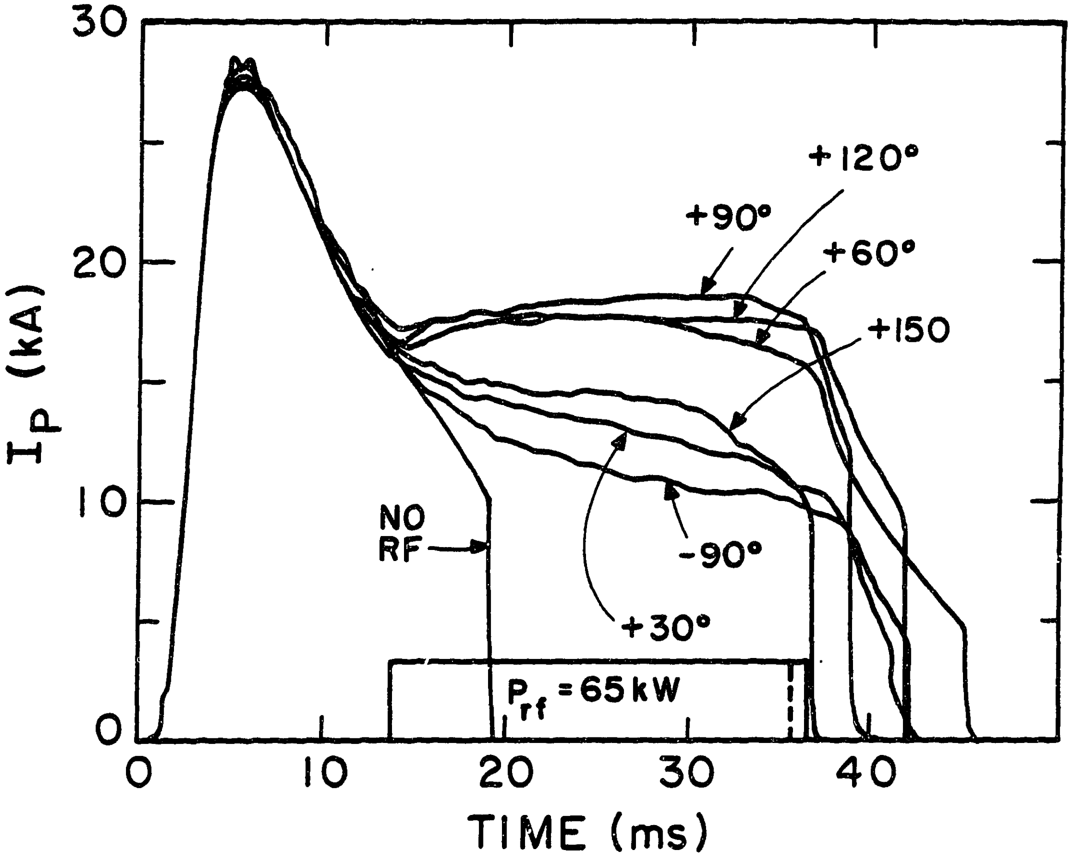

Fig. 4.7: Plasma current traces for various waveguide phasings at $\bar{n}_e \simeq 7 \times 10^{12}\,\text{cm}^{-3}$.

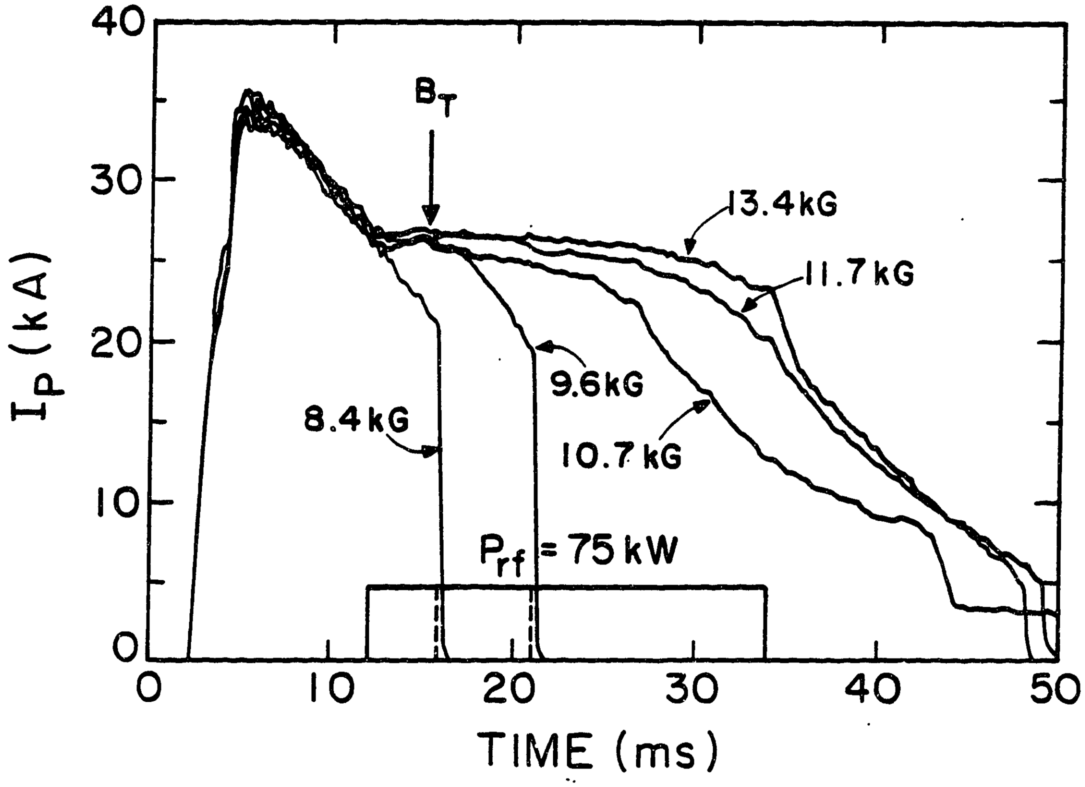

Fig. 4.8: Plasma current traces from a toroidal magnetic field scan with $\overline{n}_e \simeq 1.1 \times 10^{13}\,\mathrm{cm}^{-3}$, $\Delta\phi = +90°$. The curve labels refer to the toroidal field level at $t = 16\,\mathrm{ms}$.

labelled with the toroidal field value at the time of rf injection. The rf power level of 75 kW is insufficient to flat-top the current, even at the highest magnetic field of 13.4 kG. Lowering the toroidal field to 11.7 kG has a relatively small effect on the plasma current, at least for the first 15 ms of rf injection. Lowering the toroidal field to 10.7 kG has a more appreciable effect on the current earlier in the rf pulse (8% less current after 10 ms of rf injection). Eventually, however, the Parail-Pogutse instability turns on (at $t = 26\,\mathrm{ms}$), causing a more pronounced decrease in the current. At the lowest toroidal field, 8.4 kG, the rf produces a negligible change in the plasma current. To date, flat-topped discharges have only been produced with initial values of the toroidal field in the range $11\,\mathrm{kG} \leq B_T \leq 13.6\,\mathrm{kG}$, representing a variation of less than 20%. Higher fields are not available. This range of toroidal fields is insufficient to establish a steady-state efficiency scaling, given that the variation of the field during the rf pulse is of comparable size.

4.4 Nonthermal Electron Effects

In the previous sections of this chapter, the gross features of flat-top current drive discharges have been described. In this section, we report on some of the more detailed observations of non-thermal effects associated with the generation of an energetic electron tail. The most direct evidence for a superthermal electron population comes from the measurements of the plasma hard x-ray bremsstrahlung radiation described in Chapter 6. Here we describe three additional phenomena which are associated with the presence of a fast electron tail: 1) nonthermal electron cyclotron emission, 2) instability behavior, and 3) equilibrium shifts due to nonthermal plasma pressure.

4.4.1 Non-Thermal Electron Cyclotron Emission

Measurements of the extraordinary mode (X-mode) polarized electron cyclotron emission were made during 2.45 GHz current drive experiments. Radiation at the frequency of 71 GHz was detected using a microwave horn antenna located inside the tokamak vacuum vessel on the low field side (see Ref. 41 for details about the antenna and receiver circuitry). The 71 GHz frequency corresponds to the second harmonic ($2\omega_{ce}$) emission from the plasma center at a toroidal field of 12.5 kG. However, higher harmonics may also contribute to the cyclotron emission because of relativistic effects ($\omega = n\omega_{ce}/\gamma$) and because the toroidal field of Versator decays with time.

Previously, non-thermal cyclotron emission had been observed from Versator during low density ohmic discharges and during OH-assisted 800 MHz current drive experiments ($\bar{n}_e < 6 \times 10^{12}\,\mathrm{cm}^{-3}$).[41,65] Periodic step-like increases in the cyclotron emission were accompanied by bursts of rf emission, hard x-rays, and spikes on the loop voltage. This behavior has been attributed to a runaway-driven anisotropy instability described by Parail and Pogutse.[69] Such behavior is also observed in the 2.45 GHz experiments and will be discussed in the next subsection.

The main interest here is in the quasi-steady nonthermal cyclotron emission observed during 2.45 GHz flat-top discharges when the toroidal electric field is nearly equal to zero and no bursting instability behavior is evident (see Figs. 4.2 and 4.7). Under these conditions, the cyclotron emission level rises relatively slowly ($\tau \sim 2\,\mathrm{ms}$) and then remains fairly constant until the termination of the rf pulse. The quasi-steady level of the cyclotron emission is nearly constant over the entire range of the 2.45 GHz flat-top data, and it is more than an order of magnitude above bulk thermal levels. The radiation temperature of the emission is on the order of a few keV, a level comparable to that observed during Parail-Pogutse instability activity. Qualitatively these measurements indicate that the rf produces an energetic tail of superthermal electrons with a perpendicular temperature many times higher than that of the bulk Maxwellian distribution. This observation is consistent with the predictions of the 2-d numerical studies of lower hybrid current drive[55,56] discussed in Chapter 2. Note that the rise time of the emission ($\tau \sim 2\,\mathrm{ms}$) corresponds to the pitch-angle scattering time of a current carrying tail electron with energy $\varepsilon \sim 25\,\mathrm{keV}$.

4.4.2 Anomolous Doppler Instability

In low density ohmically heated plasmas ($\overline{n}_e < 6 \times 10^{12}\,\mathrm{cm}^{-3}$), highly anisotropic electron distribution functions can develop due to the acceleration of runaway electrons in the direction of the magnetic field by the dc ohmic electric field. Such plasmas in Versator exhibit unstable behavior, with relaxation oscillations on the loop voltage, step-like increases in non-thermal X-mode polarized cyclotron emission and bursts of hard x-rays and rf emission. Similar characteristics have been observed in numerous other tokamaks and are explained by theories which invoke an instability of plasma waves due to the anomolous doppler effect.[8,69,70] The anomolous doppler instability is also observed during lower hybrid current drive experiments when inductive electric fields are present during rf injection. In the present 2.45 GHz current drive experiments, the instability is observed during rf injection if the rf power is insufficient to flat-top the current (see Fig. 4.6), or in the ohmic phase of the discharge prior to the rf injection if the density is sufficiently low (see Fig. 4.4), or immediately after the termination of the rf pulse (see Fig. 4.11 at $t = 27\,\mathrm{ms}$). In all of these cases, a toroidal electric field is present which may accelerate electrons to runaway velocities. The instability is most prevalent at low densities where runaway electrons are most easily produced. When instability occurs during rf injection, it tends to inhibit flat-topping. This partially accounts for the sparceness of low density efficiency data in Fig. 4.5.

Typical traces are shown in Fig. 4.9 for a 2.45 GHz rf-driven discharge at $\overline{n}_e = 5 \times 10^{12}\,\mathrm{cm}^{-3}$. The periodic spikes on the loop voltage, the X-mode polarized cyclotron emission at 71 GHz, and the limiter hard x-ray signals are well correlated with each other. In general, the tail instability occurs more readily when the discharge is positioned slightly to the inside. Fig. 4.10 shows a discharge similar to Fig. 4.9 except that it is positioned more towards the outside. In this case the tail mode is stabilized for a short period in the middle of the rf pulse, resulting in a higher plasma current. From an analysis of the $\beta_\theta + \ell_i/2$ signal, the outward plasma motion during the quiescent period is due almost entirely to the increase of the plasma current. The comparison of these discharges demonstrates that there

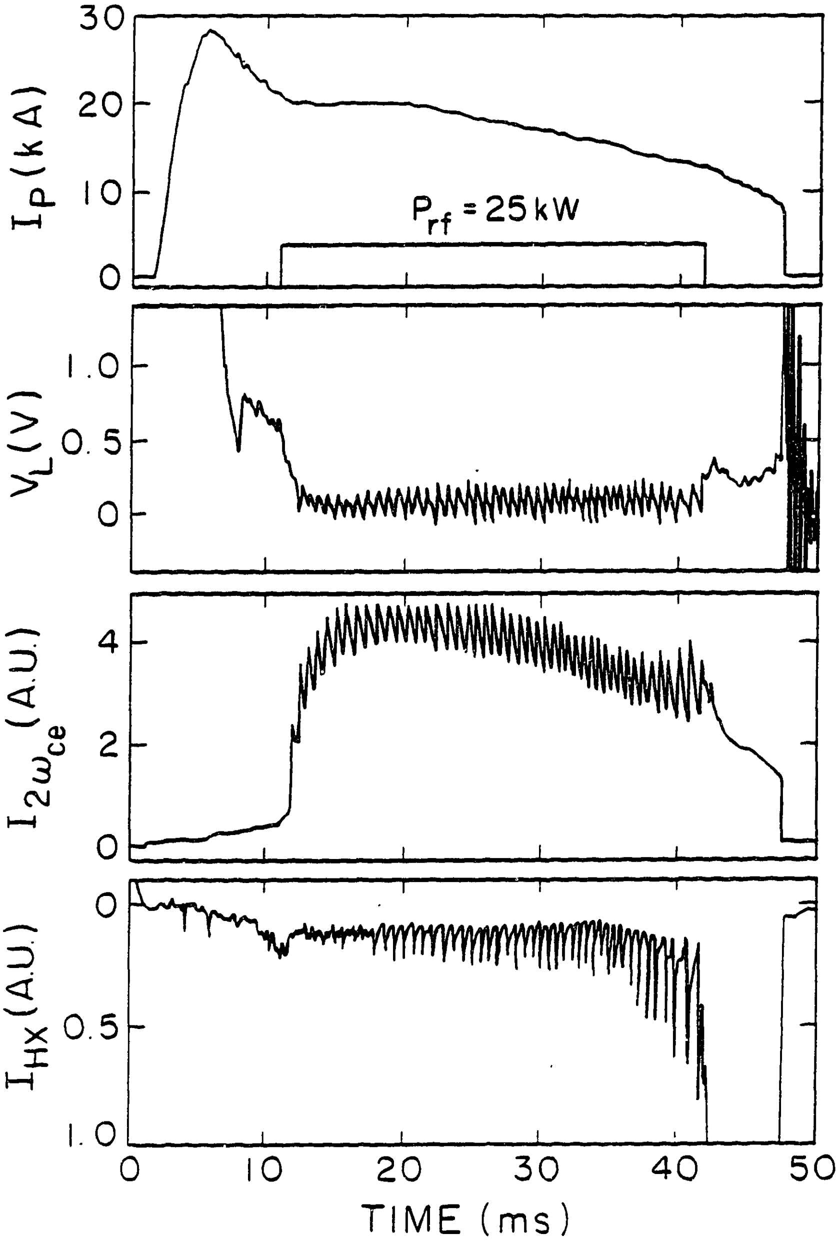

Fig. 4.9: Typical traces from a 2.45 GHz rf-driven discharge at $\overline{n}_e = 5 \times 10^{12}\,\text{cm}^{-3}$ showing evidence of Parail-Pogutse instability activity. Note the strong correlation between the periodic spikes on the loop voltage, the $2\omega_{ce}$, and the limiter hard x-ray signals.

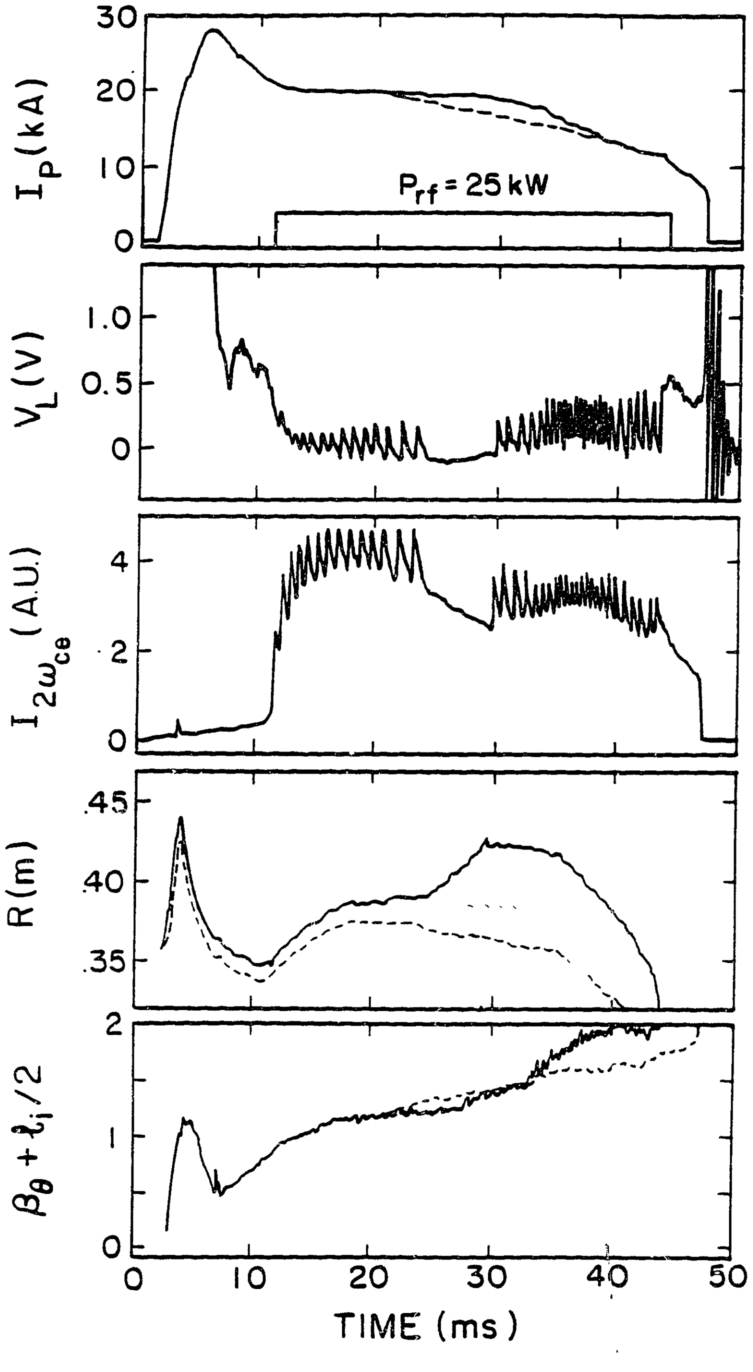

Fig. 4.10: Comparison between an rf-driven discharge where the Parail-Pogutse instability is temporarily stabilized (solid traces) with the discharge shown in Fig. 4.9 (dashed traces).

is significant rf current loss when the anomolous doppler instability is active.

In the Parail-Pogutse theoretical model,[69] instability occurs when runaway electrons are accelerated by a longitudinal electric field, creating a highly anisotropic distribution function with $T_{\|} \gg T_{\perp}$. Electron plasma waves $\omega \simeq \omega_{pe} k_{\|}/k$ are driven unstable when the accelerating runaways reach sufficiently high velocities so that the resonance condition $v_{\|} = (\omega + \omega_{ce})/k_{\|}$ is satisfied. The growth of waves at the "anomolous doppler resonance" is balanced by damping at the Cherenkov resonance, $v_{\|} = \omega/k_{\|}$. When the tail extends to sufficiently high velocities $[v_b > 3(\omega_{ce}/\omega_{pe})^{3/2} v_{cr}]$, instability occurs because the wave damping takes place on the flattened portion of the distribution function beyond the runaway critical velocity, $v_{cr} = eE_0/m\nu(v_{cr})$. During the first stage of the instability, electrons satisfying the anomolous doppler resonance condition are pitch angle scattered into the perpendicular direction. This non-collisional scattering process acts to isotropize the electron distribution function.[69] It is believed that the increase in transverse energy $(T_{\perp})$ during the instability is responsible for the sudden nonthermal increases observed in the X-mode polarized cyclotron emission. Bursts of plasma hard x-ray bremsstrahlung emission perpendicular to the magnetic field are also observed, as will be described in Chapter 6.

4.4.3 Equilibrium Shift of the Plasma

In 2.45 GHz flat-top discharges, the radial equilibrium position of the plasma shifts dramatically to the outside upon the injection of rf power. In the case shown in Fig. 4.1, the plasma moves 5 cm towards the outside even though flat-topping the vertical field current before the rf injection causes the plasma to move initially towards the inside. At lower densities, the effects are even more severe, with outward shifts of $8 - 10$ cm routinely observed. In this case, an auxiliary vertical field bank with a fast rise time must be fired along with the rf system to maintain equilibrium control. However, this procedure interferes with flat-topping because of the large transient positive loop voltage which is induced. These difficulties further account for the sparsity of low density current drive efficiency data in Fig. 4.5.

From an analysis of the Shafranov equilibrium equation (4.1), the outward motion must be due to an increase in $\beta_\theta + \ell_i/2$. In Fig. 4.1, $\beta_\theta + \ell_i/2$ increases from 1.2 just before the rf injection to 1.8 during injection. The initial value of $\beta_\theta + \ell_i/2$ may be an overestimate since there is inward plasma motion. To account for the equilibrium shift in this discharge, $\beta_\theta + \ell_i/2$ must increase by at least 0.6 when the rf is fired.

This change in $\beta_\theta + \ell_i/2$ could be due to a narrowing of the current profile (ℓ_i), or to an increase in the average plasma pressure (β_θ), or to a combination of both. Preliminary hard x-ray profile measurements of the fast electron tail during flat-top discharges indicate that the current profile does not narrow (see Chapter 6). This suggests that the equilibrium shift is due instead to an increase of β_θ.

A general expression for β_θ, appropriate for a plasma with a high energy, anisotropic tail is given by:[71]

$$\beta_\theta = \frac{\frac{1}{2}\overline{P}_{\|} + \frac{1}{4}\overline{P}_{\perp}}{B_\theta^2(a)/2\mu_0}, \tag{4.5}$$

where $P_{\|} = nm\langle\gamma v_{\|}^2\rangle$ and $P_{\perp} = nm\langle\gamma v_{\perp}^2\rangle$. The bars in the above expression indicate an average over the plasma cross section, while the angle brackets indicate an average over the velocity distribution function. Considering the contribution from the Maxwellian bulk plasma, given by $\beta_\theta = (\overline{n_e T_e} + \overline{n_i T_i})/(B_\theta^2(a)/2\mu_0)$, substantial changes in the bulk density and bulk temperature or their profiles are needed to account for observed equilibrium shifts. In the discharge of Fig. 4.1, however, the line-averaged density is approximately the same before and during the rf injection. Therefore, only large bulk temperature increases ($\sim$ 300 eV or more) or flattening of the temperature profile could explain the in/out motion. In fact, Thomson scattering measurements have shown that the bulk electron temperature drops substantially during quasi-steady-state discharges. Typically, at $\overline{n}_e \sim 7 \times 10^{12}\,\mathrm{cm}^{-3}$, the temperature drops from 300 eV just before the rf pulse to 100 eV during the rf pulse with a decay time of approximately 5 ms. These measurements rule out increases in the bulk plasma pressure as the cause of the outward plasma motion.

The high energy bremsstrahlung emission measured during quasi-steady-state current drive has been modelled using a simple distribution function $f(p_{||}, p_{\perp})$ to describe the non-thermal electron tail component (see Chapter 6). This model distribution consists of a flat plateau in the resonant region of momentum space $0 \leq p_{||} \leq p_2$, and circular pitch-angle scattering contours outside the resonant region. Given this model, two free parameters characterize the distribution function: 1) $T_{\perp}$, the perpendicular tail temperature, and 2) $\varepsilon_2(p_2)$, the parallel kinetic energy corresponding to the upper limit of the plateau at p_2. Two representative cases have been fit to the experimental x-ray spectra measured during discharges similar to Fig. 4.1. For Model I, $T_{\perp} = 35\,\text{keV}$ and $\varepsilon_2 = 60\,\text{keV}$, while for Model II, $T_{\perp} = 10\,\text{keV}$ and $\varepsilon_2 = 160\,\text{keV}$. The corresponding values for β_θ calculated using Eqn. (4.5) are 0.5 for Model I, and 1.1 for Model II. We conclude that the outward motion of the plasma observed during 2.45 GHz current drive is consistent with the additional pressure generated by the rf tail.

4.5 Current Ramp-up

In addition to sustaining the plasma current at a constant level with 2.45 GHz rf, it has also been possible to ramp up the plasma current, with negative loop voltage, at densities $\overline{n}_e \leq 7 \times 10^{12}\,\text{cm}^{-3}$. Ramp-up rates as high as 400 kA/s, for periods up to 15 ms, have been achieved at a density of $\overline{n}_e = 3 \times 10^{12}\,\text{cm}^{-3}$ with an rf power level of 44 kW. For this case, the efficiency of converting rf energy to poloidal field energy is given by $\epsilon = (\dot{W} - P_{ext})/P_{rf} = 0.14 \pm 0.04$, where $W = \frac{1}{2}LI^2$ and $L = L_{int} + L_{ext}$. The large uncertainty in the ramp-up efficiency is due primarily to uncertainties in $L_{int} = \mu_0 R(\ell_i/2)$. For the efficiency estimate above, it was assumed that $\ell_i/2 = 0.85 \pm 0.2$.

At the higher densities, the ramp-up efficiencies are reduced, partly because of the limited rf power available. A typical ramp-up discharge at a density of $\overline{n}_e = 7 \times 10^{12}\,\text{cm}^{-3}$ is shown in Fig. 4.11. In this case the current ramp-up rate $\dot{I} = 190\,\text{kA/s}$ was sustained for a period of approximately 15 ms with 76 kW of rf power. In order to illustrate the inductive power flow for this discharge, the temporal behavior of the various inductive terms in Eqn. (4.3) have been plotted in

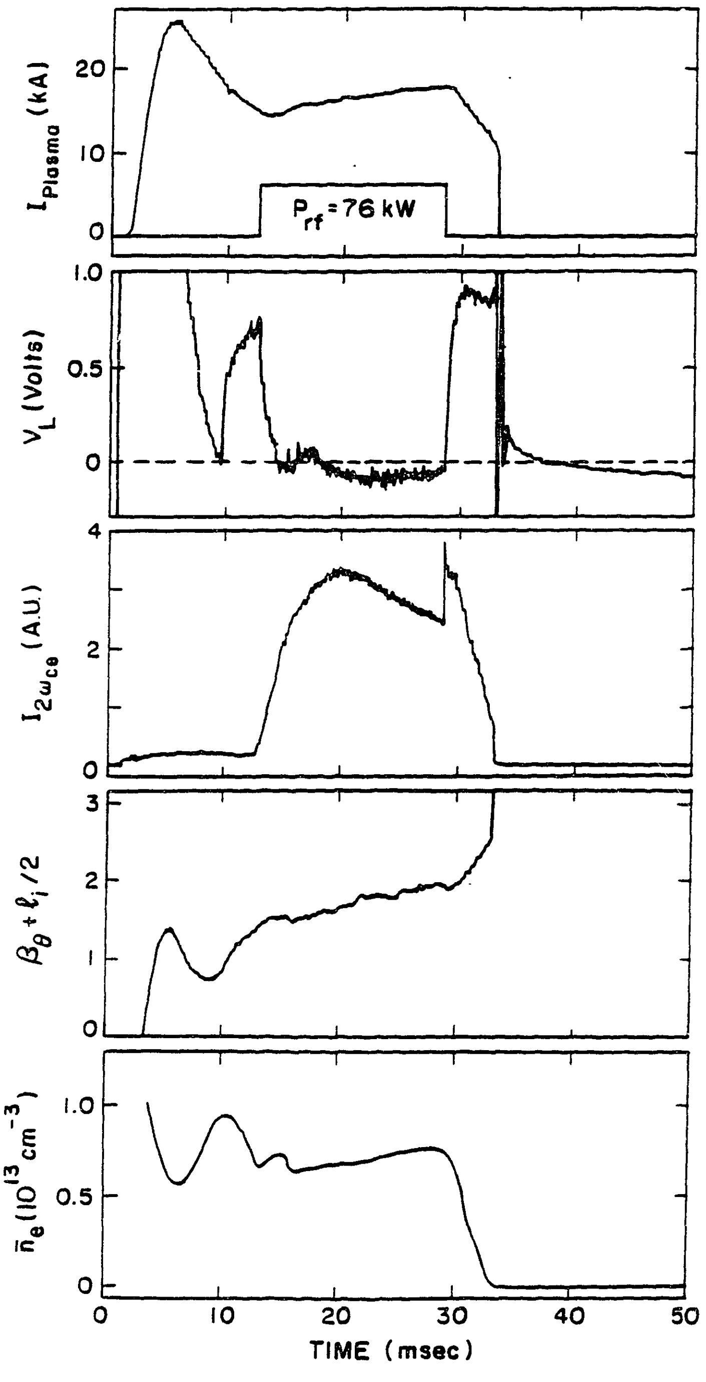

Fig. 4.11: 2.45 GHz ramp-up discharge at a density of $\overline{n}_e \simeq 7 \times 10^{12}\,\mathrm{cm}^{-3}$. The current ramp-up rate is $\dot{I} \simeq 190\,\mathrm{kA/s}$ and the ramp-up efficiency is $\epsilon = (\dot{W} - P_{ext})/P_{rf} \simeq 0.05$.

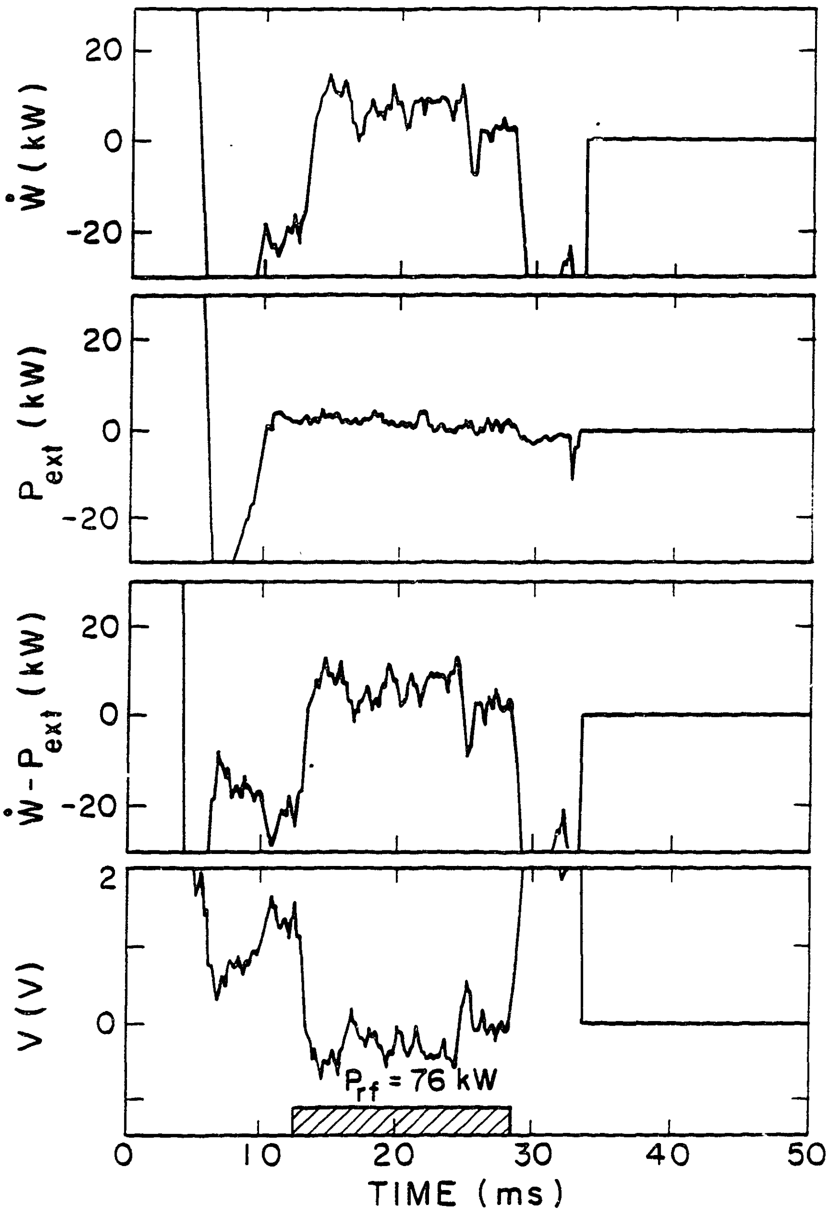

Fig. 4.12: Traces showing the inductive power flow during the ramp-up discharge of Fig. 4.11.

Fig. 4.12. The power flowing into the poloidal field is positive ($\dot{W} > 0$) since the plasma current is ramping up ($\dot{I} > 0$) and the plasma position is moving towards the outside ($\dot{L}_{ext} > 0$). A short period of enhanced ramp-up efficiency ($\dot{W} \sim +12\,\mathrm{kW}$) is observed during the first few milleseconds of rf injection. Averaging over the rf pulse length, we find that $\dot{W} = +5.3\,\mathrm{kW}$. The average inductive power supplied by the vertical field system (since the VF current is being ramped up to maintain equilibrium) is $P_{ext} = +1.2\,\mathrm{kW}$. Thus, the net inductive power flow is given by $\dot{W} - P_{ext} = +4.1\,\mathrm{kW}$, which implies an efficiency of $\epsilon = 0.05$. Finally, the calculated loop voltage in the plasma averages to $V = -0.24\,\mathrm{V}$ over the rf pulse. Assuming a bulk electron temperature of 100 eV, this voltage drives a back current in the bulk plasma $V/R_{sp} \simeq -0.24\,\mathrm{V}/170\,\mu\Omega = 1.4\,\mathrm{kA}$, which dissipates a power given by $V^2/R_{sp} \simeq 0.34\,\mathrm{kW}$. Hence, from Eqn. (2.49), $P_{el}/P_{rf} = 0.060$. The level of efficiency from this discharge and other ramp-up discharges will be compared to the Fisch/Karney theory[30] in Section 4.7.

4.6 Measurements of the Plasma Current Decay Rate

When the OH primary is open-circuited at densities above $\overline{n}_e = 1.0 \times 10^{13}\,\mathrm{cm}^{-3}$, the plasma current decays with time, even with high power 2.45 GHz rf injection and optimum waveguide phasing, $\Delta\phi = +90°$. A typical discharge with $\overline{n}_e \simeq 1.2 \times 10^{13}\,\mathrm{cm}^{-3}$ and $B_T \simeq 12\,\mathrm{kG}$ is shown in Fig. 4.13. During the 78 kW rf pulse, the plasma current decays at an average rate of $\dot{I}_{rf} \simeq -350\,\mathrm{kA/s}$ from an initial level of $I \simeq 18\,\mathrm{kA}$. Without the application of rf power, the current decay rate is $\dot{I}_{OH} \simeq -1500\,\mathrm{kA/s}$. The loop voltage measured outside the vacuum chamber drops to zero during the rf pulse. However, the calculated loop voltage at the plasma center remains slightly positive, approximately $V \simeq +0.3\,\mathrm{V}$. Typically, there is a transient period during the first 3 – 5 ms of rf injection when the plasma current decay rate is reduced, and the loop voltage is driven relatively negative. Similar behavior was observed in the flat-top current drive regime. After this transient period, however, the plasma current decay rate and the loop voltage remain nearly constant along with other plasma parameters such as the density and in/out position.

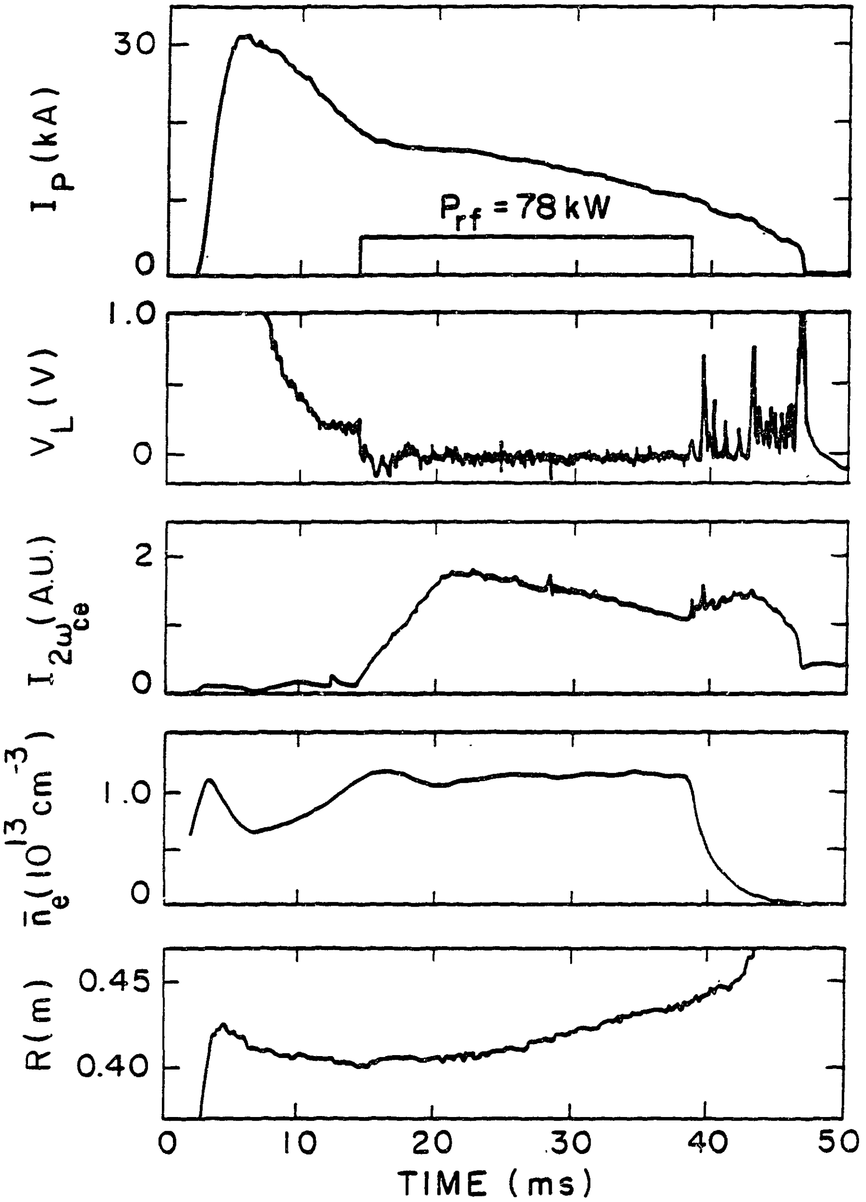

Fig. 4.13: A typical discharge at $\bar{n}_e \simeq 1.2 \times 10^{13}\,\mathrm{cm}^{-3}$ where the injected rf power level of 78 kW is insufficient to flat-top the plasma current.

Despite the presence of the dc electric field, there appears to be no bursting tail instability activity during the rf pulse in Fig. 4.13. Following the termination of the rf pulse, however, the instability appears to turn on, as indicated by the loop voltage spikes and the bursts of X-mode polarized electron cyclotron emission. At higher densities, where the current decays at a faster rate, bursts of cyclotron emission have been observed during the rf pulse. As shown in Fig. 4.13, the steady level of cyclotron emission is strongly enhanced during the rf pulse, although not quite to the level observed in the lower-density quasi-steady- state current drive regime. This enhancement becomes smaller at higher densities. For $\overline{n}_e \simeq 1.7 \times 10^{13}\,\mathrm{cm}^{-3}$, the steady level of cyclotron emission during the rf pulse is approximately one-fourth the level observed at densities $\overline{n}_e \leq 1.0 \times 10^{13}\,\mathrm{cm}^{-3}$.

The dependence of the plasma current decay rate on the plasma density during rf injection is shown in Fig. 4.14 for the range $\overline{n}_e = 1.0 - 1.7 \times 10^{13}\,\mathrm{cm}^{-3}$. The rf power level varied between $75 - 90\,\mathrm{kW}$ in these discharges and the phasing was $\Delta\phi = +90°$. For comparison, data from similar discharges with no rf injection has also been plotted. At the lowest densities ($\overline{n}_e \leq 1.3 \times 10^{13}\,\mathrm{cm}^{-3}$), the current decay rate was substantially reduced by the rf, and long rf pulse lengths ($> 20\,\mathrm{ms}$) could be used. In these cases, $\dot{I}$ was averaged over the rf pulse, excluding the first 6 ms transient period. For the higher density discharges ($\overline{n}_e > 1.3 \times 10^{13}\,\mathrm{cm}^{-3}$), the rf pulse lengths were relatively short ($< 10\,\mathrm{ms}$) because of the rapid current decay. In those cases, $\dot{I}$ was averaged over the entire pulse length. Since these latter measurements include the transient period at the beginning of the rf pulse, they represent underestimates of the plasma current decay rate under steady conditions. This implies that the $\dot{I}$ versus $\overline{n}$ curve in Fig. 4.14 for rf discharges, may actually decrease faster at higher densities than indicated (shown by the downward arrows). Because of these considerations, measurements at even higher densities ($\overline{n}_e > 1.7 \times 10^{13}\,\mathrm{cm}^{-3}$) were considered infeasible.

From the data in Figure 4.14, it appears that some toroidal current is driven by 2.45 GHz rf at densities up to $\overline{n}_e = 1.7 \times 10^{13}\,\mathrm{cm}^{-3}$, nearly three times the 800 MHz limit. Since we do not have sufficient power available to flat-top the

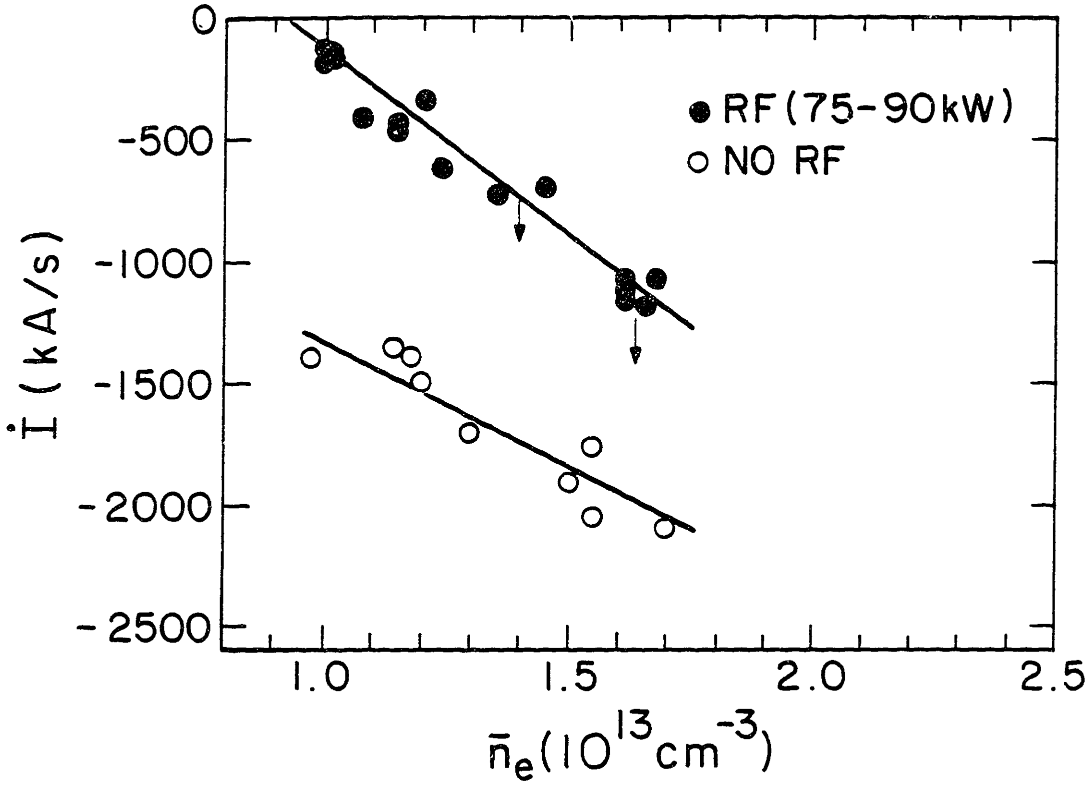

Fig. 4.14: Plasma current decay rate versus line-averaged density $\bar{n}_e = 1.0 - 1.7 \times 10^{13}\,\mathrm{cm}^{-3}$ for $P_{rf} = 75 - 90\,\mathrm{kW}$ and $\Delta\phi = +90^\circ$ (solid circles). For comparison, data has also been plotted from discharges with no rf injection (open circles). The arrows are explained in the text.

current at $\overline{n}_e > 1.0 \times 10^{13}\,\mathrm{cm}^{-3}$, the steady-state current drive efficiency is not known. Furthermore, because of the difficulties explained above in extrapolating the data in Fig. 4.14 to higher densities, we cannot conclude from these results what the upper density limit is for 2.45 GHz current drive.

4.7 Comparison of the 2.45 GHz Current Drive Experiment with the Fisch/Karney Ramp-up Theory

The Fisch/Karney theory[30] of current ramp-up with lower hybrid waves was described in Subsection 2.2.3. This theory predicts the efficiency of converting rf energy into poloidal field energy, generalizing previous theories of steady-state current drive and rf-enhanced conductivity by encompassing the regime where the dc electric field dominates over collisions in influencing the fast electrons. In this section, our experimental measurements of 2.45 GHz current drive are compared with this theory.

In Fig. 4.15, the experimental data is plotted in terms of P_{el}/P_{rf} and $u = v_{ph}/v_R$ along with the theoretical curve given by equation (2.45). Three types of rf-driven discharges previously described in this chapter have been included in our analysis: 1) flat-top discharges, where the electric field is equal to zero ($u = 0$) and the hot electrons are slowed down entirely by collisions ($P_{el} = 0$), 2) ramp-up discharges, where the electric field opposes the current ($u > 0$) and the hot electrons lose energy to the poloidal magnetic field ($P_{el} > 0$), and 3) discharges with decaying current, where the electric field is in the same direction as the current ($u < 0$) and the hot electrons drain energy from the poloidal field ($P_{el} < 0$). The experimental database covers a wide range of parameters: $\overline{n}_e = 0.3 - 1.7 \times 10^{13}\,\mathrm{cm}^{-3}$, $I = 10 - 24\,\mathrm{kA}$, $P_{rf} = 8 - 90\,\mathrm{kW}$, $\Delta\phi = +30°, +60°, +90°, +120°, +150°$. Altogether, 82 discharges have been included in our analysis. As seen in Fig. 4.15, the scatter in the data is small considering the range of discharge parameters, and the agreement between theory and experiment is quite good. A detailed description of the procedure used in the data analysis follows.

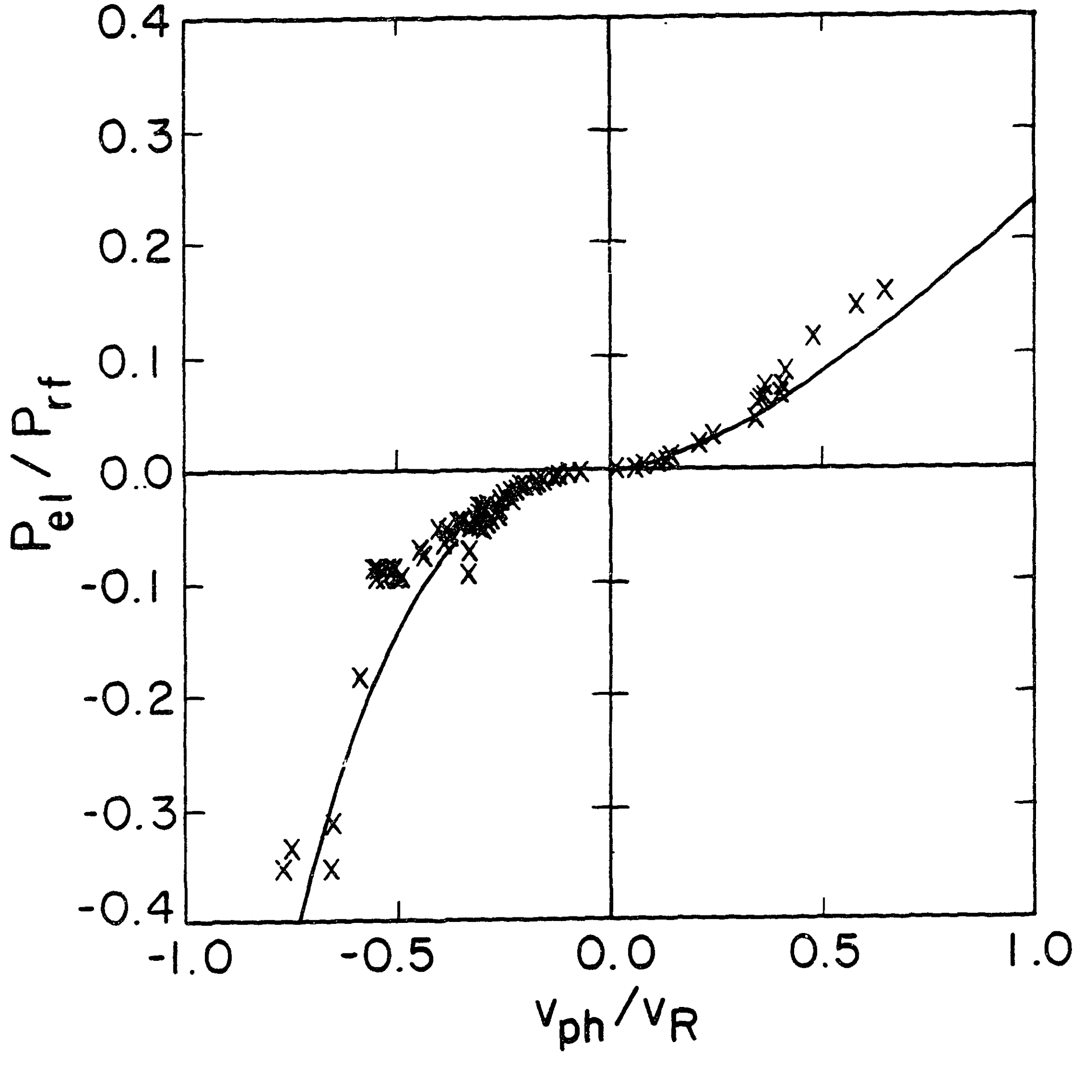

Fig. 4.15: Ramp-up efficiency P_{el}/P_{rf} versus $u = v_{ph}/v_R$. Experimental 2.45 GHz current drive data presented in this chapter is plotted along with the Fisch/Karney theoretical curve, assuming $Z_{eff} = 2$, $\alpha = P_{abs}/P_{rf} = 0.75$ and $N_{\|}^{\sim} = 9$.

As shown in Chapter 2, the quantity P_{el}/P_{rf} can be expressed in terms of experimental quantities by using the poloidal field power flow relation. The result was:

$$\frac{P_{el}}{P_{rf}} = \frac{\dot{W} - P_{ext} + V^2/R_{sp}}{P_{rf}}, \tag{4.6}$$

where $W = LI^2/2$ is the stored energy of the poloidal magnetic field, P_{ext} is the power flow from the external field coils, and V is the voltage given by $V = (P_{ext} - \dot{W})/I$. This quantity can be compared to the theoretical quantity P_{el}/P_{abs} by assuming that the power absorbed by the hot electrons, P_{abs}, is a fraction α of the total injected rf power P_{rf}. This leads to the relationship:

$$\frac{P_{el}}{P_{rf}} = \alpha\frac{P_{el}}{P_{abs}} = \alpha\frac{\partial G(u, Z_{eff})/\partial u}{u}, \tag{4.7}$$

where $G(u, Z_{eff})$ is given by equation (2.45).

The experimental determination of $\dot{W} - P_{ext}$ requires measurements of the plasma current I, the total plasma inductance $L = \mu_o R[\ln(8R/a) - 2 + \ell_i/2]$ and the vertical field current I_V. As previously discussed, the determination of $\ell_i/2$ from an analysis of the Shafranov equilibrium equation is highly uncertain due to the significant contribution of the β_θ term during current drive. In the present analysis we assume that $\ell_i/2 = 0.85$. This number is based on Thomson temperature profiles measured during ohmic discharges and on $\beta_\theta + \ell_i/2$ measurements made prior to rf injection in current-driven discharges. The total plasma inductance L is then evaluated using in/out position measurements. The power flow from the external vertical field coils is given by $P_{ext} = I(M_V \dot{I}_V + M_{PVF}\dot{I}_{PVF})$ where I_{PVF} is the programmable vertical field current (when utilized), and $M_V \simeq 3.5\,\mu$H and $M_{PVF} \simeq 3\,\mu$H are the mutual inductances between the coil sets and the plasma loop. Note that we are only considering discharges in which the OH primary was open-circuited during the rf pulse.

In general, $\dot{W} - P_{ext}$ does not remain constant during the entire rf pulse. Typical $\dot{W} - P_{ext}$ traces have been shown for a flat-top discharge (Fig. 4.3), and for a ramp-up discharge (Fig. 4.12). In some instances, relatively high transient values of $\dot{W} - P_{ext}$ are observed during the first few milleseconds of rf injection, possibly indicating the presence of runaway electrons in the target plasma. As long as these electrons are confined, they can contribute to the poloidal field energy if the voltage is driven negative during the rf pulse. The enhanced current drive efficiency at the beginning of the rf pulse might also be due to the higher bulk electron temperature. In the present analysis, we have chosen to time-average $\dot{W} - P_{ext}$ over the entire duration of the rf pulse. In most cases, the rf pulse length exceeded 15 ms. However, in some cases where the decay rate of the plasma current was high, the rf pulse length was cut short by the termination of the plasma discharge.

The ohmic power dissipation in the bulk plasma, V^2/R_{sp}, is not well known in these experiments due to the lack of bulk electron temperature data. For the present analysis we have assumed uniformly that $Z_{eff} = 2$, and $T_{e0} = 100\,\mathrm{eV}$, which corresponds to $R_{sp} \simeq 170\,\mu\Omega$. Fortunately, in most cases the estimated value of V^2/R_{sp} makes less than a 10% contribution to P_{el}, and hence the error introduced by this procedure is believed to be small. The largest uncertainty arises for those cases in Fig. 4.15 which are the farthest from the origin because V is relatively large, and the contribution of the V^2/R_{sp} term to P_{el} is substantial (up to 40%).

The quantity $u = v_{ph}/v_R$, the ratio of the parallel phase velocity of the waves to the effective runaway velocity of the electrons (see Chapter 2), may be determined using the following expression:

$$u = \frac{7.23}{N_{\parallel}^{*}} \sqrt{\frac{V}{1.5\bar{n}_e(10^{13}\,\mathrm{cm}^{-3})}}, \tag{4.8}$$

where we have used the central density, given by $n = 1.5\bar{n}_e$. The quantity $N_{\parallel}^{*}$ is defined as the parallel refractive index of the waves when they are absorbed. Note that $N_{\parallel}^{*}$ may be different from the launched $N_{\parallel}$-value of the wave due to toroidal wave propagation effects.

The two parameters which are most difficult to measure experimentally, α and $N_{\parallel}^{*}$, must be chosen in order to compare experiment with theory. If instead we assume that the theory is correct, then by fitting the experimental data to the theory, we can obtain estimates for α and $N_\parallel^*$. For the case shown in Fig. 4.15, we chose the value $\alpha = 0.75$ and then varied the parameter $N_\parallel^*$ until the best fit was obtained with $N_\parallel^* = 9$. Reasonably good agreement between the data and the theory can also be achieved with other combinations of α and $N_\parallel^*$. For instance, with $\alpha = 0.25$, 0.50, and 1.00, the best fits were obtained with $N_\parallel^*$ values of 6, 7.5, and 10 respectively. However, in the case with $\alpha = 0.25$ a good fit could not be obtained simultaneously for both $u > 0$ and $u < 0$ with a single $N_\parallel^*$ value. The overall fit between theory improves with higher values of α.

In the limit $u \to 0$, the Fisch/Karney ramp-up theory reduces to the steady-state theory of Fisch and Boozer discussed in Subsection 2.2.2. As a check on the ramp-up analysis, we can compare the experimentally determined flat-top efficiency ($\tilde{\eta} = \bar{n}IR/P(10^{20}\,\mathrm{m}^{-3})(\mathrm{kA})(\mathrm{m})/\mathrm{kW} = 0.0072$) to that predicted by the Fisch/Boozer theory. By combining equations (2.38) and (2.41), and using $n = 1.5\bar{n}$, and $P_{abs} = \alpha P_{rf}$, the theoretical efficiency may be written as:

$$\tilde{\eta} = \frac{\bar{n}(10^{20}\,\mathrm{m}^{-3})I(\mathrm{kA})R(\mathrm{m})}{P_{rf}(\mathrm{kW})} = \frac{1.38\alpha}{N_\parallel^{*2}}\frac{4}{5 + Z_{eff}}. \tag{4.9}$$

Equating the theoretical and experimental efficiencies we can then pick a value for α and solve for $N_\parallel^*$ as before. For $Z_{eff} = 2$, and α values of 0.25, 0.50, 0.75, and 1.00, the resulting $N_\parallel^*$ values are 5.2, 7.4, 9.1, and 10.5 respectively. This is in good agreement with the previous results.

These results suggest that most of the injected rf power is absorbed by the hot electrons, but only after the launched waves undergo a significant $N_\parallel$ upshift. This is consistent with our expectations since the launched wave spectrum in these experiments is concentrated at low-$N_\parallel$ values ($1 < N_\parallel < 4$), while the quasi-linear condition for strong Landau damping [equation (2.21)] requires $N_\parallel > 7.0/\sqrt{T_e(\mathrm{keV})} = 22$ for a 100 eV plasma. It must be emphasized, however, that the Fisch/Karney and Fisch/Boozer theories assume a narrow resonant wave spectrum which can be characterized by a single value of $N_\parallel^*$. The $N_\parallel^*$ values deduced from our comparison of theory and experiment are at best representative of a realistic broad wave spectrum, and therefore, our results must be interpreted cautiously.

Keeping this caveat in mind, there are still several points worth noting about the data in Figure 4.15. First, from a phase scan conducted at $\overline{n}_e \simeq 7 \times 10^{12}\,\text{cm}^{-3}$ (see Fig. 4.7), the dependence of $N_{\|}^{*}$ on waveguide phasing was examined. Interestingly, the best fit between the ramp-up theory and the experiment was obtained by assuming the same $N_{\|}^{*}$ for all phase settings (+30°, +60°, +90°, +120°, +150°). This is in contrast to the PLT experiment where a constant $N_{\|}$ upshift factor of 1.4 appeared to best fit the data for $\Delta\phi = +60°$, +90°, and +135°. Our results indicate that the $N_{\|}^{*}$ value of the damped wave is rather insensitive to the initial $N_{\|}$ value of the launched wave, possibly because the $N_{\|}$ upshift needed for strong absorption is large.

Second, it is rather remarkable that a single value of α would appear to fit the data fairly well over such a wide range of densities when accessibility is expected to limit the penetration of low-$N_{\|}$ waves to the interior of the plasma. Note in particular that as the density is increased from $\overline{n}_e = .3 \times 10^{13}\,\text{cm}^{-3}$ to $1.7 \times 10^{13}\,\text{cm}^{-3}$, $N_{\|acc}$ at the plasma center increases from 1.8 to 3.2. However, if a mechanism exists by which the waves propagating in the plasma can undergo sufficiently large $N_{\|}$ upshifts, then it is possible that the accessibility condition given by equation (4.4) does not impose a severe restriction on wave penetration. Therefore, a relatively weak dependence of α on density may be consistent with the large $N_{\|}$ upshifts inferred from our ramp-up analysis. There is some indication from the data in Figure 4.15 that accessibility may become important for the highest density discharges ($\overline{n}_e \geq 1.4 \times 10^{13}\,\text{cm}^{-3}$). These points (located in the region $u < 0$) consistently lie above the curve which best fits the rest of the data, indicating that α is lower for these points. However, this trend may also be due to transient effects. Because of the high rate of current decay at high densities, the rf pulse lengths were necessarily short. Hence, the relatively high values for P_{el}/P_{rf} often observed during the first few milliseconds of rf injection are weighted more heavily in these cases.

Chapter 5

2.45 GHz Current Drive and Electron Heating Experiments in Ohmically Heated Discharges

In the previous chapter it was shown that the LHCD density limit could be raised by increasing the rf frequency from 800 MHz to 2.45 GHz, without raising the toroidal magnetic field strength. In this chapter, we attempt to determine the upper density limit for current drive at 2.45 GHz on Versator. As shown in Section 5.1, current drive effects in combined ohmic/rf discharges include plasma current increases, loop voltage drops and nonthermal x-ray and electron cyclotron emission. Although these effects become relatively small, they do not disappear entirely, even at densities above $\overline{n}_e \simeq 2 \times 10^{13}\,\mathrm{cm}^{-3}$. We have also observed substantial increases in the line-averaged density during rf injection for $\overline{n}_e \leq 2 \times 10^{13}\,\mathrm{cm}^{-3}$. It is shown in Section 5.2 that these density increases are due to an improvement in the global particle confinement time. In Section 5.3, preliminary attempts at bulk electron heating in the density range $\overline{n}_e = 1.0 - 1.5 \times 10^{13}\,\mathrm{cm}^{-3}$ with $\Delta\phi = \pi$ are discussed.

5.1 High Density Current Drive Effects

With the available rf power ($P_{rf} \leq 95\,\mathrm{kW}$) it has not been possible to flat-top the plasma current at densities above $\overline{n}_e = 1.0 \times 10^{13}\,\mathrm{cm}^{-3}$. The measurements described in Section 4.6 indicate that some of the plasma current may still be rf-driven at densities up to $\overline{n}_e = 1.7 \times 10^{13}\,\mathrm{cm}^{-3}$, since the rate of decay of the plasma current is reduced. However, with the OH transformer primary open-circuited, the study of current drive at high densities became difficult due to the high rate of decay of the plasma current. In a further attempt to determine the density limit for 2.45 GHz current drive on Versator, we have injected rf power into ohmically heated discharges. The advantage of this approach is that the plasma parameters can more easily be maintained nearly constant during the rf pulse. The main disadvantage is that the behavior of the superthermal resonant electrons may become dominated by the higher dc electric field rather than the rf. In this subsection, we describe the current drive effects observed at densities up to $\overline{n}_e = 2.5 \times 10^{13}\,\mathrm{cm}^{-3}$.

A typical OH discharge with a density of $\overline{n}_e \simeq 1.7 \times 10^{13}\,\mathrm{cm}^{-3}$ is shown in Fig. 5.1. The plasma current is started up in the usual manner by charging up the OH transformer in the positive direction and then rapidly swinging the OH flux in the negative direction back to zero. In this case, however, instead of open-circuiting the transformer primary when the flux reaches zero, a low voltage OH capacitor bank with a long LC time constant is fired to continue the flux swing through zero in the negative direction. This induces an initial loop voltage of approximately 2 V which decays to zero by the end of the 30 ms discharge when the OH primary current reaches its extreme negative value. For the discharge of Fig. 5.1, about 30 kA of plasma current is driven by the OH transformer alone.

When 66 kW of 2.45 GHz rf power is injected, an increase in the plasma current is observed, along with a drop in the loop voltage and an increase in the electron cyclotron emission. The relative waveguide phasing for Fig. 5.1 was $\Delta\phi = +90°$, and the average toroidal magnetic field during the rf pulse was 12 kG. The difference between the plasma current with and without rf injection, $\Delta I = I_{rf} - I_{OH}$, steadily increases during the 10 ms rf pulse. By the end of the pulse, $\Delta I = 5.6\,\mathrm{kA}$. The loop voltage drop is approximately 15%. The rf enhancement of the cyclotron emission, while clearly observable, is substantially below the level observed in the lower density regime where current flat-topping is possible.

In Fig. 5.1, no bursting cyclotron emission, loop voltage spikes, or other signs of the Parail-Pogutse instability are evident. At lower densities, however, these effects do appear. Often, one tail mode burst occurs immediately following the termination of the rf pulse. The outward motion of the plasma during rf injection, as seen in Fig. 5.1, is due primarily to the increase in the plasma current. At lower densities ($\overline{n}_e \leq 1.4 \times 10^{13}\,\mathrm{cm}^{-3}$), where current increases were much larger, the plasma equilibrium could not be maintained during high power rf injection because of vertical field power supply limitations. The density (not shown) for the discharge in Fig. 5.1 was maintained nearly constant during the rf pulse with

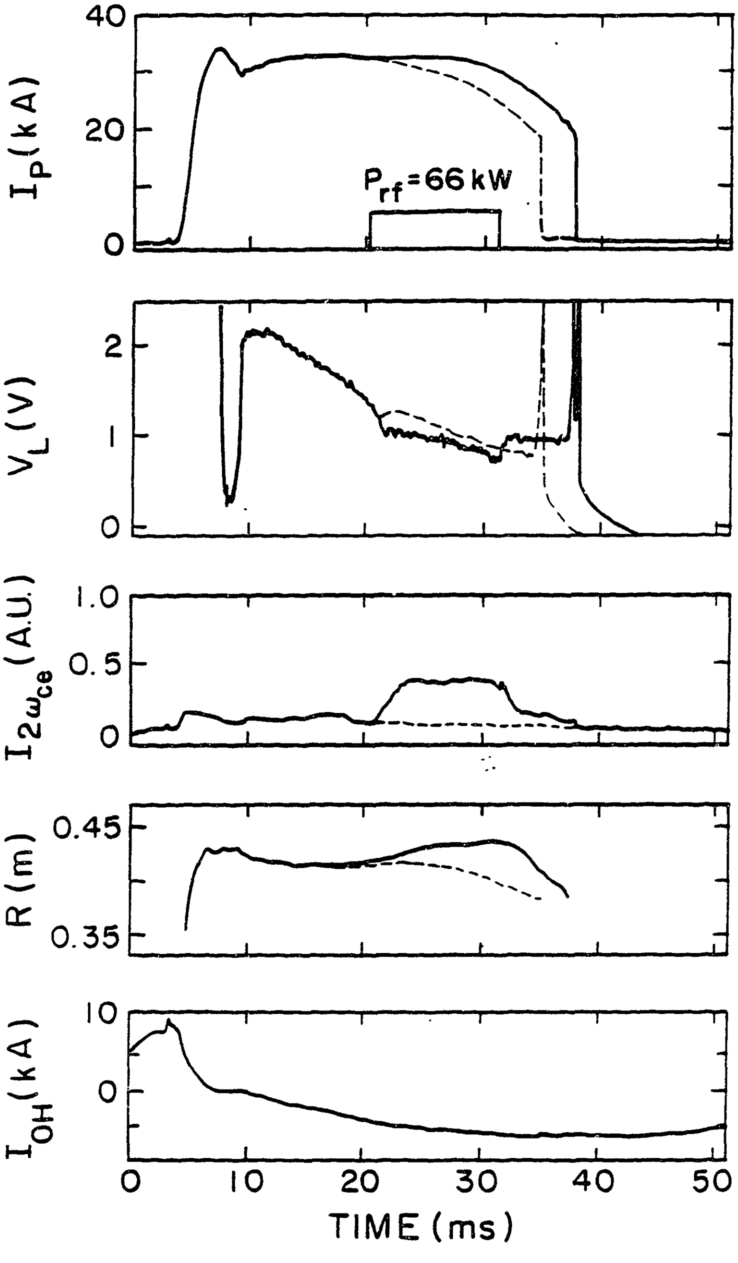

Fig. 5.1: A comparison of ohmically-heated discharges with (solid traces) and without (dashed traces) the injection of 2.45 GHz rf power, showing the rf current drive effects. The discharge parameters are: $\overline{n}_e = 1.7 \times 10^{13}\,\mathrm{cm}^{-3}$, $B_T = 12\,\mathrm{kG}$, $P_{rf} = 66\,\mathrm{kW}$, $\Delta\phi = +90°$.

careful programming of the gas puffer. With a constant gas feed rate, 2.45 GHz rf injection into OH discharges raises the line-averaged density by as much as a factor of two. It is shown in the following section that the density increase is due to an improvement in the global partical confinement time during rf injection.

The dependence of ΔI on the rf power level, waveguide phasing, and plasma density is shown in Figs. 5.2 - 5.4. Each data point was obtained by comparing two discharges, one with and one without rf injection. The current increase, $\Delta I = I_{rf} - I_{OH}$, was measured 5 ms after the rf firing time for uniformity. For rf pulse lengths longer than this, variations in the plasma density and in/out position became problematic.

As shown in Fig. 5.2, ΔI increases approximately linearly with the injected rf power level, with $\Delta I/P = 0.03\,\mathrm{kA/kW}$ for $\overline{n}_e \simeq 1.7 \times 10^{13}\,\mathrm{cm}^{-3}$. The dependence on waveguide phasing at $\overline{n}_e \simeq 1.8 \times 10^{13}\,\mathrm{cm}^{-3}$ is shown in Fig. 5.3. Although the incident rf power level was fixed at 85 kW, the net injected power ranged from 66 to 84 kW because of variations in the antenna reflectivity with changes in waveguide phasing (see Fig. 3.6). Correcting for this effect, we plot $\Delta I/P$, where P is the net injected power. Although typical current increases are quite small at this density ($\Delta I \sim 1 - 2\,\mathrm{kA}$), the phase dependence is still evident, with larger ΔI occurring when the rf waves are launched primarily in the direction of the ohmic drift. We note that the power and phase dependence of ΔI measured in these experiments is very similar to the results obtained in previous OH-assisited 800 MHz current drive experiments on Versator using a 4-waveguide side-launch antenna ($N_{\|} \sim 2.5$).[7,65] The density dependence of ΔI during 2.45 GHz current drive is shown in Fig. 5.4 for the following parameters: $\overline{n}_e = 1.4 - 2.5 \times 10^{13}\,\mathrm{cm}^{-3}$, $P_{rf} = 75 - 90\,\mathrm{kW}$, $\Delta\phi = +90°$. Small current increases are observed even at the highest densities, although for $\overline{n}_e \geq 2.2 \times 10^{13}\,\mathrm{cm}^{-3}$, the current increases last only for the first few milleseconds of rf injection. In addition, the plasma density tends to decrease rather than increase during the rf pulse. This latter effect will be discussed in the next section.

In Fig. 5.5, the rf-enhanced level of 71 GHz cyclotron emission, $I_{2\omega_{ce}}$, is plot-

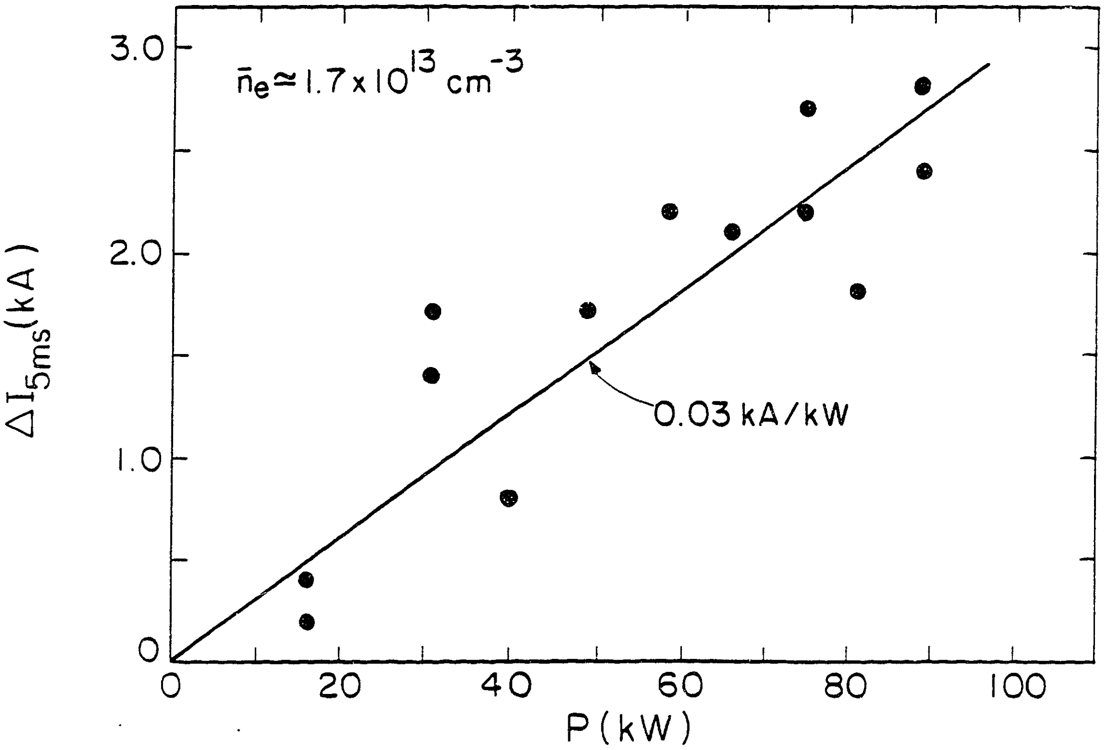

Fig. 5.2: The current increase $\Delta I = I_{rf} - I_{OH}$, measured 5 ms into the rf pulse, versus the injected rf power level P_{rf} for $\bar{n}_e \simeq 1.7 \times 10^{13}\,\mathrm{cm}^{-3}$, $\Delta\phi = +90°$.

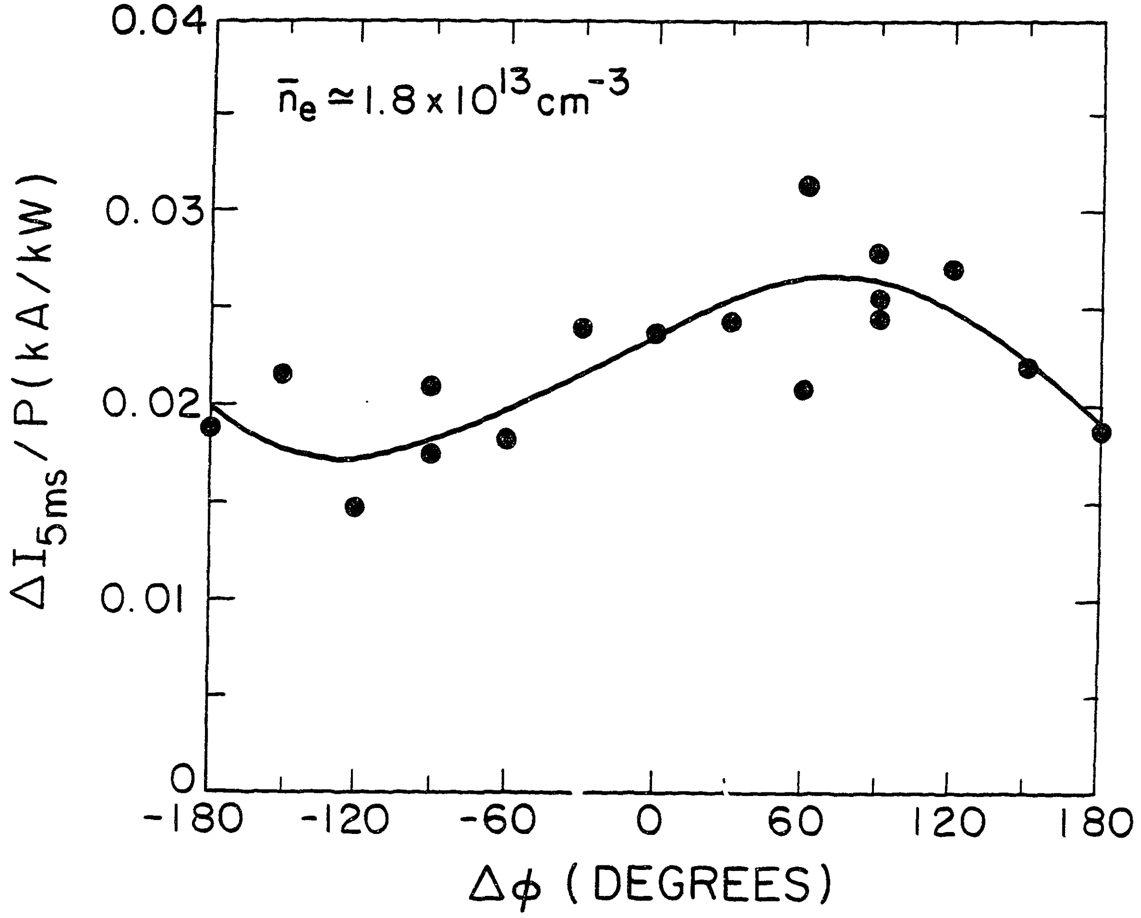

Fig. 5.3: Dependence of the normalized current increase, $\Delta I/P_{rf}$, on the waveguide phasing $\Delta\phi$, with $P_{rf} = 66 - 84$ kW. and $\bar{n}_e \simeq 1.8 \times 10^{13} \mathrm{cm}^{-3}$.

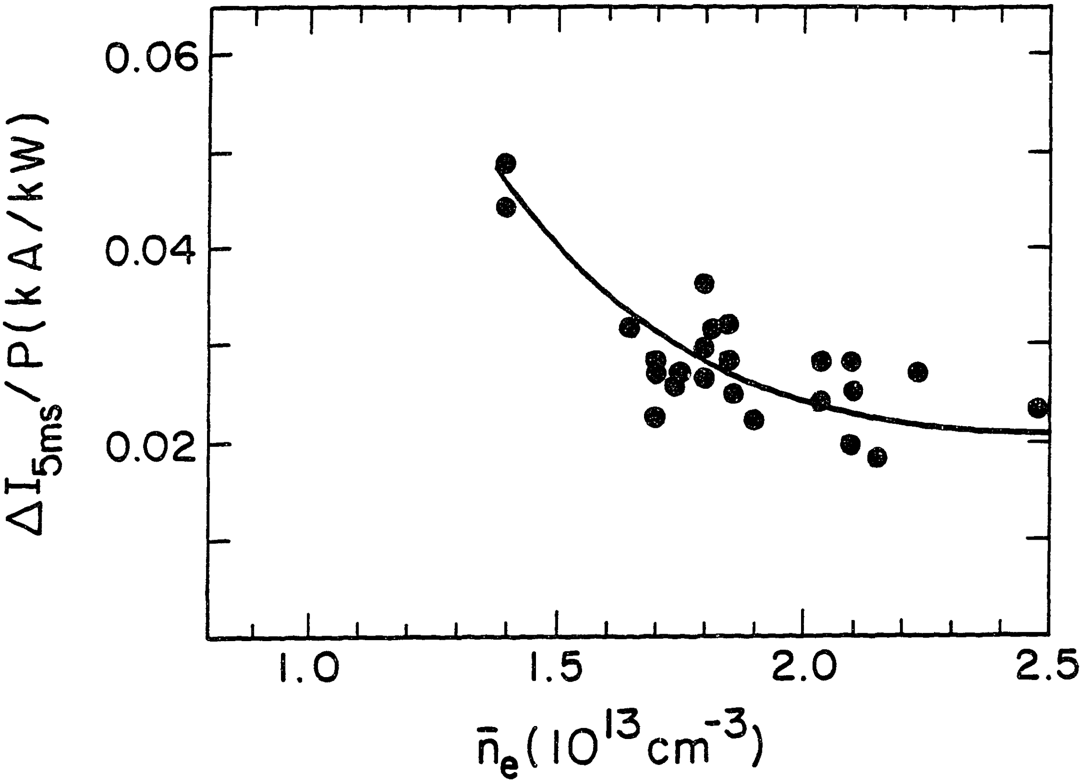

Fig. 5.4: Normalized current increase $\Delta I/P_{rf}$ versus line-averaged density for $P_{rf} = 75 - 90\,\text{kW}$, $\Delta\phi = +90°$.

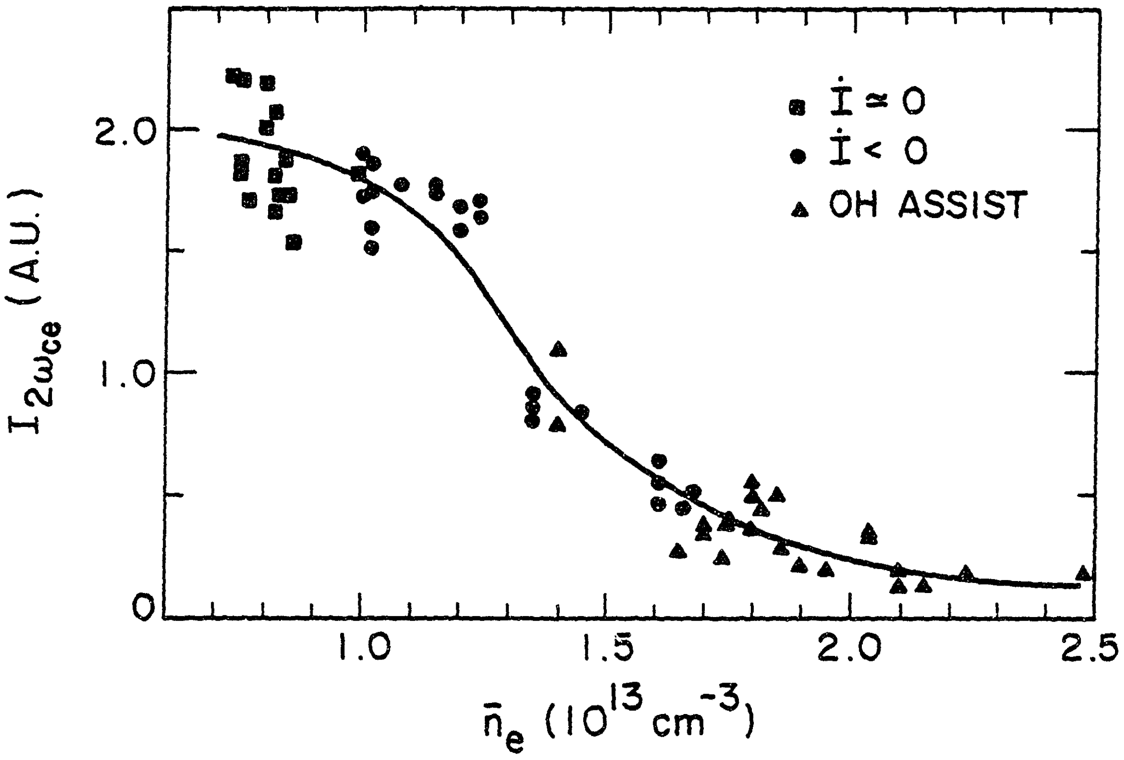

Fig. 5.5: Rf-enhanced level of 71 GHz cyclotron emission versus density for three types of discharges: 1) quasi-steady-state discharges with $\dot{I} \simeq 0$ (squares), 2) decaying current discharges with $\dot{I} < 0$ (dots), and 3) combined ohmic/rf discharges (triangles).

ted versus the density $\overline{n}_e$ for OH-assisted discharges. For comparison, cyclotron emission data has also been plotted for lower density discharges in which the OH primary was open-circuited. These include the quasi-steady-state ($\dot{I} \simeq 0$) and decaying current ($\dot{I} < 0$) discharges described in Chapter 4. The rf power level exceeded 75 kW for all of the data points shown, and the waveguide phasing was $\Delta\phi = +90^\circ$. Based on the overlap of the data, it appears that the level of cyclotron emission observed during rf injection is fairly independent of the type of discharge.

The data in Fig. 5.5 shows qualitatively the variation of current drive effects (i.e. superthermal electron tails) over the density range $\overline{n}_e = .7 - 2.5 \times 10^{13}\,\mathrm{cm}^{-3}$. At densities below $\overline{n}_e = 1.0 \times 10^{13}\,\mathrm{cm}^{-3}$, where the quasi-steady-state efficiency scales as $I/P \propto \overline{n}^{-1}$, the cyclotron emission is enhanced by more than an order of magnitude above thermal levels. As the density is raised above $\overline{n}_e = 1.0 \times 10^{13}\,\mathrm{cm}^{-3}$, the current drive efficiency appears to decrease more rapidly with density, as indicated by the current decay rate measurements of Section 4.6. This is shown dramatically in Fig. 5.5 by the order of magnitude decrease in the cyclotron emission level as the density is increased from $\overline{n}_e = 1 \times 10^{13}\,\mathrm{cm}^{-3}$ to $\overline{n}_e = 2 \times 10^{13}\,\mathrm{cm}^{-3}$. While small current drive effects are observed for densities as high as $\overline{n}_e = 2.5 \times 10^{13}\,\mathrm{cm}^{-3}$, it appears that an effective density limit for 2.45 GHz lower hybrid current drive on Versator has been encountered at $\overline{n}_e \simeq 2 \times 10^{13}\,\mathrm{cm}^{-3}$. We note that for the highest density discharges, $\omega_{pe}^2(0)/\omega_{ce}^2 > 2.5$. In these cases, only waves with $N_{\parallel} > 3.5$ will propagate to the plasma center, which corresponds to $\varepsilon \leq 21$ keV electrons. Thus, the electron tail is hardly energetic.

Hence, we expect that poor accessibility at least partially accounts for the reduction of current drive effects at high densities. Nevertheless, these experiments indicate that if sufficient rf power were available, 2.45 GHz quasi-steady-state current drive might be achievable on Versator at densities more than three times the 800 MHz limit.

5.2 Particle Confinement Studies

As indicated in the previous section, large increases (up to a factor of two) in the line-averaged density are observed when 2.45 GHz rf power is injected into ohmically heated plasmas with the gas feed rate held constant. We investigate here three possible causes for the density increases: 1) increased ionization of hydrogen, 2) increased influx of impurities, and 3) an increase in the particle confinement time. From an analysis of the global particle balance, it is found that for an initial density of $\overline{n}_e = 1.3 \times 10^{13}\,\mathrm{cm}^{-3}$, the global partical confinement time τ_p increases by a factor of two during S-band current drive.

5.2.1 Density and Ionization Behavior

Typical density behavior is shown in Fig. 5.6 for ohmically heated discharges with and without rf injection. The gas feed rate, controlled with a piezoelectric puff valve, was held constant during the entire time interval shown. In these experiments, the line-averaged density was measured both with the 75 GHz zebra-stripe interferometer and with the 139 GHz microwave scattering diagnostic configured as a conventional interferometer in order to confirm the interpretation of high density data. In Fig. 5.6 the line-averaged density before the rf firing time at $t = 20\,\mathrm{ms}$ is $\overline{n}_e = 1.1 \times 10^{13}\,\mathrm{cm}^{-3}$. Without rf, the density remains nearly constant. In contrast, when 65 kW of rf power is injected with +90° waveguide phasing, the density rises by nearly a factor of two, to $\overline{n}_e = 2.0 \times 10^{13}\,\mathrm{cm}^{-3}$. The density typically starts to rise approximately 1 ms after the beginning of the rf pulse. Once the maximum value is reached, in this case 6 ms later, sawtooth oscillations with slow-rise and fast-fall characteristics appear on the density trace. During the remainder of the rf pulse, the density decays slightly or remains constant, depending on the in/out plasma motion. Following the termination of the rf pulse, however, the density always decays rapidly.

The ionization rate of hydrogen is inferred from the brightness of the H_α line emission. For the plasma conditions in these experiments, the H_α emissivity is

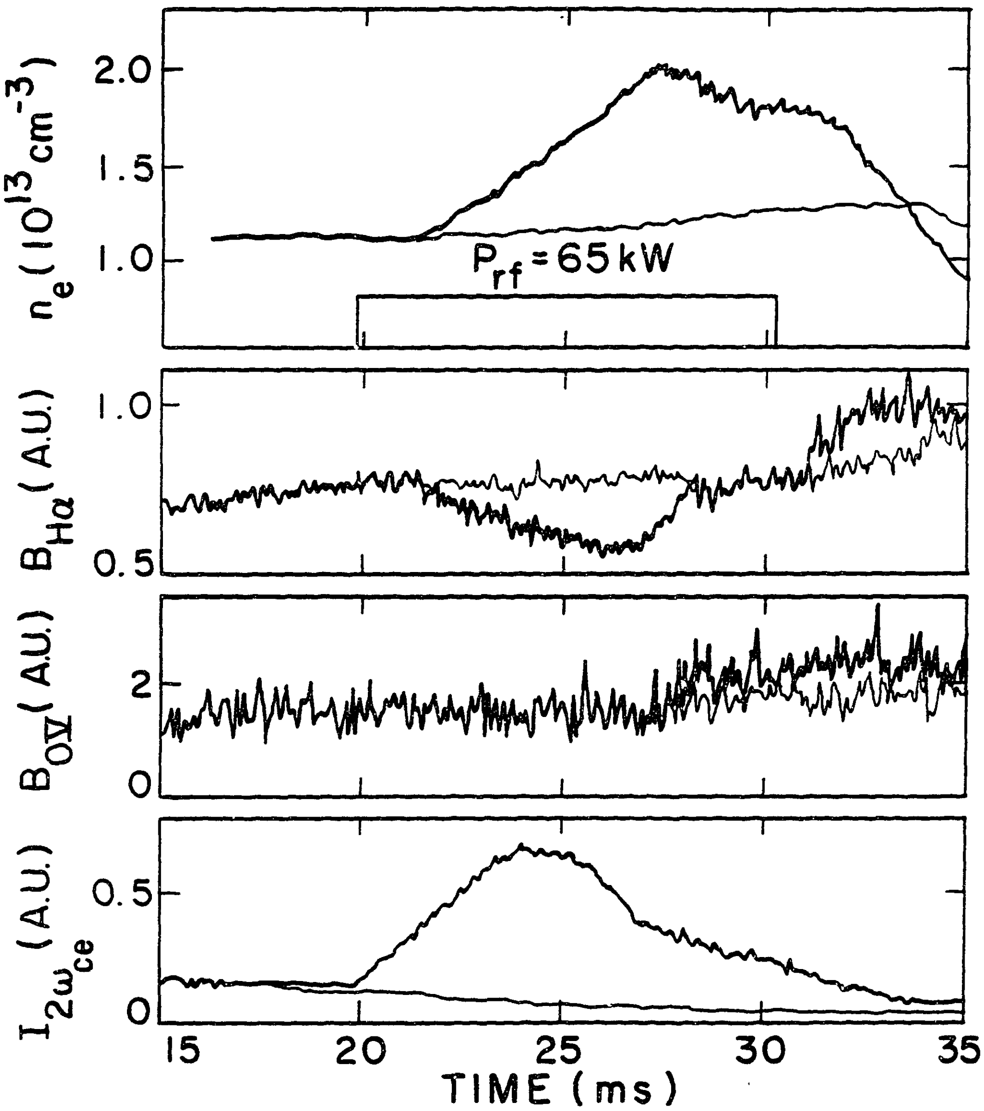

Fig. 5.6: Traces showing the temporal evolution of the density, H_α brightness, O V impurity line brightness, and the $2\omega_{ce}$ emission during ohmically heated discharges with and without 2.45 GHz rf injection. In both cases the gas feed rate was fixed during the entire time interval shown.

proportional to the volumetric hydrogen ionization rate.[72] The H_α brightness was measured using a photodiode detector with a narrow band interference filter and a focussing lens.[73] As shown in Fig. 5.6, the H_α brightness level, B_{H_α} measured from the edge of the plasma decreases during the density rise. In the ohmic discharge, with the same rate of gas feed, the H_α brightness level remains nearly constant. The maximum reduction in the H_α brightness level during the rf pulse is approximately 30%. Note, however, that once the density reaches its maximum level of $\bar{n}_e = 2.0 \times 10^{13}\,\mathrm{cm}^{-3}$, the H_α emission quickly returns to its original level. The observed decrease in the H_α emission during rf injection indicates a reduction in the recycling rate of neutral hydrogen from the tokamak chamber walls. Such a reduction is consistent with an improvement in the global particle confinement time since the loss rate of particles to the walls would be reduced.

The behavior of impurity species was also monitored during rf injection using the VUV monochrometer. As shown in Fig. 5.6, the brightness of the O V impurity line (emitted from the outer region of the plasma) remains constant during the first 7 ms of the rf pulse, during the density rise. Once the density maximum is reached, however, the O V brightness increases slightly. Other impurity lines surveyed, including C V (emitted near the plasma center) and C III (emitted near the edge) exhibit similar temporal behavior. If an influx of impurities was responsible for the observed density rise during current drive, then the impurity line radiation would have been enhanced noticeably.[74] Since it remained constant, we conclude that the density increase in Fig. 5.6 was due neither to an influx of impurities nor to increased ionization of hydrogen, but rather to an improvement in the global particle confinement time τ_p. A quantitative estimate of the τ_p increase requires spatial profile measurements of the density and the H_α emission.

The behavior of the electron cyclotron emission during the density rise shown in Fig. 5.6 is consistent with the density dependence plotted previously in Fig. 5.5. The emission level begins to rise immediately upon rf injection, but saturates approximately 4 ms later when the density reaches a level of $\bar{n}_e \simeq 1.4 \times 10^{13}\,\mathrm{cm}^{-3}$. As the density continues to increase, the cyclotron emission level decreases. In general, 2.45 GHz current drive effects are diminished when the density is allowed to increase, and it appears from Fig. 5.6 that both current drive effects and particle confinement effects are limited to densities $\bar{n}_e \leq 2 \times 10^{13}\,\mathrm{cm}^{-3}$.

5.2.2 Determination of τ_p

The global particle balance equation is given by:

$$\tau_p = \frac{N_e}{S - dN_e/dt}, \tag{5.1}$$

where N_e is the total number of electrons, S is the total ionization source term, and τ_p is the global particle confinement time. The total number of electrons is given by the volume integral of the density profile,

$$N_e = 4\pi^2 R \int_0^a r n_e(r)\,dr, \tag{5.2}$$

where $n_e(r)$ is obtained from Abel-inverted interferometer data. The determination of S from the H_α brightness measurements is less straightforward because of possible localized sources of ionization occurring near the gas puff valve, limiters, and the mouth of the 2.45 GHz waveguide grill (via rf-induced breakdown). A complete toroidal and poloidal H_α survey was not possible in these experiments because of port access limitations. Hence, an absolute determination of S could not be made. The H_α emission was monitored at various times from three different toroidal locations (see Fig. 1.2). The two available tangential side ports afforded a direct view of the limiter and the rf antenna. The third port, located below the tokamak, was used for radial scans of the plasma cross section. The time dependence of the H_α signal was approximately the same at each toroidal location. Hence, we have assumed that the temporal evolution of S is independent of the toroidal location, deducing relative changes in S from the Abel-inverted H_α profile measurements. The ionization source term is then given by:

$$S(t) \propto \int_0^a r E_\alpha(r,t)\,dr, \tag{5.3}$$

where it has been assumed that the H_α emissivity, E_α, is proportional to the volumetric hydrogen ionization rate.[72] The source term $S(t)$ is then normalized, using equation (5.1), by choosing a reasonable value for τ_p just prior to rf injection which is consistent with the observed density behavior in ohmic discharges.

Abel-inverted profiles of the density $n_e(r)$ and the H_α emissivity $E_\alpha(r)$ are shown in Fig. 5.7. The line-averaged density just before the rf injection ($t = 19\,\mathrm{ms}$) is $\overline{n}_e = 1.3 \times 10^{13}\,\mathrm{cm}^{-3}$. As the density rises during the rf pulse to a maximum of $\overline{n}_e = 1.9 \times 10^{13}\,\mathrm{cm}^{-3}$, the density profile steadily broadens, while the H_α emissivity profile, which is localized to the outer region of the plasma cross section, remains nearly unchanged.

The time histories of N_e, S and τ_p calculated from these profile measurements are shown in Fig. 5.8. While the total number of electrons in the plasma increases by 50%, the total ionization source term decreases by more than 30%. The global particle confinement time τ_p, calculated from Eqn. (5.1), increases by a factor of two during the 2.45 GHz rf pulse. The improvement in τ_p appears to saturate and even decline somewhat as the line averaged density rises to a level near $\overline{n}_e = 2 \times 10^{13}\,\mathrm{cm}^{-3}$.

5.2.3 The Dependence of τ_p on P_{rf}, $\Delta\phi$, and $\overline{n}_e$

The particle confinement improvement during current drive depends on the injected rf power level as shown in Fig. 5.9. In this power scan the initial density was $\overline{n}_e = 1.3 \times 10^{13}\,\mathrm{cm}^{-3}$. Changes in the density and H_α emission were measured during a 7 ms rf pulse. With +90° current drive phasing, the density rise $\Delta\overline{n}_e$ and the drop in the H_α brightness increase linearly with the rf power level, except at the highest power levels where the effects begin to saturate. The global particle confinement time estimated from these density and H_α measurements shows a similar behavior, increasing with the applied rf power level until $\Delta\overline{n}_e$ becomes so large that the line-averaged density exceeds $\overline{n}_e = 1.8 \times 10^{13}\,\mathrm{cm}^{-3}$. If the particle confinement improvement is associated with the rf current drive process, then the saturation of τ_p is consistent with the reduction of other current drive effects at densities near $\overline{n}_e \simeq 2 \times 10^{13}\,\mathrm{cm}^{-3}$. Further support for the dependence of improved particle

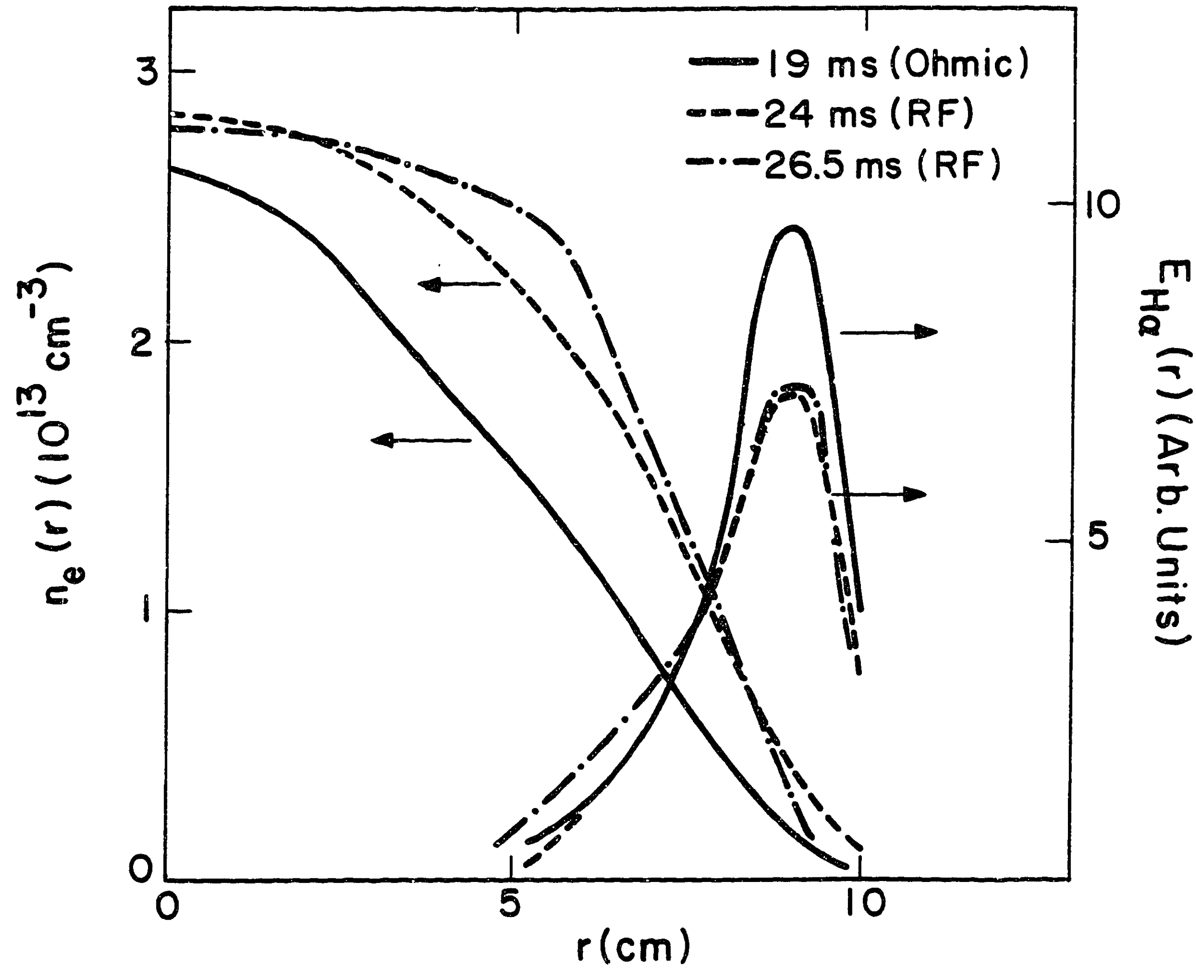

Fig. 5.7: Abel-inverted density and H_α emissivity profiles before and during rf injection. The line-averaged density rises from $\overline{n}_e = 1.3 \times 10^{13}\,\mathrm{cm}^{-3}$ just before rf injection ($t = 19\,\mathrm{ms}$) to a maximum level during the rf pulse of $\overline{n}_e = 1.9 \times 10^{13}\,\mathrm{cm}^{-3}$ at $t = 26.5\,\mathrm{ms}$.

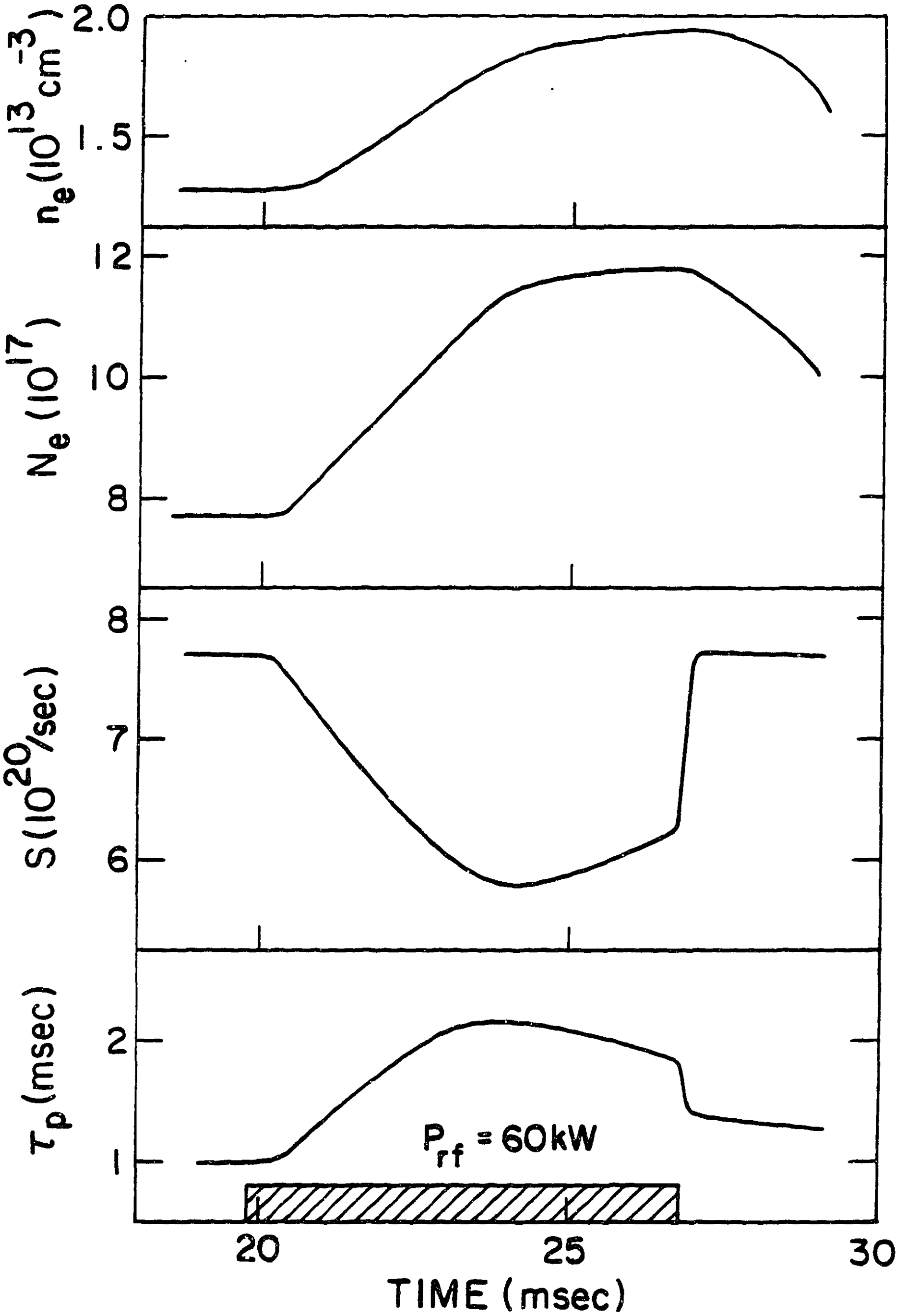

Fig. 5.8: Temporal evolution of the total electron number N_e, the ionization source term S, and the global particle confinement time τ_p calculated from the profiles of Fig. 5.7.

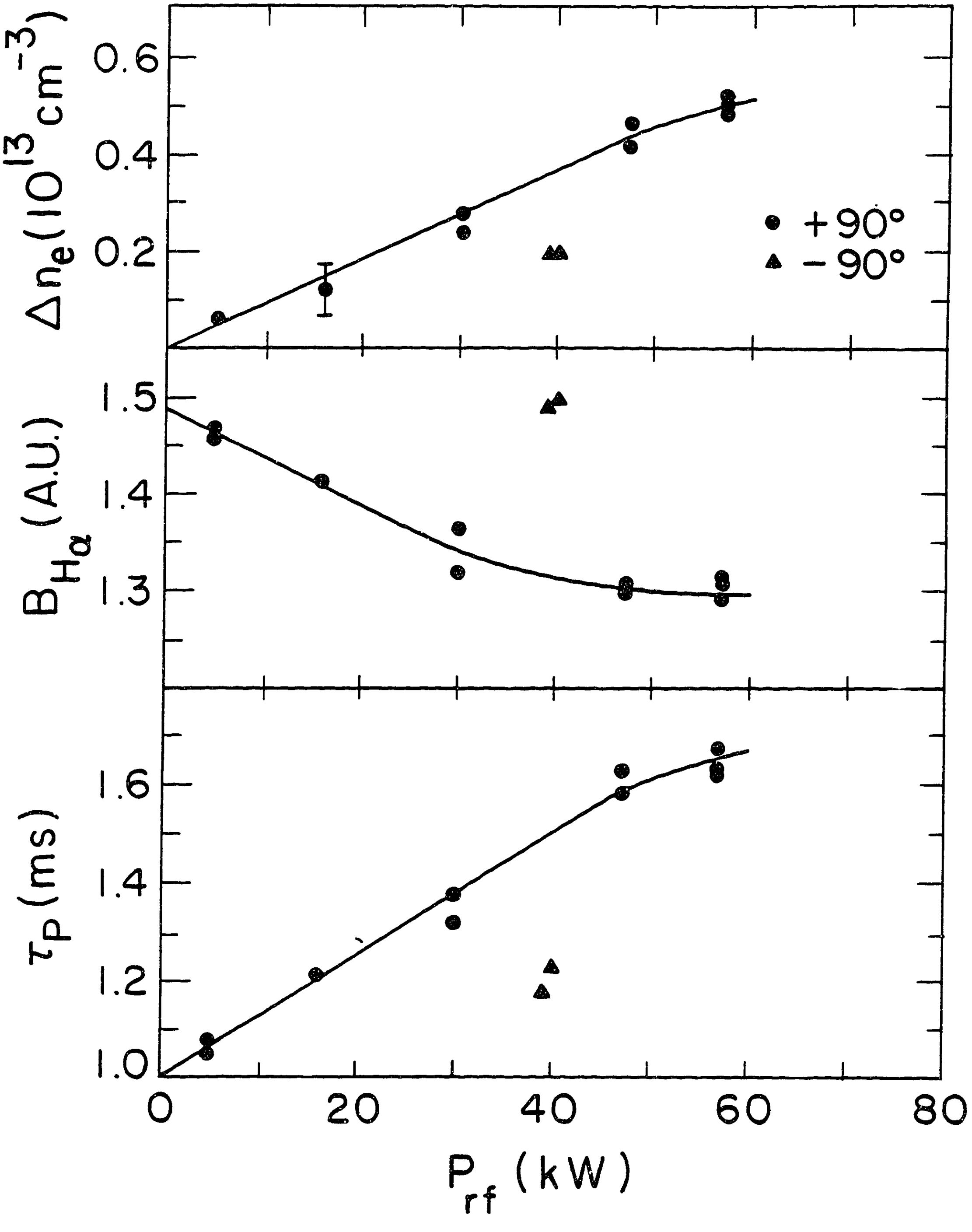

Fig. 5.9: Density rise $\Delta\bar{n}_e$, H_α brightness level, and global particle confinement time versus the rf power level for an initial density of $\bar{n}_e = 1.3 \times 10^{13}\,cm^{-3}$ and $\Delta\phi = +90°$ (current drive phasing). Also shown are two points with the waveguide phasing reversed to $\Delta\phi = -90°$.

confinement upon rf current drive is found from the dependence of τ_p on waveguide phasing. Two data points with $\Delta\phi = -90°$, taken during the same power scan, are plotted in Fig. 5.9. In these cases, the increase in τ_p was less than half of that with $+90°$ phasing at the same power level.

The dependence of $\Delta\overline{n}_e$ on the density level prior to rf injection is shown in Fig. 5.10 for the range $\overline{n}_e = 0.8 - 2.6 \times 10^{13}\,\mathrm{cm}^{-3}$. The data was compiled from several experimental runs. For these measurements a 7 ms rf pulse length was used. The rf power level was in the range $P_{rf} = 60 - 70\,\mathrm{kW}$, except at the lowest densities where it was reduced slightly in order to avoid excessive outward plasma motion. Since the density behavior depended sensitively on the plasma equilibrium position, the programmable vertical field bank was utilized in order to control the in/out motion during the rf pulse.

As shown in Fig. 5.10, the density rise during rf injection can be as large as a factor of two when the initial density is sufficiently low ($\overline{n}_e \sim 1 \times 10^{13}\,\mathrm{cm}^{-3}$). At higher densities, the effects become smaller. There also appears to be an upper density limit for improved particle confinement. For a toroidal field strength of 11 kG, this limit occurs at a density of $\overline{n}_e \simeq 2.1 \times 10^{13}\,\mathrm{cm}^{-3}$. Below this limit, density rises are accompanied by decreases in the H_α emission. Above the limit, slight density decreases are observed, accompanied by small increases in the H_α emission. These latter observations indicate that the bulk particle confinement may actually be degraded by the rf at the higher densities. Note that this density limit coincides approximately with the diminution of other current drive effects at $\overline{n}_e \simeq 2 \times 10^{13}\,\mathrm{cm}^{-3}$, as described in the previous section of this chapter. A similar transition in particle confinement behavior has been observed at the upper density limit for strong wave-electron interaction ($\overline{n}_c \simeq 5 \times 10^{13}\,\mathrm{cm}^{-3}$) on the FT tokamak,[76] where 2.45 GHz rf power is used as well. As shown in Fig. 5.10, when the toroidal field strength is lowered from 11 kG to 9 kG, the density rise observed during rf injection is substantially reduced. In addition, the upper density limit for improved particle confinement decreases to $\overline{n}_e \simeq 1.6 \times 10^{13}\,\mathrm{cm}^{-3}$. This dependence on the toroidal magnetic field suggests that poor wave accessibility is responsible

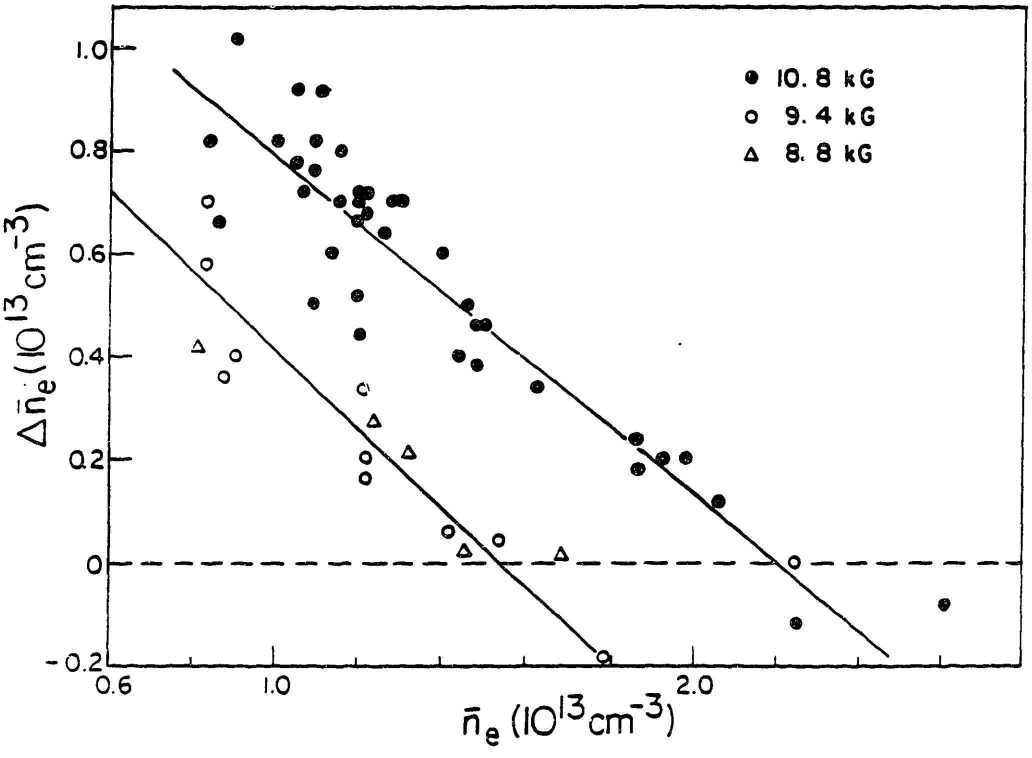

Fig. 5.10: Dependence of the density rise $\Delta\bar{n}_e$ on the initial density prior to the rf injection. For these discharges, $\Delta\phi = +90°$, and $P_{rf} = 60 - 70\,\text{kW}$, except at the lower densities where the power was reduced slightly to avoid outward motion of the plasma.

for the upper density limit for improved τ_p during 2.45 GHz current drive.

5.2.4 Discussion

The results of the previous subsection indicate that the improvement in particle confinement during rf current drive experiments is related to the generation of a superthermal electron tail since the dependence of τ_p on the rf power level, waveguide phasing and density is very similar to other current drive effects. In order to explain the factor-of-two density increases observed in the experiment, however, a mechanism which links the presence of a superthermal electron tail to bulk particle confinement must be established. Possible candidates include: 1) a reduction in magnetic fluctuations due to suppression of MHD activity during current drive, 2) a modification of the electrostatic potential profile of the plasma,[75] and 3) a reduction in low frequency drift wave activity. So far, only the first of these possibilities has been explored. Preliminary measurements of the MHD activity during current drive have beed carried out using $\dot{B}_\theta$ loops to measure poloidal field fluctuations and a gas-filled proportional counter to measure soft x-ray fluctuations. Typical signals are shown in Fig. 5.11 (for the same discharge as shown previously in Fig. 5.6). The 2 mm interferometer signal indicates that the density rises during the first 7 ms of the rf pulse from $\overline{n}_e = 1.0 \times 10^{13}\,\mathrm{cm}^{-3}$ to $\overline{n}_e = 2.0 \times 10^{13}\,\mathrm{cm}^{-3}$. During this time, the level of poloidal field fluctuations appears to decrease as indicated by the reduced amplitude of the $\dot{B}_\theta$ signal. Once the density reaches the maximum level, however, the poloidal field fluctuations return to their original level. Also at this time, large sawtooth oscillations (slow rise/fast fall) appear on the density trace as well as on the soft x-ray signal from the center of the plasma. While these effects may indicate a change in the MHD behavior, it is not known whether this is responsible for the sudden degradation in particle confinement when the density reaches $\overline{n}_e \simeq 2 \times 10^{13}\,\mathrm{cm}^{-3}$ (see the H_α trace in Fig. 5.6). More detailed studies of the MHD activity during current drive are clearly warranted.

Density increases during lower-hybrid current drive have been observed previously in several tokamaks, including Versator II[7], JIPP T-II[77], WEGA[24], and

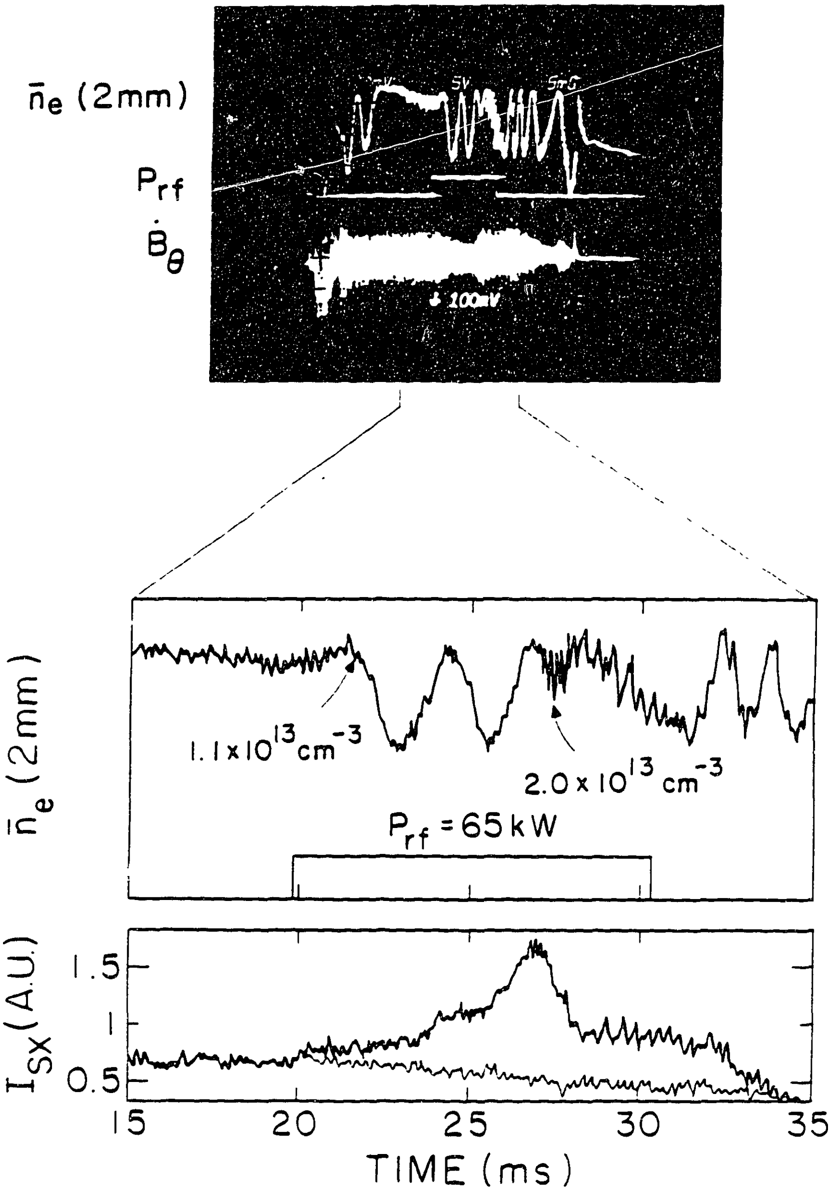

Fig. 5.11: Temporal behavior of the poloidal field fluctuation level $\dot{B}_\theta$, line-averaged density $\overline{n}_e$ and soft x-ray emission level I_{SX} behavior during rf injection when improved particle confinement is observed. During the density rise, the level of MHD fluctuations appears to be reduced. Once the density reaches the maximum level of $\overline{n}_e = 2.0 \times 10^{13}\,\mathrm{cm}^{-3}$ at $t = 27\,\mathrm{ms}$, the poloidal field fluctuations return to their original level, and pronounced sawtoothing is observed on the density and soft x-ray traces.

JFT-2[78]. The Versator II 800 MHz current drive experiment was the first to show that the density increases were due to an improvement in the global particle confinement time.[31,32] In those studies, which were conducted in the low density regime ($\overline{n}_e \leq 6 \times 10^{13}\,\mathrm{cm}^{-3}$), factor-of-two increases in τ_p were observed only when the anomolous doppler relaxation instability was stabilized by the rf. Under certain conditions, the tail instability could be completely suppressed with the injection of as low as 4 kW of rf power, with $\Delta\phi = +90^\circ$. However, further increases in the rf power level produced no additional improvement in particle confinement. The τ_p improvement was phase dependent; however, this was due to the fact that with $+90^\circ$ phasing, stabilization of the tail mode was possible, while with -90° phasing, it was not.

The 2.45 GHz particle confinement experiments on Versator were conducted in a relatively high density regime ($\overline{n}_e > 8 \times 10^{13}\,\mathrm{cm}^{-3}$) where there was no evidence of tail instability spikes during the ohmic discharges or during rf injection. We note that density rises do occur during 2.45 GHz rf injection in the flat-top current drive regime ($\overline{n}_e \leq 1.0 \times 10^{13}\,\mathrm{cm}^{-3}$). However, with the OH transformer primary open-circuited, direct comparisons between discharges with and without rf injection are not straigtforward. There is also evidence that at low densities stabilization of the bursting anomolous doppler instability with 2.45 GHz rf does lead to a density increase. Unfortunately, stabilizing the tail instability at low densities in Versator II resulted in an uncontrollable outward plasma motion which may have had a significant effect on the density behavior. Further work is needed to compare 800 MHz and 2.45 GHz current drive in a common operating regime in order to determine whether the physical mechanism responsible for the improved particle confinement is related in the two experiments.

5.3 Electron Heating Experiments

A preliminary search for 2.45 GHz bulk electron heating has been carried out at the following plasma parameters: $\overline{n}_e = 1.0 - 1.5 \times 10^{13}\,\mathrm{cm}^{-3}$, $I_p = 40 - 60\,\mathrm{kA}$, $B_T \simeq 12\,\mathrm{kG}$, $P_{rf} \leq 81\,\mathrm{kW}$, $\Delta\phi = \pi/2,\ \pi$. With a relative waveguide phasing of

π, the Brambilla spectrum is symmetric and peaks at $|N_{\|}| \simeq 5$ with a FWHM of $\Delta N_{\|} \sim 4$. In most cases the input rf power level was comparable to, or even greater than, the ohmic input power level. The central bulk electron temperature was measured with Thomson scattering.[79] The behavior of the superthermal electron population was also monitored using both the soft and hard x-ray PHA diagnostics, as well as the $2\omega_{ce}$ diagnostic.

In experiments with a relative waveguide phasing of $\Delta\phi = \pi$, there has been no evidence of significant bulk electron heating, even though the rf power does generate a superthermal electron tail, as indicated by nonthermal cyclotron and x-ray emission (see Chapter 6). In a typical case with $\overline{n}_e = 1.3 \times 10^{13}\,\mathrm{cm}^{-3}$ and $I_p \simeq 40\,\mathrm{kA}$, the injection of 77 kW of rf power for 7 ms produced a current increase $\Delta I \simeq 3.4\,\mathrm{kA}$ and a loop voltage drop $\Delta V/V \simeq 0.2$, reducing the ohmic input power from 60 to 50 kW during the rf pulse. The central electron temperature remained relatively constant at $T_{e0} \simeq 350\,\mathrm{eV}$ before, during, and after the rf pulse.

The lack of bulk heating may be due to the relatively low $N_{\|}$ values of the launched waves, combined with poor electron tail energy confinement. From equation (2.21) strong Landau damping is expected to occur when $N_{\|} \geq 7.0[T_e(keV)]^{-1/2} \simeq 12$ for a 350 eV plasma. The launched wave spectrum, however, ranges from $N_{\|} \simeq 3$ to $N_{\|} \simeq 7$. Low $N_{\|}$ waves tend to interact with high energy tail electrons which collide relatively infrequently with the bulk electrons. Unless the tail confinement time is greater than the collisional thermalization time, bulk heating will be inefficient.

In an attempt to improve tail confinement and to provide a hotter ohmic target plasma in these heating experiments, the ohmic current was raised to the 60 kA level. While the ohmic temperature increased slightly to $T_{e0} \simeq 430\,\mathrm{eV}$ ($P_{OH} \sim 90\,\mathrm{kW}$), no significant bulk heating was observed when 80 kW of rf power was injected into discharges at $\overline{n}_e \simeq 1.1 \times 10^{13}\,\mathrm{cm}^{-3}$.

In another set of experiments with +90° waveguide phasing, the bulk electron temperature actually decreased during rf injection. With $\overline{n}_e = 1.4 \times 10^{13}\,\mathrm{cm}^{-3}$

and $I_p \simeq 40\,\mathrm{kA}$, the injection of 57 kW of rf power produced a loop voltage drop of $\Delta V/V \simeq 0.4$. The central electron temperature decreased from 350 eV before the rf pulse to 275 eV during the rf pulse. This result eliminates bulk electron heating as the cause of the observed increases in the toroidal current and the drops in the single turn loop voltage in this density regime.

Other lower hybrid experiments (Alcator A,[62] FT,[25] Alcator C,[80] ASDEX,[81] PLT,[82] JFT-2,[78] WEGA,[83] ATC[84]) have observed bulk electron heating at comparable densities. Noteworthy results have been obtained in the FT experiment ($f = 2.45\,\mathrm{GHz}$, $N_{\|} \simeq 1.3 - 2.5$, $\bar{n}_e \simeq 3 \times 10^{13}\,\mathrm{cm}^{-3}$, $B_T = 8\,\mathrm{T}$) where temperature increases of $\Delta T_e \sim 700\,\mathrm{eV}$ and $\Delta T_i \sim 200\,\mathrm{eV}$ were produced with $P_{rf} = 250\,\mathrm{kW}$, and Alcator C ($f = 4.6\,\mathrm{GHz}$, $N_{\|} \simeq 2 - 4.5$, $\bar{n}_e = 1.3 \times 10^{14}\,\mathrm{cm}^{-3}$, $B_T = 8\,\mathrm{T}$) where temperature rises of $\Delta T_e \simeq 1000\,\mathrm{eV}$ and $\Delta T_i \simeq 700\,\mathrm{eV}$ were achieved with $P_{rf} = 850\,\mathrm{kW}$. In the latter case, where silicon-carbide-coated graphite limiters were used, Z_{eff} rose from 1.5 to 4. More recently on Alcator C,[85] up to 1.4 MW has been injected into plasmas at lower toroidal fields $B_T \simeq 6\,\mathrm{T}$, resulting in temperature increases of $\Delta T_e \simeq 600\,\mathrm{eV}$, $\Delta T_i \simeq 250\,\mathrm{eV}$, and $\Delta Z_{eff} \sim 0.5$. In previous 800 MHz experiments on Versator with the wide-gap 4-waveguide side-launching antenna ($N_{\|} \sim 5.5$ for $\Delta\phi = \pi$), no bulk electron heating was observed for $\bar{n}_e = 1 - 3 \times 10^{13}\,\mathrm{cm}^{-3}$ and $P_{rf} \simeq 100\,\mathrm{kW}$, although soft x-ray tail enhancements were observed[40].

In recent 2.45 GHz experiments on PLT[86] in the density range $\bar{n}_e = 0.8 - 1.5 \times 10^{13}\,\mathrm{cm}^{-3}$, strong electron heating ($\Delta T_{e0} \sim$ several keV) has been observed during current drive with $\Delta\phi = +60°$, $+90°$. The heating occurs in the central region of the plasma, and only when the MHD sawtooth instability present in ohmic discharges, is stabilized by the rf. The mechanism for the stabilization is not yet understood. In the Versator 2.45 GHz experiments, we observe sawtooth activity with the soft x-ray proportional counter during ohmic discharges with high density and/or high current. So far, we have not observed a stabilization of these sawteeth during rf injection with $\Delta\phi = +90°$, although changes in the sawtooth behavior have been observed during the particle confinement experiments. Further work in this area is needed, expecially at lower densities ($\overline{n}_e < 1 \times 10^{13}\,\mathrm{cm}^{-3}$) where current drive effects are relatively large.

In order to understand the lack of bulk electron heating during 2.45 GHz experiments on Versator II, it is useful to consider the global power balance equations for the bulk plasma and the electron tail (see Fig. 4.2 for a power flow diagram). In the steady state, neglecting both the radiated power and the power flow to the ions, the power balance equation for the bulk electrons may be written in the following simplified form:

$$\frac{E_b}{\tau_b} = \frac{V^2}{R_{sp}} + P_{tb}, \tag{5.4}$$

where $E_b = \frac{3}{2}\int n_e(r)T_e(r)dV$ is the stored energy of the bulk electrons, τ_b is the global bulk energy confinement time, and V^2/R_{sp} is the ohmic power dissipated by the bulk current (assuming Spitzer resistivity). The total collisional power flow from the tail electrons to the bulk electrons, P_{tb}, can be obtained from the global power balance equation for the tail electrons, given by:

$$\frac{E_t}{\tau_t} = \alpha P_{rf} - P_{tb} - P_{el}, \tag{5.5}$$

where E_t is the stored energy in the electron tail, τ_t is the global tail energy confinement time, α is the rf power absorption efficiency, and P_{el} is the inductive power flow from the tail to the poloidal magnetic field (see Fig. 4.2). Again, we have neglected the radiated power. The behavior of the bulk electron temperature during quasi-steady-state current drive is the most straightforward to analyze since we may neglect the V^2/R_{sp} term in Eqn. (5.4) as well as the P_{el} term in Eqn. (5.5). In this case, bulk heating is due entirely to collisional slowing down of the tail electrons generated by the rf. Hence, the power balance equations become:

$$\begin{aligned} \frac{E_b}{\tau_b} &= P_{tb} \\ \frac{E_t}{\tau_t} &= \alpha P_{rf} - P_{tb}. \end{aligned} \tag{5.6}$$

From the above equations, it can be seen that the bulk electron cooling from 300 eV to 100 eV observed during steady state current drive may be the result of one or more of the following effects: 1) rf degradation of the bulk confinement time τ_b, 2) the elimination of the ohmic input power, V^2/R_{sp}, 3) inefficient absorption of rf power ($\alpha \ll 1$), and 4) a low tail confinement time, τ_t. An evaluation of the bulk confinement time requires Thomson scattering profile measurements. Since these have not yet been carried out, we will attempt only to evaluate P_{tb} using the tail power balance relation in Eqn. (5.6). In the following chapter we attempt to determine the electron tail distribution function $f_t(\mathbf{p})$ from the x-ray measurements in order to obtain estimates for E_t and P_{tb} during steady state current drive.

Chapter 6

X-ray Measurements

In this chapter, measurements of the plasma x-ray emission in the energy range 1 – 500 keV are described. The primary objective of these studies during lower hybrid current drive and electron heating experiments has been to determine the properties of the electron distribution function $f(\mathbf{v})$. To accomplish this, soft and hard x-ray pulse height analysis diagnostics have been developed for Versator in order to measure the non-thermal x-ray emission from rf-generated electron tails. These diagnostic systems are described in Section 6.1. The interpretation of the x-ray emission can be quite complex since the photon energy is not identical to the energy of the scattered electron. In Section 6.2, the theory of thermal and non-thermal x-ray emission will be outlined.

In Section 6.3, we present results from 800 MHz and 2.45 GHz lower hybrid current drive experiments. During 2.45 GHz flat-top current drive, an energetic electron tail is generated in the center of the plasma, with energies up to to 160 keV. Simulations of the x-ray emission, using a simple model distribution function, are described in Section 6.4. From our analysis, we have determined that: 1) $T_\perp$ is slightly larger than expected from 2-d theory, 2) approximately 90% of the plasma kinetic energy is stored in the tail, and 3) less than 10% of the injected rf power is dissipated by collisions between tail electrons and bulk electrons. This latter finding indicates poor radial tail confinement (compared to the tail thermalization time), which may explain the lack of bulk heating during electron heating experiments, and the bulk cooling observed during current drive.

6.1 X-ray PHA Experimental Technique

In x-ray pulse height analysis[87] (PHA), individual x-ray photons incident on a detector generate output pulses which are proportional to the photon energy $h\nu$.

The spectrum of photon energies is determined by sorting the pulses according to their height. Two x-ray PHA diagnostics have been developed for Versator, one utilizing a Si(Li) detector to measure the plasma soft x-ray emission (1 – 25 keV), and the other using a NaI(Tl) scintillator to measure the plasma hard x-ray emission (20 – 500 keV). In this section, we describe these two x-ray diagnostics, along with the data analysis procedure used to determine the absolute intensity of the plasma x-ray emission.

6.1.1 Si(Li) Detector PHA Diagnostic

The soft x-ray detector is a liquid nitrogen cooled, lithium-drifted silicon detector. Incident photons create electron-hole pairs in the silicon crystal, generating charge pulses proportional to the photon energies. A charge sensitive preamplifier converts the charge pulses into voltage pulses. Good detector energy resolution is necessary because the soft x-ray spectra emitted from thermal plasmas have steep slopes. In addition, good resolution allows the identification of impurity lines. The Canberra Si(Li) detector Model 7383 (thickness = 5 mm, active area = 80mm^2) has a resolution of 280 eV for Fe-55 (5.9 keV), with an amplifier shaping time constant of 1 μs.

Figure 6.1 shows how the Si(Li) detector is connected to the Versator tokamak. The entire system, which is under vacuum to prevent air absorption of low energy photons, may be tilted up or down in order to scan the plasma cross section. In order to avoid pulse pile-up in the electronics, the photon counting rate is controlled with a pair of lead apertures. The front aperture, which is continuously variable, defines the cross sectional area of the plasma seen by the detector, while the fixed rear aperture defines the solid angle subtended by the detector. Various absorber foils (Be, Al) may be placed in front of the detector in order to accelerate the counting process and improve statistics at higher energies where counts are relatively infrequent. By eliminating the lowest energy photons, the variable aperture may be opened without increasing the overall count rate.

In order to reduce the background level of x-rays originating from the tokamak

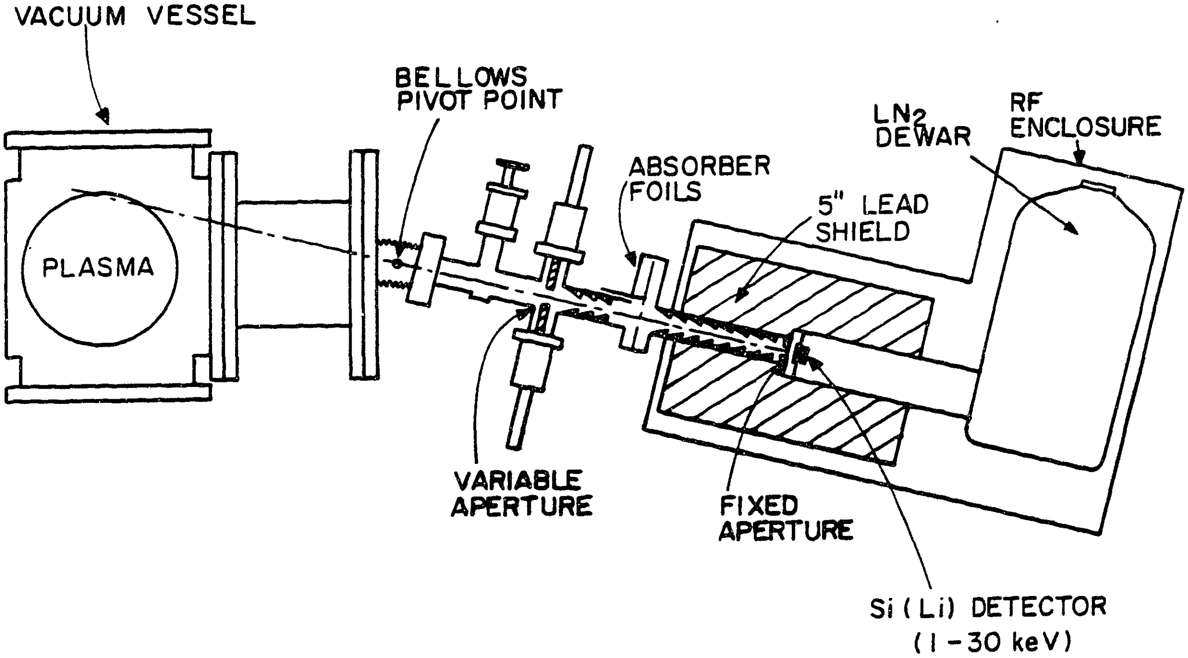

Fig. 6.1: Diagram of the Si(Li) detector used to measure the plasma soft x-ray emission in the energy range 1 – 25 keV.

walls and limiters, the Si(Li) detector is enclosed in five inches of lead shielding. In addition, a series of lead collimators restricts the detector field of view to a narrow region around the front aperture. The collimators are conical shaped to eliminate flourescence. The Si(Li) detector is also quite sensitive to the electrical, mechanical and rf noise present near the tokamak during plasma discharges. The ceramic electrical break eliminates the electrical noise problems associated with plasma disruptions. The bellows, along with rubber foot pads on the support structure, eliminate direct mechanical coupling to the machine. Rf pickup in the detector's sensitive front-end electronics (problematic during LH experiments), is eliminated by enclosing the Si(Li) detector and pre-amp in a copper rf-shielded enclosure. In addition, all of the input and output cables entering the rf enclosure are filtered with low-pass pi-section filters.

The remainder of the electronics in the Si(Li) detector PHA system is shown in Fig. 6.2. The spectroscopy amplifier shapes the pre-amp output pulses for optimum peak detection by the multi-channel analyzer (MCA). Problems occur when two pulses arrive sufficiently close together that the MCA can no longer resolve the individual peaks. In this case, spectral distortion is possible since a pair of pulses may be converted into a single "double" pulse.[87,88] The pile-up rejector (PUR) detects such events and inhibits their processing by the MCA. Meanwhile, the total incoming count rate is recorded by the scalers. In this way, the missing pulses due to pile-up rejection may be accounted for. However, due to the finite pulse pair resolution time of the PUR circuitry ($\tau \sim .5\mu s$), pulse pile-up is still problematic at sufficiently high count rates. We choose to alleviate these problems by: 1) maintaining relatively low count rates ($\sim 10 - 15\,\mathrm{kHz}$), and 2) by using absorber foils to eliminate low energy counts when collecting the high energy portion of the spectrum.

Typically, 1000 – 3000 counts are needed for a complete x-ray spectrum with acceptable statistics at high photon energies. For a gate pulse duration of 10 ms, and a count rate of 10 kHz, this requires from 10 to 30 plasma shots. X-ray data from up to four non-overlapping time intervals may be stored during a single shot

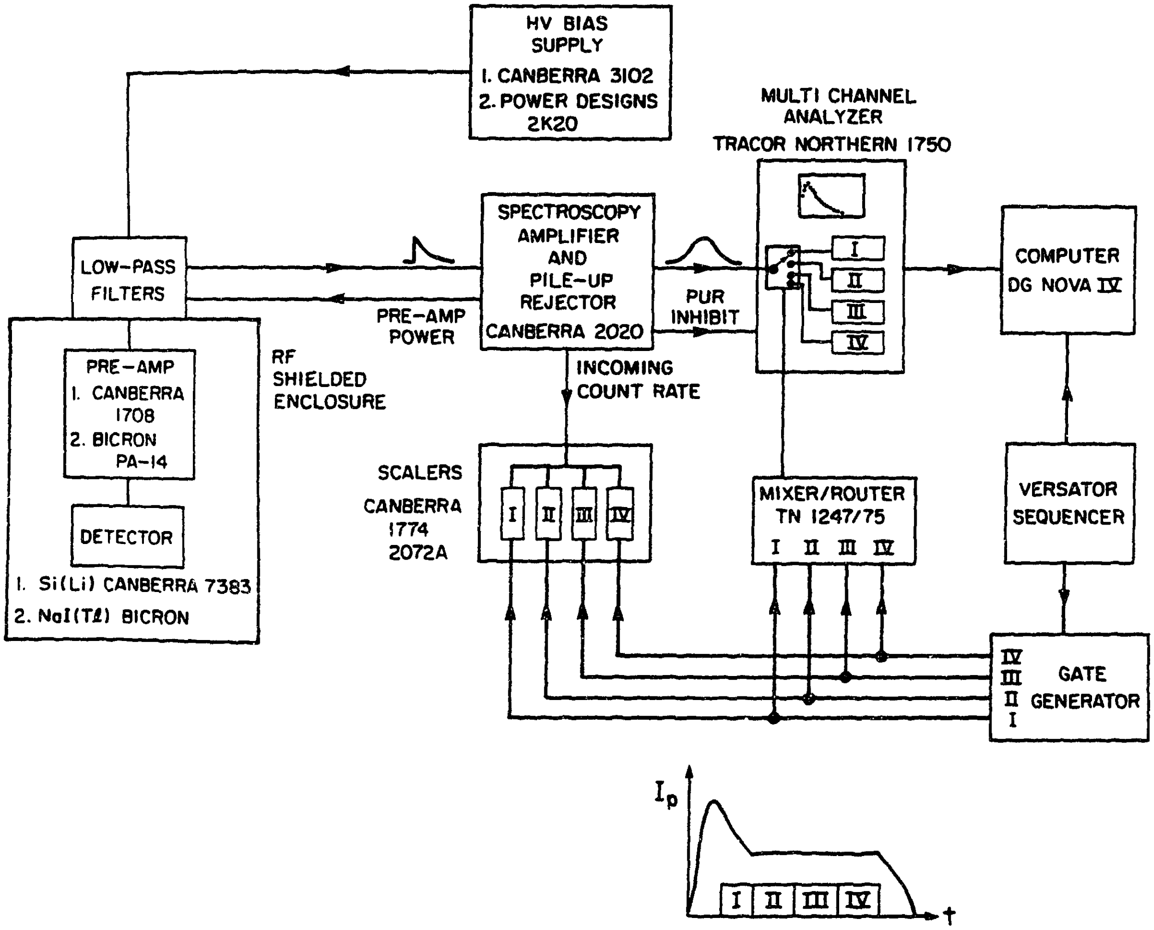

Fig. 6.2: Block diagram of the PHA electronics.

by using the mixer/router in conjunction with the MCA. The mixer/router directs the x-ray data from each time interval into the appropriate MCA memory group. After accumulating a sufficient number of MCA counts for the desired statistics, the completed x-ray spectrum is transferred to the computer for further analysis.

6.1.2 The NaI Detector PHA System

The Si(Li) detector becomes nearly transparent to incident photons with energies exceeding 25 keV. In order to measure higher energy x-ray spectra, the NaI(Tl) PHA system, shown in Fig. 6.3, is used. At the higher photon energies, Compton scattering begins to dominate over photoelectric absorption. Therefore, a large detector volume is required to insure that the Compton scattered photons are fully absorbed within the detector. We have used a 3″ × 3″ NaI crystal, which has a photo-peak efficiency nearly equal to one for photon energies up to several hundred keV. Since the x-ray spectra at high energies tend to be relatively flat, the resolution requirements of the NaI detector are not severe. The resolution of our Bicron NaI(Tl) crystal at 662 keV (Cs-137) is 7.5%.

Due to the NaI detector's large size, it is much more sensitive than the Si(Li) detector to background radiation eminating from the limiters and walls of the tokamak. Therefore, we have enclosed the detector in a 2200 pound lead shield, with fourteen inches above, six inches below, and nine inches to the side of the detector. With the front aperture plugged, the background level of x-rays is negligible, even during runaway discharges.

In order to minimize the effects of wall radiation, the detector has been positioned beneath the tokamak so that it views a top port which is recessed 8 cm from the plasma. Radial scans of the entire plasma cross section are carried out by moving the detector/lead shield assembly along a track located underneath the torus. We have not directly determined the contribution of wall radiation by putting a window on the top port which is transparent to hard x-rays. However, profile measurements during ohmic discharges from the extreme edge of the plasma

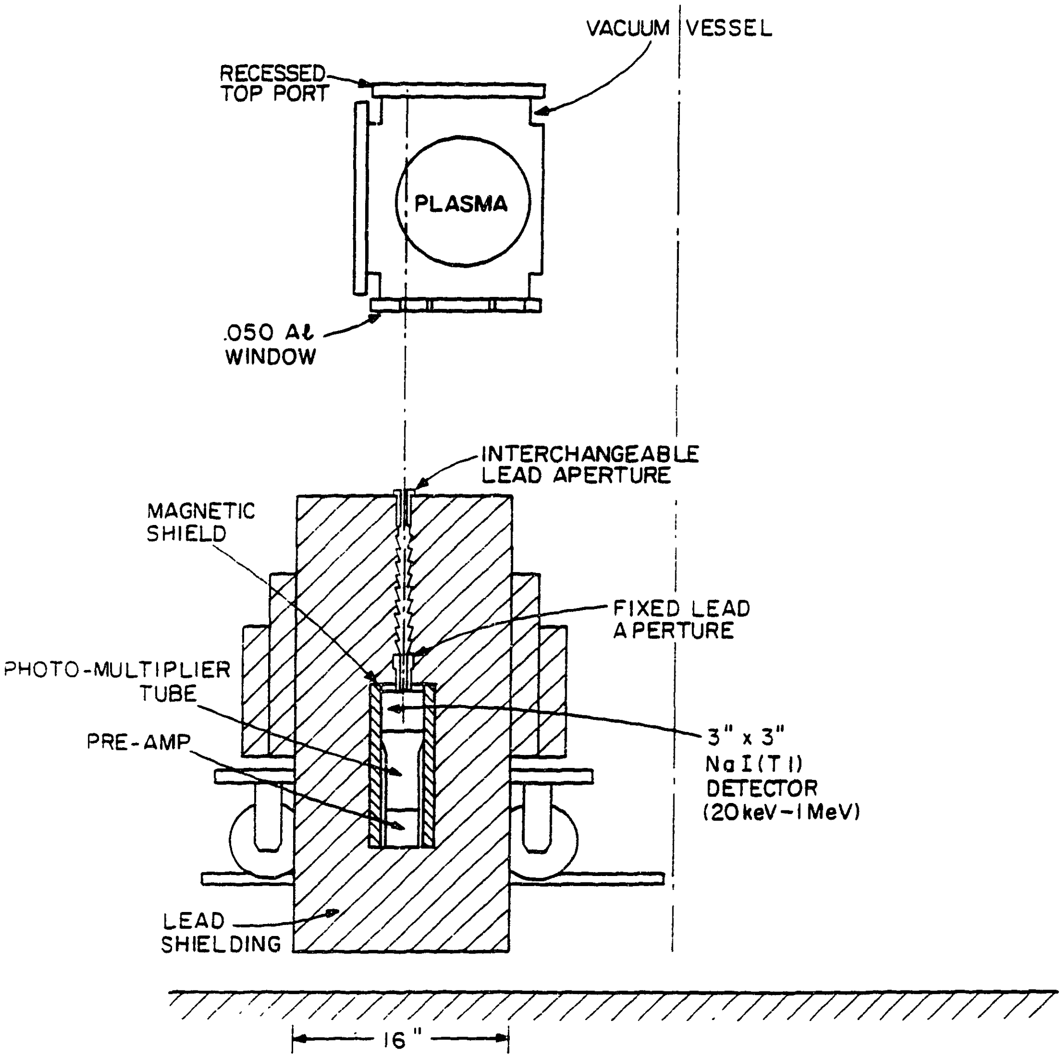

Fig. 6.3: The NaI detector used to measure the plasma hard x-ray emission in the energy range 20 – 500 keV.

show negligibly low count rates, indicating that the wall radiation contribution is probably unimportant.

The 50 mil Al window on the bottom port along with the 30 mil Al casing around the NaI crystal determine the low energy cut-off ($\sim$ 20 keV). Two lead apertures define the viewing area and the detector solid angle. The top aperture is interchangeable to allow count rate adjustments. Conical shaped lead collimators between the two apertures reduce the possibility of flourescence. The detector assembly is housed inside a one inch thick soft iron cylinder in order to shield the photomultiplier tube from magnetic interference. Rf pickup in the preamp during lower-hybrid heating experiments is eliminated with low pass filters on the signal cables. The remainder of the PHA electronics for the NaI system is identical to the Si(Li) detector system.

6.1.3 Data Analysis

In order to obtain the absolute chord-averaged x-ray emission from the measured raw spectral data, corrections must be applied for the detector geometry, collection time, and for the various absorber foils. These corrections, used in the computer analysis of both Si(Li) and NaI data are given by:

$$\frac{dW}{dk\,d\Omega_k} = \tag{6.1}$$

$$\frac{\exp \sum_j (\mu_j x_j)}{\eta} \left[\tau \sum_i (N_i \beta_i) \right]^{-1} \gamma\, \ell^{-1} \left(k \frac{\Delta n}{\Delta k} \right) \qquad \frac{\mathrm{keV}}{\mathrm{kev\,cm^3\,sec\,ster}},$$

where $dW/dk d\Omega_k$ is the chord-averaged power radiated per unit volume per unit photon energy interval per unit solid angle. The quantity k is the energy of a given MCA channel, Δk is its width, and Δn is the number of raw spectral counts. The correction for a given combination of absorber foils is given by the term $\exp \sum_j (\mu_j x_j)$ where $\mu_j(k)$ is the absorption coefficient[89] and x_j is the thickness of the jth foil. The efficiency of the detector is given by $\eta(k)$. The correction for the detector geometry is given by $\beta = A_1 A_2 / d_{12}^2$ where A_1 is the area of the variable front aperture, A_2 is the area of the rear fixed aperture, and d_{12} is the distance between the apertures. The summation over i allows for the possibility that the aperture settings may be changed during the collection of a single spectrum. The total collection time is $\sum_i N_i \tau$, where N_i is the number of shots with aperture i, and τ is the gate duration for each shot. The factor γ corrects for pile-up and is equal to the total number of scaler counts divided by the total number of MCA counts. The factor ℓ is the chord length, which is given by $\ell = 2(a^2 - y^2)^{1/2}$ where a is the minor radius and y is the minimum radius along the chord. Hard x-ray data is often plotted in terms of the photon count rate $dN/dt\, dk\, d\Omega$, where N is the number of photon counts. This may be obtained from the photon intensity given by Eqn. (6.1) simply by dividing by the photon energy k.

6.2 X-ray Emission Processes

The x-ray emission from a plasma primarily consists of: 1) bremsstrahlung radiation due to free-free electron transitions in the Coulomb fields of ions, 2) recombination radiation due to free electron capture into ion bound states, and 3) line radiation due to electron transitions between ion bound states. The first two components, bremsstrahlung and recombination radiation, make up the continuum portion of the x-ray spectrum. For thermal plasmas, soft x-ray measurements of the continuum spectrum (mainly recombination radiation) may be used to determine T_e and Z_{eff}, as shown in Subsection 6.2.1. For highly non-thermal plasmas, hard x-ray measurements provide the most direct picture of the fast electron tail. In this case, the x-ray emission is dominated by electron-ion bremsstrahlung. In Subsection 6.2.2, we describe the properties of bremsstrahlung radiation and show how the x-ray emission from an arbitrary electron distribution function may be calculated.

6.2.1 Thermal Soft X-ray Emission

The total continuum radiation from a non-relativistic, Maxwellian plasma, including bremsstrahlung and recombination radiation, may be written as:[88,90]

$$\frac{dW_{tot}(T_e,k)}{dk} = 3\times 10^{-15} n_e^2 \sum_i \frac{n_i Z_{iN}^2}{n_e} \sum_j \gamma_{ij} \frac{n_{ij}}{n_i}$$

$$\times T_e^{-1/2} \exp(-k/T_e) \qquad \frac{\mathrm{keV}}{\mathrm{kev\,cm^3\,s}}, \tag{6.2}$$

where $dW_{tot}(T_e,k)/dk$ is the power radiated per unit volume per unit photon energy interval dk, n_e is the density of electrons, n_i is the density of ion species i, T_e is the electron temperature in keV, and k is the photon energy. The enhancement of recombination over bremsstrahlung for ion species i depends on the charge state j and is given by the factor $\gamma_{ij} - 1$. The relative abundances of the various charge states, n_{ij}/n_i, are usually calculated from coronal equilibrium models. The recombination radiation spectrum exhibits steps or edges where the photon energy is equal to the ionization potentials of the final bound levels. Apart from the recombination edges, the shape of the x-ray continuum spectrum is approximately exponential, with $dW(T_e,k)/dk \propto \exp(-k/T_e)$. Hence, the electron temperature is indicated by the slope of the continuum spectrum plotted on a semi-log scale. The absolute level of the x-ray emission is determined by n_e and T_e, along with the concentrations and charge state distributions of the various impurity species present in the plasma. If n_e and T_e are known, then Z_{eff} can be determined from the enhancement of the x-ray emission over the level radiated from a pure hydrogen plasma.

The line radiation observed at energies exceeding 1.5 keV consists mainly of K, L, and M shell emission from high-Z impurities. The power radiated can be written as:[88]

$$P_L(T_e)_{ij} = n_e n_i \left(\frac{n_{ij}}{n_i}\right) \langle \sigma v(T_e)\rangle_{ij} k \qquad \frac{\mathrm{keV}}{\mathrm{cm^3\,s}}, \tag{6.3}$$

where $\langle \sigma v(T_e)\rangle_{ij}$ is the total excitation cross section averaged over a Maxwellian distribution. Excitation processes include electron impact excitation, dielectronic recombination and cascading following recombination to upper quantum levels. If the charge state distribution of the impurity species is known, then the high-Z impurity concentration can be determined from the intensity of the line radiation. We have not attempted such measurements because inner shell line radiation is generally not observed in thermal discharges on Versator. In non-thermal discharges, however, K_α impurity line radiation from Ti, Fe, Ni, and Cr is routinely observed.

A typical thermal soft x-ray spectrum from a Versator ohmically-heated discharge at $\bar{n}_e = 1.5 \times 10^{13}\,\mathrm{cm}^{-3}$ is shown in Fig. 6.4. For this case, the continuum slope indicates an electron temperature of $T_{e0} = 380\,\mathrm{eV}$. The steeper slope at low photon energies is due to profile effects and to the possible contribution of unresolvable Fe L lines located at energies $k < 1.8\,\mathrm{keV}$. Profile effects are important only for low photon energies, $k \leq 3T_e$, since the colder outer regions of the plasma emit x-ray spectra with steep slopes. In this particular case, Molybdenum-L line radiation was observed at $k \simeq 2.4\,\mathrm{keV}$, due to a Molybdenum rail limiter.

In order to estimate Z_{eff} from Fig. 6.4, we will use the values for $\bar{\gamma}_i = \sum_j \gamma_{ij} n_{ij}/n_i$ plotted in Ref. 88 for the impurity species carbon and oxygen, which make up the dominant contributions to Z_{eff} in Versator. The values given for $T_{e0} = 400\,\mathrm{eV}$ are $\bar{\gamma}_O \simeq 35$, and $\bar{\gamma}_C \simeq 10$. For simplicity, we will assume a single impurity species, and estimate a lower limit for Z_{eff} with oxygen and an upper limit for Z_{eff} with carbon. In this case, the total enhancement of the x-ray continuum over that of a pure hydrogen plasma is given by:

$$\begin{aligned} \varsigma &= \frac{dW_{tot}(T_e,k)/dk}{dW_{ff}(T_e,k,Z=1)/dk} \\ &= \sum_i \bar{\gamma}_i \frac{n_i Z_{iN}^2}{n_e} = \left(n_p Z_p^2 + \bar{\gamma}_i n_i Z_{iN}^2\right)/n_e, \end{aligned} \tag{6.4}$$

where the subscript p represents the background plasma, in this case hydrogen. Using the charge balance equation,

$$n_e = n_p Z_p + n_i Z_i,$$

we may write

$$Z_{eff} = \sum_i \frac{n_i Z_i^2}{n_e} = Z_i \left(Z_i - Z_p\right) \frac{n_i}{n_e} + Z_p, \tag{6.5}$$

where

$$\frac{n_i}{n_e} = \frac{\varsigma - Z_p}{\bar{\gamma}_i Z_{iN}^2 - Z_i Z_p}.$$

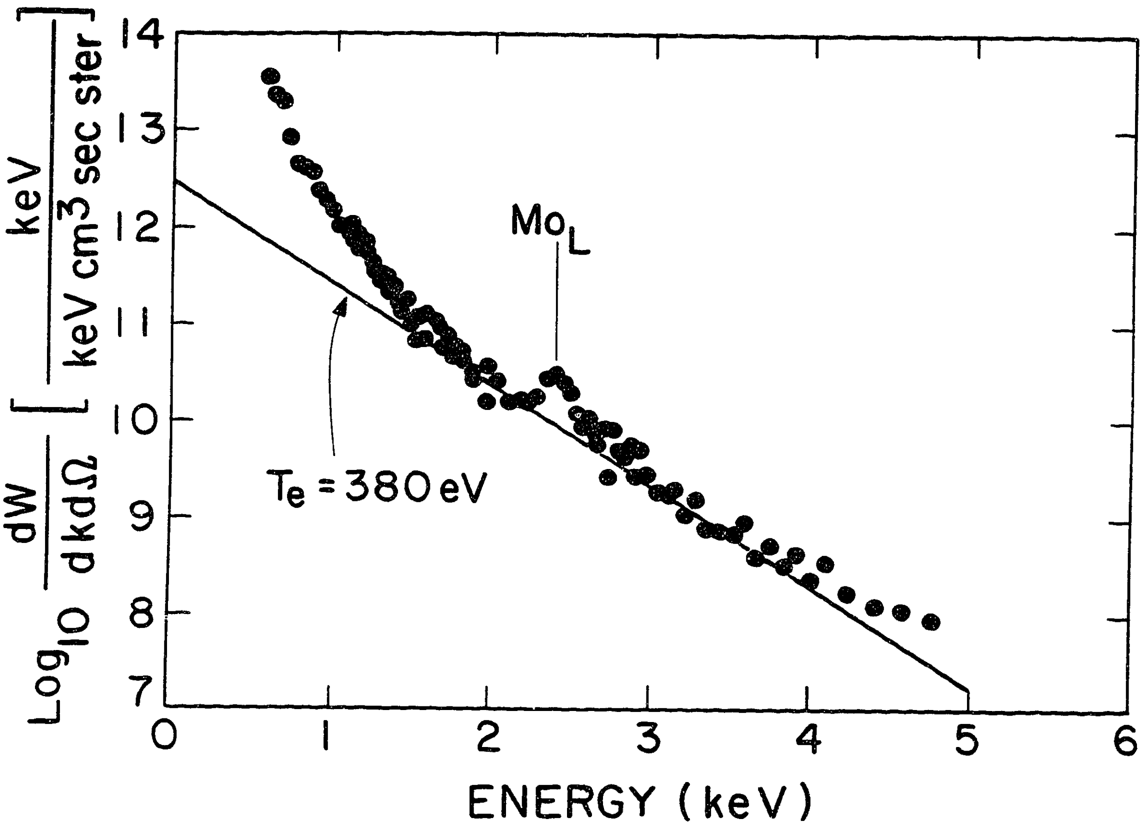

Fig. 6.4: Thermal soft x-ray spectrum from Ohmically-heated discharges at $\overline{n}_e = 1.5 \times 10^{13}\,\text{cm}^{-3}$.

Experimentally, ς can be determined from the zero intercept of the x-ray spectrum along with the density n_e and the temperature T_e:

$$\varsigma = \frac{dW(k = 0, T_e)/dk\, T_e^{1/2}}{3 \times 10^{-15} n_e^2}. \tag{6.6}$$

For Fig. 6.4, $n_e(0) \simeq 2.3 \times 10^{13}\,\mathrm{cm}^{-3}$, based on Thomson profile measurements. For the fit shown, $\varsigma \simeq 25$. [Note that Fig. 6.4 is plotted in units of keV/(keV cm^3 sec ster) and hence we must multiply by 4π to obtain $dW(k = 0, T_e)/dk$)]. Using Eqn. (6.5), we find $Z_{eff} = 1.6$ for a pure carbon impurity species, and $Z_{eff} = 3.0$ for a pure oxygen species. Thomson scattering estimates of Z_{eff} are typically near two for these types of gettered discharges.[39] Without information regarding the relative abundances of the dominant impurity species, more accurate estimates of Z_{eff} from the x-ray measurements are not possible.

Soft x-ray temperature profile measurements during ohmic discharges are generally in good agreement with Thomson scattering measurements except at low densities.[39] For densities $\overline{n}_e \leq 1.5 \times 10^{13}\,\mathrm{cm}^{-3}$, non-thermal electron tails are observed, and due to the addition of nonthermal x-rays, the soft x-ray temperatures begin to exceed the Thomson values. Nonthermal soft x-ray spectra have also been observed during rf heating experiments, including ECH,[38] and lower hybrid current drive[7] and electron heating.[40] In most of these cases, soft x-ray measurements of T_e and Z_{eff} were unreliable.

6.2.2 Relativistic Bremsstrahlung Emission

In the previous subsection it was shown that for typical thermal plasmas, the x-ray continuum is dominated by recombination radiation (by a factor of 25). The x-ray continuum radiation from high energy electron tails ($T > 100\,\mathrm{keV}$), on the other hand, is dominated by electron-ion bremsstrahlung.[35,91] This is a result of the fact that bremsstrahlung emission scales as $T_e^{1/2}$ while recombination scales as $T_e^{-1/2}$.

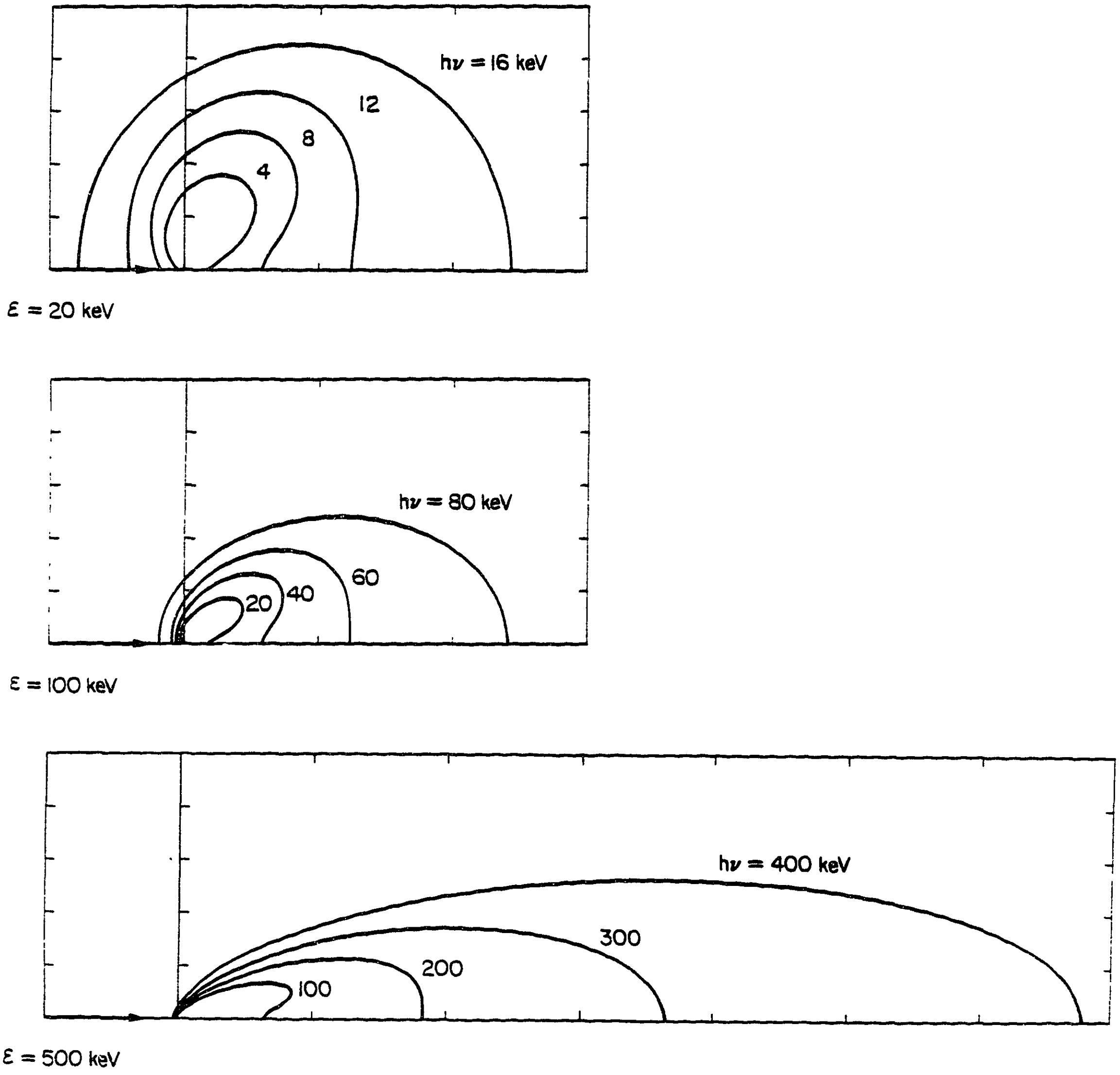

Fig. 6.5: Calculated bremsstrahlung radiation pattern for 5, 50, and 500 keV electrons travelling from left to right, and incident on a stationary ion located at the origin.

Figure 6.5 illustrates the basic properties of relativistic bremsstrahlung emission.[92] Plotted is the calculated bremsstrahlung radiation pattern, for 5, 50, and 500 keV electrons travelling from left to right, and incident on a stationary ion located at the origin. For a given electron kinetic energy ε, photons are emitted in all directions with energies $k < \varepsilon$. It is this property of bremsstrahlung radiation that makes it particularly difficult to unfold the x-ray emission data in order to determine the electron distribution function $f(\mathbf{v})$. Clearly, the most direct "picture" of $f(\mathbf{v})$ is obtained from the highest energy photons (i.e. hard x-rays) since relatively few electrons contribute to their emission. Furthermore, since the high energy bremsstrahlung x-rays are emitted mainly in the forward direction, they provide information about the direction of travel of the emitting electron. This latter property of bremsstrahlung emission has been exploited effectively on both the PLT[34,35,93] and Alcator C[36] tokamaks where the anisotropy of the fast electron distribution relative to the magnetic field was determined by measuring the hard x-ray emission as a function of angle with respect to the magnetic field. So far on Versator, only measurements from the perpendicular direction with respect to $\mathbf{B}$ have been carried out.

An example of a hard x-ray spectrum taken during a 2.45 GHz electron heating experiment with $\bar{n}_e \simeq 1.1 \times 10^{13}\,\mathrm{cm}^{-3}$ is shown in Fig. 6.6. For comparison, we have also plotted soft x-ray data on the same absolute intensity scale. A significant enhancement of both the soft and hard x-ray emission is produced by the rf injection. In general, soft x-ray tail temperatures are lower than hard x-ray tail temperatures. During the rf pulse, the slope of the soft x-ray tail is approximately 10 keV while the slope of the hard x-ray spectrum is approximately 40 keV. In Section 6.4, we will present a more detailed analysis of hard x-ray spectra measured during 2.45 GHz steady state current drive.

In the remainder of this section, we describe briefly how the bremsstrahlung emission spectrum may be calculated from a model electron distribution function. In order to include the possibility of anisotropic distribution functions, we use the cross section for relativistic bremsstrahlung which is differential in photon energy k

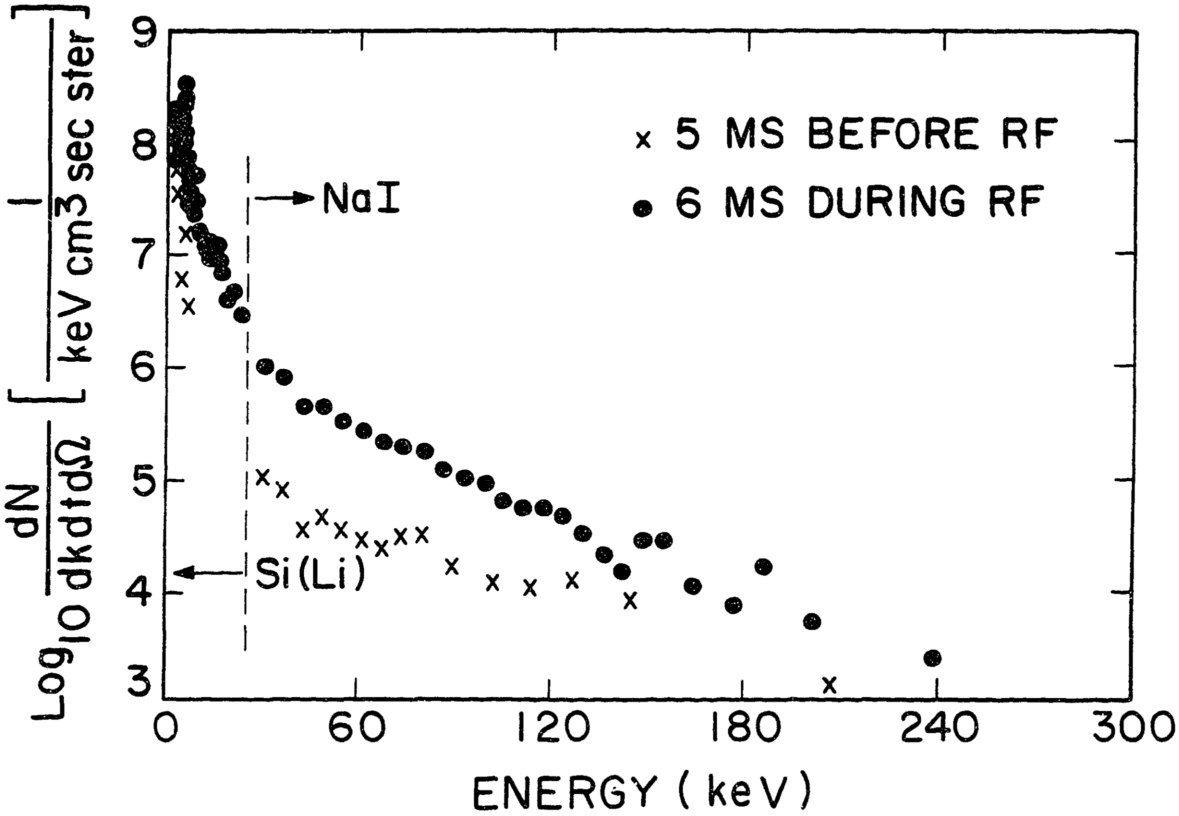

Fig. 6.6: Hard and soft x-ray spectra taken during the same 2.45 GHz electron heating run at $\overline{n}_e \simeq 1.1 \times 10^{13}\,\mathrm{cm}^{-3}$.

and emission angle θ_k, and is given by:[92]

$$\frac{d\sigma(Z_i, p, k, \theta_k)}{dk\, d\Omega_k} \qquad \frac{\text{cm}^2}{\text{keV ster}}, \tag{6.7}$$

where Z_i is the nuclear charge (neglecting screening effects), p is the electron momentum, and $d\Omega_k$ is the solid angle subtended by the detector. The photon emission rate, dN/dt, is obtained by multiplying the cross section by the (stationary) ion target density n_i and the electron beam flux $n_e v$, and then summing over the ion species:

$$\frac{dN(k, p, \theta_k)}{dt\, dk\, d\Omega_k} = \sum_i n_i n_e v \frac{d\sigma(Z_i, p, k, \theta_k)}{dk\, d\Omega_k} \qquad \frac{1}{\text{kev cm}^3\,\text{sec ster}}. \tag{6.8}$$

The total photon emission rate is obtained by integrating equation (6.8) over the normalized electron distribution function, $f(\mathbf{p}) = f(p_{\|}, p_{\perp})$ where $p_{\|}$ and $p_{\perp}$ are the momentum components parallel and perpendicular to the magnetic field. This gives:

$$\begin{aligned} \frac{dN(\theta_d, k; f)}{dk\, dt\, d\Omega_k} &= c n_e^2 Z_{eff} \int_{-\infty}^{+\infty} dp_{\|} \int_0^{2\pi} d\varphi_p \int_{\sqrt{(k+1)^2-(p_{\|}^2+1)}}^{+\infty} p_{\perp} dp_{\perp} \\ &\times \left[f(p_{\|}, p_{\perp}) \frac{p}{\sqrt{p^2+1}} \frac{d\sigma(p, k, \theta_k)}{dk\, d\Omega_k} \right] \quad \frac{1}{\text{keV cm}^3\,\text{sec ster}}, \end{aligned} \tag{6.9}$$

where θ_d is the detector angle with respect to $\mathbf{B}$. The relationship between θ_k and θ_d is given by:

$$\cos\theta_k = \cos\theta_d \cos\theta_p + \sin\theta_p \cos\varphi_p \sin\theta_d$$

where $\cos\theta_p = p_{\|}/p$, and $\sin\theta_p = p_{\perp}/p$. The angle φ_d has been arbitrarily set equal to zero. Note that Eqn. (6.9) has been written in relativistic units with momentum normalized to mc and energy normalized to mc^2. The lower limit of integration over momentum space is determined by equating the electron kinetic energy ε to the photon energy k:

$$p_{min} = \sqrt{(\varepsilon_{min} + 1)^2 - 1} = \sqrt{(k+1)^2 - 1}. \tag{6.10}$$

Using equation (6.9), the photon emission rate for an arbitrary electron distribution function $f(p_{\|}, p_{\perp})$ may be calculated.

6.3 X-ray Measurements During Lower Hybrid Current Drive and Electron Heating Experiments

In the low density "slideaway" regime, where 800 MHz current drive is effective, substantial superthermal x-ray tails are observed even in the absence of rf power. It was conjectured previously[7] that such preformed tails were necessary for current drive because they provided high velocity "seed" electrons upon which low-$N_{||}$ waves could damp. Their disappearance at high densities would then explain the 800 MHz density limit. In Subsection 6.3.1, we briefly review some early measurements of the plasma hard x-ray emission during 800 MHz top-launch current drive experiments. Unfortunately, due to the presence of the ohmic electric field, significant enhancements in the plasma hard x-ray emission were not observed during rf injection. In more recent studies, described in Subsection 6.3.2, the plasma hard x-ray emission has been measured during quasi-steady-state current drive with the OH primary open-circuited. In this case, the hard x-ray measurements clearly show the rf-generation of an energetic electron tail in the center of the plasma, even when the preformed tail in the target plasma is negligibly small. Measurements during 2.45 GHz electron heating experiments also show an order of magnitude rf-enhancement of the hard x-ray emission.

6.3.1 800 MHz Current Drive Experiments

The plasma hard x-ray emission was measured during 800 MHz lower hybrid current drive experiments[31] in which waves were launched from a top-mounted four-waveguide grill ($N_{||} \simeq 8$ for $\Delta\phi = +90°$). Typical spectra are shown in Fig. 6.7 for a density of $\overline{n}_e = 3 \times 10^{12}\,\mathrm{cm}^{-3}$. A substantial level of hard x-ray emission was observed even before rf injection. The x-ray spectrum is exponential, with a slope of 35 keV, and a maximum detected photon energy of approximately 400 keV. Although the injection of 25 kW of rf power produces substantial current drive effects, such as loop voltage drops and current increases, the shape of the hard x-ray spectrum was unaffected. In this particular case, the intensity level was enhanced slightly (by less than a factor of two). However, in other similar cases, the hard x-ray intensity level remained the same or even decreased during the rf pulse. The shape of the hard x-ray radial profile was also unaffected by the rf injection, as shown in Fig. 6.8. In the energy range 50 – 300 keV, the x-ray profile is strongly peaked on the axis, with or without rf. The FWHM is less than 6 cm, compared to the plasma diameter of 26 cm.

It is believed that these x-ray measurements were dominated by the effects of runaway electrons, driven by the OH electric field. This hypothesis was supported by the observation of strong bursts of plasma x-ray emission which correlated with other signatures of the runaway-driven Parail-Pogutse instability.[69] This instability was routinely observed before, during, or after rf injection in low density plasmas. Figure 6.9 shows the correlation of the plasma x-ray bursts with the limiter hard x-ray bursts, loop voltage spikes, and periodic losses in rf-driven current associated with the instability. All of these phenomena are consistent with pitch angle scattering of energetic electrons in velocity space from the parallel to the perpendicular direction when the instability occurs. Since the bremsstrahlung emission from such electrons is strongly peaked in the forward direction, the perpendicular x-ray emission increases suddenly when the pitch angle scattering occurs. Similar measurements on PLT[93] have indicated that the sudden increase in the perpendicular x-ray emission is accompanied by a simultaneous decrease in the parallel hard x-ray emission.

Under certain conditions, bursts of x-ray emission were also observed with the Si(Li) detector. When the Si(Li) detector was scanned from the side of the tokamak it was found that the bursts were emitted primarily from the upper half of the plasma. This may indicate the presence of ripple-trapped electrons (due to the spacing of the TF coils). Such ripple-trapping leads to grad-B drift, which for electrons in Versator is in the upward direction. Pitch angle scattering of electrons at the anomolous doppler resonance into the perpendicular direction, combined with slowing down in the parallel direction due to instability growth, could lead to such ripple-trapping.

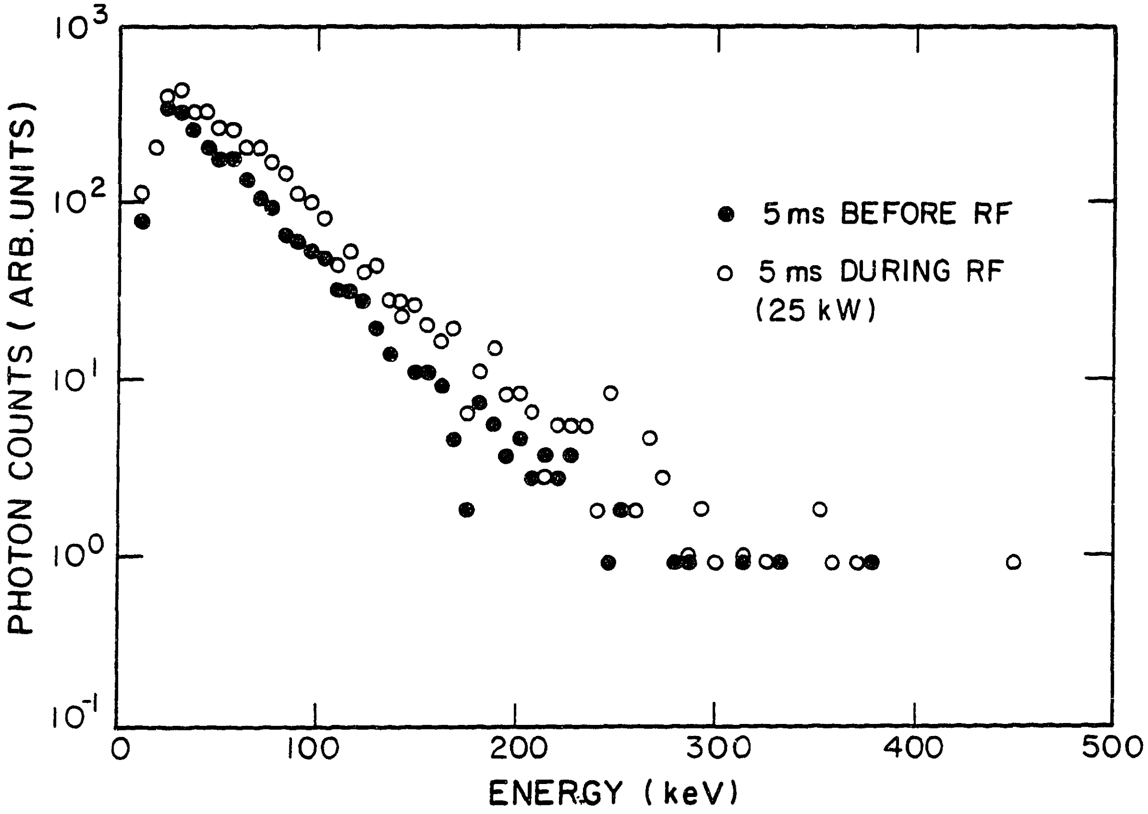

Fig. 6.7: Hard x-ray spectra measured before and during 800 MHz top-launch current drive with $\overline{n}_e = 3 \times 10^{12}\,\mathrm{cm}^{-3}$, $\Delta\phi = +90^\circ$, $P_{rf} = 25\,\mathrm{kW}$.

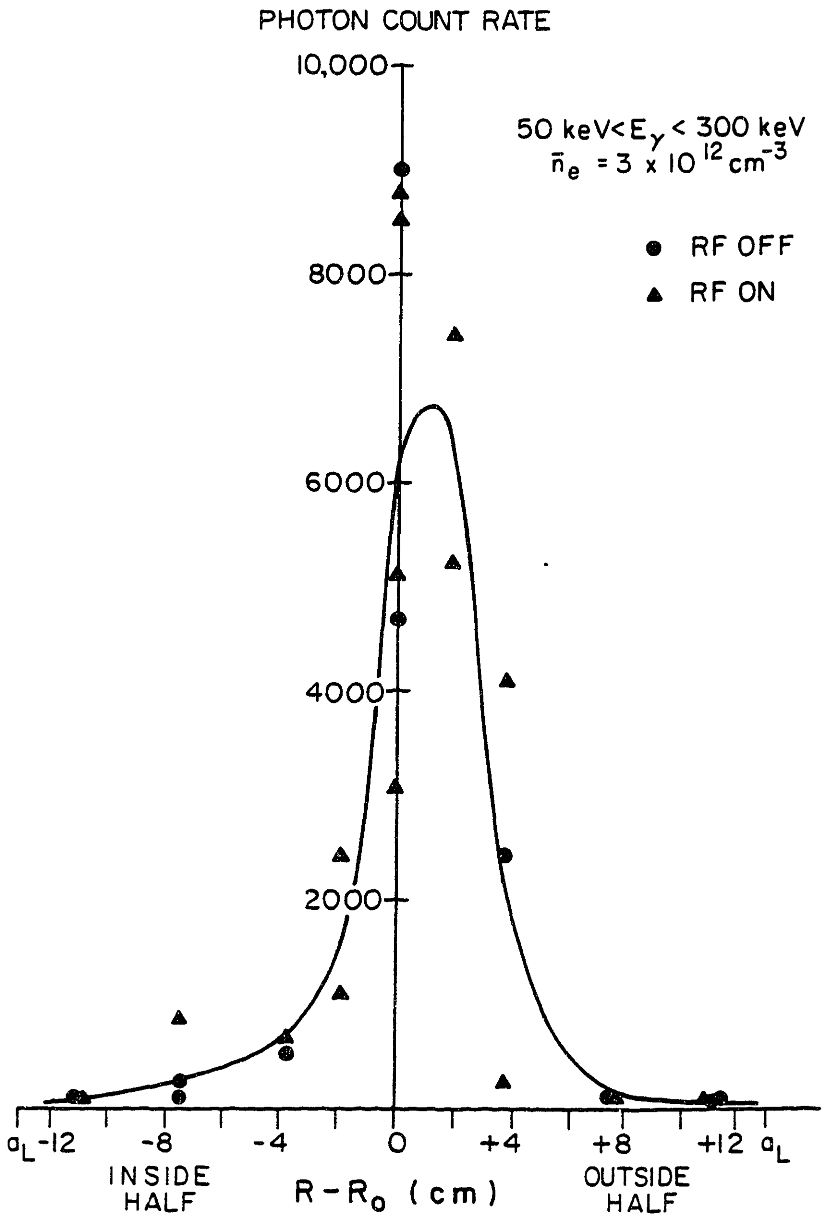

Fig. 6.8: Hard x-ray radial profile measured during 800 MHz top-launch current drive (same parameters as Fig. 7.7).

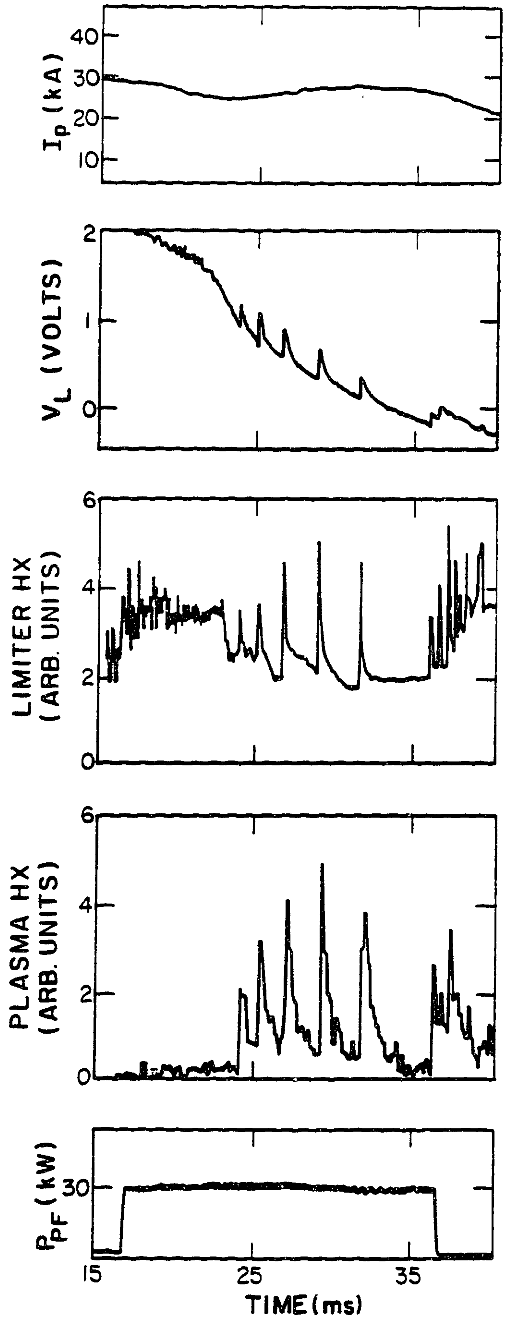

Fig. 6.9: Correlation of the plasma hard x-ray bursts with other signatures of the Parail-Pogutse instability during 800 MHz current drive.

6.3.2 2.45 GHz Current Drive and Electron Heating Experiments

The results of the previous subsection indicate the importance of eliminating the ohmic dc electric field during current drive in order to obtain a "clean" picture of the electron distribution function from x-ray measurements. Accordingly, we have measured the plasma hard x-ray emission during 2.45 GHz quasi-steady-state current drive with the OH primary open-circuited.

Typical hard x-ray spectra measured before and during rf injection are shown in Fig. 6.10. In this case, 18 kA of plasma current was maintained nearly constant for 20 ms with 75 kW of rf power. The plasma density was $\bar{n}_e \simeq 7 \times 10^{12}\,\mathrm{cm}^{-3}$ and the average toroidal field was $B_T = 12\,\mathrm{kG}$. The hard x-ray emission level prior to rf injection is negligible. When the rf power is turned on, an energetic electron tail is generated which extends in energy to at least 160 keV. The slope of this spectrum ($\sim$ 22 keV) is considerably steeper than the 800 MHz case shown in the previous subsection. However, there is still no evidence of a high energy cut-off. In fact, the x-ray spectrum in Fig. 6.10 extends well beyond the energy limit given by the accessibility condition, given by Eqn. (2.8b). Even if we consider the high field region of the plasma at $R = R_0 - a/2$, we estimate $\varepsilon_{acc} \simeq 90\,keV$.

The observation of x-rays at higher energies may be due to: 1) the presence of a small dc electric field, which generates energetic runaway electrons, 2) a significant perpendicular tail component ($T_\perp$) which adds to the parallel energy, and 3) a violation of the accessibility condition. The latter two possibilities will be considered further when the theoretical modelling of this spectrum is discussed in Section 6.4.

The possibility of runaway electrons cannot be excluded without an accurate estimate of the central loop voltage. Unfortunately, this requires a knowledge of $\ell_i(t)$, which is difficult to measure. Assuming a constant current profile with $\ell_i = 1.7$, we estimate a central loop voltage of $V_L \leq .1$ V. The corresponding critical runaway energy is $\varepsilon_{run} \geq 140\,\mathrm{keV}$. Hence, it appears that the first possibility is unlikely.

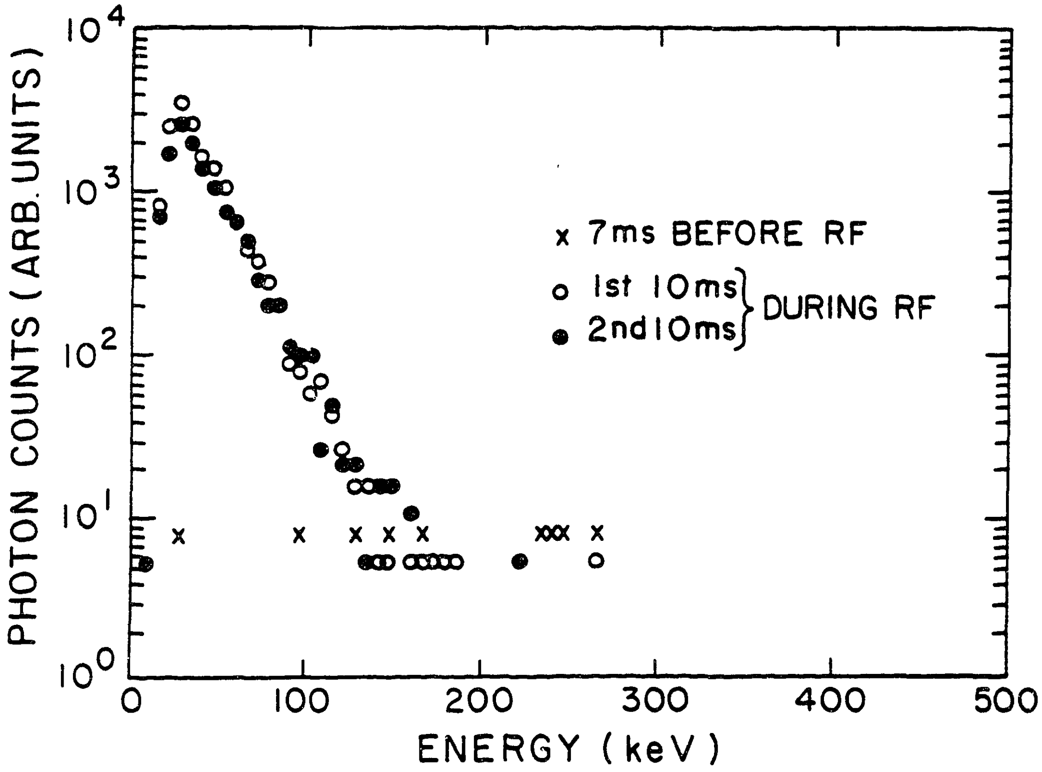

Fig. 6.10: Hard x-ray spectra before and during 2.45 GHz quasi-steady-state current drive with $\overline{n}_e \simeq 7 \times 10^{12}\,\mathrm{cm}^{-3}$, $B_T = 12\,\mathrm{kG}$, $P_{rf} = 75\,\mathrm{kW}$.

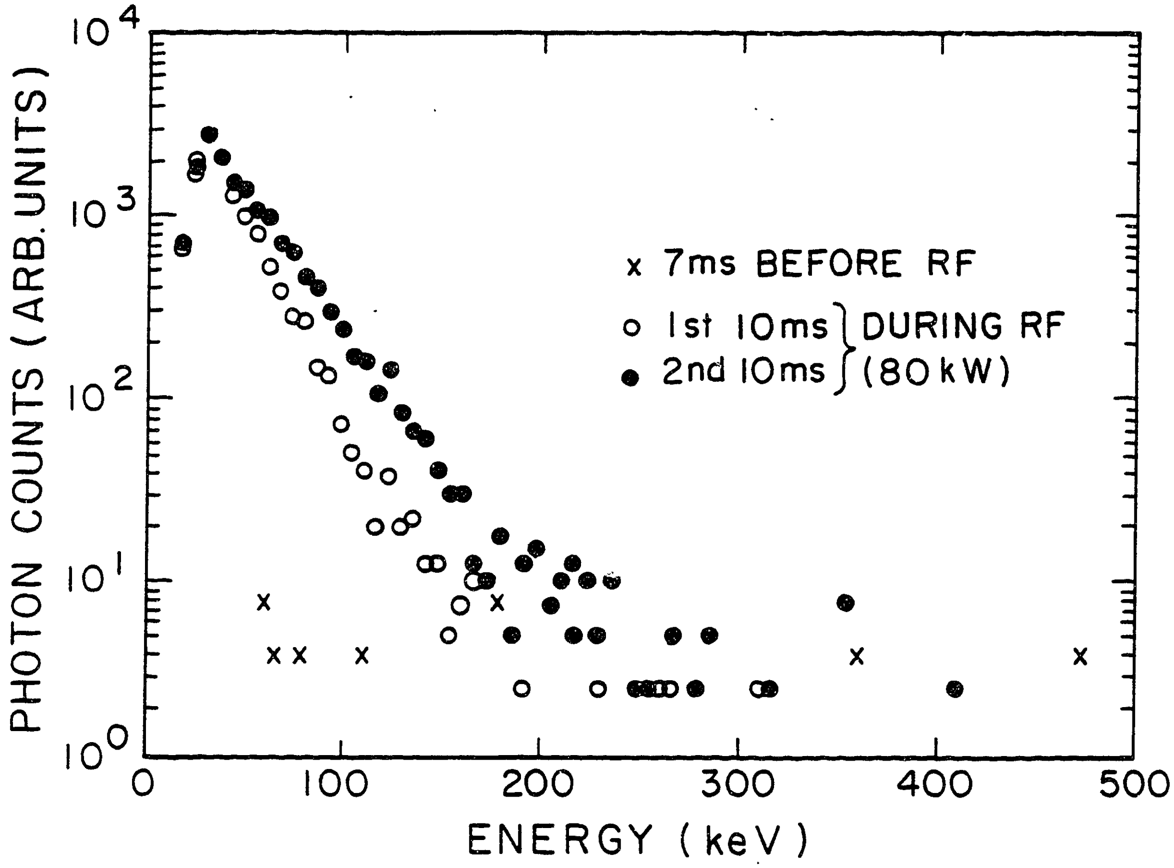

Fig. 6.11: Hard x-ray spectra before and during 2.45 GHz current drive at $\bar{n}_e \simeq 1.1 \times 10^{13}\,\mathrm{cm}^{-3}$, where the injected rf power (80 kW) was insufficient to flat-top the plasma current.

For comparison, Fig. 6.11 shows the behavior of the hard x-ray emission spectrum when a small inductive electric field is induced by plasma current decay (see Fig. 4.13). During these measurements, the density was $\overline{n}_e \simeq 1.1 \times 10^{13}\,\mathrm{cm}^{-3}$, and the rf power level was 80 kW. While 17 kA of plasma current was maintained at a constant level during the first 10 ms of the rf pulse, the rf power level was insufficient to maintain the current during the second half of the pulse. During this time, the current decay rate was $\dot{I} \simeq -280\,\mathrm{kA/s}$ and the estimated loop voltage at the center of the plasma was $V_L = +0.24\,\mathrm{V}$. Small bursts of $2\omega_{ce}$ emission were also observed, indicating that the anomolous doppler instability was active. The estimated runaway critical energy for this case is 90 keV, which is close to the accessibility limit. The x-ray spectrum measured during the first 10 ms of the rf pulse is nearly identical to the quasi-steady-state case shown in Fig. 6.10. In contrast, the spectrum during the second 10 ms of the rf pulse exhibits a flatter slope, and extends to higher energies (up to several hundred keV). Apparently, the inductive electric field induced by the plasma current decay accelerates rf-generated plateau electrons to higher energies, enhancing the x-ray emission. Additional x-ray enhancement may result from the pitch angle scattering of runaway electrons to the perpendicular direction by the Parail-Pogutse instability.

It is possible to generate large preformed superthermal electron tails, even in relatively high density plasmas ($\overline{n}_e \sim 1 \times 10^{13}\,\mathrm{cm}^{-3}$), by lowering the gas input rate during the start-up phase of the tokamak discharge. In such cases, runaway electrons generated at the beginning of the discharge trigger the Parail-Pogutse instability, producing a sudden nonthermal increase in the $2\omega_{ce}$ emission[41] (see Fig. 4.4), as well as a high level of plasma hard x-ray emission. Figure 6.12 shows the hard x-ray emission measured before and during flat-top current drive with a preformed superthermal electron tail. The density during the hard x-ray measurements was $\overline{n}_e \simeq 9 \times 10^{12}\,\mathrm{cm}^{-3}$. In this case, 22 kA of plasma current was sustained for 21 ms with 85 kW of injected rf power. Despite the preformed tail, the hard x-ray spectra measured at three different times during the rf pulse are virtually the same as of Fig. 6.10, where no significant preformed tail was evident.

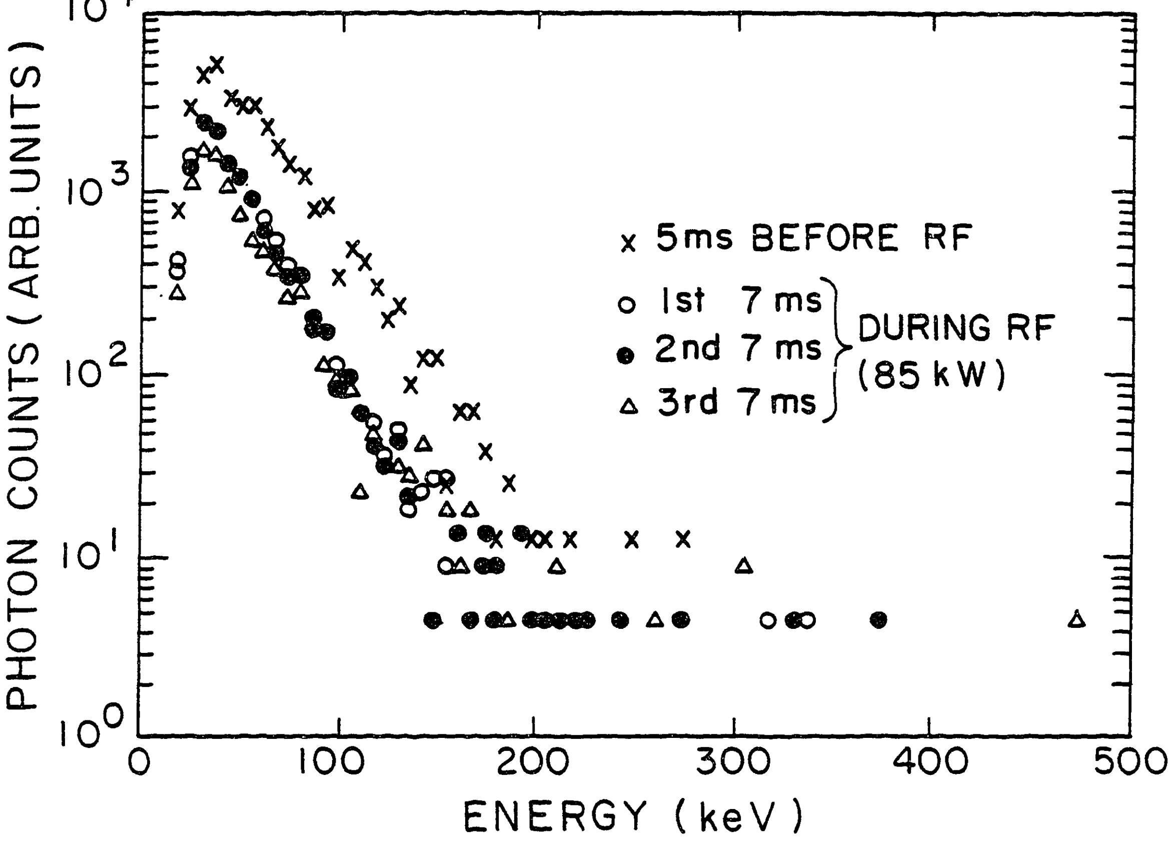

Fig. 6.12: Hard x-ray emission before and during 2.45 GHz flat-top current drive with a preformed superthermal electron tail at $\overline{n}_e \simeq 9 \times 10^{12}\,\text{cm}^{-3}$.

These measurements indicate that the final state of the electron distribution function during quasi-steady-state current drive is independent of the initial target plasma distribution. Furthermore, a preformed tail does not appear necessary for initiating steady state current drive. Therefore, the 800 MHz current drive density limit is not due to the disappearance of preformed tails at densities above $\overline{n}_e \simeq 6 \times 10^{12}\,\mathrm{cm}^{-3}$. Of course, this conclusion was evident without the x-ray measurements since raising the rf frequency increased the density limit without changing the target plasma conditions.

The radial profile of the hard x-ray emission in the energy range 30–250 keV is shown in Fig. 6.13. The discharge conditions are similar to those of Fig. 6.12. For comparison, profiles measured with no rf injection are shown in Fig. 6.14. Without rf injection, the profiles are strongly peaked on axis with a FWHM $\simeq$ 5 cm. During flat-top current drive, the profiles are also peaked on axis, although they are distinctly asymmetric, with enhanced emission from the high field side of the plasma cross section. The overall emission level also appears to decrease with time during the rf pulse. This trend was less apparent on the semi-log plots of the emission spectra. Similar behavior was observed in the $2\omega_{ce}$ emission during these discharges, and is not presently understood.

The enhanced hard x-ray emission on the high field side may be a result of magnetic mirror effects, in particular, the constancy of the magnetic moment $\mu = \frac{1}{2}mv_\perp^2/B$. Since the toroidal field is stronger on the inside of the torus, the perpendicular energy of circulating particles is correspondingly greater on the inside of a given flux surface. For a flux surface with radius r, the difference in perpendicular kinetic energy between the inside and the outside is given by:

$$\frac{\varepsilon_{\perp in}}{\varepsilon_{\perp out}} \simeq \frac{B_{in}}{B_{out}} = \frac{R_0 + r}{R_0 - r}. \tag{6.11}$$

For $r = a/2$, $\varepsilon_{\perp in}/\varepsilon_{\perp out} \simeq 1.4$. Since perpendicular energy is gained at the expense of parallel energy, the circulating particles spend more time on the inside of the flux surface. Trapped particles may also play an important role if $T_\perp \sim T_\parallel$, since the fraction of trapped particles for an isotropic distribution function can be quite high

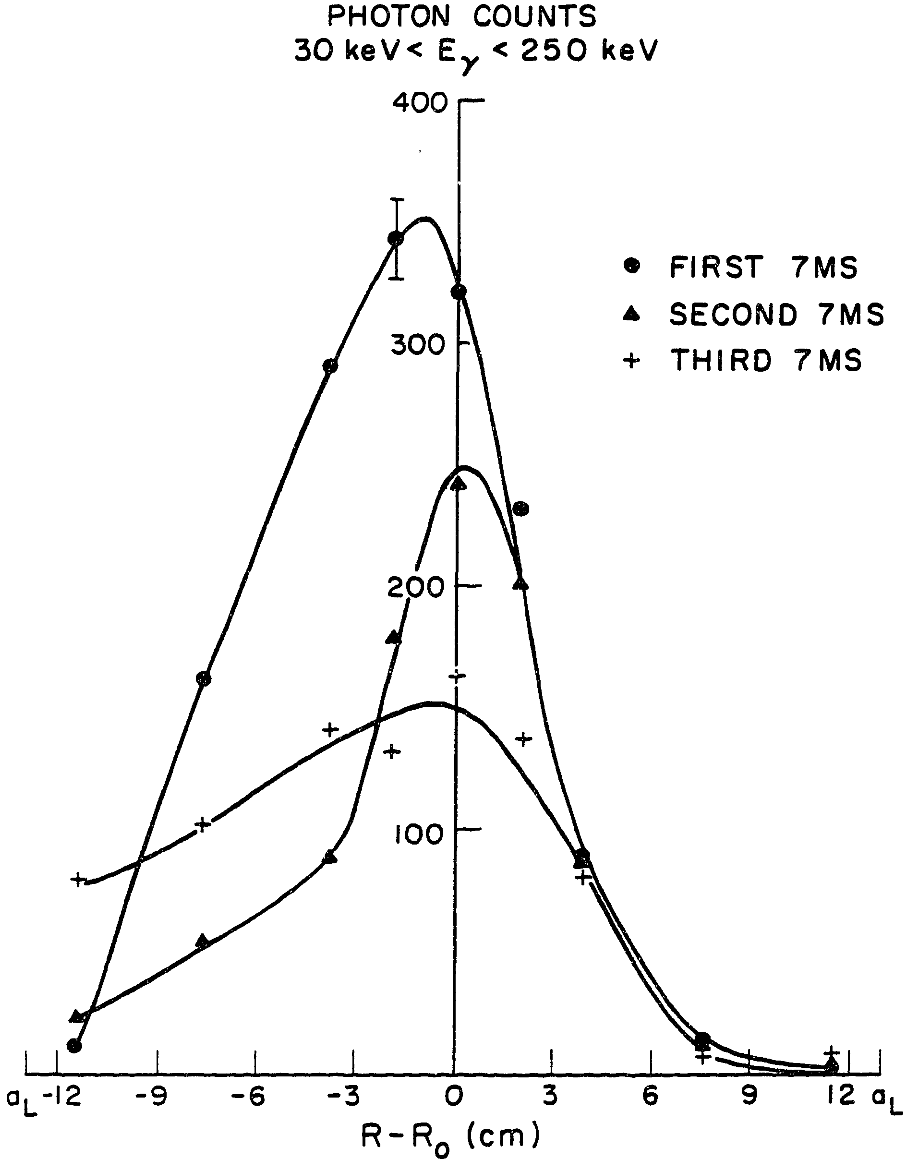

Fig. 6.13: Radial profile of the hard x-ray emission during 2.45 GHz quasi-steady-state current drive. The discharge conditions are similar to those of Fig. 6.12.

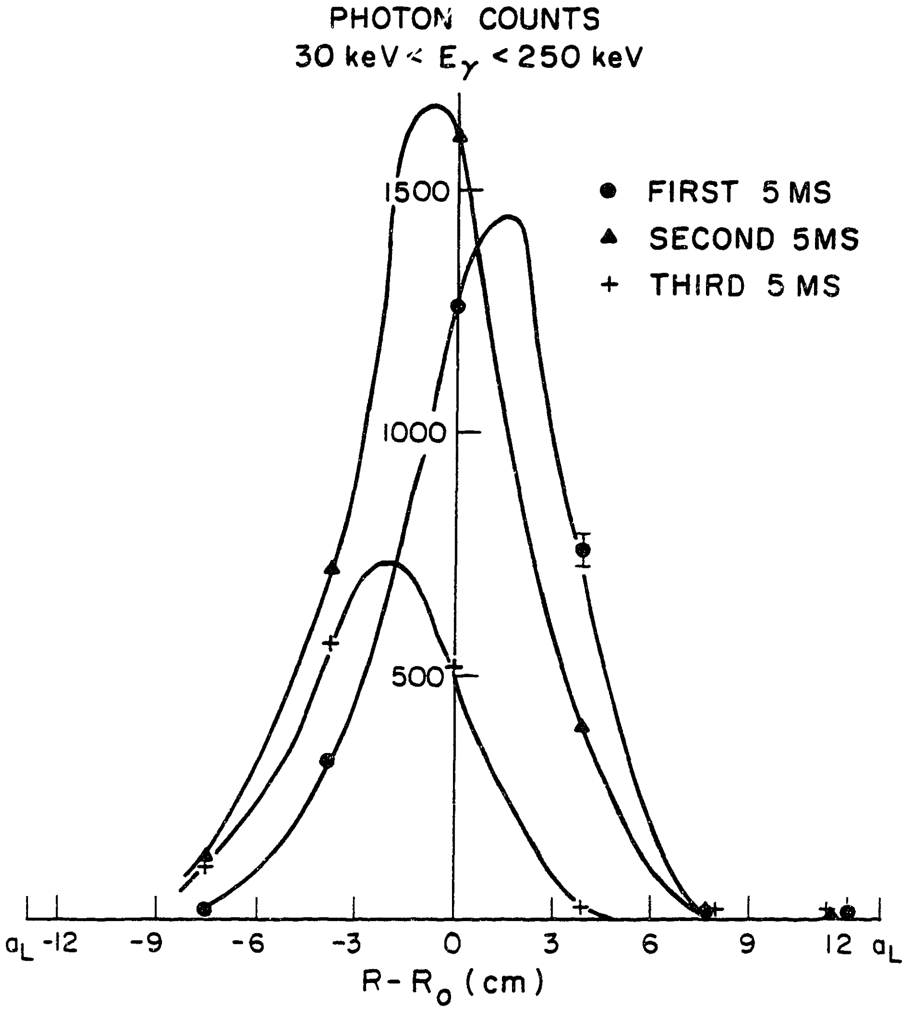

Fig. 6.14: Radial profile of the hard x-ray emission with no rf injection for plasma conditions similar to Fig. 6.12

at large radii:

$$\frac{n_{tr}}{n} = \left(\frac{2r}{R+r}\right)^{1/2} . \tag{6.12}$$

For $r = a/2$, $n_{tr}/n = 0.53$. For anisotropic distribution functions with $T_{\|}/T_{\perp} \gg 1$ this fraction will be smaller. A complete analysis will not be attempted here because further measurements of the hard x-ray profile are warranted, including 1) a repeat of the measurement with a transparent window on the top port to eliminate any possible contribution from wall radiation, 2) more detailed spectral measurements to compare $T_{\perp}$ on the inside with the outside, 3) measuring the profile from the side to see if it is up/down symmetric (soft x-ray measurements during electron heating experiments indicate that this is the case), and 4) measuring a tangential profile to see if the parallel energy is larger on the outside.

Soft and hard x-ray measurements have been performed during the 2.45 GHz electron heating experiments discussed previously in Section 6.2. Injection of high power rf ($P_{rf} \simeq 90\,\mathrm{kW}$) into ohmic discharges with $\bar{n}_e = 1.1 \times 10^{13}\,\mathrm{cm}^{-3}$ produced no significant change in the bulk electron temperature as measured by Thomson scattering, although current drive effects (loop voltage drops and current increases) were evident. The soft x-ray spectrum shown in Fig. 6.15 indicates a substantial rf-enhancement of the fast electron tail. The enhancement in the x-ray emission from 5 to 100 keV is approximately a factor of 10 (see Fig. 6.6). The tail enhancement persists even after rf shut-off, although at that time the anomolous doppler instability turns on, indicating that runaways are generated by the ohmic electric field.

The radial profile of the soft x-ray emission was measured by scanning the Si(Li) detector from the side of the tokamak. Plotted in Fig. 6.16 is the soft x-ray intensity level at 15 keV as a function of chord radius, obtained by fitting a straight line to the soft x-ray tail in the range 10 – 25 keV. The profile is strongly peaked near the midplane of the tokamak. In contrast to the in/out hard x-ray profiles during current drive, this profile is nearly symmetric. The solid curve is the chord intensity calculated for a gaussian emission profile with a 5 cm radius. The fit to the data is fairly good except for one data point just above the midplane. It is

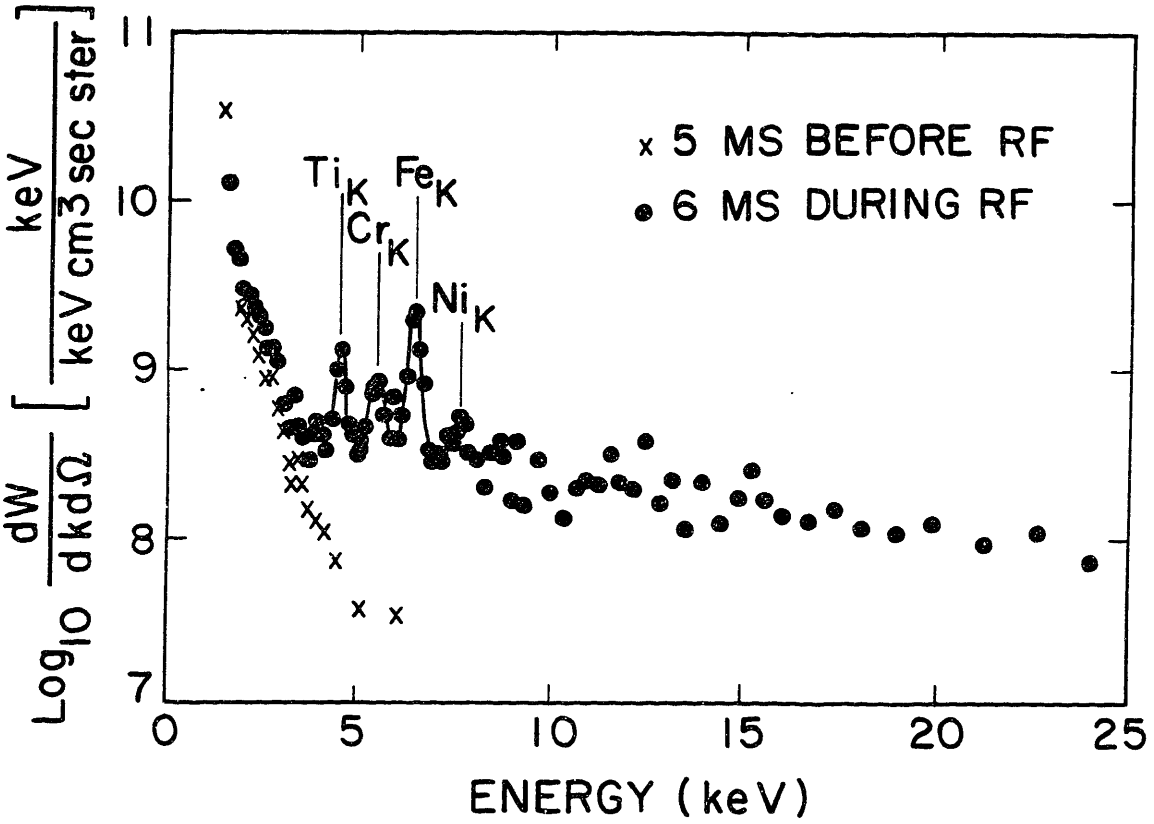

Fig. 6.15: Soft x-ray spectra measured during electron heating experiments at $\overline{n}_e \simeq 1.1 \times 10^{13}\,\mathrm{cm}^{-3}$ with $P_{rf} \simeq 90\,\mathrm{kW}$ and $\Delta\phi = 180°$.

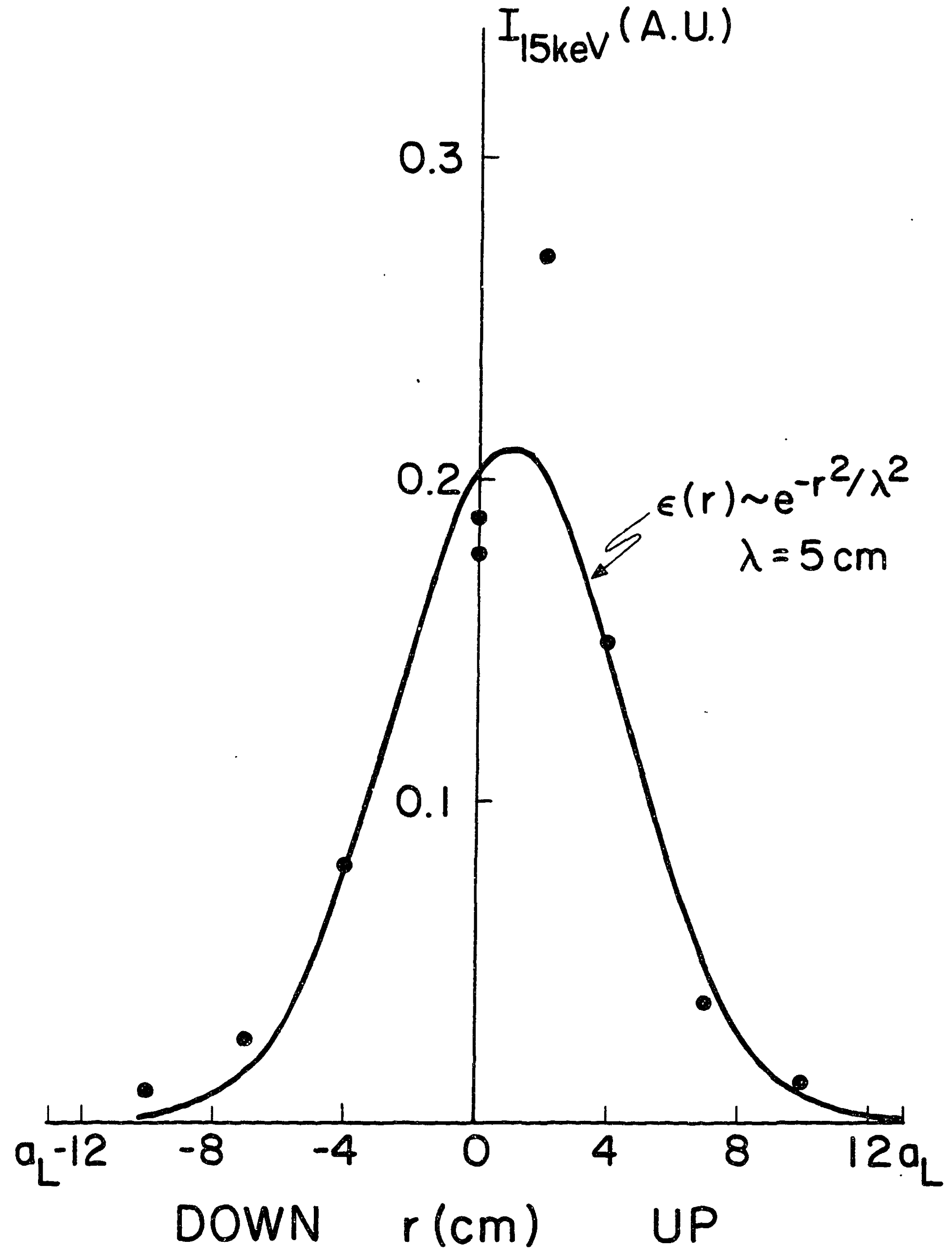

Fig. 6.16: Soft x-ray radial profile for the photon energy $k = 15$ keV measured during 2.45 GHz electron heating experiments with discharge conditions similar to Fig. 6.15. The solid curve is the chord intensity calculated for a gaussian emission profile with a 5 cm radius.

possible that the emission profile is more strongly peaked than a gaussian very near the axis.

6.4 Modelling of the Hard X-ray Bremsstrahlung Emission During 2.45 GHz Steady State Current Drive

In order to estimate some of the properties of the fast electron tail during 2.45 GHz current drive, we have modelled the hard x-ray emission using a relativistic bremsstrahlung code.[36] With this code, the x-ray emission from an arbitrary distribution function $f(\mathbf{p})$ may be calculated. Because of the difficulties discussed earlier regarding the interpretation of bremsstrahlung emission, an unambiguous determination of $f(p_{||}, p_{\perp})$ will not be possible in these experiments since only perpendicular hard x-ray measurements were carried out. The anisotropy of the fast electron distribution can be determined only by measuring the hard x-ray emission as a function of angle with respect to the magnetic field. Such investigations have been undertaken on the PLT and Alcator C tokamaks. The form of our model distribution is based on their results.

6.4.1 The Model Distribution Fuction

In the PLT[34,93] and Alcator[36] x-ray experiments, the anisotropy of the electron tail distribution has been modelled using a quasi-Maxwellian function with four adjustable parameters, namely the forward, backward, and perpendicular temperatures given by $T_{||F}$, $T_{||B}$, and $T_{\perp}$ respectively, and a high energy cut-off given by ε^*. ("Forward" corresponds to the direction along the magnetic field opposite to the direction of the plasma current.) The results from both experiments indicate that a plateau was generated by the rf in the forward direction since $T_{||F} > T_{||B}$. However, the perpendicular and the backward components of the electron distribution were also substantial since $T_{||B} \simeq T_{\perp} \simeq 100 T_e$. In addition, fast electrons with energies exceeding the accessibility limit were observed since $\varepsilon^* > \varepsilon_{acc}$.

These experimental findings are consistent with numerical solutions of the

Fokker-Planck equation,[5,55,56] which include the effects of rf quasi-linear diffusion in the forward parallel direction, as well as collisional scattering. In particular, for a broad wave spectrum, $v_1 < c/n_{\|} < v_2$, where $v_2/v_1 \gg 1$, substantial broadening of the plateau in the perpendicular direction is predicted ($T_\perp \gg T_e$) due to pitch angle scattering of resonant electrons. Furthermore, the pitch angle scattering of particles out of the plateau region results in a significant backward population, $T_{\|B} \simeq T_\perp$, as well as a forward component in the region $v_{\|} > v_2$ beyond the wave spectrum. Hence, the observation of x-rays at energies $k > \varepsilon_{acc}$ does not necessarily imply a violation of the accessibility condition. Finally, since typically 30% of the rf power spectrum is launched in the $-N_{\|}$ direction, this may also contribute to a large $T_{\|B}$.

In order to model the perpendicular bremsstrahlung measurements, we will use a modified form of the "three temperature" distribution function which is consistent with the Fokker-Planck theory, as well as the Alcator C and PLT data:

$$\begin{aligned} f(\mathbf{p}) &= C_N \exp\left(-\frac{p^2}{2T_\perp}\right) & p_{\|} &< 0 \\ &= C_N \exp\left(-\frac{p_\perp^2}{2T_\perp} - \frac{p_{\|}^2}{2T_{\|F}}\right) & 0 \le p_{\|} &\le p_2 \\ &= C_N^{*} \exp\left(-\frac{p^2}{2T_\perp}\right) & p_{\|} &> p_2, \end{aligned}$$

where

$$C_N^{*} = C_N \exp\left(-\frac{p_2^2}{2T_{\|F}} + \frac{p_2^2}{2T_\perp}\right). \tag{6.13}$$

The constant C_N satisfies the condition $\int d^3\mathbf{p}\, f(\mathbf{p}) = 1$. The region $0 \le p_{\|} \le p_2$ represents the rf plateau. Note that we have neglected relativistic effects[5] which widen the resonance region at high values of $p_\perp$. We will assume that the plateau is nearly flat in the forward direction by fixing $T_{\|F}$ at a large value (1000 keV). In order to simulate the effects of pitch angle scattering out of the plateau region, we have assumed that in the regions $p_{\|} < 0$ and $p_{\|} > p_2$ the contours of $f(\mathbf{p})$ are given by circles, $p_\perp^2 + p_{\|}^2 = const.$ These circular contours are matched to the plateau contours at the boundaries $p_{\|} = 0$ and $p_{\|} = p_2$.

Given these assumptions, our model distribution has the following properties:

1) $T_\perp(p_\parallel) = const$, which is a reasonable first approximation to the 2-d Fokker-Planck calculations, 2) $T_{\parallel B} = T_\perp$, which is consistent with the PLT and Alcator measurements, and 3) $f(\mathbf{p})$ is completely described by two parameters, p_2 and $T_\perp$, which are well suited to comparison with perpendicular x-ray measurements. By adjusting the parameters p_2 and $T_\perp$, it may be possible to determine whether the energetic photons observed experimentally are due to 2-d effects (high $T_\perp$) or to a violation of the accessibility condition (high p_2).

Finally, in order to calculate the properties of the electron tail distribution function, we will need to account for profile effects. Once again, due to a lack of detailed data, we will assume the simplest model, namely that of a homogeneous distribution function in space:

$$f(r,\mathbf{p}) = n_t(r) f(\mathbf{p}), \tag{6.14}$$

where $n_t(r)$ is the local tail density. We have no strong experimental evidence to support an inhomogeneous model, such as the two-step PLT model,[35] since within our large uncertainties, the slope of the hard x-ray spectra measured at various radii are approximately the same. For $n_t(r)$ we use a gaussian profile with a 5 cm radius. which is consistent with the hard and soft x-ray profile measurements.

6.4.2 Comparison with Experiment

The values of $T_\perp$ and $\varepsilon_2(p_2)$ in our model distribution function have been estimated by comparing the calculated x-ray emission for $\theta_d = 90^\circ$ with the experimental data shown previously in Fig. 6.12. A contour plot of $f(p_\parallel, p_\perp)$ for the parameters $T_\perp = 35\,\mathrm{keV}$ and $\varepsilon_2 = 60\,\mathrm{keV}$ (Model I), is shown in Fig. 6.17a). The value of ε_2 corresponds to the accessibility condition on the high field side of the plasma, at $R = R_0 - a/2$. The calculated x-ray emission is shown in Fig. 6.17b) along with the experimental data. The agreement is quite good over the entire energy range of the data. The slope of the spectrum was fit by adjusting $T_\perp$, while the absolute intensity level was fit by adjusting the tail density n_{t0}, and Z_{eff}. The sensitivity of the fit is approximately $\pm 10\,\mathrm{keV}$ for $T_\perp$ and $\pm 40\,\mathrm{keV}$ for ε_2. Other

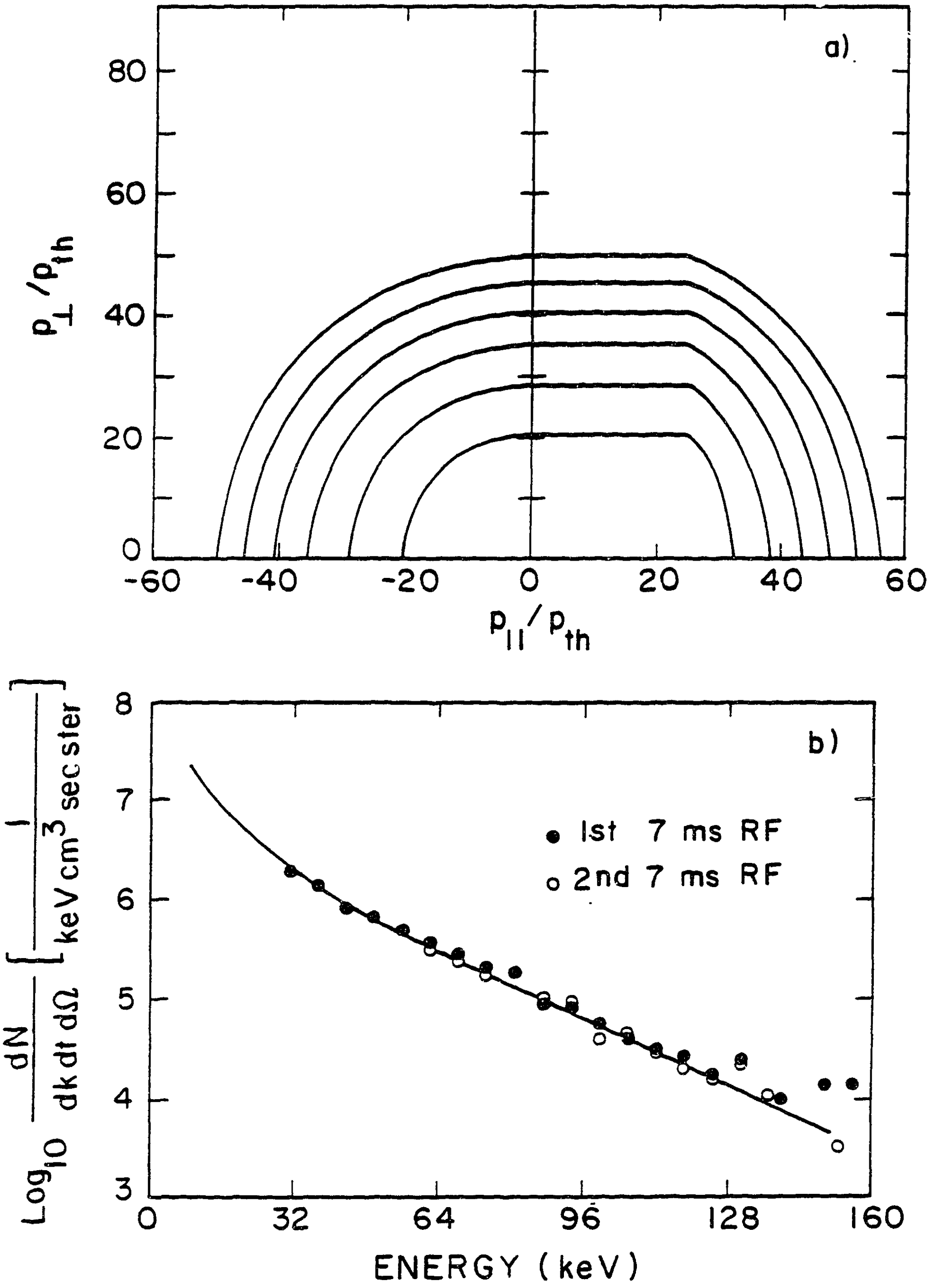

Fig. 6.17: Top: contour plot of the model distribution function with $T_\perp = 35\,\mathrm{keV}$ and $\varepsilon_2 = 60\,\mathrm{keV}$ (Model I). Bottom: the calculated x-ray emission for Model I is plotted with the experimental data from Fig. 6.12.

combinations of $T_\perp$ and ε^* also produce resonable fits to the data, as shown in Fig. 6.18. In this case we assumed the values $T_\perp = 10\,\mathrm{keV}$ and $\varepsilon_2 = 160\,\mathrm{keV}$ (Model II). For this lower value of $T_\perp$, it was necessary to assume a higher value of ε_2 in order to to avoid a high energy cut-off in the calculated x-ray spectrum. For still lower values of $T_\perp$, the fit to the data is relatively poor, compared to Models I and II, even with arbitrarily high values of ε_2. Note that the experimental data can also be fit well with an isotropic distribution ($\varepsilon_2 = 0$), with $T_\perp \simeq 40\,\mathrm{keV}$. However, we reject this model as unphysical since the net current is zero. Models I and II represent the realistic range of parameter space $(T_\perp, \varepsilon_2)$ which is consistent with the experimental x-ray data.

We now turn to the matter of the energetic photons with energies $k > 60\,\mathrm{keV} \sim \varepsilon_{acc}$. Within the framework of this analysis, Model distributions I and II represent two extreme ways of generating a significant number of energetic electrons with $\varepsilon > \varepsilon_{acc}$. In Model I, which is nearly isotropic, the energetic electrons are generated with a high value of $T_\perp$. In Model II, which is highly anisotropic, they are generated with a high value of $\varepsilon_2(p_2)$, such that $\varepsilon_2(p_2) > \varepsilon_{acc}$. It is not possible to choose between these two models based on comparisons with the x-ray data. Therefore, we cannot conclude from this analysis whether or not the accessibility condition is violated. However, if Model I is correct, and the accessibility condition is indeed valid, then the corresponding value for $T_\perp$ is extremely large ($\sim 350 T_e$). In fact, the range of $T_\perp$ values spanned by Models I and II ($10 - 35\,\mathrm{keV}$) lies slightly above that predicted by 2-d Fokker-Planck theory due to collisional scattering effects According to the 1-d analytical model of Fuchs et al.,[56] $T_\perp$ should be in the range $6 - 8\,\mathrm{keV}$ for a wave spectrum $v_1 < c/n_\parallel < v_2$, with $v_1/v_e = 2.8$ and $v_2/v_e = 25$, where $v_e = (2T_e/m)^{1/2}$. Here, the lower endpoint, v_1, was determined by the condition for strong Landau damping, Eqn. (2.21), while the upper endpoint, v_2 was determined by the accessibility condition, Eqn. (2.8b).

6.4.3 Derived Tail Properties

The tail electron density may be calculated from the shape of the model

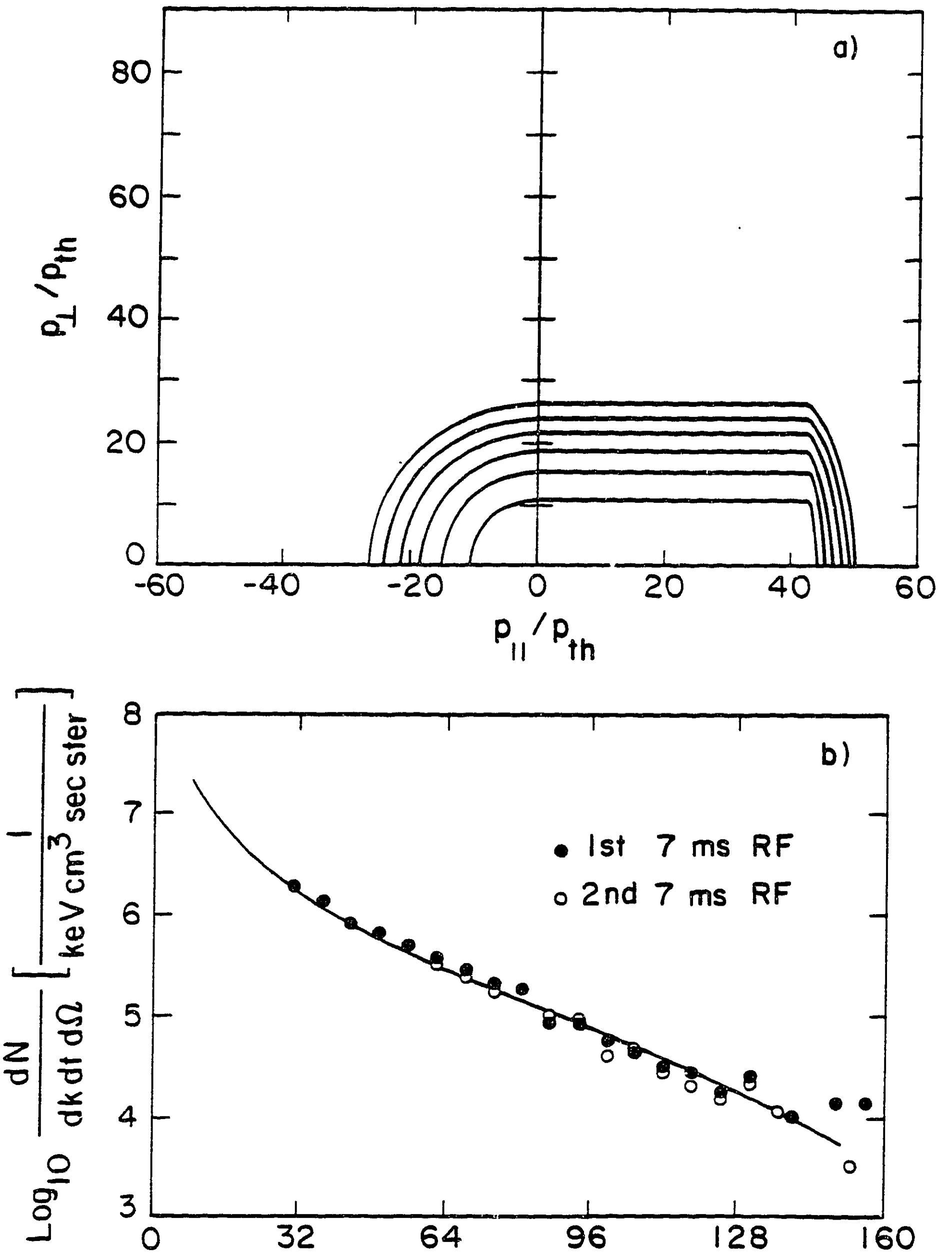

Fig. 6.18: Top: contour plot of the model distribution function with $T_\perp = 10\,\mathrm{keV}$ and $\varepsilon_2 = 160\,\mathrm{keV}$ (Model II). Bottom: comparison of calculated x-ray emission for Model II with the experimental data from Fig. 6.12

distribution function by normalizing to the plasma current:[35,36]

$$I_p = n_{t0} e \int_0^a 2\pi r\, dr \frac{n_t(r)}{n_{t0}} \int_0^\infty d^3\mathbf{p}\, v_\parallel f(\mathbf{p}). \tag{6.15}$$

For $I_p = 22\,\mathrm{kA}$, we find $n_{t0} = 5.4 \times 10^{11}\,\mathrm{cm}^{-3}$ for Model I, while $n_{t0} = 2.0 \times 10^{11}\,\mathrm{cm}^{-3}$ for Model II. Since the central bulk electron density is $n_{e0} \simeq 1.4 \times 10^{13}\,\mathrm{cm}^{-3}$, this implies a fractional tail density n_{t0}/n_{e0} in the range 1.4 – 3.9%. The tail density may also be determined from the absolute level of the hard x-ray emission if Z_{eff} were known. Here we shall use the values of n_{t0} determined above to estimate Z_{eff}. Note that the experimental data in Fig. 6.17 and Fig. 6.18 have been plotted in absolute units $[1/(\mathrm{keV\,cm^3\,sec\,ster})]$. For Model I, we estimate $Z_{eff} = 4.6$ while for Model II, we find $Z_{eff} \simeq 1$. Although direct experimental measurements of Z_{eff} during current drive are not available, our best estimates place Z_{eff} somewhere in between these values.

The total energy stored in the fast electron tail may also be calculated using the model distributions:[35,36]

$$E_t = n_{t0} mc^2 2\pi R_0 \int_0^a 2\pi r\, dr \frac{n_t(r)}{n_{t0}} \int_0^\infty d^3\mathbf{p}\, \varepsilon\, f(\mathbf{p}), \tag{6.16}$$

where $mc^2\varepsilon$ is the kinetic energy. For model I, we find $E_t = 94\,\mathrm{J}$, while for Model II, $E_t = 38\,\mathrm{J}$. For comparison, we estimate the stored energy of the bulk electrons to be $E_b \simeq 8\,\mathrm{J}$, based on ohmic Thomson temperature profiles with $T_{e0} = 100\,\mathrm{eV}$. Hence, the majority of the plasma kinetic energy (83 – 92%) resides in the tail electrons during current drive.

Similarly, we may estimate the contribution to β_θ from the tail using Equation (4.5):

$$\beta_{\theta t} = \frac{n_{t0} mc^2}{B_\theta^2(a)/2\mu_0} \frac{1}{\pi a^2} \int_0^a 2\pi r\, dr \frac{n_t(r)}{n_{t0}} \times \int_0^\infty d^3\mathbf{p} \left(\frac{1}{2}\frac{p_\parallel^2}{\gamma} + \frac{1}{4}\frac{p_\perp^2}{\gamma} \right) f(\mathbf{p}). \tag{6.17}$$

For Model I, we find $\beta_{\theta t} = 1.1$, while for Model II, $\beta_{\theta t} \simeq 0.5$. The estimated value for the bulk is $\beta_{\theta b} \simeq 0.1$. As a further consistency check, we may use these values for β_θ, along with the tail density profile, $n_t(r)$, to estimate the equilibrium value of $\beta_\theta + \ell_i/2$. For the 5 cm gaussian tail profile, we calculate $\ell_i = 1.8$. Hence, for Model I, $\beta_\theta + \ell_i/2 = 2.1$, while for Model II, $\beta_\theta + \ell_i/2 = 1.5$. The value determined from equilibrium measurements was $\beta_\theta + \ell_i/2 \simeq 1.8$.

If the tail distribution is known, then it is also possible to calculate the collisional power flow to the bulk electrons due to slowing down collisions. It is given by:[35,36]

$$P_{tb} = (3.66 \times 10^{-32}) 2\pi R_0 \int_0^a 2\pi r dr\, n_t(r) n_b(r) \times \int_{p_{min}}^{\infty} d^3\mathbf{p} \frac{\gamma}{p} f(\mathbf{p}) \qquad \text{Watts,} \tag{6.18}$$

where p_{min} is the location of the intersection of the tail distribution with the bulk distribution. It should be pointed out that this calculation is subject to considerable error, compared with the previous estimates of n_t and E_t. The added uncertainty arises in this case because the collisional power dissipation is dominated by the lowest energy electrons (since $\nu \propto v^{-3}$), whereas the modelling of bremsstrahlung emission is most accurate for the highest energy electrons. With this warning in mind, we find $P_{tb} \simeq 8$ kW for Model I and $P_{tb} \simeq 4$ kW for Model II. This should be compared with $P_{rf} \simeq 85$ kW injected into the plasma.

Finally, we use the power balance equation (5.6) in order to estimate the tail confinement time. Since the estimated power radiated by cyclotron emission and bremsstrahlung emission is negligible,[36] the tail confinement time is given by:

$$\tau_t = \frac{E_t}{\alpha P_{rf} - P_{tb}}, \tag{6.19}$$

where α is the fraction of injected rf power absorbed. Since $P_{tb} \ll P_{rf}$, the main uncertainty encountered in calculating τ_t arises from α. Here we will assume that $\alpha = 0.75$, which is consistent with the ramp-up analysis discussed in Chapter 4, as well as ray tracing calculations to be discussed in the next chapter. We then determine that $\tau_t \simeq 1.6$ ms for Model I. while $\tau_t \simeq 0.6$ ms for Model II. Typical bulk electron confinement times during ohmic discharges in Versator are $\tau_e \sim 1$ ms.

6.4.4 Discussion

In this section we have estimated some properties of the fast electron tail during steady state current drive by fitting the calculated x-ray spectrum for a simple model distribution function to the experimental data. The tail properties derived for two representative model distribution functions are summarized in Table 6.1. The spread of the values (factors of 2 - 3) between the two cases is indicative of the uncertainties associated with using only perpendicular bremsstrahlung measurements for determining the electron distribution function. Future measurements of the angular distribution of the bremsstrahlung emission may help to reduce these uncertainties.

The maximum possible range of $T_\perp$ values obtained from the x-ray analysis (10 – 35 keV) are comparable to or greater than those predicted by 2-d numerical solutions of the Fokker-Planck equation for the case of steady state current drive (6 – 8 keV). This is particularly interesting in light of the fact that the estimated tail confinement time, $\tau_t \simeq 0.6 - 1.6\,\mathrm{ms}$, is less than the collisional pitch angle scattering time ($\tau_\perp \simeq 3\,\mathrm{ms}$ for $\langle T \rangle \simeq 55\,\mathrm{keV}$). It appears, therefore, that a non-collisional mechanism may be responsible for enhanced pitch-angle scattering of the tail electrons from the parallel to the perpendicular direction. One possible mechanism is the anomolous doppler instability. It has recently been proposed[94] that waves $\omega \simeq \omega_{pe} k_{\|}/k$ may be driven unstable at the anomolous doppler resonance, $k_{\|} v_{\|} = \omega + \omega_{ce}$, during steady state current drive if wave damping at the Cherenkov resonance, $\omega = k_{\|} v_{\|}$, occurs on the plateau. A necessary condition for instability growth is that the plateau be sufficient broad to include both resonances:[94]

$$v_2/v_1 > 1 + \frac{\omega_{ce}}{\omega_{pe}}. \qquad (6.20)$$

This condition is easily satisfied during 2.45 GHz current drive experiment on Versator, and emission in the frequency rance $\omega < \omega_{pe}$ has been observed during flat-top current drive.[95] However, a quasi-linear calculation of the $T_\perp$ enhancement over collisional scattering due to the anomolous doppler instability has not yet been carried out.

Table 6.1

Summary of X-ray Modelling Results

	MODEL I	MODEL II
$T_\perp$	35 keV	10 keV
ε_2	60 keV	160 keV
n_t/n_b	.039	.014
I_+/I_-	2.6	16.4
$c/\langle v_\parallel\rangle$	9.2	3.4
E_t	94 J	38 J
$\beta_{\theta t}$	1.1	0.5
P_{tb}	8 kW	4 kW
τ_t	1.6 ms	0.6 ms

During the 2.45 GHz flat-top current drive experiments, most of the total plasma kinetic energy (80 – 90%) is stored in the hot electron tail. The collisional power flow from the tail to the bulk is quite small—only 5 – 10% of the total input rf power. The reason for this is that the tail confinement time ($\tau_t \simeq 0.6 - 1.6\,\mathrm{ms}$) is short compared to the collisional slowing down time ($\tau_S \simeq 4\,\mathrm{ms}$ for $\langle T \rangle \simeq 55\,\mathrm{keV}$). Hence, radial confinement losses from the tail dominate over collisional losses. It is therefore not surprising that substantial bulk cooling is observed during flat-top current drive since the reduction in the ohmic input power to the bulk (typically $\Delta P_{OH} \sim -25\,\mathrm{kW}$) exceeds the bulk heating from the rf-generated tail ($P_{tb} \simeq 4 - 8\,\mathrm{kW}$). A more quantitative analysis, including a determination of the bulk confinement time, awaits Thomson profile measurements. Poor radial tail confinement ($P_{tb} \ll P_{rf}$) also explains the lack of success during electron heating experiments with $\Delta\phi = \pi$, despite the high power rf injection, $P_{rf} \simeq P_{OH}$.

Poor radial tail confinement might also contribute to the relatively low 2.45 GHz steady state current drive efficiency, $\tilde{\eta} = .0072$, observed on Versator. For comparison, on Alcator C ($f = 4.6\,\mathrm{GHz}$) the estimated tail confinement time[36] is comparable with the collisional slowing down time due to operation at higher densities, near $\overline{n}_e \sim 3 \times 10^{13}\,\mathrm{cm}^{-3}$. Under these conditions, the tail losses are dominated by collisions, and $\tilde{\eta} = 0.12$. It should be noted, however, that similar results may also hold on PLT due to the larger machine size. If confinement losses dominate over collisional power dissipation on Versator, then it becomes difficult to explain the observed current drive efficiency scaling, $I/P \propto 1/n$, unless τ_t decreases with density. This issue will be addressed further in the concluding chapter.

Chapter 7

Conclusion

In this concluding chapter, the major experimental results of this thesis are reviewed, and the relationship between these results is discussed. The main conclusions drawn from this work are then summarized.

7.1 Summary of Results

In the preceeding chapters of the thesis, experiments have been described in which up to 95 kW of 2.45 GHz rf power was injected into Versator II plasmas with a four-waveguide phased-array grill. The rf coupling in these experiments was quite good, with reflectivities in the range $R = P_{ref}/P_{fwd} = 0.05 - 0.10$ for relative waveguide phasings $\Delta\phi = 90 - 180^\circ$ and densities $\overline{n}_e \geq 5 \times 10^{12}\,\mathrm{cm}^{-3}$. Incident power levels of up to 100 kW ($2.9\,\mathrm{kW/cm}^2$) were achieved by eliminating the cyclotron resonance layer from the evacuated antenna waveguides with an external magnetic field coil.

Fully rf-driven "flat-top" discharges ($\dot{I} \simeq 0, V_L \simeq 0$) with the OH primary open-circuited have been produced in the density range $\overline{n}_e = 0.2 - 1.0 \times 10^{13}\,\mathrm{cm}^{-3}$. The maximum flat-top density represents nearly a factor of two increase over the 800 MHz density limit of $\overline{n}_e \simeq 6 \times 10^{12}\,\mathrm{cm}^{-3}$. Due to the low toroidal field strength in these experiments ($B_T \leq 13\,\mathrm{kG}$), the parameter $\omega_{pe}^2/\omega_{ce}^2$ has exceeded unity, which is a record achievement. The flat-top current drive efficiency scaling for $\Delta\phi = +90^\circ$ is given by $\tilde{\eta} = \overline{n}(10^{20}\,\mathrm{m}^{-3})I(\mathrm{kA})R(\mathrm{m})/P_{rf}(\mathrm{kW}) = 0.0072$.

Current ramp-up ($\dot{I} > 0$, $V_L < 0$) has also been achieved at low densities $\overline{n}_e \leq 7 \times 10^{12}\,\mathrm{cm}^{-3}$, with ramp-up rates as high as $\dot{I} \simeq 400\,\mathrm{kA/s}$, and maximum efficiencies of $\epsilon = (\dot{W} - P_{ext})/P_{rf} = 0.14$ at $\overline{n}_e \simeq 3 \times 10^{12}\,\mathrm{cm}^{-3}$. This level of efficiency is in agreement with the theory of Fisch and Karney[30] if it is assumed that

$a = P_{abs}/P_{rf} \simeq 0.75$ and $N_{\|}^{*} \simeq 9$ where $N_{\|}^{*}$ is the parallel refractive index of the resonant waves. These values also fit the experimental data for flat-top discharges as well as those with decaying current.

At densities above $\overline{n}_e = 1.0 \times 10^{13}\,\mathrm{cm}^{-3}$, it was not possible to fully sustain the plasma current with the OH primary open-circuited because of insufficient rf power available, although reductions in the plasma current decay rate were observed at densities up to $\overline{n}_e \simeq 1.7 \times 10^{13}\,\mathrm{cm}^{-3}$. In experiments where rf power was injected into ohmically sustained plasmas, current increases, loop voltage drops, and enhanced $2\omega_{ce}$ emission were observed at densities exceeding $\overline{n}_e = 2 \times 10^{13}\,\mathrm{cm}^{-3}$, although these effects became quite small at the highest densities. In addition, we observed increases in the global particle confinement time τ_p during current drive of up to a factor of two. The particle confinement time increased with the rf power level and depended strongly on the waveguide phasing, suggesting that the improved confinement was related to the generation of a fast electron tail. The exact mechanism responsible for this relationship is not yet understood. There also appeared to be an upper density limit for improvements in τ_p at $\overline{n}_e \sim 2 \times 10^{13}\,\mathrm{cm}^{-3}$ which depended on the level of the toroidal magnetic field.

Electron heating experiments in the density range $\overline{n}_e = 1.0 - 1.5 \times 10^{13}\,\mathrm{cm}^{-3}$, with $\Delta\phi = \pi$ and $P_{rf} \geq P_{OH}$, produced no bulk heating. When $\Delta\phi = \pi/2$ phasing was used. bulk cooling was observed, typically from $T_{e0} \simeq 350\,\mathrm{eV}$ to 275 eV. In flat-top discharges at $\overline{n}_e \simeq 8 \times 10^{12}\,\mathrm{cm}^{-3}$, where $P_{OH} \simeq 0$ during rf injection, the bulk cooling was even more severe, typically from $T_e = 300\,\mathrm{eV}$ to $T_{e0} \simeq 100\,\mathrm{eV}$. The lack of bulk heating may be due to a deterioration in the bulk energy confinement time, or to a low rf absorption efficiency, or to poor radial confinement of the fast electron tail.

We have measured x-ray emission spectra and radial profiles during 800 MHz and 2.45 GHz current drive using Si(Li) detector and NaI detector pulse height analysis diagnostics. Measurements made during 2.45 GHz steady-state current drive indicate that an energetic electron tail is generated in the central region of the plasma, with energies up to at least 160 keV. The final steady state x-ray emission spectrum is fairly independent of the number of target plasma superthermals present before the rf injection. From simulations of the relativistic bremsstrahlung x-ray emission, using a simple model distribution function, we have estimated that: 1) $T_\perp \geq 10\,\mathrm{keV}$, 2) most of the plasma energy ($\sim 90\%$) is stored in the fast electron tail, and 3) a small fraction ($\sim 10\%$) of the injected rf power is actually dissipated due to tail-bulk collisions. The latter result is consistent with the lack of significant bulk electron heating observed during the flat-top current drive experiments.

7.2 Discussion

Although the implications of each of these experimental results have been pointed out in the previous chapters, two topics in particular deserve further discussion. Based on the comparison of the 2.45 GHz and 800 MHz current drive experiments, our conclusions about the physical mechanism responsible for the lower hybrid current drive density limit will be summarized first. Subsequently, we will examine possible explanations for the relatively low 2.45 GHz quasi-steady-state current drive efficiency obtained in these experiments. In Section 7.2.3, we will present the numerical results from the Bonoli-Englade simulation model[42] for steady-state current drive.

7.2.1 The Density Limit

We have already concluded from the 2.45 GHz quasi-steady-state results in Chapter 4 that the 800 MHz density limit is not due to the inaccessibility of low-$N_\|$ waves to the plasma center. Since the $N_\|$ spectra launched from the 800 MHz and 2.45 GHz four-waveguide side-launch antennas were similar, and since the toroidal field has remained the same for each frequency, the penetration of the higher frequency waves at higher densities is expected to be worse according to the linear theory of lower-hybrid wave propagation presented in Chapter 2. When toroidal upshifts in $N_\|$ are included in the analysis, the fraction of wave power which is accessible may be improved somewhat. However, toroidal wave propagation effects cannot change the value of $N_{\|acc}$, since it is determined by the plasma parameters.

Nonlinear effects may still alter the value of $N_{\|acc}$. Recently, wave scattering from density fluctuations has been proposed[96] as a mechanism to stimulate the coupling between the slow and fast wave lower hybrid modes, tending to raise the value of $N_{\|acc}$. Since the mode coupling is predicted to increase with density, this mechanism has also been proposed to explain the "density limit." Although the predicted decrease in efficiency with density is much more gradual than the sharp cut-off observed in the Versator II 800 MHz experiment, measurements of the density fluctuation level are needed before the importance of this non-linear effect in the present experiment can be assessed.

We have also concluded from these experiments that the 800 MHz density limit cannot be due to the disappearance of a preformed electron tail above the critical density, since the target plasmas in both experiments were essentially the same. Furthermore, in the 2.45 GHz experiments, we have found that varying the number of target plasma superthermals before the rf pulse had little effect on the 2.45 GHz quasi-steady-state current drive efficiency or the steady state x-ray emission spectrum measured at later times during the rf pulse. Fully rf-driven discharges with the 2.45 GHz rf system have been achieved with negligible levels of hard x-ray emission ($h\nu > 20\,\text{keV}$) from the initial Ohmic target plasma, indicating that operation in the low density "slideaway" regime[8] is not a necessary condition for lower hybrid current drive. Finally, we note that slideaway phenomena during current drive should not depend on the driving frequency, especially in the present experiment where the launched wave spectrum was the same for both 2.45 GHz and 800 MHz.

The most likely remaining explanation of the 800 MHz density limit is a shift of strong rf interaction from electrons to ions, either due to parametric instabilities,[12,17,19,20,22–24] or due to quasi-linear ion Landau damping.[12,17,25] An experimental investigation of ion tail production and parametric excitation at the 800 MHz frequency was outside the scope of this thesis. We note that in previous 800 MHz ion heating experiments,[40] parametric decay and ion tail formation were observed at densities well above the critical density ($\overline{n}_e > 1.3 \times 10^{13}\,\text{cm}^{-3}$).

However, a clear correlation between the disappearance of current drive, and the appearance of parametric decay and ion tails has not yet been established. Further measurements are needed at lower densities where the current drive effects disappear. It appears that a direct switchover from electron Landau damping to ion Landau damping, due to linear mode conversion in the center of the plasma, can be ruled out in the 800 MHz experiments at low toroidal magnetic fields, $B_T < 12\,\mathrm{kG}$. Under these conditions, there is no mode conversion layer present in the plasma.

Because of the 2.45 GHz rf power limitations ($P_{rf} \leq 95\,\mathrm{kW}$), it has not been possible to determine the steady state current drive efficiency $\tilde{\eta}$ at densities above $\overline{n}_e = 1 \times 10^{13}\,\mathrm{cm}^{-3}$. Furthermore, an upper density limit for the 2.45 GHz current drive experiment has not been clearly established, although current drive effects in ohmically heated discharges become substantially diminished at densities exceeding $\overline{n}_e \sim 2 \times 10^{13}\,\mathrm{cm}^{-3}$. A 2.45 GHz "density limit" could result from poor wave accessibility at the highest densities since $\omega_{pe}^2(0)/\omega_{ce}^2 \sim 3$ ($N_{\|acc} = 2.7$). Collisional damping of wave power in the plasma periphery might also lead to a reduction in wave penetration at high densities. Another possible mechanism which could lead to a 2.45 GHz density limit is parametric decay.

So far, only preliminary measurements of the high frequency spectra near the pump frequency have been carried out using an electrostatic rf probe located in the limiter shadow on the top of the torus (see Fig. 1.1). Typical parametric decay spectra at low densities ($\overline{n}_e \leq 1.5 \times 10^{13}\,\mathrm{cm}^{-3}$) exhibit a symmetric frequency broadening of the pump wave which may be due to low frequency ($\leq 1\,\mathrm{MHz}$) density fluctuations. Higher density spectra ($\overline{n}_e \geq 2 \times 10^{13}\,\mathrm{cm}^{-3}$) show more pronounced broadening below the pump frequency. and often exhibit several lower sidebands separated from the pump wave by multiples of $\omega_{ci}/2\pi$ corresponding to a radial position near the outside edge of the plasma. This suggests that the sidebands are generated near the antenna. However, it is not clear from our measurements whether parametric decay could be the cause of reduced wave penetration at higher densities due to pump wave depletion. or whether it is merely a consequence of a buildup of wave energy density in the plasma periphery caused by poor wave accessibility and weak Landau absorption in the center of the plasma. Further measurements with several probes placed at various toroidal locations around the tokamak are needed, as well as a comparison of experimentally measured thresholds with theory to determine the process by which the parametric processes are occurring. In addition, charge exchange measurements would be useful to determine whether the decay waves are damping on ions in the edge region of the plasma.

7.2.2 2.45 GHz Current Drive Efficiency

As shown in Table 1.1, the quasi-steady-state current drive efficiency $\tilde{\eta} = 0.0072$ measured in the present 2.45 GHz experiment on Versator, is approximately a factor of 15 below the level observed on other tokamaks where flat-topping experiments have been carried out (Alcator C,[11] PLT,[10] ASDEX,[22] and Petula B[97]), even though the launched wave spectra are similar in all of the experiments. In part, this may be due to the poor accessibility of low-$N_{\|}$ waves in the Versator II experiment since the toroidal field strength is relatively low ($B \sim 11\,\mathrm{kG}$, $\omega_{pe}^2/\omega_{ce}^2 \sim 0.3 - 1.2$). However, according to the Fisch theory,[3] the steady state current drive efficiency should scale approximately as $\tilde{J}/\tilde{P}_d \propto 1/N_{\|acc}^2$, where the value of $N_{\|acc}$ is given by Eqn. (2.8b). Assuming total absorption of the injected rf power, this scaling predicts a factor of two decrease in the current drive figure of merit $\tilde{\eta}$ over the density range $\bar{n}_e = 0.2 - 1.0 \times 10^{13}\,\mathrm{cm}^{-3}$. If the inaccessible rf power were taken into account, the calculated efficiency would decrease even more rapidly with density. Since $\tilde{\eta} = \bar{n}IR/P$ is approximately constant over the density range $\bar{n}_e = 0.2 - 1.0 \times 10^{13}\,\mathrm{cm}^{-3}$ in the present experiment, we conclude that the Fisch model does not correctly predict the density scaling of the current drive efficiency.

An even greater discrepancy with the Fisch theory[3] arises when the magnitude of the rf current J is calculated for the launched wave spectrum $1 < N_{\|} < 4$. Since the condition for strong electron Landau damping in a 100 eV plasma is $N_{\|} \geq 22$, essentially zero current is predicted. This raises the following question: how do the rf waves with high phase velocities damp on the bulk plasma to form a substantial quasi-linear plateau? A number of theories have been proposed to resolve this "spectral gap" problem. One mechanism whereby high phase velocity waves can interact with low parallel velocity electrons is the anomolous doppler instability.[98] However, in the present experiment, where negligible levels of hard x-ray emission have been observed just prior to quasi-steady-state current drive, it is not clear how the instability is triggered initially to generate the rf plateau. Other non-linear mechanisms which can generate $N_{\|}$ upshifts in the launched wave spectrum include ponderomotive effects,[99] parametric instabilities,[100] and the scattering of waves from density fluctuations.[101] Toroidal wave propagation effects can also account for significant increases in $N_{\|}$ (factors of three or more), and this mechanism[42] appears to be sufficient to account for the observed current drive efficiencies in Alcator and PLT.

The relatively low current drive efficiency on Versator may be due to the low bulk electron temperature ($T_{e0} = 100\,\mathrm{eV}$). The linear correlation between bulk electron temperature and the level of current drive efficiency observed in present-day experiments has been previously pointed out.[4] For example, on Alcator C and PLT, both the current drive efficiency ($\tilde{\eta} \geq 0.1$) and the bulk electron temperature ($T_{e0} \gtrsim 1\,\mathrm{keV}$) exceed the values measured on Versator by approximately an order of magnitude. This trend cannot be understood from the Fisch theory[3] [see Eqn. (2.39)]. However, it may be related to the spectral gap problem, since the launched wave spectra in all of the experiments are nearly the same. A wide spectral gap, due to a low bulk temperature, could reduce the current drive efficiency if the condition for strong electron Landau damping was not satisfied, i.e. if $\alpha = P_{ELD}/P_{rf} \ll 1$. Increased collisional damping at low plasma temperatures could also play an important role in reducing the resonant absorption efficiency. Alternatively, the spectral gap in lower temperature plasmas may be closed because of larger $N_{\|}$ upshifts in the launched wave spectrum. In this case, the current drive efficiency would be relatively low because of a larger decrease in the parallel phase velocity of the resonant waves.

The comparison of the 2.45 GHz current drive data in Chapter 4 with the Fisch-Karney ramp-up theory[30] indicates that the absorption efficiency in the present experiment is reasonably high ($\alpha \geq 0.50$). The low current drive efficiency might be explained by substantial $N_{\|}$-upshifts in the launched wave spectrum ($N_{\|}^{*} \simeq 9$). Interestingly, the $N_{\|}^{*}$ value deduced from the Versator 2.45 GHz data analysis is substantially higher than those values estimated on Alcator C ($N_{\|}^{*} \sim 3.5$) and PLT ($N_{\|}^{*} \sim 2.8$) from similar analyses. This would nearly account for the difference in steady state efficiencies, since $\tilde{\eta} \sim 1/N_{\|}^{*2}$. However, this simple picture suggested by the ramp-up analysis must be interpreted cautiously since the theory assumes a narrow wave spectrum, it neglects the back current generated by the $-N_{\|}$ component of the Brambilla spectrum, and it assumes that the confinement time of the tail particles is long compared to the slowing down time due to bulk collisions. This last condition may not be satisfied in the Versator II experiments.

An alternative explanation for the low current drive efficiency is suggested by the x-ray analysis of Chapter 6. Those results indicated that the fraction of the injected rf power actually dissipated due to tail-bulk collisions was quite small ($P_d \leq 0.1P_{rf}$), implying that most of the absorbed power may be lost due to poor radial confinement of the fast electron tail. In the steady-state current drive and ramp-up theories outlined in Chapter 2, it was assumed that the confinement time of the tail particles greatly exceeded the slowing down time due to bulk collisions, so that $P_{rf} = P_d$. However, it is clear that if the tail particles were confined for a relatively short time compared to their collisional slowing time, $\tau_t < \nu_s^{-1}$, their contribution to the current would be reduced, lowering the current drive efficiency. This picture is consistent with the analysis of the ramp-up data. If the finite confinement time of the tail particles had been properly taken into account, and the theoretical value for the efficiency P_{el}/P_{rf} was reduced, then to match the experimental data to the theory, a lower value of $N_{\|}^{*}$ would have been chosen. Hence, the high value deduced for $N_{\|}^{*}$ may not necessarily represent a typical resonant wave phase velocity, but rather, it may reflect poor tail confinement. Since poor radial confinement of the fast electron tail particles results in both a lower current drive efficiency $\tilde{\eta}$ and a low bulk temperature T_e, this effect may also be consistent with the apparent temperature dependence of $\tilde{\eta}$ observed in different experiments. The importance of tail confinement has been noted very recently in the Alcator C experiments at low densities.[36]

In summary, the results from the present experiment suggest that the simple steady state current drive model of Fisch[3] does not include a number of effects which may play an important role in determining the experimental current drive efficiency and its scaling with density. These include: 1) reduced wave absorption by Landau damping on tail electrons due to a wide spectral gap, poor accessibility, or collisional damping in the edge plasma, 2) $N_{\|}$ upshifts which may be necessary to fill in the spectral gap, and 3) tail confinement losses which may occur on time scales comparable to or less than the collisional slowing down time. These effects have been incorporated into the Bonoli-Englade steady-state current drive simulation code[42] which has been used to model our experimental results.

7.2.3 Bonoli-Englade Code Modelling Results

The Bonoli-Englade simulation model[42] for steady state lower hybrid current drive consists of a toroidal ray tracing code and a relativistic 1-d Fokker-Planck calculation. Upshifts in the parallel refractive index due to toroidal wave propagation effects provide the mechanism to fill in the spectral gap in velocity space. By combining the ray-tracing code with the Fokker-Planck calculation, the damping of the waves and the subsequent quasi-linear flattening of the distribution function is treated in a self-consistent manner. The model incorporates 2-d effects into the 1-d Fokker-Planck equations by using the analytic prescription of Fuchs et al.[56] The confinement of energetic tail electrons is modelled in the Fokker Planck equation by including a term $(\partial f_e/\partial t)_\tau = f_e/\tau_t(p_{\|})$, where $\tau_t = \tau_0\gamma^3$ is the form chosen for the global tail confinement time,[102] with τ_0 approximately given by the bulk energy confinement time.

Typical conditions used in the modelling of Versator II 2.45 GHz steady state current drive were as follows: $\overline{n}_e = 8 \times 10^{12}\,\mathrm{cm}^{-3}$, $n_{e0} = 1.5\overline{n}_e$, $n_{ea} = 0.1n_{e0}$, $T_{e0} = 130\,\mathrm{eV}$, $T_{i0} = 50\,\mathrm{eV}$, $T_{ea} = T_{ia} = 20\,\mathrm{eV}$ (edge temperatures), $Z_{eff} = 2$, $B_T = 11\,\mathrm{kG}$, $\Delta\phi = \pi/2$, $P_{rf} = 76\,\mathrm{kW}$, and a hydrogen plasma. The value used for the electron tail confinement time was $\tau_0 \simeq 1.5\,\mathrm{ms}$, which is consistent with the x-ray estimates of Chapter 6. Under these conditions, 66 kW of the 76 kW of injected power was absorbed, with 23 kW due to collisional damping. A total of 43 kW was absorbed by electron Landau damping, with 20 kW going into electron tail losses. The remaining power was unaccounted for because the ray propagation was terminated after numerous passes through the plasma. Thus, $P_{rf} = 76\,\mathrm{kW}$, $P_{coll} = 23\,\mathrm{kW}$, $P_\tau = 20\,\mathrm{kW}$, $P_d = 23.6\,\mathrm{kW}$. The total rf current generated was $I_{rf} = 17.4\,\mathrm{kA}$, with the forward current $I_{rf+} = 33.4\,\mathrm{kA}$ due to waves with positive $N_{\|}$ and the backward current $I_{rf-} = 16.0\,\mathrm{kA}$ due to waves with negative $N_{\|}$. The steady state efficiency was $\tilde{\eta} = 0.0073$, which was in good agreement with the experimental value.

The resulting quasi-linear distribution function in the parallel direction is shown in Fig. 7.1 for the radius $r = 2.28\,\mathrm{cm}$, which corresponds to the peak of the rf current profile. On the positive side of the distribution function, the rf-generated plateau extends from $w_1 = v_{\|}/v_e \simeq 2.4$ to $w_2 = v_{\|}/v_e \simeq 24$, with the upper limit corresponding to the accessibility condition [see Eqn. (2.8b)], and the lower limit corresponding to the condition for strong electron Landau damping [see Eqn. (2.21)]. There is also a significant plateau generated in the $-v_{\|}$ direction by the negative component of the Brambilla spectrum $-9 < N_{\|} < -6$, which is sufficiently large to cancel one-half of the rf current generated in the forward direction by the $+N_{\|}$ spectrum. The presence of this large back current effectively reduces the current drive efficiency by a factor of three $[(I_+ - I_-)/(I_+ + I_-) \simeq 1/3]$.

Although the launched waves experience large upshifts in $N_{\|}$ ($\times 2 - 3$) due to toroidal effects, these are not sufficient to bridge the spectral gap on the positive side of the distribution function. On the negative side, because of the higher $N_{\|}$ values launched, toroidal upshifts are sufficient to close the gap. The result would be a net negative current except that a high-$N_{\|}$ component in the Brambilla spectrum ($11 < N_{\|} < 15$) flattens the positive distribution function in the region near $\varepsilon \simeq 1\,\mathrm{keV}$. However, when the bulk electron temperature is lowered in the code from 130 eV to 100 eV (the experimental value), the computed efficiency drops by

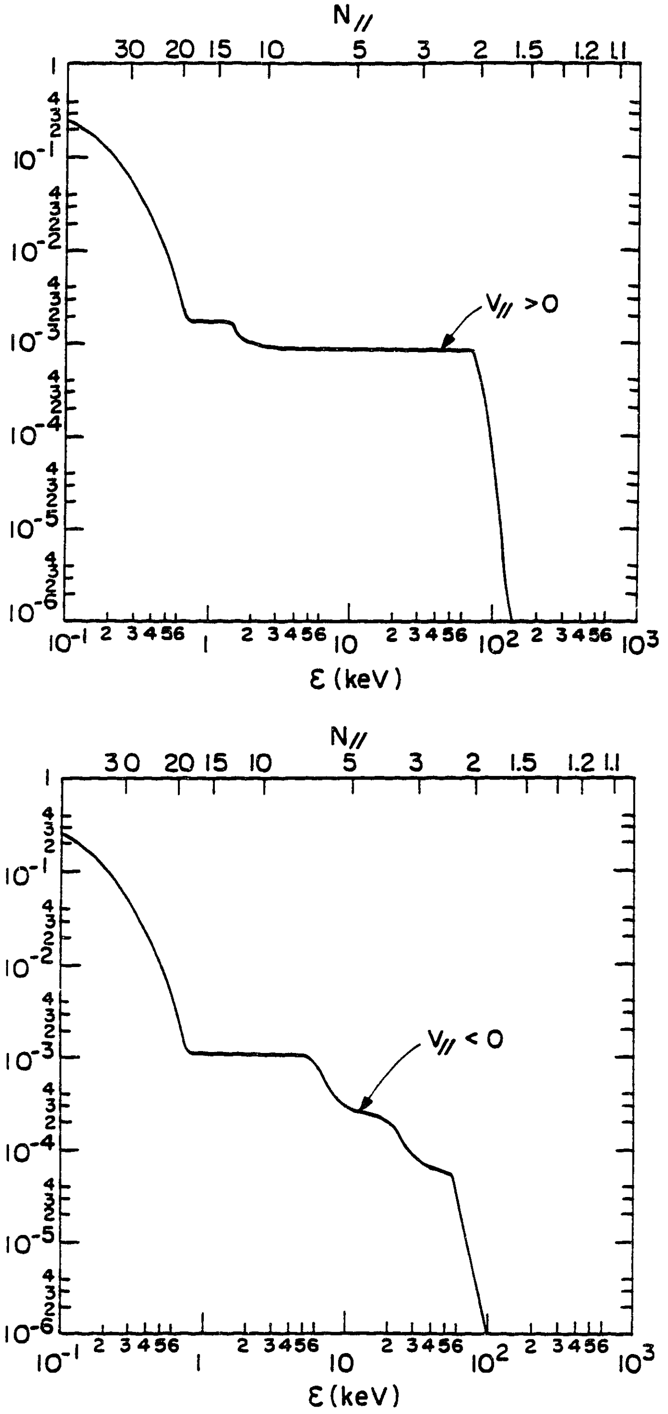

Fig. 7.1: Quasi-linear electron distribution function calculated at a radial location $r = 2.28\,\mathrm{cm}$ versus the parallel kinetic energy.

nearly a factor of two, due to a decrease in electron Landau damping and an increase in the collisional damping. These results indicate that in the present experiments toroidal upshifts of $N_{||}$ may not be sufficient to close the spectral gap.

The dependence of the current drive efficiency on the tail confinement time, the value of τ_0 was varied while the density and temperature were fixed at $\overline{n}_e = 8 \times 10^{12}\,\mathrm{cm}^{-3}$ and $T_{e0} = 130\,\mathrm{eV}$ respectively. When τ_0 was reduced from 1.5 ms to 0.5 ms, the current drive efficiency $\tilde{\eta}$ dropped substantially, from 0.0073 to 0.0036, due to an increase in the fractional tail losses P_τ / P_{ELD} from 0.465 to 0.669. On the other hand, when the tail confinement parameter was raised to $\tau_0 = 150\,\mathrm{ms}$ so that the tail losses were nearly zero, $P_{ELD} \simeq P_d$, the current drive efficiency increased only by 50%, to $\tilde{\eta} = 0.011$. While the level of current drive efficiency predicted by the code clearly depends on the value chosen for τ_0, it appears from this latter result that poor tail confinement alone cannot account for the relatively low current drive efficiency observed in the Versator II tokamak.

Finally, the dependence of the current drive efficiency on density was investigated over the range $\overline{n}_e = 0.4 - 1.2 \times 10^{13}\,\mathrm{cm}^{-3}$, with the confinement time ($\tau_0 = 1.5\,\mathrm{ms}$) and the bulk temperature ($T_e = 130\,\mathrm{eV}$) held constant. The value of $\tilde{\eta}$ predicted by the code increased very slightly from $\tilde{\eta} = 0.006$ to $\tilde{\eta} = 0.008$, in reasonable agreement with the experimental results. The density independence of $\tilde{\eta}$ appears to be the result of two offsetting trends. On the one hand, as the density is raised, wave accessibility worsens and collisional damping increases, tending to lower the current drive efficiency as discussed previously. Note in particular that in the code, P_{coll}/P_{rf} increases from 0.184 to 0.421, while P_{ELD}/P_{rf} decreases from 0.700 to 0.474 over the density interval studied. On the other hand, as the density is raised, the tail losses are reduced because the collisional slowing down time scale decreases relative to the fixed confinement time. In the code, the fractional power dissipated by tail-bulk collisions, P_d/P_{ELD}, increases from 0.37 to 0.74 over the density range, tending to raise the efficiency. Given the simple assumptions made regarding the bulk temperature and confinement time parameters, the agreement with experiment must be regarded as somewhat fortuitous. More accurate experimental estimates of the tail confinement time, as well as bulk temperature measurements as a function of density, are needed to improve the model. Nevertheless. these results do provide one possible explanation for the observed density scaling of the current drive efficiency in the present experiment.

In summary, the Bonoli-Englade code simulations indicate that the order of magnitude lower current drive efficiency observed in the present experiment, compared to Alcator C and PLT. may be due to a combination of effects including poorer wave accessibility, a lower bulk electron temperature and increased collisional damping. larger negative rf current generation due to waves with $N_{\|} < 0$, and poorer electron electron tail confinement. A possible explanation for the observed scaling of the current drive efficiency with density has been suggested, namely that the deleterious effects of poor accessibility and collisional damping at higher densities are offset by reductions in tail confinement losses due to increasing tail-bulk collisionality. Finally, although toroidal upshifts in the $N_{\|}$ values of the launched wave spectrum may lead to significant electron Landau damping, additional non-linear mechanisms may be required to fill in the spectral gap when the bulk temperature is sufficiently low ($T_e \leq 100\,\mathrm{eV}$). These results indicate the importance of including wave propagation and wave absorption physics into the theory of lower hybrid current drive.

7.3 Conclusions

To summarize, the slow-wave lower hybrid current drive "density limit" depends on the wave frequency. Steady-state current drive above the "density limit" can be achieved by raising only the rf frequency, without changing the launched-wave $N_{\|}$-spectrum or increasing the toroidal magnetic field. From our 2.45 GHz experiments, we have eliminated several possible explanations for the 800 MHz density limit. The most likely remaining candidate appears to be a switchover of wave interaction from electrons to ions due to parametric decay when $\omega/\omega_{LH} < 2$. We also have demonstrated that fully rf-driven discharges can be achieved with $\omega_{pe}^2/\omega_{ce}^2 \geq 1$, as long as ω is sufficiently high to avoid the density limit. An upper density limit for 2.45 GHz current drive on Versator has yet to be firmly established due to power limitations. Nevertheless, current drive effects in ohmically-heated discharges, including improvements in the global particle confinement time, are observed at densities at least a factor of three above the 800 MHz limit.

The relatively low quasi-steady-state current drive efficiency $\tilde{\eta} = 0.0072$ observed in the present experiment may be due to a number of factors including the poor accessibility of low-$N_{\parallel}$ waves, the low bulk temperature (spectral gap), and the relatively poor confinement of the energetic electron tail. The latter two effects should become less important in future devices with good confinement and higher bulk temperatures. Even so, the accessibility condition, which applies to the slow-wave lower hybrid experiments today, restricts the upper range of resonant wave phase velocities to $v_{\phi} \leq c/2$ when $\omega_{pe}^2/\omega_{ce}^2 \sim 1$. The maximum value of $\tilde{\eta}$ predicted by the Fisch-Karney theory[5] in that regime is $\tilde{\eta} \simeq 0.5$ (MKS units used before). In order to achieve more efficient lower hybrid current drive at a dielectric constant of $\omega_{pe}^2/\omega_{ce}^2 \sim 1$, it may be necessary to use low frequency $(\omega^2/\omega_{ce}\omega_{ci} \ll 1)$ fast waves. Linear theory predicts good accessibility for low-$N_{\parallel}$ waves $(N_{\parallel} \sim 1.1)$ which are the most efficient in driving current ($\tilde{\eta} \simeq 1 - 2$ may be possible). However, the existence or lack of a density limit for fast wave current drive schemes remains to be investigated experimentally.

References

1. N.J. Fisch, in *Heating in Toroidal Plasmas, Proceedings of the 2nd Joint Grenoble-Varenna Int. Symp.* (Como, Italy), EUR 7997EN, Vol. II, 1980, p. 1157.

2. J.G. Cordey, *Plasma Phys. and Controlled Fusion* **26**, 123 (1984).

3. N.J. Fisch, *Phys. Rev. Lett.* **41**, 873 (1978).

4. M. Porkolab, IEEE Trans. on Plasma Sci. **PS-12**, No. 2, 107 (1984); and M. Porkolab, in *Wave Heating and Current Drive in Plasmas*, V.L. Granatstein and P.L. Colestock, Eds. New York: Gordon and Breach, 1985, p. 219.

5. C.F.F. Karney and N.J. Fisch, *Phys. Fluids* **28**, 116 (1985).

6. T. Yamamoto et al., *Phys. Rev. Lett.* **45**, 716 (1980).

7. S.C. Luckhardt et al., *Phys. Rev. Lett.* **48**, 152 (1982).

8. B. Coppi, F. Pegoraro, R. Pozzoli, and G. Rewoldt, *Nucl. Fusion* **16**, 309 (1976).

9. G. Fussman et al., *Phys. Rev. Lett.* **47**, 1004 (1981).

10. S. Bernabei et al., *Phys. Rev. Lett.* **49**, 1255 (1982).

11. M. Porkolab et al., *Phys. Rev. Lett.* **53**, 450 (1984).

12. Y. Takase et al., *Phys. Rev. Lett.* **53**, 274 (1984); and Y. Takase et al., *Phys. Fluids* **28**, 983 (1985).

13. F. Jobes et al., *Phys. Rev. Lett.* **52**, 1005 (1984).

14. S. Kubo et al., *Phys. Rev. Lett.* **50**, 1994 (1983).

15. K. Toi et al., *Phys. Rev. Lett.* **52**, 2144 (1984).

16. F.C. Jobes et al.. *Phys. Rev. Lett.* **55**, 1295 (1985).

17. Y. Takase, in *Radiofrequency Plasma Heating (Sixth Topical Conf).* (Callaway Gardens, GA), D.G. Swanson, Ed. New York: Amer. Inst. of Phys.. 1985, p. 186.

18. F. Leuterer et al., *Phys. Rev. Lett.* **55**, 75 (1985).

19. J-G. Wegrowe and F. Engelmann, *Comments Plasma Phys. Controlled Fusion* **8**, 211 (1984).

20. W. Hooke, *Plasma Phys. and Controlled Fusion* **26**, 133 (1984).

21. M. Porkolab, S. Bernabei, W.M. Hooke, and R.W. Motley, *Phys. Rev. Lett* **38**, 230 (1977).

22. F. Leuterer et al., in *Proceedings of the Tenth International Conference on Plasma Physics and Controlled Fusion Research* (London, England). Vienna: IAEA, 1984, Paper No. IAEA-CN-44/F-IV-3.

23. T. Yamamoto et al., in *Non-Inductive Current Drive in Tokamaks, Proceedings of the IAEA Technical Comm. Meeting* (Culham, England), D.F.H. Start, Ed. Abington, U.K.: Culham Lab, 1983, Vol. I, p. 224.

24. G. Tonon et al., in *Heating in Toroidal Plasmas III, Proceedings of the 3rd Joint Grenoble-Varenna Int. Symp.* (Grenoble, France, 1982), EUR 7997EN, Vol. II, p. 1157.

25. F. Alladio et al., in *Proceedings of the Tenth International Conference on Plasma Physics and Controlled Fusion Research* (London, England). Vienna: IAEA, 1984, Paper No. IAEA-CN-44/F-II-3.

26. S.C. Luckhardt et al., in *Heating in Toroidal Plasmas III, Proceedings of the 3rd Joint Grenoble-Varenna Int. Symp.* (Grenoble, France, 1982), EUR 7997EN, Vol. II, p. 529.

27. J. Ramos, MIT Plasma Fusion Center Report No. PFC/RR-82-28 (1982).

28. S.C. Luckhardt, private communication.

29. M.J. Mayberry et al., *Phys. Rev. Lett.* **55**, 829 (1985).

30. N.J. Fisch and C.F.F. Karney, *Phys. Rev. Lett.* **54**, 897 (1985).

31. B. Lloyd et al., in *Non-Inductive Current Drive in Tokamaks, Proceedings of the IAEA Technical Comm. Meeting* (Culham, England), D.F.H. Start, Ed. Abington, U.K.: Culham Lab, 1983, Vol. I, p. 224.

32. S.C. Luckhardt et al., MIT Plasma Fusion Center Report No. PFC/JA-84-42 (1984) (to be published in *Phys. Fluids*).

33. M.J. Mayberry et al., *Bull. Amer. Phys. Soc.* **30**, 1622 (1985).

34. S. von Geoler et al., *Nucl. Fusion* **25**, 1515 (1985).

35. J. Stevens et al., *Nucl. Fusion* **25**, 1529 (1985).

36. S. Texter, Ph.D. thesis, Dept. of Physics, Massachusetts Institute of Technology (1985).

37. B. Richards, Ph.D. thesis, Dept. of Physics, Massachusetts Institute of Technology (1981).

38. K.E. Hackett, Ph.D. thesis, Dept. of Physics, Massachusetts Institute of Technology (1983).

39. A.S. Fisher, Ph.D. thesis, Dept. of Physics, Massachusetts Institute of Technology (1983).

40. S.F. Knowlton. Ph.D. thesis, Dept. of Physics, Massachusetts Institute of Technology (1983).

41. F.S. McDermott, Ph.D. thesis, Dept. of Physics, Massachusetts Institute of Technology (1984).

42. P. Bonoli and R. Englade, MIT Plasma Fusion Center Report No. PFC/JA-86-5 (1986) (to be published).

43. M. Porkolab, "Radio-Frequency Heating of Magnetically Confined Plasma," in *Fusion*, E. Teller, Ed. New York: McGraw-Hill, 1981, Ch. 13.

44. P. Bonoli, in *IEEE Trans. on Plasma Sci.* **PS-12**, No. 2, 95 (1984); and P. Bonoli, in *Wave Heating and Current Drive in Plasmas*, V.L. Granatstein and P.L. Colestock, Eds. New York: Gordon and Breach, 1985, p. 175.

45. A. Bers, in *Proc. Third Topical Conf. on Radio Frequency Plasma Heating* (Pasadena. CA), 1978, Paper A-1.

46. T.H. Stix. *The Theory of Plasma Waves.* New York: McGraw-Hill, 1962.

47. V.E. Golant, *Sov. Phys. Tech. Phys.* **16**, 1095 (1962).

48. F. Troyon and F.W. Perkins, in *Proc. Second Topical Conf. on Radio Frequency Plasma Heating* (Texas Tech. Univ., Lubbock, Tx), 1974, Paper B4.

49. P.M. Bellan and M. Porkolab, *Phys. Fluids* **19**, 995 (1976).

50. T.H. Stix, *Phys. Rev. Lett.* **15**, 878 (1965).

51. M. Brambilla, *Plasma Physics* **18**, 669 (1976).

52. C.F.F. Karney, *Phys. Fluids* **21**, 1584 (1978); and C.F.F. Karney, *Phys. Fluids* **22**, 2188 (1979).

53. M. Brambilla. *Nucl. Fusion* **18**, 493 (1978).

54. N.J. Fisch and A.H. Boozer, *Phys. Rev. Lett.* **45**, 720 (1980).

55. C.F.F. Karney and N.J. Fisch, *Phys. Fluids* **22**, 1817 (1979).

56. V. Fuchs et al.. *Phys. Fluids* **28**, 3619 (1985).

57. N.J. Fisch, *Phys. Rev. A* **24**, 3245 (1981).

58. K. Hizinidis and A. Bers, *Phys. Fluids* **27**, 2669 (1984).

59. N.J. Fisch, *Phys. Fluids* **28**, 245 (1985).

60. C.F.F. Karney, N.J. Fisch, and F.C. Jobes, Princeton Plasma Physics Laboratory Report No. PPPL-2152 (1984) (to be published in *Phys. Rev. A*).

61. C.S. Liu, V.S. Chan, and Y.C. Lee, *Phys. Rev. Lett.* **55**, 2583 (1985).

62. The klystrons were used previously for the Alcator A ion heating experiments; see J.J. Schuss et al., *Nucl. Fusion* **21**, 427 (1981).

63. M. Brambilla. *Nucl. Fusion* **16**, 47 (1976).

64. J. Stevens et al.. *Nucl. Fusion* **21**, 1259 (1981).

65. S.C. Luckhardt et al., in *Heating in Toroidal Plasmas III, Proceedings of the 3rd Joint Grenoble-Varenna Int. Symp.* (Grenoble, France, 1982), EUR 7997EN, Vol. II, 1982, p. 529.

66. M. Brambilla, *Nucl. Fusion* **19**, 1343 (1979).

67. S.F. Knowlton, M. Porkolab, and S.C. Luckhardt, in *Heating in Toroidal Plasmas III, Proc. of the 3rd Joint Varenna-Grenoble Int. Symp.* (Grenoble, France, 1982) EUR 7997 EN, Vol. III, p. 1149.

68. V.S. Mukhovatov and V.D. Shavranov, *Nucl. Fusion* **11**, 65 (1971).

69. V.V. Parail and O.P. Pogutse, *Nucl. Fusion* **18**, 303 (1978).

70. K. Molvig, M.S. Tekula, and A. Bers, *Phys. Rev. Lett.* **38**, 1404 (1977).

71. A. Mondelli and E. Ott, *Phys. Fluids* **17**, 1017 (1974).

72. L.C. Johnson and E. Hinnov, *J. Quant. Spectrosc. Radiat. Transfer* **13**, 333 (1973)

73. The H_α and VUV measurements were performed by K-I. Chen.

74. K-I. Chen, private communication.

75. W.M. Stacey and D.J. Sigmar, *Nucl. Fusion* **19**, 1665 (1979).

76. V. Pericoli-Ridolfini, *Plasma Phys. and Controlled Fusion* **27**, 709 (1985).

77. K. Ohkubo et al., in *Heating in Toroidal Plasmas III, Proc. of the 3rd Joint Varenna-Grenoble Int. Symp.* (Grenoble, France, 1982) EUR 7997EN, Vol. II, p. 1149.

78. K. Uehara and T. Nagashima, in *Heating in Toroidal Plasmas III. Proc. of the 3rd Joint Varenna-Grenoble Int. Symp.* (Grenoble. France, 1982) EUR 7979EN. Vol. II, p. 485.

79. The Thomson scattering measurements were performed by K-I. Chen.

80. M. Porkolab et al., *Phys. Rev. Lett.* **53**, 1229 (1984).

81. F. Söldner et al., in *Proc. of the 12th European Conf. on Controlled Fusion and Plasma Phys.* (European Phys. Soc., Budapest, Hungary, 1985), L. Pócs, A. Motvai. Eds., Vol. 2, p. 244.

82. J.E. Stevens et al., in *Proc. of the 12th European Conf. on Controlled Fusion and Plasma Phys.* (European Phys. Soc., Budapest, Hungary, 1985), L. Pócs, A. Motvai, Eds., Vol. 2, p. 192.

83. C. Gormezano et al., in *Heating in Toroidal Plasmas III, Proc. of the 3rd Joint Varenna-Grenoble Int. Symp.* (Grenoble, France, 1982) EUR 7979EN, Vol. II, p. 439.

84. S. Bernabei et al., in *Proc. of Symp. on Plasma Heating in Toroidal Devices* (Varenna, Italy). (Editrice Compositori, Bologna, Italy, 1976), p. 68.

85. M. Porkolab et al., *Bull. Amer. Phys. Soc.* **30**, 1493 (1985).

86. R.E. Bell et al.. *Bull. Amer. Phys. Soc.* **30**. 1571 (1985): and T.K. Chu et al., in *Radiofrequency Plasma Heating (Sixth Topical Conf.)* (Callaway Gardens, GA, 1985). D.G. Swanson, Ed. New York: Amer. Inst. of Phys., 1985, p 131.

87. S. von Goeler et al., Princeton Plasma Physics Lab. Report No. MATT-1060 (1974); and S. von Goeler. in *Diagnostics for Fusion Experiments (Proc. Course Varenna, Italy).* E. Sindoni and C. Wharton, eds., Oxford: Pergamon, 1978, p. 79.

88. E. Silver et al., *Rev. Sci. Instrum.* **53**. 1198 (1982).

89. F. Briggs and R. Lighthill, Sandia Lab. Report No. SC-RR-710507 (1971).

90. S. von Goeler et al., *Nucl. Fusion* **15**, 301 (1975).

91. S. von Goeler et al., Princeton Plasma Physics Lab. Report No. PPPL-2010.

92. M.W. Koch and J.W. Motz, *Rev. Mod. Phys.* **31**, 920 (1959).

93. S. von Goeler et al., in *Proceedings of the Fifth Topical Conference on RF Plasma Heating* (University of Wisconsin, Madison, 1983), p. 96.

94. S.C. Luckhardt, in *Radiofrequency Plasma Heating (Sixth Topical Conf.)* (Callaway Gardens, GA), D.G. Swanson, Ed. New York: Amer. Inst. of Phys., New York, 1985, p. 158.

95. S.C. Luckhardt et al., *Bull. Amer. Phys. Soc.* **30**, 1621 (1985).

96. P.L. Andrews. *Phys. Rev. Lett.* **54**, 2022 (1985).

97. C. Gormezano et al., in *Radiofrequency Plasma Heating (Sixth Topical Conference)* (Callaway Gardens, GA), D.G. Swanson, Ed. New York: Amer. Inst. of Phys., 1985, p. 111.

98. C.S. Liu. V.S. Chan, D.K. Bhadra, and R.W. Harvey. *Phys. Rev. Lett.* **48**. 1479 (1982).

99. E. Canobbio and R. Croci, in *Radiofrequency Plasma Heating (Sixth Topical Conference)* (Callaway Gardens, GA), D.G. Swanson, Ed. New York: Amer. Inst. of Phys., 1985, p. 143.

100. K.L. Wong, J.R. Wilson and M. Porkolab. *Phys. Fluids* **25**, 359 (1982).

101. P.T. Bonoli and E. Ott, *Phys. Fluids* **25**, 359 (1982).

102. H.E. Mynick and J.D. Strachan, *Phys. Fluids* **24**, 695 (1981).